Paleoenvironments and petrologic history of the Hartmann's Valley, Karasburg, and Sutton Island members of the Murray formation, Gale crater, Mars

A Dissertation Presented for the
Doctor of Philosophy
Degree
The University of Tennessee, Knoxville

Samantha Justine Gwizd
May 2023

DEDICATION

To mom and dad (back ‘em).

ACKNOWLEDGEMENTS

This research was funded in part by JPL subcontract #1546201, and would not be possible without NASA’s Mars Science Laboratory (MSL) Curiosity rover mission. I would like to acknowledge the tremendous efforts of the MSL team in providing operational support to the Curiosity rover and for giving me the truly amazing opportunity to participate in mission operations and experience scientific collaboration with a team of people around the world.

Thank you to my advisor, Dr. Chris Fedo, for all of your guidance, support, and advice throughout this degree. I will be forever grateful that you took me with you to Mars and gave me this incredible and unique opportunity to develop my sedimentology and stratigraphy skills on another planet. Thank you to my committee members Drs. Linda Kah, Molly McCanta, Drew Steen, and Michael Essington, for your insightful feedback and invaluable support. I would also like to acknowledge the support of Dr. Brad Thomson for his helpful advice and encouragement of my future career path.

Thank you to many EPS graduate students past and present, including: the Fedo lab group throughout the years (Jason, Morgan, Constance, Cat, Kristan), my fellow martian Rachel, Audrey, Diego, Jessi, Ari, Cole, Megan, Claire, Nadine, Tyler, Cam H., Cam H. II, Cam M., Hannah, Maggie, CJ, Louisa, Aidan, Sarah, and Joe (and everyone’s dogs and cats for their snuggles). It takes an academic village, and I’m eternally grateful for mine.

Endless thank-yous to the many others in my non-academic village, without whom this dissertation would not have been possible: Mom & Dad, Grandma Myrna, Z & D, Katie, Megan, RTCF lifting crew (Josh & Brandon)- thank you!

And of course, my dog Watson: thank you for the endless snuggles and forced breaks to go outside and look at nature. “The world would be a nicer place if everyone had the ability to love as unconditionally as a dog”.

ABSTRACT

Today, the surface of Mars is predominantly shaped by aeolian processes, yet stratigraphic and compositional evidence suggests that rivers, deltas, and lakes occurred in the geologic past. Orbital and rover analyses of stratigraphy provides evidence that Gale crater, the site of the Mars Science Laboratory Curiosity rover mission, once contained paleolake and lake-margin environment(s) recorded in the 320 m thick Murray formation. This research utilizes combined sedimentologic, stratigraphic, and compositional analyses to investigate three stratigraphic members of the Murray formation. The primary goal of these chapters is to determine ancient environments and sedimentary processes recorded in stratigraphy and to assess the evolution of aqueous systems compared to the overall Murray formation.

Chapter 1 presents facies and geochemical analyses of the Hartmann's Valley and Karasburg members, which were initially distinguished by intervals of meter-scale cross-stratified sandstone. Three facies are described: cross-stratified sandstone, planar-laminated sandstone, and planar-laminated mudstone. Sandstone facies represent wet aeolian dune and interdune environments along a lake margin, and mudstone facies represent deposition in a long-lived lake basin. Compositional trends record moderate chemical weathering and hydrodynamic sorting of sediment in transport. The stratigraphic distribution of facies is indicative of an interval of lake expansion.

Chapter 2 details facies analysis of the overlying Sutton Island member, which consists of two facies associations: (a) Facies Association 1 (FA1) and (b) Facies Association 2 (FA2). Facies Association 1 represents the lowermost and uppermost intervals of stratigraphy, and consists of distal delta plain facies. Facies Association 2 represents the middle interval of stratigraphy and consists of planar-laminated mudstone, interpreted to represent deposition in a lacustrine environment characterized by sufficient standing water to allow for accommodation of strata. The first transition from FA1 to FA2 is interpreted to represent a rapid transgression, followed by a forced regression from FA2 back to FA1.

Chapter 3 focuses on the compositional record of source rock, weathering, transport, and diagenesis within the Sutton Island member stratigraphy through contextualization with Facies Associations interpreted in Chapter 2. Facies represent a basaltic source primarily from the crater rim. Moderate weathering is indicated by weathering indices and geochemical trends. Immobile oxides provide some evidence for hydrodynamic sorting, and geochemical overlap between facies and grain sizes may be indicative of an aphyric source composition or a restricted grain-size range between FA1 and FA2. Overall, whole-rock geochemical signatures highlight the longevity of aqueous processes from sediment formation through lithification.

PREFACE

"I never realized how beautiful this place was."

-Harry Potter and the Half Blood Prince (film)

TABLE OF CONTENTS

LIST OF TABLES

LIST OF FIGURES

LIST OF ADDITIONAL FILE ATTACHMENTS

INTRODUCTION

Depositional environments of ancient Mars

Sedimentary deposits comprise a significant component of the Martian landscape (Squyres et al., 2004; Milliken et al., 2010; Grotzinger et al., 2015; Edgett et al., 2020). Initial images from the Mariner missions of the 1960s and 1970s identified channel-like features and canyons within layered strata, potentially indicating erosion by water (McCauley et al., 1972). More recent, higher resolution orbital images of stratigraphy corroborate those initial geomorphic observations with interpretations of paleolakes, rivers, and deltas based on stratigraphy, geochemistry, and mineralogy (Fedo et al., 2022; Malin and Edgett, 2000; Warner et al., 2010; Weitz et al., 2010). In addition to paleoenvironments, widespread transitions from clay to sulfate to oxide mineralogy are identified in the stratigraphy from imaging spectrometry (Bibring et al., 2006; Milliken et al., 2010), and preserve a record of climate evolution on Mars (Grotzinger et al., 2015) from very Earth-like early on to the cold, hyper-arid planet of today.

To fully understand environmental transitions in the ancient Martian landscape, combined assessments of depositional environments and compositional trends recorded in stratigraphy is crucial at the highest possible resolutions. Recent decades of robotic exploration on the surface of Mars have enabled further resolution of depositional processes and compositional signatures of sedimentary facies down to grain scales (Grotzinger et al., 2015; Grotzinger & Milliken, 2012; McLennan et al., 2019). Studies of rover-explored stratigraphic successions have identified facies whose sedimentary structures, textures, and compositional trends show considerable diversity of aqueous environments within the stratigraphic record. Fluvial (Caravaca et al., 2022; Edgar et al., 2017; Williams et al., 2013), lacustrine (Edgar et al., 2014, 2020; Fedo et al., 2022; Stack et al., 2019), wet aeolian (Grotzinger et al., 2005; Gwizd et al., 2022), and deltaic (Grotzinger et al., 2015; Mangold et al., 2021) environments have been documented at Gale crater, Jezero crater, and Meridiani Planum, highlighting the prevalence of aqueous activity within the ancient Martian landscape and supporting hypotheses that Mars was once habitable (Grotzinger et al., 2014).

Constraints from the stratigraphic record at Gale crater

Gale crater, a 155-km diameter complex impact crater and the site of the Mars Science Laboratory (MSL) Curiosity rover mission, formed in the late Noachian/Early Hesperian astride the dichotomy boundary between the southern highlands and the northern plains of Mars (~3.55-3.8 Ga; Thomson et al., 2011; Schwenzer et al., 2012; Le Deit et al., 2013). Sediment infill is interpreted to have occurred within a few hundred million years after crater formation (Grotzinger et al., 2015; Palucis et al., 2014). Exhumed strata are subdivided into two main regions: (1) the intracrater plains (Aeolus Palus), and (2) the central mound (Aeolus Mons, informally Mount Sharp). Mount Sharp is an ideal location to study depositional environments and compositional signatures due to the continuous exposure of stratigraphy throughout the 5.5-km high mound. The Murray formation, which comprises the lowermost 320 m of stratigraphy within the Mount Sharp group, is subdivided into seven stratigraphic members that consist of lacustrine (Edgar et al., 2020; Fedo et al., 2022; Stack et al., 2019) and lacustrine-margin (Gwizd et al., 2022) environments thought to be capable of sustaining aqueous activity and standing water in lake basins throughout deposition. The chapters in this study present detailed facies analysis and stratigraphic interpretations in three Murray formation members, the Hartmann's Valley member (25 m), Karasburg member (40 m), and Sutton Island member (95 m). The primary goal of this research is to evaluate facies and sedimentary processes recorded in the members and the evolution of the associated depositional environments.

The compositional record of sedimentary processes

Central to this research is the link between facies and sediment processes along the source-to-sink pathway (Johnsson et al., 1993). Depositional processes that transport sediment are capable of hydrodynamic sorting, causing changes in mineralogical proportions and overall composition from the starting source composition (Fedo et al., 2015; Mangold et al., 2011; Nesbitt & Young, 1996). Such processes are unique to the specific facies and sedimentary structures within different depositional environments, and interpretations of individual facies therefore provide a framework from which to evaluate compositional signatures.

Whole-rock geochemical signatures do not solely record transport processes but provide a composite record of source-rock composition (Bedford et al., 2019; Fedo et al., 1996), weathering (Babechuk et al., 2014; Nesbitt & Wilson, 1992; Mangold et al., 2019), transport processes (Siebach et al., 2017), and diagenesis (Fedo et al., 1995, 1997) within a basin. Consequently, it is critical to decipher each of these signatures to fully understand the link between facies and compositions within a sedimentary succession. This research evaluates whole-rock compositional signatures from Alpha Particle X-Ray

Spectrometer (APXS) data at the facies level within the Hartmann’s Valley, Karasburg, and Sutton Island members to establish the geochemical signatures of source rock composition, weathering, sediment transport, and diagenesis and determine the link between sedimentary processes and composition.

Overview of the present study

The following three chapters evaluate facies and geochemical signatures and interpret the depositional environments and sedimentary processes recorded within the Hartmann’s Valley, Karasburg, and Sutton Island stratigraphic members of the Murray formation. Data utilized include images of the field areas acquired with the High Resolution Imaging Science Experiment (HiRISE) orbiter, several cameras from the Curiosity rover payload, and the APXS instrument from the Curiosity rover payload.

Chapter 1: Sedimentological and geochemical perspectives on a marginal lake environment recorded in the Hartmann's Valley and Karasburg members of the Murray formation, Gale crater, Mars

Chapter one utilizes images and geochemical data to investigate the sedimentology, stratigraphy, and geochemical signatures of the Hartmann’s Valley and Karasburg members of the Murray formation. Prior to this work, these members were noted for intermittent exposures of meter-scale trough-cross-stratification (Fedo et al. 2018), representing a shift in facies from the underlying Pahrump Hills member (Stack et al., 2019). Detailed descriptions and measurements of sedimentary structures and textures from Navigation Camera (Navcam), Mast Camera (Mastcam), Mars Hand Lens Imager

(MAHLI), and Remote Micro-Imager images are combined with APXS geochemistry to establish the characteristics and stratigraphic distribution of facies and to decipher whole-rock geochemical signatures within the sedimentary succession. From the acquired measurements and observations, we develop an integrated depositional and compositional model of the environments comprising the Hartmann's Valley and Karasburg member and discuss the implications regarding the evolution of depositional systems at Gale crater.

Chapter 2: Evolution of a lake margin recorded in the Sutton Island member of the Murray formation, Gale crater, Mars

Chapter two presents detailed analyses of facies and stratigraphy of the Sutton Island member of the Murray formation. Prior to this work, the Sutton Island member was interpreted to consist of an assemblage of heterolithic facies (Fedo et al. 2018; Stein et al., 2018). Detailed descriptions and measurements of outcrop thicknesses, sedimentary structures, and textures from Navigation Camera (Navcam), Mast Camera (Mastcam), and Mars Hand Lens Imager (MAHLI) images are utilized to characterize facies and assess their stratigraphic distributions. Facies associations are determined from stratal stacking patterns. Sedimentologic and stratigraphic interpretations of facies associations are used to model the evolution of environments within the Sutton Island member through time, which ultimately contributes to the larger-scale assessment of depositional environments recorded in the Murray formation.

Chapter 3: Compositional signatures of sediment history recorded in the Sutton Island member of the Murray formation, Gale crater, Mars

Chapter three contextualizes the findings of chapter two with assessments of whole-rock geochemical data to evaluate sedimentary processes recorded in the Sutton Island member. Prior to this work, compositional signatures in the Sutton Island member had been interpreted to represent the interaction of basaltic sediment with variable aqueous compositions pre- and post-lithification (Bristow et al., 2018; Rapin et al., 2019; Sun et al., 2019; Thompson et al., 2020). This study utilizes APXS geochemistry to deduce source rock composition, weathering, transport, and diagenesis at the facies level. Results are incorporated into an integrated compositional and depositional model to evaluate sedimentary processes recorded in the stratigraphy. This work contributes to our understanding of aqueous activity recorded in the Murray formation.

References

Babechuk, M. G., Widdowson, M., & Kamber, B. S. (2014). Quantifying chemical weathering intensity and trace element release from two contrasting basalt profiles, Deccan Traps, India. *Chemical Geology*, *363*, 56-75. https://doi.org/10.1016/j.chemgeo.2013.10.027

Bedford, C. C., Bridges, J. C., Schwenzer, S. P., Wiens, R. C., Rampe, E. B., Frydenvang, J., & Gasda, P. J. (2019). Alteration trends and geochemical source region characteristics preserved in the fluviolacustrine sedimentary record of Gale crater, Mars. *Geochimica et Cosmochimica Acta*, *246*, 234-266. https://doi.org/10.1016/j.gca.2018.11.031

Bibring, J. P., Langevin, Y., Mustard, J. F., Poulet, F., Arvidson, R., Gendrin, A., et al. (2006). Global mineralogical and aqueous Mars history derived from OMEGA/Mars Express data. *science*, *312*(5772), 400-404. https://doi.org/10.1126/science.1122659

Bristow, T. F., Rampe, E. B., Achilles, C. N., Blake, D. F., Chipera, S. J., Craig, P., et al. (2018). Clay mineral diversity and abundance in sedimentary rocks of Gale crater, Mars. *Science Advances*, *4*(6). https://doi.org/10.1126/sciadv.aar3330

Caravaca, G., Mangold, N., Dehouck, E., Schieber, J., Zaugg, L., Bryk, A. B., et al. (in press) From Lake to River: Documenting an Environmental Transition across the Jura/Knockfarril Hill Members Boundary in the Glen Torridon Region of Gale crater (Mars). *Journal of Geophysical Research: Planets*, https://doi.org/ 10.1029/2021JE007093

Edgar, L. A., Fedo, C. M., Gupta, S., Banham, S. G., Fraeman, A. A., Grotzinger, J. P., et al. (2020). A lacustrine paleoenvironment recorded at Vera Rubin Ridge, Gale crater: Overview of the sedimentology and stratigraphy observed by the Mars Science Laboratory Curiosity Rover. *Journal of Geophysical Research: Planets*, *125*(3). https://doi.org/10.1029/2019je006307

Edgar, L. A., Grotzinger, J. P., Bell III, J. F., & Hurowitz, J. A. (2014). Hypotheses for the origin of fine-grained sedimentary rocks at Santa Maria crater, Meridiani Planum. *Icarus*, 234, 36-44. https://doi.org/10.1016/j.icarus.2014.02.019

Edgar, L. A., Gupta, S., Rubin, D. M., Lewis, K. W., Kocurek, G. A., Anderson, R. B., et al. (2017). Shaler: in situ analysis of a fluvial sedimentary deposit on Mars. *Sedimentology*, *65*(1), 96-122. https://doi.org/10.1111/sed.12370

Edgett, K. S., Banham, S. G., Bennett, K. A., Edgar, L. A., Edwards, C. S., Fairén, A. G., et al., (2020). Extraformational sediment recycling on Mars. *Geosphere*, *16*(6), 1508-1537. https://doi.org/10.1130/GES02244.1

Fedo, C. M., Bryk, A. B., Edgar, L. A., Bennett, K. A., Fox, V. K., Dietrich, W. E., et al. (2022). Geology and stratigraphic correlation of the Murray and Carolyn Shoemaker formations across the Glen Torridon region, Gale crater, Mars. *Journal of Geophysical Research: Planets*. https://doi.org/10.1029/2022JE007408

Fedo, C. M., Eriksson, K. A., & Krogstad, E. J. (1996). Geochemistry of shales from the Archean (~ 3.0 Ga) Buhwa Greenstone Belt, Zimbabwe: implications for provenance and source-area weathering. *Geochimica et Cosmochimica Acta*, *60*(10), 1751-1763. https://doi.org/10.1016/0016-7037(96)00058-0

Fedo, C. M., Grotzinger, J., Gupta, S., Fraeman, A., Edgar, L., Edgett, K., et al. (2018). Sedimentology and stratigraphy of the Murray formation, Gale crater, Mars. In the 49th Lunar and Planetary Science Conference, Abstract #2083.

Fedo, C. M., McGlynn, I. O., & McSween Jr, H. Y. (2015). Grain size and hydrodynamic sorting controls on the composition of basaltic sediments: Implications for interpreting Martian soils. *Earth and Planetary Science Letters*, *423*, 67-77. https://doi.org/10.1016/j.epsl.2015.03.052

Fedo, C. M., Nesbitt, H.W., & Young, G. M. (1995). Unraveling the effects of potassium metasomatism in sedimentary rocks and paleosols, with implications for paleoweathering conditions and provenance. *Geology*, *23*(10), 921-924. https://doi.org/10.1130/0091-7613(1995)023<0921:UTEOPM>2.3.CO;2

Fedo, C. M., Young, G. M., Nesbitt, H. W., & Hanchar, J. M. (1997). Potassic and sodic metasomatism in the southern province of the Canadian Shield: evidence from the Paleoproterozoic Serpent Formation, Huronian Supergroup, Canada. *Precambrian Research*, *84*(1-2), 17-36. https://doi.org/10.1016/S0301-9268(96)00058-7

Grotzinger, J. P., Arvidson, R. E., Bell III, J. F., Calvin, W., Clark, B. C., Fike, D. A., et al. (2005). Stratigraphy and sedimentology of a dry to wet eolian depositional system, Burns formation, Meridiani Planum, Mars. *Earth and Planetary Science Letters*, *240*(1), 11-72. https://doi.org/10.1016/j.epsl.2005.09.039

Grotzinger, J. P., Gupta, S., Malin, M. C., Rubin, D. M., Schieber, J., Siebach, K., et al. (2015). Deposition, exhumation, and paleoclimate of an ancient lake deposit, Gale crater, Mars. *Science*, *350(*6257). https://doi.org/10.1126/science.aac.7575

Grotzinger, J. P., & Milliken, R. E. (2012). The sedimentary rock record of Mars: Distribution, origins, and global stratigraphy. https://doi.org/10.2110/pec.12.102.0001

Grotzinger, J. P., Sumner, D. Y., Kah, L. C., Stack, K., Gupta, S., Edgar, L., et al. (2014). A habitable fluvio-lacustrine environment at Yellowknife Bay, Gale crater, Mars. *Science*, *343*(6169), 1242777. https://doi.org/10.1126/science.1242777

Gwizd, S., Fedo, C., Grotzinger, J., Banham, S., Rivera-Hernández, F., Stack, K. M., et al. (2022). Sedimentological and Geochemical Perspectives on a Marginal Lake Environment Recorded in the Hartmann's Valley and Karasburg Members of the Murray Formation, Gale Crater, Mars. *Journal of Geophysical Research: Planets*, *127*(8). https://doi.org/10.1029/2022JE007280

Johnsson, M.J. (1993). The system controlling the composition of clastic sediments. *In: Processes Controlling the Composition of Clastic Sediments*, *Geological Society of America Special Paper* (Eds. Johnsson, M.J. & Basu, A.), *284*, 1-19.

Le Deit, L., Hauber, E., Fueten, F., Pondrelli, M., Rossi, A. P., & Jaumann, R. (2013). Sequence of infilling events in Gale Crater, Mars: Results from morphology, stratigraphy, and mineralogy. *Journal of Geophysical Research: Planets*, *118*(12), 2439-2473. https://doi.org/10.1002/2012JE004322

McCauley, J. F., Carr, M. H., Cutts, J. A., Hartmann, W. K., Masursky, H., Milton, D. J., et al. (1972). Preliminary Mariner 9 report on the geology of Mars. *Icarus*, *17*(2), 289-327. https://doi.org/10.1016/0019-1035(72)90003-6

Malin, M. C., & Edgett, K. S. (2000). Sedimentary rocks of early Mars. *Science*, 290(5498), 1927–1937. https://doi.org/10.1126/science.290.5498.1927

Mangold, N., Baratoux, D., Arnalds, O., Bardintzeff, J. M., Platevoet, B., Grégoire, M., & Pinet, P. (2011). Segregation of olivine grains in volcanic sands in Iceland and implications for Mars. *Earth and Planetary Science Letters*, *310*(3-4), 233-243. https://doi.org/10.1016/j.epsl.2011.07.025

Mangold, N., Dehouck, E., Fedo, C., Forni, O., Achilles, C., Bristow, T., et al. (2019). Chemical alteration of fine-grained sedimentary rocks at Gale crater. *Icarus*, *321*, 619-631. https://doi.org/10.1016/j.icarus.2018.11.004

Mangold, N., Gupta, S., Gasnault, O., Dromart, G., Tarnas, J. D., Sholes, S. F., et al. (2021). Perseverance rover reveals an ancient delta-lake system and flood deposits at Jezero crater, Mars. *Science*, *374*(6568), 711-717. https://doi.org/10.1126/science.abl4051

McLennan, S. M., Grotzinger, J. P., Hurowitz, J. A., & Tosca, N. J. (2019). The sedimentary cycle on early Mars. *Annual Review of Earth and Planetary Sciences*, *47*, 91-118. doi:10.1146/annurev-earth-053018-060332

Milliken, R. E., Grotzinger, J. P., & Thomson, B. J. (2010). Paleoclimate of Mars as captured by the stratigraphic record in Gale Crater. *Geophysical Research Letters*, 37(4). https://doi.org/10.1029/2009GL041870

Nesbitt, H. W., & Wilson, R.E. (1992), Recent chemical weathering of basalts. *American Journal of Science*, *292*(10), 740–777. https://doi.org/10.2475/ajs.292.10.740

Nesbitt, H. W., & Young, G. M. (1996). Petrogenesis of sediments in the absence of chemical weathering: effects of abrasion and sorting on bulk composition and mineralogy. *Sedimentology*, *43*(2), 341-358. https://doi.org/10.1046/j.1365-3091.1996.d01-12.x

Palucis, M. C., Dietrich, W. E., Hayes, A. G., Williams, R. M., Gupta, S., Mangold, N., et al. (2014). The origin and evolution of the Peace Vallis fan system that drains to the Curiosity landing area, Gale Crater, Mars. Journal of Geophysical Research: Planets, 119(4), 705–728. https://doi.org/10.1002/2013JE004583

Rapin, W., Ehlmann, B. L., Dromart, G., Schieber, J., Thomas, N. H., Fischer, W. W., et al. (2019). An interval of high salinity in ancient Gale crater lake on Mars. *Nature Geoscience*, *12*(11), 889-895. https://doi.org/10.1038/s41561-019-0458-8

Schwenzer, S. P., Abramov, O., Allen, C. C., Bridges, J. C., Clifford, S. M., Filiberto, J., et al. (2012). Gale Crater: Formation and post-impact hydrous environments. *Planetary and Space Science*, *70*(1), 84-95. https://doi.org/10.1016/j.pss.2012.05.014

Siebach, K. L., Baker, M. B., Grotzinger, J. P., McLennan, S. M., Gellert, R., Thompson, L. M., & Hurowitz, J. A. (2017). Sorting out compositional trends in sedimentary rocks of the Bradbury group (Aeolis Palus), Gale crater, Mars. *Journal of Geophysical Research: Planets*, *122*, 295–328. https://doi.org/10.1002/2016JE005195

Squyres, S. W., Grotzinger, J. P., Arvidson, R. E., Bell III, J. F., Calvin, W., Christensen, P. R., et al. (2004). In situ evidence for an ancient aqueous environment at Meridiani Planum, Mars. *science*, *306*(5702), 1709-1714. https://doi.org/10.1126/science.1104559

Stack, K. M., Grotzinger, J. P., Lamb, M. P., Gupta, S., Rubin, D. M., Kah, L. C., et al. (2019). Evidence for plunging river plume deposits in the Pahrump Hills member of the Murray formation, Gale crater, Mars. *Sedimentology*, 66(5), 1768–1802. https://doi.org/10.1111/sed.12558

Stein, N., Grotzinger, J. P., Schieber, J., Mangold, N., Hallet, B., Newsom, H., et al. (2018). Desiccation cracks provide evidence of lake drying on Mars, Sutton Island member, Murray formation, Gale crater. *Geology*, 46(6), 515–518. https://doi.org/10.1130/G40005

Sun, V. Z., Stack, K. M., Kah, L. C., Thompson, L., Fischer, W., Williams, A. J., et al. (2019). Late-stage diagenetic concretions in the Murray formation, Gale crater, Mars. *Icarus*, *321*, 866-890. https://doi.org/10.1016/j.icarus.2018.12.030

Thompson, L.M., Berger, J.A., Spray, J.G., Fraeman, A.A., McCraig, M.A., O'Connell-Cooper, C.D., et al. (2020). APXS-derived compositional characteristics of Vera Rubin Ridge and Murray formation, Gale crater, Mars: Geochemical implications for the origin of the ridge. *Journal of Geophysical Research: Planets*, *125*(10). https://doi.org/10.1029/2019JE006319

Thomson, B. J., Bridges, N. T., Milliken, R., Baldridge, A., Hook, S. J., Crowley, J. K., et al. (2011). Constraints on the origin and evolution of the layered mound in Gale crater, Mars using Mars Reconnaissance Orbiter data. *Icarus*, 214(2), 413–432. https://doi.org/10.1016/j.icarus.2011.05.002

Warner, N., Gupta, S., Lin, S. Y., Kim, J. R., Muller, J. P., & Morley, J. (2010). Late Noachian to Hesperian climate change on Mars: Evidence of episodic warming from transient crater lakes near Ares Vallis. *Journal of Geophysical Research: Planets*, *115*(E6). https://doi.org/10.1029/2009JE003522

Weitz, C. M., Milliken, R. E., Grant, J. A., McEwen, A. S., Williams, R. M. E., Bishop, J. L., et al. (2010). Mars Reconnaissance Orbiter observations of light-toned layered deposits and associated fluvial landforms on the plateaus adjacent to Valles Marineris. *Icarus*, *205*(1), 73-102. https://doi.org/10.1016/j.icarus.2009.04.017

Williams, R. M. E., Grotzinger, J. P., Dietrich, W. E., Gupta, S., Sumner, D. Y., Wiens, R. C., et al. (2013). Martian fluvial conglomerates at Gale crater. *Science*, *340*(6136), 1068–1072. https://doi.org/10.1126/science.1237317

CHAPTER 1 : SEDIMENTOLOGICAL AND GEOCHEMICAL PERSPECTIVES ON A MARGINAL LAKE ENVIRONMENT RECORDED IN THE HARTMANN'S VALLEY AND KARASBURG MEMBERS OF THE MURRAY FORMATION, GALE CRATER, MARS

A version of this chapter is published in the Journal of Geophysical Research: Planets by Samantha J. Gwizd et al.:

Gwizd, S., Fedo, C.M., Grotzinger, J.P., Banham, S., Rivera-Hernández, F., Stack, K.M., Siebach, K., Thorpe, M., Thompson, L., O'Connell-Cooper, C., Stein, N., Edgar, L., Gupta, S., Rubin, D., Sumner, D., Vasavada, A.R. (2022). "Sedimentological and geochemical perspectives on a marginal lake environment recorded in the Hartmann's Valley and Karasburg members of the Murray formation, Gale crater, Mars." *Journal of Geophysical Research, Planets*

This article was written by S. J. Gwizd and utilizes images and chemical data acquired using the Mars Science Laboratory Curiosity rover. Co-authors L. Thompson, C. O'Connell-Cooper, K. Siebach, and M. Thorpe contributed instrument information and assisted with data analysis of APXS data. Co-authors C.M. Fedo, J.P. Grotzinger, S. Banham, F. Rivera-Hernández, K.M. Stack, S. Gupta, D. Rubin, D. Sumner, and A.R. Vasavada contributed stratigraphic interpretations and provided sedimentologic and stratigraphic measurements. Co-author C.M. Fedo primarily assisted with editing of the article prior to submission. Prior to submission, the article was assessed by remaining co-authors and sent to the MSL science team for further editing. The article underwent one round of revisions by the editor, associated editor, and two anonymous reviewers before it was accepted for publication.

Abstract

This study utilizes instruments from the Curiosity rover payload to develop an integrated paleoenvironmental and compositional reconstruction for the 65-m thick interval of stratigraphy comprising the Hartmann's Valley and Karasburg members of the Murray formation, Gale crater, Mars. The stratigraphy consists of cross-stratified sandstone (Facies 1), planar-laminated sandstone (Facies 2), and planar-laminated mudstone (Facies 3). Facies 1 is composed of sandstone showing truncated sets of concave-curvilinear laminae stacked into cosets. Sets are estimated to be meter- to sub-meter-scale, consistent with low-height dunes. Thin stratigraphic intervals of Facies 1 and stacking patterns with Facies 2 and 3 support a wet aeolian dune interpretation. Meter-thick packages of planar-laminated sandstone (Facies 2) are interpreted to represent interfingering dune-interdune strata. Facies 3 consists of meter-thick packages of planar-laminated mudstone interpreted to represent lacustrine deposition with persistent standing water. Integration of geochemistry with each facies reveals some compositional control based on depositional process. Models for source rock composition from Alpha Particle X-Ray Spectrometer measurements show that facies derived from a basaltic source. Alteration indices and geochemical trends provide evidence that moderate chemical weathering occurred before compositional changes due to diagenesis. Differences of wt% $FeO_{(T)}$ and TiO_2 between facies are minimal, though trends between facies point to sediment sorting in transport. Comparisons to terrestrial basaltic sedimentary systems indicate that the Hartmann's Valley and Karasburg facies reflect deposition in an environment where diverse subaqueous and subaerial facies persisted adjacent to a long-lived body of water.

Introduction

Sedimentary successions, which are ubiquitous across Mars, have become prime mission targets in the search for understanding paleoenvironments including those potentially suitable for supporting life (e.g. Fairén et al., 2010; Grotzinger et al., 2014; Hurowitz et al., 2017; Malin & Edgett, 2000). Decades of Mars exploration have produced datasets with increasing coverage and resolution, which continue to refine interpretations of water-generated features represented in geomorphologic, stratigraphic, and compositional records across the planet.

Rover-based evidence for ancient lacustrine (e.g., Edgar et al., 2020; Grotzinger et al., 2015; Stack et al., 2019), aeolian (e.g. Banham et al., 2018; Grotzinger et al., 2005), and fluvial (e.g. Edgar et al., 2017; Williams et al., 2013) environments is abundant within the explored sedimentary successions. Interpretations of stratigraphy from landscape- to grain-scales correlate with compositional records from orbital spectroscopy datasets that show distinct intervals of clay-, sulfate-, and Fe-oxide-dominated strata (Christensen et al., 2000; Fraeman et al., 2020; Milliken et al., 2010), supporting hypotheses that aqueous activity was widespread and dynamic through time.

Gale crater (5°S, 138°E), a 155 km diameter complex crater located along the dichotomy boundary just south of the equator, was the destination for the Mars Science Laboratory (MSL) Curiosity rover mission (Figure 1.1). The crater formed ~3.7 Ga (Le Deit et al., 2013; Thomson et al., 2011) and is filled by a younger succession of Hesperian (~3.6 Ga) strata, which is now exposed as a central mound. This stratigraphic succession represents an ideal location to study depositional environments and compositional signatures due to the continuous stratigraphy exposed in the 5.5 km-high central mound (Figure 1.1a; Aeolis Mons, informally Mount Sharp; Grotzinger et al., 2012), which encompasses the globally documented transitions from clay- to sulfate- to Fe-oxide enriched bedrock (Bibring et al. 2006; Milliken et al., 2010).

The facies (Edgar et al., 2020; Fedo et al., 2018; Grotzinger et al., 2015; Stack et al., 2019) and geochemistry (Hurowitz et al., 2017; Mangold et al., 2019; Siebach et al., 2017) of the ~300 m thick Murray formation (Figure 1.1c), are consistent with lacustrine (and lacustrine-margin) environments that experienced long durations of standing water capable of generating hundreds of meters of preserved sediment . Bedrock geochemical and mineralogical signatures provide compositional constraints regarding basaltic source rocks (Bedford et al., 2019; Siebach et al., 2017) and the extent of chemical weathering (Frydenvang et al., 2020; Mangold et al., 2019), and diagenesis (Achilles et al., 2020; Bristow et al., 2021; Kronyak et al., 2019; Sun et al., 2019). In this context, the Hartmann's Valley and Karasburg stratigraphic members of the Murray formation remain described and interpreted at a cursory level, which precludes a full understanding of paleoenvironments and compositional evolution. A significant change in depositional processes and paleoenvironments is preserved in these two members as they record the first transition in the Murray formation stratigraphy from laminated mudstone to meter-scale cross-stratified sandstone. Development of a depositional model for the Hartmann's Valley and Karasburg stratigraphic successions will ultimately contribute to ongoing investigations of habitable environments at Gale crater and their evolution through time.

Linked to unraveling basin evolution are the numerous chemical and physical processes that occur along the source-to-burial pathway that defines a sedimentary cycle (e.g. weathering, transport, diagenesis; Johnsson et al., 1993). Physical processes build sedimentary structures that group into sedimentary facies based on the depositional environment. The physical processes transporting sediment to the depositional environment drive hydrodynamic sorting that can cause changes in mineralogical proportions, and thus composition, from the original source composition by segregating grains based on density, size, and shape (e.g. Fedo et al., 2015; Mangold et al., 2011; McGlynn et al., 2012; Nesbitt & Young, 1996; Siebach et al., 2017). The interrelationship between depositional process, environment, and composition emphasizes the importance of simultaneous assessment of sedimentary textures and depositional processes as a framework from which to interpret composition. It is therefore critical to interpret bulk sediment composition in the context of facies and depositional environments within a sedimentary succession. Accordingly, this study builds an integrated depositional and compositional picture of the Hartmann's Valley and Karasburg members of the Murray formation.

The main objectives of this study are to characterize the facies and interpret the paleoenvironments of the Hartmann's Valley and Karasburg members of the Murray formation (Figure 1.1) and use the associated internal depositional processes to help frame the geochemical composition of both units. Specific objectives of this study are to: (i) identify sedimentary facies and assess variability and patterns, (ii) interpret associated depositional environments, (iii) assess the geochemistry to develop an understanding of source rock composition, chemical weathering, sediment transport, and diagenesis within the context of the interpreted facies and environments, and (iv) discuss implications for the evolution of the depositional systems at Gale crater.

Geologic, stratigraphic, and compositional context

Gale crater

More than 500 m of strata have been documented along the Curiosity rover traverse to date. The strata are subdivided into three groups (Figure 1.1b): (1) the Bradbury group, which comprises the intracrater plains (Aeolis Palus) and interfingers with the Mount Sharp group (Grotzinger et al., 2015; Williams et al., 2013), (2) the

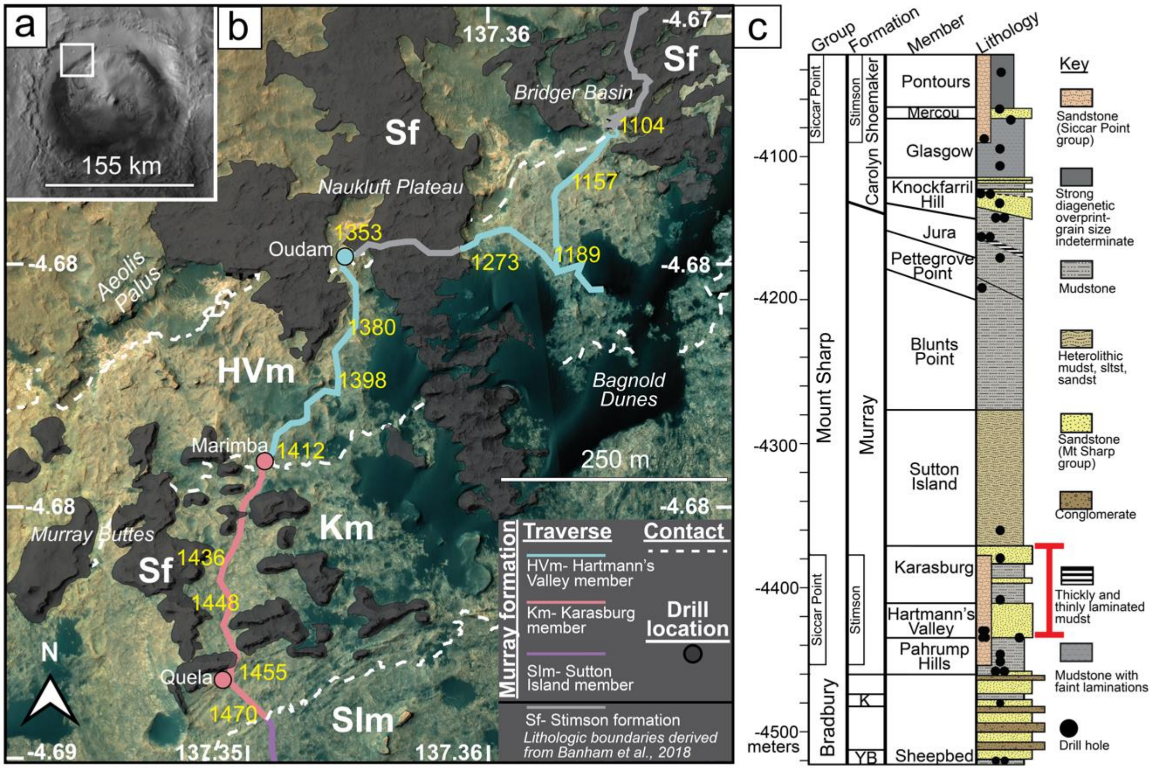

Figure 1.1 (a) Mars Reconnaissance Orbiter (MRO) Context Camera (CTX) mosaic of Gale crater providing context for Curiosity's exploration area (white box). (b) Traverse path across the Hartmann's Valley and Karasburg members of the Murray formation through the beginning of the traverse across the Sutton Island member. Key formations, features, and stratigraphic contacts are marked. Sol numbers mark the locations of several key outcrops listed in Supplemental Table 1.1. The base map is a merged HiRISE orthophoto mosaic from Calef and Parker (2016). (c) Generalized stratigraphic column showing the thickness of the strata in the underlying Bradbury group, the lacustrine Murray formation, and the overlying Carolyn Shoemaker formation. The red bracket indicates the Hartmann's Valley and Karasburg members. Also included is the unconformable Stimson formation. Modified from the MSL Sedimentology and Stratigraphy Working Group.

Mount Sharp group, which consists of the exposed Murray and Carolyn Shoemaker formation strata of the central mound (Bennett et al., 2022; Grotzinger et al., 2015), and (3) the Siccar Point group, which unconformably overlies the Mount Sharp strata (Banham et al., 2018, 2021). Basaltic sand deposits mantle the bedrock that comprises Mount Sharp (Figure 1.1b) and consist of a variety of active aeolian bedforms, including the dunes and ripples of the Bagnold dune field (Lapôtre & Rampe, 2018). The contrast between the northward slope of the landscape in the area of the crater explored by Curiosity and the near-horizontal orientation of the strata indicates that the crater basin was once filled with sediment and that the present-day landscape formed principally from erosion from aeolian activity (Grotzinger et al., 2015). Additionally, the negligible dip of the strata (Stein et al., 2020) has enabled elevation to be used as a proxy for stratigraphic height in the creation of a working stratigraphic column for the mission (Figure 1.1c; Edgar et al., 2020; Stack et al., 2019), but many are interpreted from one main transect (e.g. Stack et al., 2019).

Murray formation

<u>Stratigraphy and composition</u>

The Murray formation is subdivided into seven stratigraphic members based primarily on lithology (Figure 1.1c). Of the seven members, thorough facies analyses have been done throughout the Pahrump Hills (Grotzinger et al., 2015; Stack et al., 2019), Blunts Point, Pettegrove Point, and Jura members (Caravaca et al., 2022; Edgar et al., 2020), while more localized studies have been done throughout the Sutton Island member (Rapin et al., 2019; Stein et al., 2018). Much of the Murray formation consists of meters thick intervals of planar laminated mudstone that are interpreted to represent deposition in low-energy lacustrine basin environments (e.g. Edgar et al., 2020; Stack et al., 2019). More isolated outcrops of cross-stratified sandstone represent higher-energy deposition along marginal lacustrine settings (Fedo et al., 2018; Stack et al., 2019).

Whole-rock geochemistry and mineralogy throughout most of the Murray formation is consistent with dominantly basaltic sources (Rampe et al., 2020; Thompson et al., 2020). Subalkaline igneous compositions have been proposed as a primary source composition for the majority of the stratigraphy, with the exception of a localized silica-rich interval in the Pahrump Hills member which is thought to reflect derivation from a more evolved volcanic composition (Bedford et al., 2019; Berger et al., 2020; Morris et al., 2016; Siebach et al., 2017). Interpretations of geochemical trends attribute elemental enrichment and depletion to modification from weathering and diagenesis (Frydenvang et al., 2020; Mangold et al., 2019; Rampe et al., 2020; Thompson et al., 2020). Analyses of drilled samples by the Chemistry and Mineralogy (CheMin) instrument show shifts in the relative amounts and compositions of primary and secondary minerals and amorphous phases throughout the stratigraphy which corroborate hypotheses of weathering and diagenesis under variable aqueous conditions (Achilles et al., 2020; Bristow et al., 2018; Rampe et al., 2020).

Methods

Sedimentology and stratigraphy

Rover traverse

Stratigraphic and geochemical observations of the Hartmann's Valley member (HVm) and Karasburg member (Km) were made using data acquired along a ~2.7 km rover traverse across variable topography (Figures 1.1b & 1.2). Strata of the lower 18 m of the HVm were evaluated from multiple traverses of the same elevation range, enabling assessment of lateral facies variability (Figure 1.2). The traverse across the upper part of the HVm and the entirety of the Km was a monotonic ascent that precluded an assessment of lateral continuity. Therefore, the profile in Figure 1.2 subsequently leaves interpretations of the subsurface distribution of strata along the second portion of the traverse blank.

Instruments

Sedimentological and stratigraphic observations were conducted using images taken with a suite of cameras on the rover mast and arm. Images of bedrock taken with the Navigation Camera (Navcam; Maki et al., 2012), Mast Camera (Mastcam; Malin et al., 2017), Mars Hand Lens Imager (MAHLI; Edgett et al., 2012), and Remote Micro-Imager (RMI; Maurice et al., 2012) were used to identify and measure features from outcrop- (Navcam and Mastcam) to grain-scales (MAHLI and RMI). The elevation and location of each observation were determined from a digital elevation model created from High Resolution Imaging Science Experiment (HiRISE) stereo pair images (Calef & Parker,

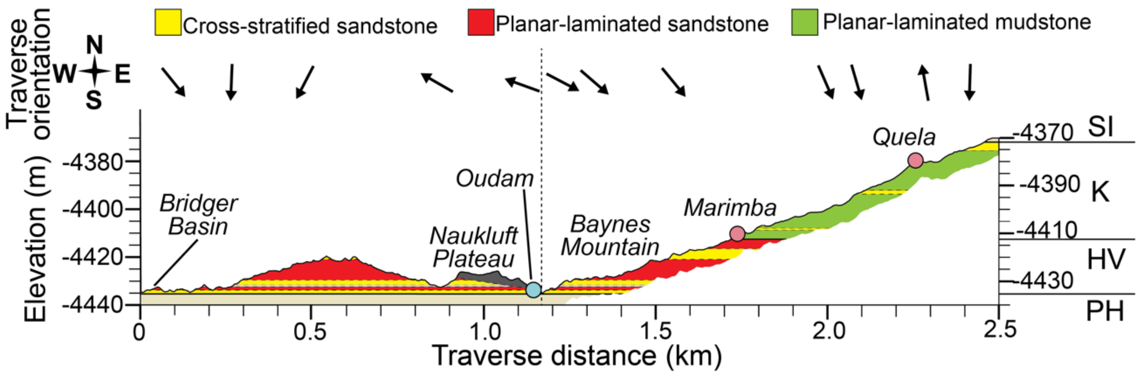

Figure 1.2 Topographic profile depicting the distribution of facies along the Curiosity rover traverse (Sols 1104-1470) across the Hartmann's Valley and Karasburg members, including the unconformable Stimson formation (grey). Facies are projected into the subsurface along the first portion of the traverse (~0-1.2 km) to show possible lateral correlations, but are not projected along the second portion of the traverse (~1.2-2.5 km) due to the largely monotonic ascent of the rover. Both segments are separated by the dashed vertical line. See Figure 1.1 for map view of traverse path. Arrows indicate changes in the drive direction along the x-axis. Vertical exaggeration is 10x.

2016; McEwen et al, 2007) and accessed through the Multi-Mission Geographic Information System (MMGIS) interface (Calef et al., 2017, 2019).

Lamination thickness and grain size

Lamination thicknesses were measured on Mastcam and MAHLI images orthogonal to bedrock using ImageJ software (Rasband, https://imagej.nih.gov). Methods utilized are similar to those of other studies at Gale crater where the distance between centers of successive laminae were measured in pixels and converted to millimeters based on the image resolution (Hurowitz et al., 2017; Stack et al., 2019; Edgar et al., 2020). Laminae boundaries were estimated when assessing images with greater standoff distances and lower resolutions. Grayscale pixel intensity was assessed as a proxy for laminae thickness on one orthogonal MAHLI image by converting the image to grayscale and assessing grayscale values across multiple laminae, where changes in grayscale intensity may signify changes in erosion associated with bedrock properties such as grain size.

Grains were identified where possible in MAHLI images, but resolution limitations and the lack of ubiquitous visible grain boundaries prevented statistically significant datasets (Gwizd et al., 2018). The Gini Index Mean Score (GIMS), a proxy for grain size based on chemical heterogeneity of bedrock derived from Chemistry and Camera (ChemCam, Wiens et al., 2012) Laser Induced Breakdown Spectroscopy (LIBS) data (See Rivera-Hernández et al., 2019 for methodology), was used to supplement interpretations of MAHLI images.

Geochemistry

Geochemical analyses utilized data acquired with the Alpha Particle X-Ray Spectrometer (APXS). The APXS measures the average composition of a 1.5-to-2 cm diameter field of view (FOV) using particle induced X-Ray emission and X-Ray fluorescence techniques (Campbell et al., 2012; Gellert et al., 2009; Gellert et al., 2015). Major-element abundances are reported in oxide weight percent (wt. %); trace elements are reported in parts per million (ppm). For detailed descriptions of methodology and data calibration, the reader is referred to Campbell et al. (2012) and Gellert et al. (2015).

A total of 26 APXS measurements from the HVm and Km stratigraphy are included in this study. Major, minor, and trace elements for the bedrock targets are listed in additional file attachment Table 1.3. Measurements with an insufficient integration time and full-width-at-half-maximum (FWHM) of spectra were excluded from analyses (Gellert et al., 2015; VanBommel et al., 2019).

Some measurements are acquired on bedrock which has been brushed with a Dust Removal Tool (DRT). The study by Schmidt et al. (2018) shows that dust is known to have an effect on bedrock composition, particularly with lighter elements, but that measurements on surfaces which have not been brushed with the DRT are still capable of recording the underlying rock composition.

This study generally considers all SO_3 to be bound in secondary Ca-, Fe-, or Mg-sulfate, consistent with previous geochemical and mineralogical findings (Achilles et al., 2020; Rampe et al., 2020; Thompson et al., 2020). The oxidation state of Fe (reported as $FeO_{(T)}$) cannot be fully constrained with the APXS instrument, and interpretations of Fe are also considered contextually with previous compositional studies of the HVm and Km (Bristow et al., 2018; Mangold et al., 2019; Achilles et al., 2020).

Geochemical tools: A-CN-K, A-CNK-FM, and AF-CNK-M molar ternary diagrams

Processes along the sediment source-to-sink path, from formation to burial, are recorded in the bulk sediment composition (Johnsson et al., 1993). Studies have determined the range of expected major elemental signatures representing chemical weathering, transport, and diagenesis in terrestrial (e.g. Fedo et al., 1995; Nesbitt & Young, 1984; Nesbitt & Young, 1996; Fedo et al., 2015) and Martian (e.g. Mangold et al., 2019; McLennan et al., 2005; Siebach et al., 2017) sedimentary systems, which each modify sediment from the original source composition. Ternary diagrams of molar Al_2O_3 – CaO* + Na_2O – K_2O (A-CN-K), Al_2O_3 – CaO* + Na_2O + K_2O – $FeO_{(T)}$ + MgO (A-CNK-FM), and Al_2O_3 + $FeO_{(T)}$ – CaO* + Na_2O + K_2O – MgO (AF-CNK-M) provide ways to visualize the nature and extent of chemical alteration from the source rock and to differentiate compositional signatures associated with weathering, sediment transport, and diagenesis (Figure 1.3). The molar proportions of major elements correspond to primary (CaO, Na_2O, K_2O, $FeO_{(T)}$, MgO) and secondary (Al_2O_3, $FeO_{(T)}$) mineral phases within the whole-rock sample. In each ternary diagram, weathering, sorting, and diagenesis in terrestrial settings generally follow predicted geochemical pathways (e.g. Babechuk et al., 2014; Fedo et al., 1995; Fedo et al., 2015; Nesbitt & Young, 1984). Although geochemical trends within sedimentary systems on Mars reveal compositional differences compared with terrestrial systems (Thorpe et al., 2020), predicted pathways nevertheless form the basis from which to evaluate sediment on Mars. Typical pathways emanate from a starting point, the unaltered source (triangle a, Figure 1.3a-c), which may be a composite of several source rock compositions (e.g. different lava flows).

Chemical weathering of basaltic source rocks produces predictable geochemical trends that coincide with enrichment in secondary alteration phases as a result of hydrolysis (Figure 1.3a-c; Babechuk et al., 2014; Nesbitt & Wilson, 1992; Nesbitt & Young, 1984). Conventional quantities that measure the extent of weathering include the *chemical index of alteration* (CIA; equation 1; Nesbitt & Young, 1982; Fedo et al., 1995) and the *mafic index of alteration* ($MIA_{(O)}$ and $MIA_{(R)}$; equations 2 & 3; Babechuk et al., 2014), both of which can be portrayed on the A-CN-K diagram (Figure 1.3a) and A-CNK-FM and AF-CNK-M diagrams (Figure 1.3b-c), respectively:

$$CIA = [Al_2O_3/(Al_2O_3+CaO^*+Na_2O+K_2O)]*100 \quad (1)$$

$$MIA_{(O)} = [(Al_2O_3 + FeO_{(T)})/(Al_2O_3+CaO^*+Na_2O+K_2O+MgO+FeO_{(T)})]*100 \quad (2)$$

$$MIA_{(R)} = [(Al_2O_3)/(Al_2O_3+CaO^*+Na_2O+K_2O+MgO+FeO_{(T)})]*100 \quad (3)$$

Equation 2 pertains to oxidizing conditions (Fe^{3+}) and includes $FeO_{(T)}$ in the numerator, and equation 3 pertains to reducing conditions (Fe^{2+}) and does not include $FeO_{(T)}$ in the numerator (Babechuk et al., 2014; Thorpe & Hurowitz, 2020). Unweathered basalts typically have CIA values that range from 35-40 (Babechuk et al., 2014). The $MIA_{(O)}$ generally follows the CIA, although it may vary depending on the behavior of Fe and Mg during clay formation, whereas the $MIA_{(R)}$ is lower than the CIA and $MIA_{(O)}$

(Babechuk et al., 2014). Weathered samples (triangle b, Figure 1.3a-c) will have greater values of CIA and $MIA_{(O,R)}$ compared to the unweathered source composition (triangle a, Figure 1.3a-c), and plot along weathering pathways toward greater enrichment in clays (e.g. kaolinite; arrow 1, Figure 1.3a-c).

The presence of hematite and dioctahedral smectite measured with CheMin from three drill samples, (1) Oudam (Facies 1), (2) Marimba- (Facies 3), and (3) Quela (Facies 3), are indicative of more oxidizing conditions (Achilles et al., 2020; Bristow et al., 2018). Mangold et al. (2019) estimated the Fe^{2+}/Fe^{3+} ratio from the Marimba drill sample at 0.059, highlighting the predominance of ferric oxides and supporting the assumption that pre- and post-burial conditions were largely oxidizing, though it is recognized that amorphous Fe-bearing phases increase the uncertainty of the Fe redox state. This study considers iron to mostly represent Fe^{3+} and utilizes the $MIA_{(O)}$ (equation 2) instead of $MIA_{(R)}$ (equation 3).

In addition to primary non-silicate phases (e.g. apatite), cementation and late-stage diagenetic fluid flow enriches bedrock in diagenetic non-silicate phases (Achilles et al., 2020), with one of the most common being Ca-sulfate (Kronyak et al., 2019; Sun et al., 2019). In the ternary diagrams in Figure 1.3, enrichment in Ca-sulfate drives data points along pathways (arrow 2, Figure 1.3a-c) toward the CN or CNK apices, lowering the apparent degree of weathering (triangle d, Figure 1.3a; triangle c, Figure 1.3b-c). The value for CaO* using molecular proportions in equations 1-3 is conventionally calculated by subtracting the stoichiometric proportion of CO_2 and P_2O_5, which are representative of non-silicate Ca-bearing phases (calcite [Cal] and apatite [Ap], respectively; Fedo et al., 1995; mineral abbreviations from Whitney & Evans, 2010). Carbonates were not detected from CheMin analyses of HVm and Km drill samples, so there is no calcite correction to make. Apatite was also not detected, although P_2O_5 was measured in all APXS targets ranging from 0.48-1.36 wt% (additional file attachment Table 1.3) and interpreted in the amorphous fraction (Achilles et al., 2020), making an exact correction uncertain. While secondary Ca-sulfates are common throughout Gale crater stratigraphy (e.g. Kronyak et al., 2019; Sun et al., 2019), some studies (McLennan et al., 2014; Siebach et al., 2017) do not remove Ca associated with sulfate and interpret geochemical trends with this consideration. Other studies filter out geochemical targets based on identification of diagenetic features in images (Mangold et al., 2019) or choose representative end-members to evaluate weathering extent (Thorpe et al., 2020). When no correction is made, the value of CaO* is equal to the measured wt% of CaO (equation 4):

$$\text{Uncorrected: } CaO^* = CaO_{(T)} \tag{4}$$

In this study, CaO* corrected for apatite and sulfate was determined by assigning P_2O_5 to apatite and some fraction of SO_3 to Ca-sulfate given its common occurrence. This study evaluates a range of possible sulfate corrections because, although CaO and SO_3 occur in a 1:1 molar ratio, the subtraction of all SO_3 results in a negative or zero value for CaO* for the majority of APXS targets. The presence of Ca-bearing silicate phases as determined by CheMin (Achilles et al., 2020) means that CaO* cannot be zero. Accordingly, we modeled the subtraction of SO_3 multiplied by $n + 0.1$, where $0 \leq n \leq 0.9$

in order to show the range of possible SO_3 outcomes. In this paper, n = 0.4 is interpreted as the maximum possible correction where CaO* > 0, leaving calcium assignable to silicates (see section "Linking depositional conditions and composition", below). The resultant equation used in this study to correct for P_2O_5 and the SO_3 phases is (equation 5):

$$\text{Corrected: } CaO^* = CaO_{(T)} - (3.33*P_2O_5) \text{ [Ap]} - (0.4*SO_3) \text{ [Ca-sulfate]} \qquad (5)$$

During sedimentary transport, sorting of basaltic sediment causes relatively finer-grained olivines and pyroxenes (Fe^{2+}, Mg^{2+}, some Ca^{2+}) to be transported and deposited alongside coarser-grained feldspars (Ca^{2+}, Na^{+}) that are hydrodynamically equivalent (Fedo et al., 2015; McGlynn et al., 2012; Nesbitt & Young, 1996; Siebach et al., 2017). The record of sorting is harder to differentiate in mafic lithologies using the feldspar-focused A-CN-K ternary diagram, although identification of size-fraction differences between finer grained phyllosilicates and coarser-grained primary phases (e.g. plagioclase) could be reasonably expected. Whole-rock samples unmix approximately along the linear trend emanating from triangle e in Figure 1.3a (arrow 3) Within the A-CNK-FM and AF-CNK-M ternary diagrams, sorting of basaltic sediment typically produces the linear trend between finer grained mafic phases and coarser grained feldspars (arrow 3, Figure 1.3a-b)

Another burial process we consider is potassium metasomatism, which causes the conversion of aluminous clays (e.g. kaolinite) to illite, or the conversion of plagioclase to

K-feldspar (Fedo et al., 1995; Yen et al., 2018). Within the A-CN-K, A-CNK-FM, and AF-CNK-M ternary diagrams, the conversion to illite causes data points to shift toward the K apex, lowering the apparent CIA. This process is illustrated in Figure 1.3a by the shift from triangles b and d to triangle c along the dashed arrow 4, and in Figure 1.3b-c by the shift from triangle a to triangle c along dashed arrow 2.

Member contacts

Geologic contacts were mapped at the Pahrump Hills-Hartmann's Valley (PHm-HVm), Hartmann's Valley-Karasburg (HVm-Km), and Karasburg-Sutton Island member (Km-SIm) boundaries (Figure 1.1b, dashed white lines) and expand on iterative efforts of the MSL Sedimentology and Stratigraphy Working Group. Interpretations are based on changes in facies, lithology, and other observable bedrock properties such as a relative increase in the degree of erosion and fracturing in overlying stratigraphic members. Increased bedrock erosion correlates to a greater degree of inundation by sand, causing bedrock to appear relatively duller in orbital images (Figure 1.4). The contact between the apparently brighter PHm bedrock (Figure 1.4a) and the apparently duller, more fractured HVm bedrock (-4436 m; Figure 1.4b) is identifiable in HiRISE and Mastcam images (Supplemental Figure 1.13), and correlates with the first appearance of cross-stratified facies characteristic of the HVm. The contact cannot be distinguished in the region west of the Naukluft Plateau from orbit or rover-based images due to sand cover and the occurrence of the overlying Stimson formation.

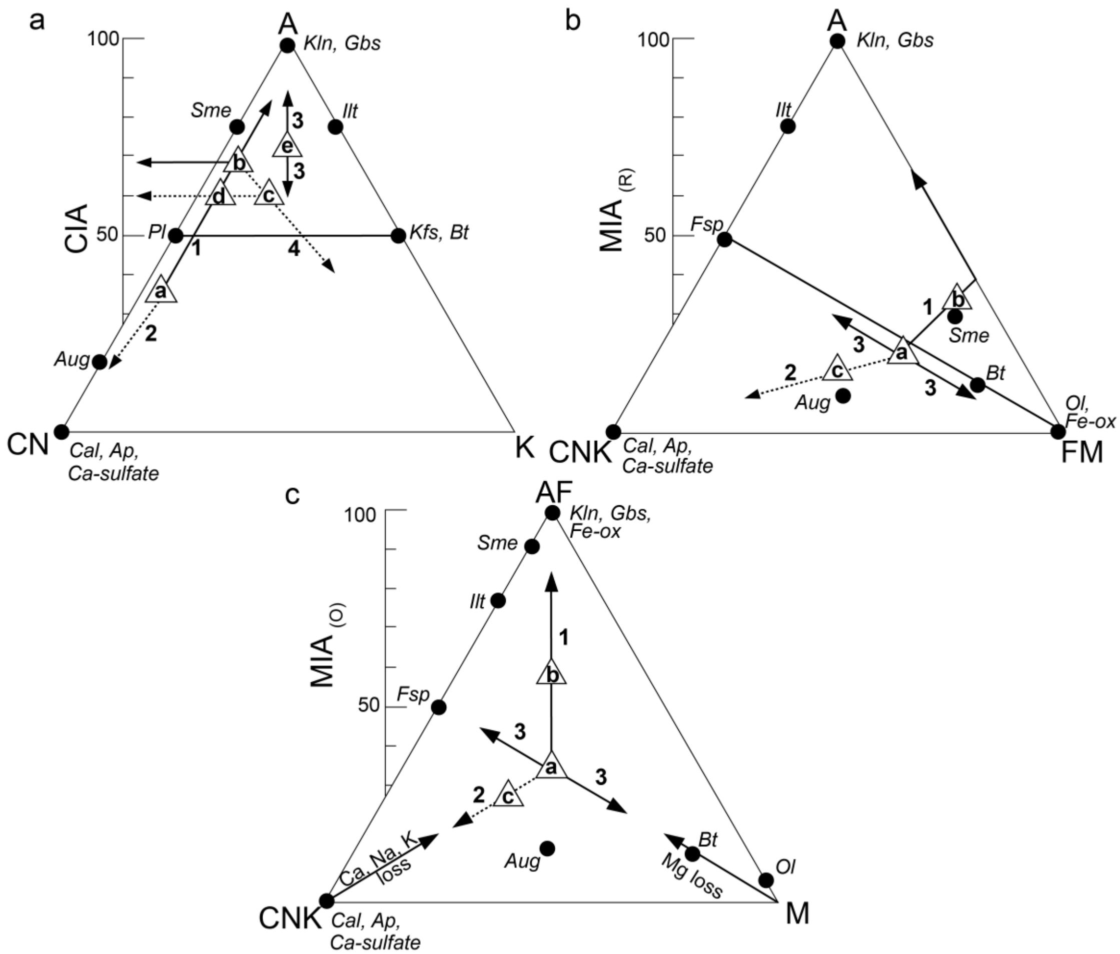

Figure 1.3 (a) A-CN-K (b) A-CNK-FM and (c) AF-CNK-M molar ternary diagrams showing the sedimentary history from (1) source rock (triangle a), (2) weathering along a predicted path (line 1) to greater values of CIA and MIA (triangle b), and diagenetic k-metasomatism and calcium sulfate enrichment (arrows 4 and 2, respectively, in (a) and arrow 2 in (b) and (c)). Within figure (a), a k-enriched composition is represented by triangle c. Within figures (b) and (c), triangle c represents a K- or Ca-enriched composition. Also depicted are expected trends produced from hydrodynamic sorting (line 3). Also included are reference minerals: Fsp = feldspar; Pl = plagioclase feldspar; Kfs = K-feldspar; Bt = biotite; Ilt = illite; Sme = smectite; Kln = Kaolinite; Gbs = gibbsite; Aug = augite; Ol = olivine; Fe-ox = Fe-oxides. Most mineral abbreviations from Whitney & Evans (2010).

The HVm-Km contact (-4412 m) is inferred based on lithologic differences between the coarser facies of the HVm and the planar-laminated mudstone facies within the Km (see section “Sedimentary Lithofacies”). The Km bedrock is relatively more eroded and fractured (Figure 1.4c) and lacks the ridged topography characteristic of the HVm landscape (Figure 1.1b). Obvious changes in bedrock properties at the HVm-Km facies boundary are not observable, and so the mapped contact between the HVm and Km is an approximation from orbital and rover images.

The Km-SIm contact (-4372 m) is also primarily inferred based on lithologic differences. The SIm bedrock (Figure 1.4d) appears relatively more eroded compared to the Km bedrock. Changes in the degree of erosion are not apparent at the lithologic boundary, and the mapped contact between the Km and SIm is also approximately located using orbital and rover images.

Sedimentary lithofacies

Three sedimentary lithofacies were identified within the HVm and Km stratigraphic succession utilizing µm-cm-scale bedrock textures, grain size, laminae, sedimentary structures, and other observable outcrop-scale characteristics (Supplemental Table 1.1; Figures 1.5-1.8). Facies are presented in order of first appearance within the stratigraphy (Figure 1.5).

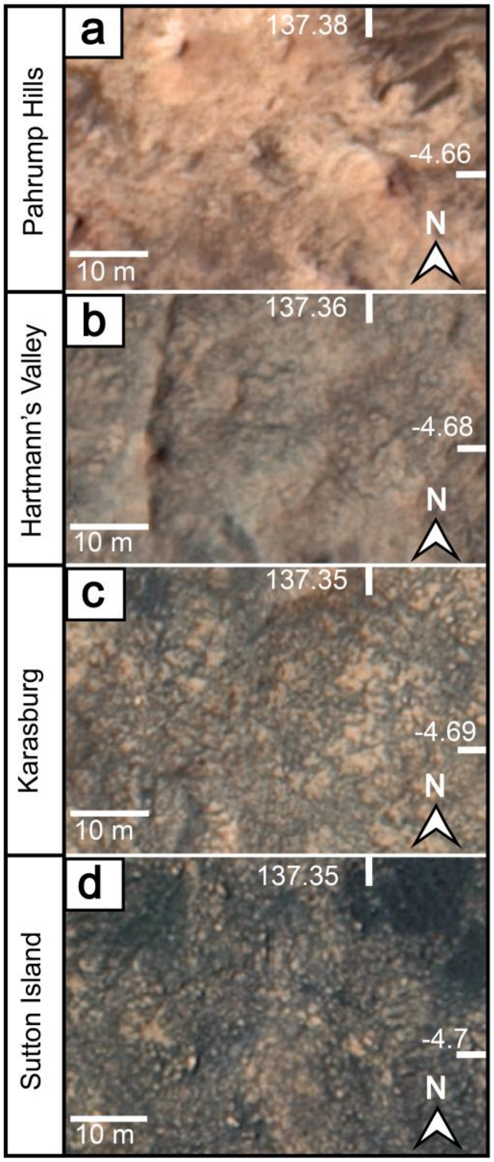

Figure 1.4 Outcrop expressions as viewed from HiRISE, showing representative bedrock of the (a) Pahrump Hills, (b) Hartmann's Valley, (c) Karasburg, and (d) Sutton Island members highlighting differences in bedrock continuity and erosion between each member.

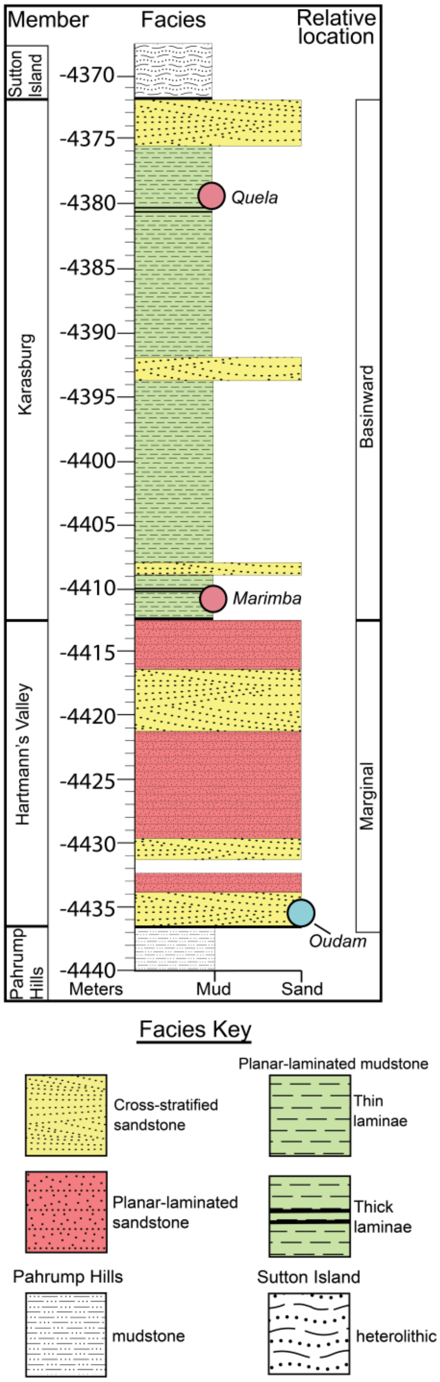

Figure 1.5 Detailed stratigraphic column for the distribution of Hartmann's Valley and Karasburg facies.

Facies 1: Cross-stratified sandstone

Description

Exposures of the cross-stratified sandstone facies were identified at multiple levels within both stratigraphic members from the base (Curiosity mission Sol 1104) to the contact between the Km and SIm (Sol 1470; Figures 1.1, 1.2, & 1.5). The majority of outcrops were imaged at distances of ~15-50 m from the rover, which prevented an assessment of contacts with underlying and overlying facies. Exposures are not laterally continuous beyond individual outcrops, though data collected over multiple rover transects both east and west of the Naukluft Plateau suggest that some lateral continuity is possible (Figure 1.2). The thickness of stratigraphic intervals across both members ranges from 1-4 m (Figure 1.5). Mineralogical data for Facies 1 was acquired from CheMin analyses of the drill sample Oudam (-4435 m).

Facies 1 is characterized by the presence of trough cross-bedding (Supplemental Table 1.1; Figure 1.6). Truncation surfaces are sub-horizontal with respect to the bounded laminae and are traceable across oblique m-scale outcrops (Figure 1.6a-b), disrupted by erosion as well as localized cross-cutting veins and nodules. Where truncation surfaces are less distinct, sets were interpreted from apparent changes in dip angle and direction (Figure 1.6c-d). Measurements of set thicknesses for outcrops with obscured or eroded upper and lower truncation surfaces represent minimum bounds for bedform height derived from individual outcrop heights and range from 50 to 100 cm.

Sets primarily consist of uniform curvilinear laminae. In several exposures, foresets curve and are asymptotic to the underlying strata (white box, Figure 1.6a, white box). Laminae that appear less curvilinear likely represent a portion of the foreset (Figure 1.6c). Outcrop orientation and imaging distance prevented measurements of laminae thickness, but comparisons of laminae with overall outcrop scale broadly constrain thicknesses to be mm-cm thick.

The majority of grain boundaries are not resolvable even in the highest-resolution MAHLI images (~15 μm/px). Limited measurements ranging in size from coarse silt to medium sand (Gwizd et al., 2018) are consistent with GIMS data across Facies 1 (Rivera-Hernández et al., 2020). One MAHLI image of the bedrock target Sacajawea consists of pervasive dark-toned and light-toned medium sand grains (Supplemental Figure 1.14). A rough surface texture observed in Mastcam and MAHLI images of the bedrock surface provides further evidence suggesting a sand-sized component in Facies 1.

Interpretation

Facies 1 is interpreted to represent a wet aeolian dune field. Preserved structures represent dune foresets and truncation surfaces, which remain after erosion of the stoss and upper lee slope by overlying dune migration (Brookfield, 1977; Rubin & Hunter, 1982). The apparent uniform laminae thicknesses and lack of discernable grain-size differences between outcrops suggests that deposition of laminae across all outcrops may have involved a similar depositional processes, although specific grainfall, grainflow, or wind-ripple deposits cannot be confidently differentiated. Grain measurements include some evidence for coarse silt (Gwizd et al., 2018), but mm-scale rough bedrock textures and pervasive fine sand grains in the target Sacajawea suggest that sand constitutes a primary size fraction. Mud-aggregate lunette dunes have been observed in terrestrial

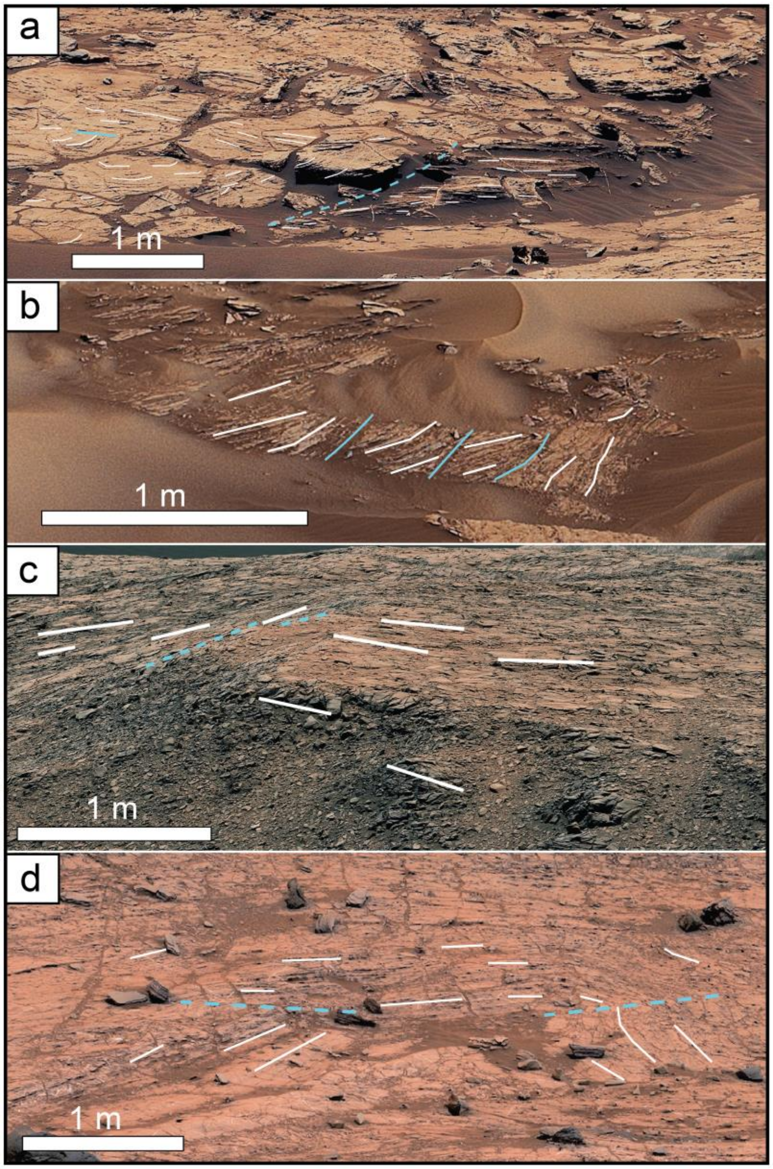

Figure 1.6 Representative outcrops of the cross-stratified sandstone facies. (a) Outcrop near the contact between the Murray and Stimson formation west of the Naukluft Plateau showing concave laminae (white lines), truncation surfaces (blue lines), and a possible inferred truncation surface (dashed blue line) based on apparent alternating dip directions between adjacent laminae. (M100 Mastcam mosaic, mcam06561, Sol 1353). (b) Baynes Mountain outcrop showing sets of laminae with apparent alternating orientations (M34 Mastcam mosaic, mcam06768, Sol 1381). (c) Keetmanshoop outcrop consisting of sets at least 1 meter thick (M100 Mastcam mosaic, mcam06838, Sol 1398). (d) Oblique view of Saddle outcrop showing truncation of laminae (M100 Mastcam mosaic, mcam04883, Sol 1101). Image credit: NASA/JPL-Caltech/MSSS.

settings, typically in arid environments, and are associated with desiccation (Bowler, 1973; Greeley, 1979). Rough textures and observations of sand-sized grains as well as a lack of any evidence for widespread desiccation structures associated with Facies 1 suggest that dunes are more likely comprised of a sand-sized component, rather than mud aggregates. Polishing from aeolian abrasion and overprinting by diagenetic mineralization could explain the absence of visible grain boundaries in certain images (Grotzinger et al., 2005; Gwizd et al., 2018).

The thicknesses and distribution of intervals of Facies 1 resemble stratigraphic records of wet aeolian environments (Mountney, 2012). Dune deposition and preservation in wet environments are controlled by increased sediment cohesion from fluctuations in the groundwater table which acts to stabilize dunes and limit dune growth (Kocurek & Havholm, 1993). This process has been documented in arid (Kocurek et al., 2007), sub-humid (Luna et al., 2011), and humid (Mountney & Russell, 2009) environments. Compared with counterparts formed in more arid environments, dunes deposited proximal to a subaqueous environments such as a coastal setting are generally smaller and more spatially isolated (Mountney & Russell, 2009) and comprise relatively thinner stratigraphic intervals (Al-Masrahy & Mountney, 2015; Mountney & Jagger, 2004). The limited thickness of stratigraphic intervals of Facies 1 (< 5 m) is similar to terrestrial records of marginal aeolian dune environments, indicating that dunes may have been comparably spatially isolated across the landscape.

Cross-stratification as described above may also form in fluvial environments, but this interpretation is considered less likely for several reasons. Sets with thicknesses of 1 m are indicative of potential water depths of >10 m, which corresponds to depths in some of the largest terrestrial river systems (Cisneros et al., 2020; Leclair & Bridge, 2001). Given the proximity of Facies 1 with Facies 3 and the lacustrine basin environment (Facies 3 detailed in "Facies 3: Planar-laminated mudstone"; Figure 1.5), such a large-scale river system would be unlikely. Additionally, there is an absence of evidence for fluvial architectural elements such as channel fills, accretion elements, and barforms within the stratigraphy (e.g. Ielpi and Rainbird, 2015; Long, 2006; Muhlbauer et al., 2020). Additionally, fluvial facies identified in the Bradbury group consist of granule- and pebble-sized clasts and exhibit varying degrees of sorting (Edgar et al., 2017; Williams et al., 2013). Even where grain boundaries are not visible in MAHLI images, rougher surface textures lack evidence for features in this size range. Altogether, these lines of evidence do not favor a fluvial interpretation.

Facies 2: Planar-laminated sandstone

Description

Exposures of planar-laminated sandstone were observed throughout the HVm and extend to the contact with Facies 3 and the Km (Figures 1.2 & 1.5). Stratigraphic intervals of Facies 2 are most commonly intercalated with Facies 1 (Figure 1.5). Thicknesses of intervals range from 1.5-8 m and cumulatively represent half of the stratigraphy in the 25 m thick HVm (Figure 1.5). No drill samples were analyzed by CheMin from Facies 2.

Facies 2 is characterized by continuous accumulations of parallel-laminated sandstone (Figure 1.7). Where exposed in cross-section, individual laminae are laterally continuous across the outcrop and can be traced across fractures, veins, and patches of sand cover (Figure 1.7a). Some outcrops consist of intervals of alternating resistant and recessive laminae (Figure 1.7a) whereas laminae in other outcrops exhibit a similar resistance to erosion (Figure 1.7b). Laminae measured from one rock target have an average thickness of 1.8 mm ± 0.38 mm (Supplemental Table 1.2). Though measurements were restricted to one target, visual comparisons suggest that this value is broadly representative of mm-scale laminae of Facies 2 across the study region.

Grains are not resolvable in MAHLI images, but several observations support a sand-grade component in contrast to laminated mud. Relative to the planar-laminated mudstone facies (see section “Facies 3: Planar-laminated mudstone”), laminae exhibit a greater resistance to erosion (Figure 1.7a-b), which may correlate with a coarser grain-size. Additionally, a rough surface texture similar to the cross-stratified sandstone facies was documented in MAHLI images of the bedrock surface (Figure 1.7c). In addition to sand, a finer grain-size component is supported by GIMS values, which range from mud to sand (Rivera-Hernández et al., 2020). Visual observations support a coarser sand component as the dominant lithology, but a range of grain sizes is considered in interpretations of depositional environments.

Interpretation

The most plausible model for deposition of Facies 2 involves a mixture of subaerial and subaqueous processes. Successions of flat-lying subaqueous and subaerial laminae can accumulate in wet interdune environments where the lowermost toeset

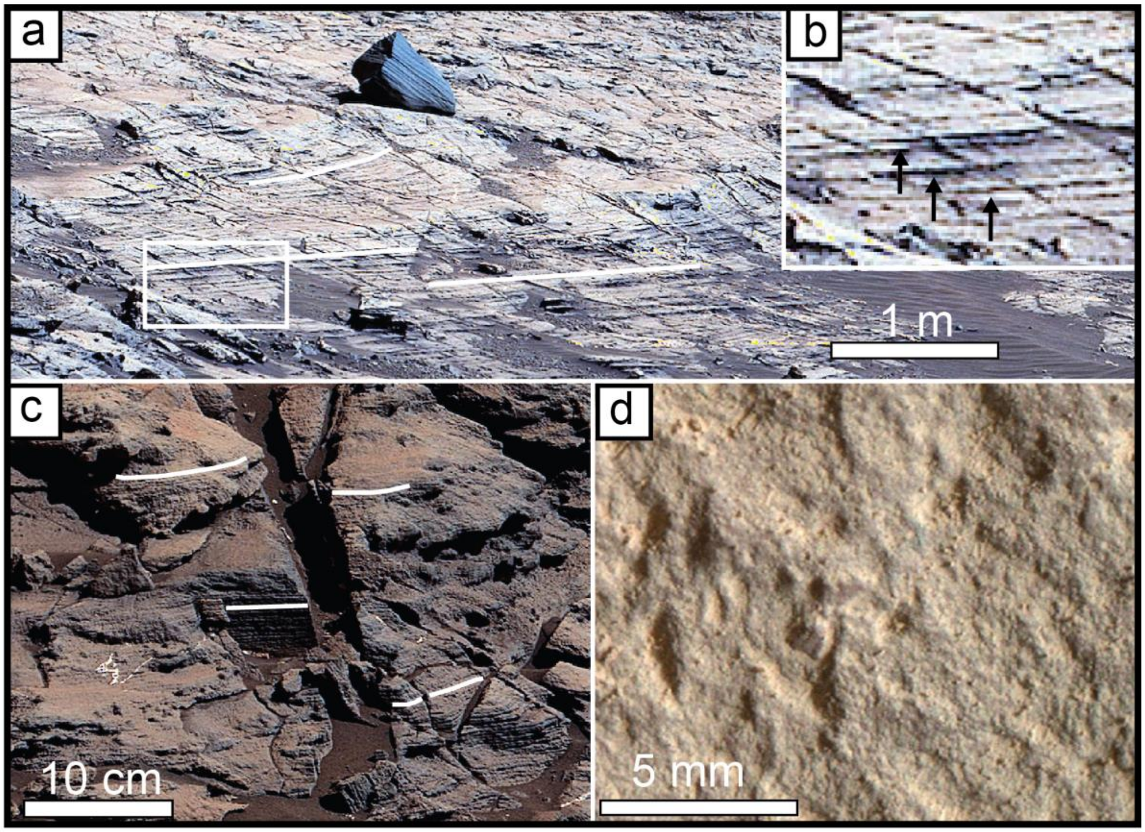

Figure 1.7 Representative outcrops of the planar-laminated sandstone facies. (a) Outcrop consisting of continuous planar laminae showing varying degrees of erosion. The region within the white box is expanded in (b) to highlight an example of alternating resistant planar laminae (M100 Mastcam mosaic, mcam05228, Sol 1157). (c) Example of a smaller-scale outcrop consisting of a continuous succession of planar laminae. Laminae are highlighted with white lines (M100 Mastcam mosaic, mcam05389, Sol 1189). (d) MAHLI target Koes showing a plan view exposure with a distinctly rough bedrock texture (MAHLI ID: mhli00419, Sol 1380). Image credit: NASA/JPL-Caltech/MSSS.

laminae of dunes become subaqueously reworked or preserved (Langford & Chan, 1989; Mountney & Jagger, 2004; Mountney & Russell, 2009). Although aeolian and interdune components cannot be distinguished within the intervals of Facies 2, modern and ancient studies of wet aeolian systems show that both subenvironments are intricately linked and that a dynamic set of depositional conditions may have produced the planar-laminated strata. In wet aeolian settings, groundwater flooding and fluvial incursion through aeolian deposits can generate laterally expansive ponded interdune environments (Mountney & Jagger, 2004; Mountney & Russell, 2009; Mountney, 2012). Deposition may therefore represent a combination of subaerial reworking, fluvial traction deposition, flooding, and localized sediment grain flows at the edge of interdune hollows. Although there is no documented evidence of preserved flow structures in the HVm to indicate large-scale changes in flow velocity, variability in the erosional resistance of laminae (Figure 1.7a) may correlate to localized changes in depositional energy.

Studies of terrestrial deposits interpret the intercalation of dune facies with thick intervals of interdune facies to indicate a water-table controlled system typically along outer erg margins (Al-Masrahy & Mountney, 2015; Mountney & Jagger, 2004). The stratigraphic stacking pattern of a water-table controlled aeolian system reflects numerous factors including sediment supply, water-table rise, local dune morphology, and climate (Mountney & Jagger, 2004; Mountney & Russell, 2006). Successions of comparably thick intervals of dune and interdune facies are indicative of sub-critically climbing strata, typically resulting from the lateral expansion of wet interdune environments and subsequent restriction in sediment supply (Mountney, 2012).

Laminae can form in sandstone from numerous depositional processes, but the thickness of stratigraphic intervals can help constrain depositional processes responsible for Facies 2. Given the apparently significant lateral extent of Facies 2 documented along the HVm traverse (Figures 1.1 & 1.2), laminae likely formed via subaqueous deposition. The stratal stacking pattern of planar-laminae and intervals of comparably thick cross-stratified sandstone facies suggests that a subaqueous interdune setting within a wet aeolian system provides the most plausible model for Facies 2. Modes of sediment deposition in wet interdune systems will vary based on the nature of the interdune environment, with common modes of deposition including subaqueous reworking of adjacent dune toeset strata and input from fluvial suspended load and bedload (Mountney & Russell, 2009). Comparably thick intervals of planar laminae can form from suspension fallout in a lacustrine basin (e.g. Boulesteix et al., 2019), but such an interpretation cannot explain the intercalations with intervals of cross-stratified sandstone (Figure 1.5). Upper-flow-regime subaqueous conditions are capable of producing horizontal laminae in river systems associated with sporadic flooding, but laminae typically occur in cm-scale packages and are associated with largely arid environments (Colombera & Mountney, 2019; McKee et al., 1967). Subaerial wind-ripple migration can generate meter-thick successions of planar-laminated sandstone associated with interdunes in a dry erg setting (Clemmensen & Abrahamsen, 1983; Hunter, 1977), but the relatively thin intervals of interbedded cross-stratified sandstone facies would be expected to be much thicker in a dry erg setting (Mountney, 2012). Given the thickness of stratigraphic intervals comprising Facies 2, a wet interdune setting is a plausible interpretation of environment, with numerous possible processes responsible for deposition of sediment.

Facies 3: Planar-laminated mudstone

Description

Exposures of planar-laminated mudstone occur only in the Km stratigraphy (Figures 1.2 & 1.5). Outcrops are consistent with the eroded and fractured bedrock characteristic of the orbital images of Km stratigraphy (Figures 1.1 & 1.4), suggesting lateral continuity across the study area. Facies 3 occurs in three stratigraphic intervals 3.5, 14, and 16.5 m thick, which cumulatively represent 85% of the Km stratigraphy (Figure 1.5). Three 1-4 m thick intervals of Facies 1are associated with Facies 3 at -4409, -4394, and -4376 m (Figure 1.5). Mineralogical data for Facies 3 was acquired from CheMin analyses of two drill samples, Marimba (-4410 m) and Quela (-4379 m).

Outcrops are comprised of continuous successions of parallel laminae that appear distinctly more recessive and erodible relative to parallel laminae in Facies 2 (Figure 1.8). The majority of laminae are distinguishable by subtle changes in erosional resistance. Laminae display relatively uniform thickness across the majority of the stratigraphic succession (Figure 1.8a). Individual laminae measured from three representative rock targets have average thicknesses of 1.3 mm ± 0.2 mm and 2.0 ± 0.5 mm, and 9.1 ± 2.4 mm (Supplemental Table 1.2). Apparent thicker and more erosionally resistant laminae were identified at two stratigraphic intervals (-4410 m and -4380 m; Figures 1.5 & 1.8b), but the majority of Facies 3 is characterized by mm-scale recessive laminae.

Individual laminae are traceable laterally across outcrops except where disrupted by cross-cutting fractures, veins, or concretions. Laminae show variable resistance to weathering, but overall are more recessive than the planar-laminated sandstone facies. Randomly distributed resistant laminae are characterized by sharp boundaries which are generally associated with diagenetic textures (Figure 1.8c). Recessive laminae lack diagenetic textures and are generally smooth (Figure 1.8d). Transects of gray-scale values perpendicular to the recessive MAHLI target Biula show fluctuations in intensity occurring on a similar scale as individual laminae (Figure 1.8d; Supplemental Table 1.2). This similarity in scale indicates that individual laminae correspond to changes in erosion. Intensity values do not reveal gradational patterns characteristic of specific depositional processes, such as tempestites or turbidites (Lazar et al., 2015).

Individual grains are not resolvable in MAHLI images of laminae or bedrock surfaces. The relatively smooth texture and recessive appearance of laminae (Figure 1.8) suggests that Facies 3 is fine-grained and that the lack of visible grain boundaries corresponds to sediment in the mud size fraction rather than overprinting from erosion or diagenetic textures. More than 50% of GIMS values fall in the mud- to very fine sand-size fraction, though some component of coarser sand is also indicated by GIMS values, (Rivera-Hernández et al., 2020). A finer-grained component is also supported by mineralogy of Marimba and Quela, which contain a greater amount of clay minerals (28 wt% and 16 wt%, respectively) relative to the Oudam drill sample of Facies 1 (3 wt%; Achilles et al., 2020; Bristow et al., 2018).

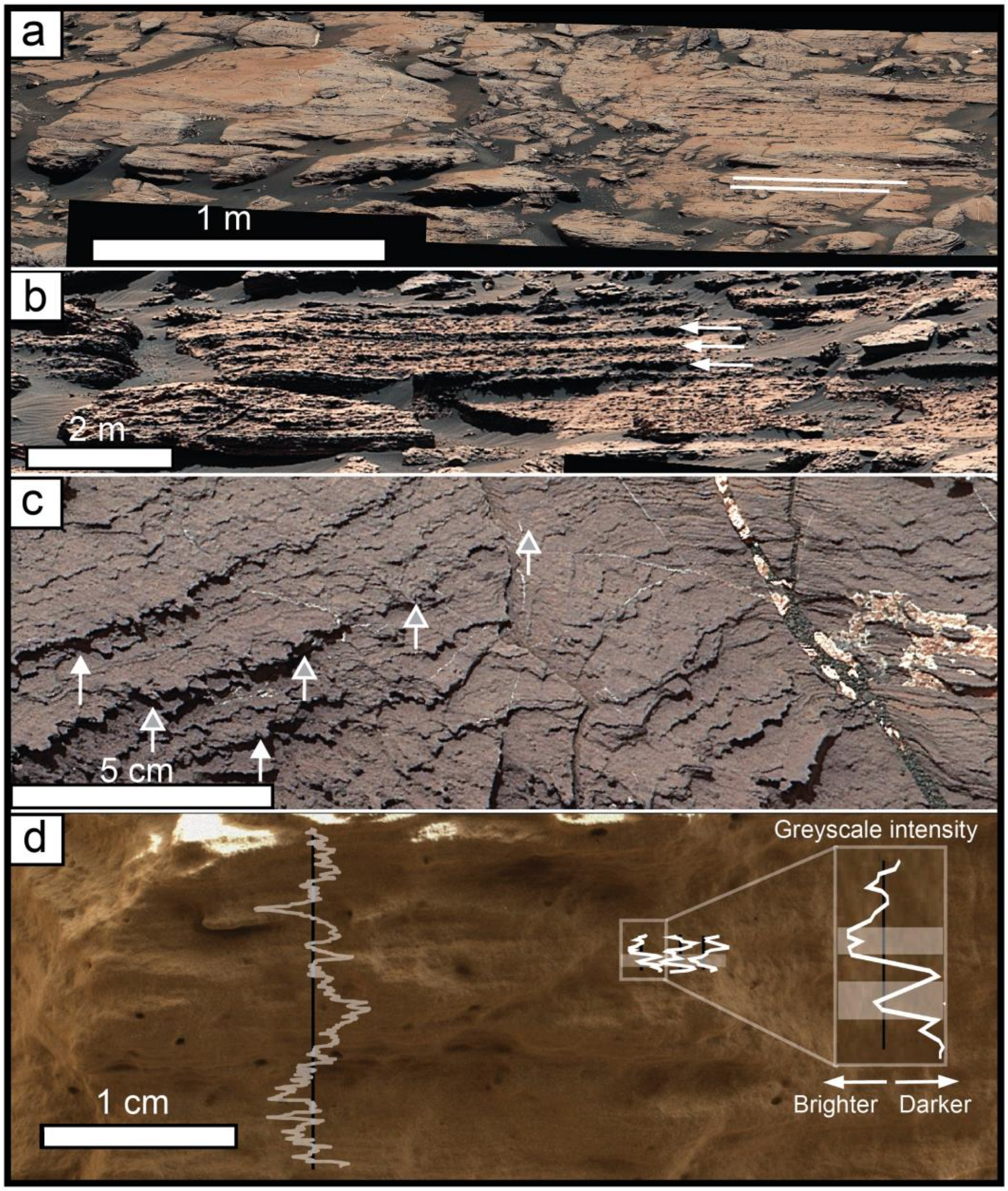

Figure 1.8 Representative outcrops of the planar-laminated mudstone facies. (a) Outcrop Kuito consisting of continuous planar laminae (white lines highlight some examples, M100 Mastcam mosaic, mcam07198, Sol 1455). (b) Examples of thicker cm-scale laminae (white arrows, M100 Mastcam mosaic, mcam07067, Sol 1429). (c) Target Caxito containing smaller-scale alternating resistant (white arrows) and recessive laminae with diagenetic textures (M100 Mastcam image, mcam07170, Sol 1448). (d) MAHLI target Buila with plots of greyscale values highlighting variability in recessive and resistant laminae (white arrows, MAHLI ID: mhli00321, Sol 1436). Image credit: NASA/JPL-Caltech/MSSS

Interpretation

Facies 3 is interpreted to have formed primarily from deposition of sediment in a lacustrine environment. The alternating resistant and recessive laminae (Figure 1.8c-d) resemble the expression of graded laminae where the fine-grained layers are more susceptible to erosion. Successions of graded varves form in glacial lacustrine settings from depositional processes which are controlled by regular changes in runoff and sediment input (Anderson & Dean, 1988). Thicker laminae could represent localized changes in sediment input or energy (Figure 1.8b), but their sparse occurrence indicates that environments were largely stable. The lateral continuity and mm-scale thickness of individual laminae are consistent with deposition from hypopycnal, homopycnal, or distal lofted hyperpycnal flow processes (Boulesteix et al., 2019), though the lack of any additional sedimentary structures precludes differentiation of the specific flows responsible for deposition. Subaqueous settling of wind-blown sediment (e.g. loess, ash) could also comprise some of this facies, but the uniform laminae thicknesses and resemblance to clastic varves suggest that laminae formed in response to allogenic or autogenic controls in sediment input (Renaut & Gierlowski-Kordesch, 2010; Zolitschka et al., 2015). Similar depositional processes are attributed to planar-laminated mudstone facies with similar outcrop expressions and laminae thicknesses in underlying and overlying members of the Murray formation (Edgar et al., 2020; Stack et al., 2019), suggesting that driving mechanisms behind sedimentation of Facies 3 may have been related.

The complete lack of evidence for subaerial exposure indicates deposition in a relatively stable depth of standing water throughout deposition of Facies 3. Terrestrial records of similar lacustrine environments typically exhibit a fluvial-deltaic facies association (e.g. Bohacs et al., 2007). The association of Km mudstone with aeolian facies does not preclude the presence of continuous standing water and may be comparable to ancient and modern unvegetated landscapes, which are associated with an increased sediment supply available for aeolian transport (e.g. Hadlari et al., 2006; Luna et al., 2012; Mountney & Russell, 2009).

Stratigraphic and depositional synthesis

Small-to-large-scale observations of the HVm and Km reveal three facies that indicate lacustrine-margin and lacustrine-basin paleoenvironments (Figures 1.6-1.8; Supplemental Table 1.1). A block diagram of the interpreted landscape is depicted in Figure 1.9. Cross-stratified and planar-laminated sandstone facies are interpreted to represent deposition of aeolian dunes and subaqueous ponded interdunes along the lacustrine margin (Figures 1.6 & 1.7). Although the depiction of cross-stratified sandstone facies in the Km portion of the stratigraphic column shows apparent interbedding with the lacustrine mudstone facies (Figure 1.5), the lack of stratigraphic evidence for associated widespread desiccation suggests that m-thick intervals of aeolian dune facies in the Km also represent deposition along the lacustrine margin (Figure 1.9). The lacustrine mudstone facies represents deposition in a lake basin in the presence of continuous standing water (Figures 1.8 & 1.9). Deposition is interpreted to be

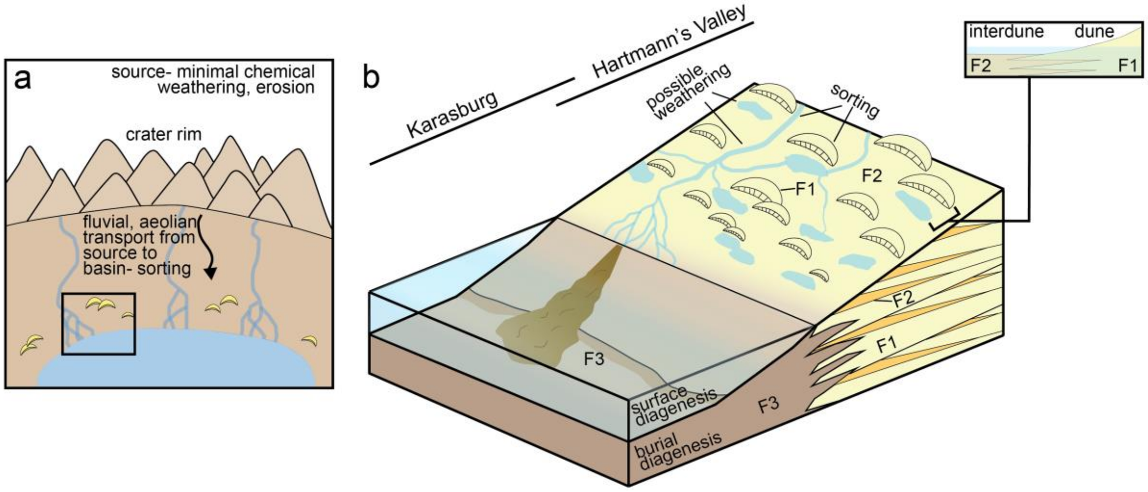

Figure 1.9 (a) Basin-scale landscape showing distal sedimentary processes interpreted in this study. Black box indicates the relative location of the Hartmann's Valley and Karasburg member environments in (b). (b) Landscape schematic for the lacustrine-margin and lacustrine depositional environments represented by the facies of the Hartmann's Valley and Karasburg members. The depiction of the lake margin stratigraphy is adapted from the model for temporally and spatially variable dune systems from Mountney, 2012 (Figure 1.4). F1 = Facies 1; F2 = Facies 2; F3 = Facies 3.

controlled by fluvial generation of sediment flows and plumes within the basin (Mulder & Zyvitski, 1995; Zavala et al., 2011), which implies that fluvial-deltaic environments occurred within the lacustrine-margin landscape (Figure 1.9). It is noted that fluvial-deltaic facies were not documented in the stratigraphy of the HVm and Km, but do occupy intervals within the underlying Pahrump Hills member (Stack et al., 2019) and Bradbury group (Grotzinger et al., 2015).

Comparisons with analogous terrestrial environments provide a basis for spatial constraints of the landscape depicted in Figure 1.9. The Skeiðarársandur glacial outwash plain in south Iceland and the Lençóis Maranhenses coastal dune system in northeast Brazil are modern analogues for wet aeolian environments adjacent to a coastline (Hilbert et al., 2016; Mountney & Russell, 2009). Wet aeolian environments in the Skeiðarársandur plain are characterized by isolated dunes with heights up to 3 m and small dune fields (up to 1 km^2) with heights up to 5 m, and subaqueous interdunes characterized by low energy fluvial streams and ponds of up to 0.3 m of standing water (Mountney & Russell, 2009). The Lençóis Maranhenses dune system comprises an area of 1052 km^2 and is characterized by dunes with heights of 50-100 cm proximal to the coast and reaching up to 30 m downwind (Parteli et al., 2006). Interdune ponds reach maximum depths of ~1 m (Dos Santos et al., 2019). Simplification of the traverse segments across the HVm and Km (Figures 1.1 & 1.2) into an E-W segment (Sol 1105-1353) and a N-S segment (Sol 1353-1471) constrains a comparably smaller area of approximately 1.4 km^2. Although variable boundary conditions (e.g. climate, tectonics, sediment supply) control the scale of each landscape (Ewing & Kocurek, 2010), the overall scales over which facies transitions are documented in both environments are comparable in scale of transitions across the study area. These environments may therefore provide plausible scenarios for the extent of the marginal landscapes beyond the region of the rover traverse.

Although spatial characteristics (e.g. areal extent, water depth) of lake systems do not directly relate to stratal stacking patterns (Bohacs et al., 2000), terrestrial studies can be used to constrain aspects of the HVm and Km stratigraphy. The continuity and uniformity of mudstone laminae and the lack of stratigraphic evidence for flooding or desiccation in the Km is consistent with terrestrial records of overfilled lake basins (e.g. Bohacs et al., 2007; Stewart & Mauk, 2017). Whereas the underlying PHm stratigraphy exhibits a progradational trend (Carroll & Bohacs, 1999; Bohacs et al., 2000), the HVm and Km stratigraphy exhibits an overall trend toward finer-grained lacustrine mudstone with intervals of aeolian sandstone at stratigraphically higher elevations (Figure 1.5), suggesting that the stratigraphy of the HVm and Km record an interval of lake expansion.

Linking depositional conditions and composition

APXS dataset

Twenty-nine APXS measurements of whole-rock geochemistry (additional file attachment table 1.3) from the HVm and Km are utilized to explore the possible fingerprints of source-rock composition, chemical weathering, sorting, and diagenesis. In order more accurately evaluate the primary geochemical trends, data are discussed bracketed by two end-member scenarios: with (equation 5) and without (equation 4) a correction for apatite and Ca-sulfate (see section “Geochemical tools”). Based on the occurrence of primary Ca-bearing silicate phases measured with CheMin (Achilles et al., 2020), the upper limit for the fraction of molar SO_3 subtracted from Ca is defined where $CaO^* \leq 0$. Within the HVm and Km APXS targets, this threshold occurs at a fraction of $0.5*SO_3$. Given the relative proportions of primary Ca phases to diagenetic Ca-sulfate measured with CheMin in Oudam, Marimba, and Quela (Achilles et al., 2020), a fraction of $0.4*SO_3$ is likely too high, but is a plausible upper bound for a Ca correction. Calculated CIA and $MIA_{(O)}$ indices from each modeled fraction of SO_3 are listed in additional file attachment table 1.4. Values of CIA calculated within the range defined by this study are similar to those determined using ChemCam in Mangold et al. (2019), lending further support for the range of modeled corrections in this study. In the following sections, uncorrected data is that where no applied Ca correction ($CaO^* = CaO_{(T)}$) is made, and Ca-corrected data correspond to values of CaO* calculated using the upper limit defined in this study.

Source rock

The composition and texture of the source rock determines the original starting point to assess all subsequent compositional changes associated with sediment formation and deposition. Though an exact provenance composition for the HVm and Hm facies cannot be determined, a compositional range can be estimated (Figure 1.10) using the geochemistry of igneous float rocks documented at Gale crater and basalt classes of Gusev crater (Figure 1.10a; additional file attachment table 1.3; McSween et al., 2008). Additional constraints derive from indirect assessments of geochemical trends of Facies

1-3 in A-CN-K ternary space (Figure 1.10b), which are compared to established alteration trends for basalt (Nesbitt & Wilson, 1992).

A direct assessment of a plausible source composition was done by averaging known Martian basaltic compositions (Figure 1.10a). Figure 1.10a includes compositions interpreted to be igneous from Gale and Gusev craters analyzed with the APXS instrument. Float rocks (n = 19) identified along the Curiosity traverse represent a diverse assemblage of alkaline and basaltic compositions (additional file attachment table 1.3; Berger et al., 2020; Schmidt et al., 2014; Thompson et al., 2016; Wiens et al., 2020). Basalts (n = 16) documented at Gusev crater are defined by their geochemistry and include the Adirondack, Irvine, Wishstone, Backstay, Algonquin, and Barnhill classes (additional file attachment table 1.3; Gellert et al., 2006; McSween et al., 2008; Ming et al., 2008). All data points were Ca-corrected for apatite. Within the A-CN-K ternary diagram (Figure 1.10a), Gale float rocks (orange circles) predominantly plot along a CIA range of 36-45, with one data point plotting at a CIA of 33 and one data point plotting at a CIA of 49. Gusev basalt classes (gray circles) predominantly plot along a CIA range of 37-40, with four data points plotting above a CIA of 45 (Figure 1.10a). An average value of all data points (black filled circle, Figure 1.10a) was generated as a plausible "homogenized" source rock composition for the HVm and Km facies and plots at a CIA of 42. Also included is the average value for Martian crust (blue filled circle, Figure 1.10a; Taylor & McLennan, 2009), which is also Ca-corrected for apatite and is similar in composition.

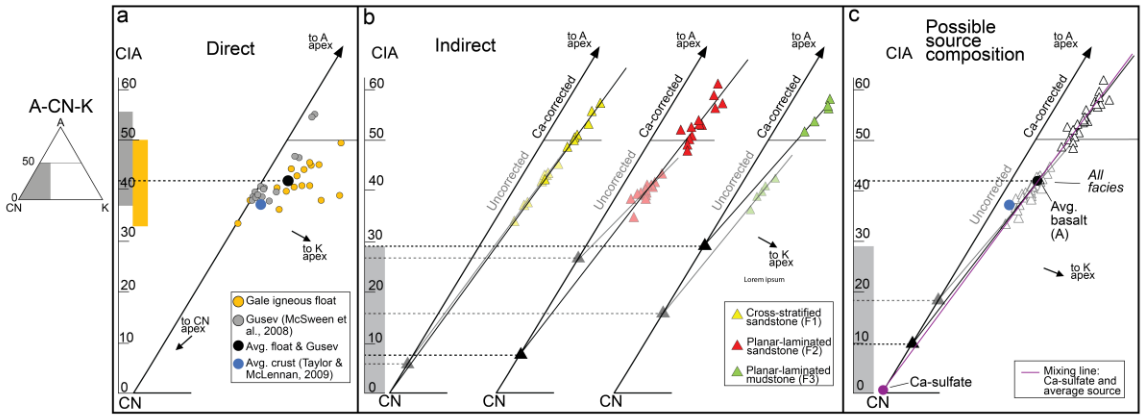

Figure 1.10 Evaluation of potential source compositional ranges in A-CN-K ternary diagrams. (a) Plot of Gale igneous float rocks, Gusev basalt classes, average Mars crust, and a calculated average of the float rocks and average Gusev basalt classes (dashed line indicates a CIA of 42). (b) Linear trendlines for individual facies with no Ca correction (faded colors; equation 4) and with the applied Ca correction for P_2O_5 and $0.4*SO_3$ (bolded colors; equation 5). Gray triangles indicate the location where uncorrected trendlines intersect the A-CN join, and black triangles indicate the location where Ca-corrected trendlines intersect the A-CN join (dashed lines). The gray box shows the range of lower bounds for source rock CIA defined by Facies 1-3 trendlines. (c) Trendlines for all uncorrected (faded triangles) and corrected (bolded triangles) facies compared to the calculated basalt source composition (black circle) and the lower bounds constrained by trendlines in (b). Also included is a mixing line between Ca-sulfate and the average basalt composition (purple line).

Linear trends produced from chemical weathering of source bedrock (arrow 1, Figure 1.3a; Nesbitt & Wilson, 1992; Thorpe et al., 2020) can be used as a means to indirectly estimate the original source composition. In the A-CN-K ternary diagram, the lowermost point along the chemical weathering path plots at low values of CIA (the vertical axis of the ternary diagram) and typically represents a measured unaltered source rock composition (triangle a, Figure 1.3a). Without an exact constraint on the unaltered source rock for the HVm and Km facies, a lower bound may be estimated from linear data arrays in sedimentary rocks that result from erosion of weathered profiles (Nesbitt et al., 1997). Data for each facies define linear arrays (Figure 1.5b) in A-CN-K space, providing guidance for estimating bulk starting composition where the line of best fit intersects the A-CN join.

Figure 1.10b shows the distribution of Facies 1-3 with no Ca correction (faded yellow, red, green filled triangles) following equation 4 and with a Ca correction (dark yellow, red, green filled triangles) following equation 5. Both the uncorrected and the corrected data for each facies plot as linear trends and show a similar range of CIA values between facies in A-CN-K ternary space (Figure 1.10b), consistent with the geochemical similarities observed across most oxides (Supplemental Figure 1.15). The gray box along the y-axis in Figure 1.10b shows the range of lower bounds for source rock CIA defined by the three facies where the best-fit line intersects the A-CN join. In the uncorrected scenario, the Facies 1 trendline intersects the A-CN join at the lowermost value of A = 6 (where A = CIA value), the Facies 2 trendline intersects at A = 16, and the Facies 3 trendline intersects at A = 27. All intersect points occur below the CIA of the averaged

Martian basalt (A = 42). In the Ca-corrected dataset, the Facies 1 trendline does not intersect the A-CN join, the Facies 2 trendline intersects at 8**,** and the Facies 3 trendline intersects at 29. Similar to the uncorrected trendlines, both intersects occur below the range of CIA for the averaged Martian basalt. In both scenarios, trendlines intersect the A-CN join at values below the averaged Martian basaltic composition as well as typical unweathered terrestrial basalts (A = 35-40; Babechuk et al., 2014).

Extrapolation of the linear trend across all facies results in an approximate intersection at the A-CN join at A = 18 for uncorrected data and A = 10 for Ca-corrected data, within the range defined by the individual trendlines (Figure 1.10c). The intersection of both trendlines with the mixing line between a Ca-sulfate end-member and the average basalt source (purple line, Figure 1.10c) provides additional support for analysis of source composition along the trendlines defined by the uncorrected and corrected data arrays. Both trendlines intersect the averaged Martian basalt source composition (black filled circle, Figure 1.10c). The geochemical similarity of HVm and Km facies to the averaged basalt indicates that the compositional variability of the Gale float rocks and Gusev basalts captures a plausible range of source compositions. An Adirondack end member and a potassic-rich end member have both been previously suggested to explain the source composition of intermittent intervals of the Murray formation (Bedford et al., 2019; Edwards et al., 2017), though some component of diagenetic K-rich phases could also cause data to deviate from the A-CN apex (see section “Diagenesis”; Mangold et al., 2019; Yen et al., 2018). Given the compositional data of basalts and the interpretation of the sedimentary rock data, the averaged basalt value derived from Martian basaltic compositions provides a reasonable estimate of a source rock compositional range for all three HVm and Km facies.

Weathering

Mineralogical and geochemical trends indicate that chemical weathering has influenced the composition of Murray formation sediments, including the stratigraphy of the HVm and Km (Bristow et al., 2018; Mangold et al., 2019). The extent of chemical weathering for the HVm and Km facies can be understood by contextualizing geochemical trends in ternary diagrams with calculated CIA and $MIA_{(O)}$ indices (see section “Geochemical tools”). Potential weathering trends are illustrated in A-CN-K, A-CNK-FM, and AF-CNK-M ternary diagrams using both uncorrected and Ca-corrected data (Figure 1.11). The addition of diagenetic Ca-sulfates raises the total calcium abundance, and thus lowers CIA so that the uncorrected data represent the minimum extent of weathering (Figure 1.11a-c); by contrast, the Ca-corrected data represent the maximum extent of weathering (Figure 1.11d-f) determined in this study because the correction was set for reaching the point where calcium initially approaches zero (discussed above). Included for comparison are data from the basaltic terrestrial Chhindwara weathering profile (black boxes), a post-Pleistocene and moderately weathered profile developed on Deccan Trap basalt (Babechuk et al., 2014).

Each of the three facies is plotted on the A-CN-K diagram (Figure 1.11a) as a way to identify whether deposition by differing processes generates changes in perceived weathering intensity. Uncorrected data plot sub-parallel to the A-CN join and span a CIA

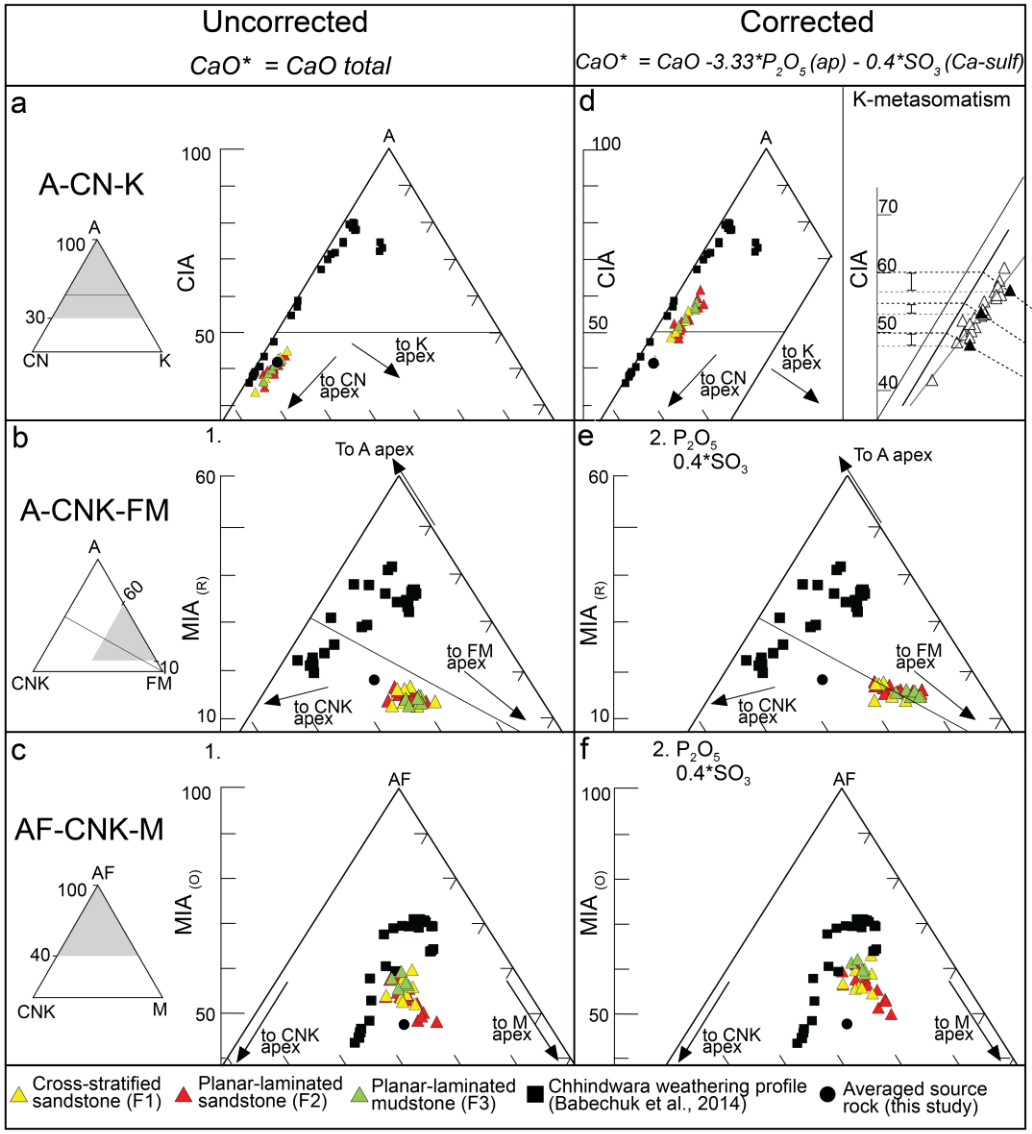

Figure 1.11 Weathering trends illustrated on A-CN-K, A-CNK-FM, and AF-CNK-M molar ternary diagrams. The shaded in regions of the triangles correspond to the zoomed in portion in A-F. The left column depicts uncorrected data in (a) A-CN-K, (b) A-CNK-FM, and (c) AF-CNK-M diagrams. The right column depicts Ca-corrected data for P_2O_5 (Ap) and 0.4*SO_3 (Ca-sulfate; equation 5) in (d) A-CN-K, (e) A-CNK-FM, and (f) AF-CNK-M diagrams. A second A-CN-K diagram in (d) includes an example of the visual correction for K-enrichment (See Fedo et al., 1995 for methodology). The terrestrial Chhindwara weathering profile (black boxes; Babechuk et al., 2014) and the average basaltic source composition (black circle) are included for reference.

range of about 11 CIA units (A = 34-45; additional file attachment table 1.4). Facies 1 data form a linear trend at a CIA range of 34-45 (yellow triangles, Figure 1.11a). Facies 2 data also form a linear trend, albeit with more scatter relative to Facies 1, along a CIA range of A = 35-43 (red triangles, Figure 1.11a)**.** Similar to Facies 1 and 2, Facies 3 data form a linear trend at a CIA range of A = 36-42 (green triangles, Figure 1.11a). Uncorrected values of CIA are similar between mud and sand facies (Figure 1.11a; additional file attachment table 1.4). The data exhibit a linear trend similar to the Chhindwara profile but are less extensively spread out, plotting in position at a level similar to corestone-rich horizons (Figure 1.11a).

As expected, corrected data shift toward the A-apex and plot along a CIA range of about 19 CIA units (A = 42-61), representing an increase in the average CIA of 13 CIA units (Figure 1.11d). This shift towards A indicates a substantially greater extent of weathering across facies, with a difference of up to 20 CIA units between corrected values and the modeled starting source composition (A = 42). Facies 1 data form a linear trend at a CIA range of A = 42-57 (yellow triangles, Figure 1.11d). Facies 2 data form a linear trend along a CIA range of A = 48-61 (red triangles, Figure 1.11d)**.** Facies 3 data form a linear trend at a CIA range of A = 52-58 (green triangles, Figure 1.11d). Corrected values for CIA are similar between mud and sand facies (Figure 1.11d; additional file attachment table 1.4), with both plotting near more weathered intervals of the Chhindwara weathering profile. Data exhibit a difference of up to 19 CIA units relative to the modeled source rock composition (A = 42), suggesting the true extent of weathering was considerable. Given the presence of secondary sulfate in the samples, the corrected data are much more likely to represent the actual compositions at the time of deposition. It is worth noting that the data array shows an increase of K_2O across the array, indicative of its subsequent addition. Following the graphical correction approach of Fedo et al. (1995), CIA values in the Ca-corrected data raise a maximum of about 2-3 units, which we consider negligible, but yields a final range of pre-diagenesis CIA values of 42-62.

On the A-CNK-FM diagram (Figure 1.11b), facies plot below the feldspar-olivine join and are more clustered compared with the spread of data from the Chhindwara weathering profile. All facies plot more proximal to the FM-apex relative to the averaged basaltic source composition (black circle, Figure 1.11b). Relative to uncorrected facies, Ca-corrected data shift toward the A-FM axis, with most data points plotting along-to-above the feldspar-olivine join (Figure 1.11e). Corrected facies overlap within A-CNK-FM ternary space, with a slight trend of Facies 3 toward the FM-A axis relative to Facies 1 and 2. All facies plot further from the averaged source relative to uncorrected facies. Compared to the Chhindwara weathering profile, corrected data remain relatively clustered and do not follow a weathering pathway (Figure 1.11e). For uncertain reasons, this observation is in contrast with the trends in Figure 1.11a and Figure 1.11d, where data appear to plot along a linear trend similar to an expected weathering pathway.

On the AF-CNK-M diagram (Figure 1.11c), uncorrected facies plot across a range of $MIA_{(O)}$ values from 48-60 (additional file attachment table 1.4). Most data points plot more proximal to the AF apex compared to the averaged basaltic source composition (black circle, Figure 1.11c). Facies overlap similarly to the other ternary diagrams, although Facies 2 exhibits a slight trend toward the M-apex and Facies 3 is more clustered toward the AF-apex compared to Facies 1 and 2. Data corrected for non-silicate calcium show a relative increase in the $MIA_{(O)}$ by an average of 5.5 MIA units, with a total range of $MIA_{(O)}$ of 13 units (additional file attachment table 1.4). Facies shift toward the AF-M axis and plot more proximal to the AF apex relative to the averaged basaltic source composition (black circle, Figure 1.11f). Facies generally exhibit a similar degree of overlap compared to the uncorrected values (Figure 1.11f). Corrected data show a more distinct trend of Facies 2 toward the M-apex, whereas data from Facies 1 and Facies 3 continue to exhibit a relatively more clustered distribution closer to the AF-apex. The Facies 2 trend coincides with the slightly greater average wt% of MgO (6.34 wt%) relative to Facies 1 (5.90 wt%) and Facies 3 (5.43 wt%). The Chhindwara trend shows the preferential weathering of plagioclase (Ca, Na) over mafic mineral weathering (Mg; Babechuk et al., 2014), which differs from the Mg-apex trend of Facies 2 and the clustered distribution of Facies 1 and 3.

The range of weathering indices and trends using non-silicate Ca-corrected data records variable amounts of chemical weathering across the HVm and Km facies (Figure 1.11; additional file attachment table 1.4). Within the A-CN-K ternary diagram (Figure 1.11d), moderately extensive chemical weathering is indicated by the range of Ca-corrected CIA values that follow a linear trend similar to that of the Chhindwara weathering profile, indicating the sediments were likely drawn from different levels of a weathering profile or experienced differential chemical weathering during transport and deposition. The geochemical trends and CIA values of Ca-corrected data (Figure 1.11d) provide evidence for considerable chemical weathering similar to interpretations of

ChemCam LIBS for the Murray formation (Mangold et al., 2019). These observations differ from the A-CNK-FM (Figure 1.11e) and the AF-CNK-M (Figure 1.11f) ternary diagrams, where facies do not follow a similarly distinct weathering pathway. One important observation is the difference between the relative position of facies relative to the A-apex in A-CN-K (Figure 1.11a & d) and A-CNK-FM (Figure 1.11b & e) ternary diagrams. Ternary diagrams for Genoa River mud and sand samples in Nesbitt et al., (1996) depict a somewhat similar scenario between both diagrams, where there is a discernable trend of mud relative to sand toward the A-apex in A-CN-K space but both mud and sand plot at a similar distance from the A-apex in A-CNK-FM ternary space. The authors attribute these trends as indicative of the effects of sorting of felsic phases (feldspar; Nesbitt et al., 1996). Although sand and mud facies overlap in A-CN-K ternary space, the difference between trends in Figure 1.11d and Figure 1.11e may reflect grain segregation due to sorting in addition to chemical weathering. This apparent discrepancy has been attributed as a shortcoming of the two-dimensional nature of the ternary diagrams (Fedo, 2021), which cannot accurately capture the full range of both felsic and mafic phases and require more context (e.g. mineralogy) when assessing trends.

Given the lacustrine and wet interdune environments interpreted for Facies 1-3 (Figure 1.9), it is likely that chemical weathering occurred and altered the geochemistry and mineralogy of HVm and Km sediment, but that other sedimentary processes (e.g. transport, diagenesis) cause the discrepancy between ternary diagrams in Figure 1.11. One important observation is the difference between the relative position of facies relative to the A-apex in A-CN-K (Figure 1.11a & d) and A-CNK-FM (Figure 1.11b & e) ternary diagrams. Regardless, because appraising potential paleoclimate/paleoweathering conditions remains critical to assessing the Martian surface evolution, the above discussion highlights the importance of making Ca corrections for primary and diagenetic non-silicate phases because the extent of sulfates, in particular, may mask the true chemical weathering extent.

Sorting

Sediment sorting during transport based on grain size and density is a common process known to affect whole rock geochemical signatures of sedimentary deposits. Experimental data and results from studies of modern and ancient basaltic sediment on Earth and Mars define distinct geochemical trends resulting from hydrodynamic sorting where fine-grained and denser mafic grains (e.g. pyroxenes, Fe- and Ti-oxides) are segregated from coarse-grained and less dense felsic grains (e.g. feldspars; Fedo et al., 2015; Mangold et al., 2011; McGlynn et al., 2012; Siebach et al., 2017; Thorpe et al., 2019). Both fluvial (Garzanti et al., 1986) and aeolian (Mangold et al., 2011) sediment transport processes are capable of segregating grains based on density, size, and shape, which cause the bulk sedimentary signature to deviate from the original source composition. This process can occur in fluvial settings via segregation of grain size populations in suspended load and bedload as well as within bedload deposits. In aeolian settings, less dense minerals may selectively be entrained in transport, leaving a lag of denser phases (Fedo et al., 2015) or compositional segregation of dunes as detected in Valles Marineris (Chojnacki et al., 2014). Given that Facies 1-3 each represent deposition by processes capable of segregating grains, some compositional change via hydrodynamic sorting is expected to occur. The relationship between grain size and composition provides the basis from which to evaluate the effects of sorting on the HVm and Km composition.

Several geochemical trends suggest that sorting of grain-size fractions in transport may have influenced bulk geochemical signatures of the HVm and Km facies. Box and whisker plots of wt% oxides show a slight enrichment of Facies 3 in $FeO_{(T)}$, though values overlap with the range of $FeO_{(T)}$ in Facies 1 (Supplemental Figure 1.15). This slight relative enrichment is observable in the Ca-corrected A-CNK-FM (Figure 1.11e) and AF-CNK-M (Figure 1.11f) ternary diagrams. The enrichment may represent segregation of fine-grained and denser mafic grains during sorting, though CheMin data for Oudam, Marimba, and Quela indicate the presence of diagenetic Fe-bearing phases (Achilles et al., 2020), complicating an interpretation of sorting solely based on Fe. The relative depletion of Facies 3 in wt% MgO (Supplemental Figure 1.15) does not correlate with the expected segregation of olivine and pyroxene, but this discrepancy could also be explained by the variable influence of Mg-bearing diagenetic phases (Sun et al., 2019).

Figure 1.12 compares Al_2O_3 and TiO_2 of the sandstone and mudstone facies to expected trends resulting from chemical weathering and hydrodynamic sorting (Young & Nesbitt, 1998). In the absence of any weathering or hydrodynamic sorting, the distribution of sediment should cluster around a specific source composition. Previous studies have determined that Ti:Al ratios will remain consistent with the original source composition up to moderate levels of chemical weathering (CIA < 80; Nesbitt & Wilson,

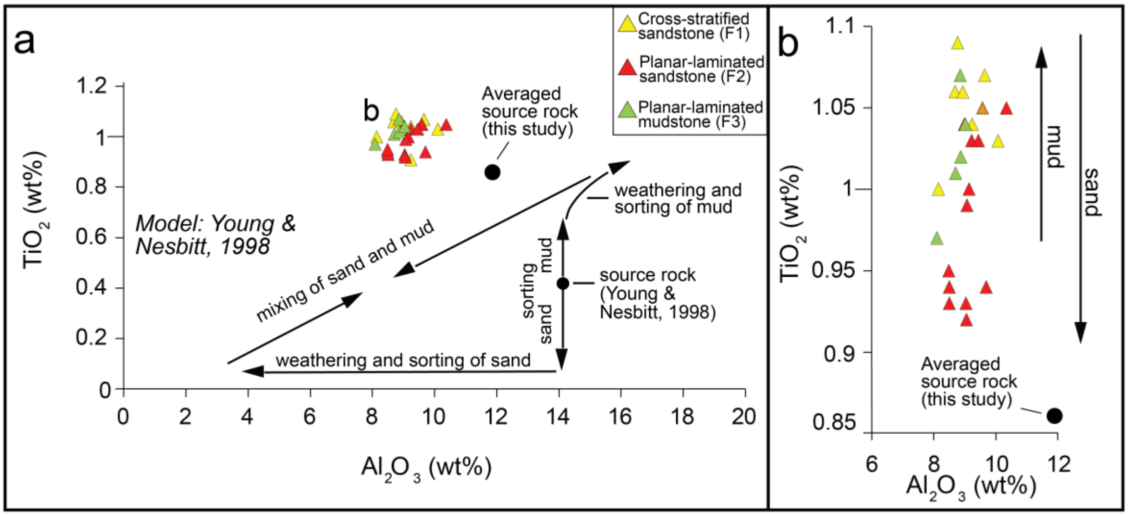

Figure 1.12 (a) Al_2O_3 and TiO_2 (wt%) of sandstone and mudstone facies compared to predicted geochemical trends of sorting (adapted from Young & Nesbitt, 1998). (b) expanded view of annotated region in (a). The average basaltic source composition (black circle) is included for reference.

1992; Young & Nesbitt, 1998). As grains are transported from continental source rocks, sorting will separate the fine-grained TiO_2-rich fraction from the coarse-grained TiO_2-poor fraction, resulting in the vertical trend indicated by the arrows in Figure 1.12a. Compared to the expected linear sorting trend, data across all three facies are clustered around a similar ranges of Al_2O_3 and a much narrower range of TiO_2 (Figure 1.12). Additionally, all facies plot above the averaged basaltic source composition defined in this study (black dot, Figure 1.12a). The expanded inset in Figure 1.12b shows that Facies 3 does not define a completely separate range of greater wt% TiO_2 compared to the Facies 1 and 2, as would be expected for finer grain sizes influenced by sorting. A slight distinction can be made between Facies 3 data points compared with Facies 1, but the overall trend is more clustered compared to model from Young and Nesbitt (1998).

Several factors may explain the overlap between facies in Figure 1.12. The range of the total grain size population between the facies is likely relatively small (fine sand and smaller) compared with other sedimentary systems where sorting is known to occur (Nesbitt & Young, 1996; Young & Nesbitt, 1998). Comparisons with compositional trends of fluvial-lacustrine (Siebach et al., 2017) and aeolian (Banham et al., 2018; Bedford et al., 2020) stratigraphy of the Bradbury group and Stimson formation, respectively, show substantially greater geochemical variation indicative of sorting compared to the HVm and Km facies. The Bradbury group consists of grains up to the pebble size fraction (Siebach et al., 2017), and the aeolian Stimson formation consists of grains from very fine to very coarse sand and as well as granule sized grains (Banham et al., 2018). A smaller total range of relatively finer grain sizes across Facies 1-3 may explain the relative distribution of each facies as well as the distribution of facies compared to the averaged source rock in Figure 1.12.

Another factor to consider is the phenocryst size in the source basalt. An experimental study by Fedo et al. (2015), where two basalt samples were mechanically crushed and sieved to simulate sediment generation and sorting, showed that isolation of individual mineral phases from an aphyric basalt sample occurred beginning at the fine sand to silt sieve fraction, but with overall limited compositional change via sorting. By contrast, a porphyritic basalt sample shows separation of olivine grains from the bulk sediment, which results in substantial compositional change between grain-size fractions. It is therefore possible that the source-rock crystal size was more aphanitic, thus influencing on the amount of variability resulting from sorting. Nevertheless, contextualization of geochemical trends with interpretations of subaerial and subaqueous depositional processes responsible for Facies 1-3 suggests that hydrodynamic sorting occurred and influenced some component of the geochemical signatures of HVm and Km facies.

Diagenesis

Stratigraphic, mineralogical, and geochemical evidence supports numerous episodes of early- and late-stage diagenetic fluid flow in the Murray formation strata. Previous studies have characterized variable amounts of compositional change on the whole rock geochemical signatures as well as enrichment in precipitated phases from distinct post-depositional fluid flow events (Achilles et al., 2020; Bristow et al., 2021;

Fraeman et al., 2020; Kronyak et al., 2019; Sun et al., 2019. Contextualization of geochemical trends within HVm and Km facies with the variable amounts of crystalline, phyllosilicate, and amorphous diagenetic phases measured in Oudam, Marimba, and Quela (Achilles et al., 2020; Bristow et al., 2018) and the macro-scale diagenetic features (e.g. veins, concretions; Kronyak et al., 2019; Sun et al., 2019) can place some relative constraints on the extent and composition of diagenetic phases.

Calcium sulfate phases are present throughout the HVm and Km stratigraphy in the form of veins, concretions, and matrix cements (Achilles et al., 2020; Thompson et al., 2020). As previously discussed, the addition of Ca-sulfates leads to significant changes in the geochemistry. Where veins and concretions are not observable within the APXS field of view, the presence of Ca-sulfate cement is supported by the correlation of wt% CaO and SO_3 (see Figure S1 of Thompson et al., 2020).

Potassium metasomatism is a common process by which aluminous clays are enriched in K^+ and converted to illite (Fedo et al., 1995). Though illite is not demonstrated to represent a significant component of the clays measured with CheMin, the linear trend in Figure 1.11a shows a slight deviation away from parallel to the A-CN join, which indicates increasing potassium enrichment through diagenesis (Fedo et al., 1995). The trend shown with HVm and Km facies demonstrates that minor diagenetic K-enrichment occurred, in agreement with the findings of Mangold et al. (2019) who calculated the amount of K^+ associated with the proportion of sanidine in Marimba and concluded that some fraction of the enrichment may have resulted from illitization.

Mineralogical data from the HVm and Km drill samples indicates a variety of additional diagenetic phases detailed in Achilles et al., 2020 and Bristow et al., 2018. In addition to hematite, amorphous and nanophase $FeO_{(T)}$, and SO_3 are interpreted to constitute a significant fraction of the Marimba (16.8%, 3.6%) and Quela (10.5%, 6.1%) mudstones relative to the Oudam sandstone (5.5%, 1.2%; Achilles et al., 2020). Such phases could be the cause of the slight Fe trend in mudstone (Figure 1.11b & c; Supplemental Figure 1.15 Diagenetic phases, which have been well-documented throughout the HVm and Km stratigraphy, represent variable fluid compositions and temperatures of formation and collectively highlight the longevity and diversity of post-depositional fluid events.

Discussion: Integrated depositional and compositional pathway

Sedimentologic, stratigraphic, and geochemical interpretations indicate that the HVm and Km facies represent deposition within and along the margin of lacustrine basin during a time consistent with modest, but appreciable, chemical weathering. Such a paleoenvironmental and paleoclimate scenario is similar to those interpreted in both underlying (Stack et al., 2019) and overlying (Caravaca et al., 2022; Edgar et al., 2020) units of the Murray formation. The long-held links between depositional sedimentary processes and whole-rock compositional signatures (Johnsson, 1993) can help to define a source-to-sink history, which we do below for the HVm and Km.

Subsequent to crater formation, the significant topographic gradient along the crater margin acted as both the likely source for sediments and a means to drive deposition downslope into the crater (Figure 1.9a; Grotzinger et al., 2015). As discussed above and previously considered (Bedford et al., 2019; Edwards et al., 2017), the source rock was basalt, similar to rocks previously encountered at Gale and Gusev craters. Given the comparatively homogenous composition between sandstones of Facies 1 and 2 and mudstones of Facies 3, it is possible the source basalt could have had an aphyric texture (Fedo et al., 2015).

Chemical (and physical) weathering of the source rock along margin of, and in the watershed feeding the rim (Ehlmann & Buz, 2014) generated sediment with many primary mineral phases mixed with clays formed by chemical weathering (Figure 1.9a). A precise characterization of climate cannot be constrained from the weathering indices in this study, but the environment had to be capable of effectively making phyllosilicates through hydrolysis and sustaining liquid water in order to carry sediment by tractive processes (Williams 2013) across the basin floor, and into deltaic systems (Grotzinger et al., 2015; Stack et al., 2019) that entered standing water (Edgar et al., 2020; Stack et al., 2019, Edgar). ChemCam LIBS data though the Murray formation suggest similar environmental conditions (Mangold et al., 2019).

All three facies, regardless of grain size, have geochemical compositions that not only overlap, but also define linear trends in A-CN-K compositional space (Figure 1.11). This type of data scatter suggests that sediments were potentially drawn from a source that exposed multiple levels of a weathering profile, a situation common in non-steady state conditions where rates of physical erosion and mass wasting outpace clay production via chemical weathering (Nesbitt et al., 1997). Studies attribute topographic variability to be a key control over the extent of chemical weathering, with steeper slopes experiencing increased sediment erosion rates and incomplete weathering (e.g. Johnsson & Stallard, 1989; Riebe et al., 2015). Given the relatively steeper topography of the crater rim, an increase of sediment erosion over chemical weathering is expected and observed.

Subsequent to weathering and erosion, sediments would have been transported away from the rim and toward the basin center and subject to physical processing (Figure 1.9). Steeper topographic conditions closer to the crater rim likely moved sediment through flooding and mass-wasting events, producing coarse-grained fans (Palucis et al., 2014), which potentially correlate downslope with fluvial deposits of the Bradbury group (Williams et al., 2013). Further along the source-to-sink pathway, sediment transport conditions are dominated by traction transport in fluvial and aeolian environments (Figure 1.9). Sorting of sediment based on grain size, shape, and density would have resulted in sedimentary compositions differentiating from the source and potentially even from each other in different grain size fractions (Fedo et al., 2015; Garzanti 1986). In the case, of the HVm and Km, the lack of substantial compositional change between facies is attributed to a generally small range of grain sizes between facies and the potential the source itself was texturally homogenous. Temporary storage of sediments in weathering profiles between major depositional episodes could have permitted some additional chemical weathering similar to what was described by Johnsson & Meade (1990) along the transport path may have provided an additional source of weathering to the coarser-grained sand facies, producing the overlapping geochemical trends in Figures 1.10 through 1.12.

At the site of deposition along the lacustrine margin and within the lacustrine basin, physical and chemical processes continued to modify sediment composition. The interfingering relationship between dune and interdune facies along the lacustrine margin (Figure 1.9b) suggests that some degree of sediment mixing between Facies 1 and 2 may have occurred, similar to terrestrial wet dune-interdune relationships (e.g. Mountney & Russell, 2009). This mixing would have homogenized the relative compositions and textures of both sand facies. Facies 3 sediments were deposited in the more marginal regions of the lacustrine basin by subaqueous flows, and subject to further alteration at the site of deposition (Bristow et al., 2018).

Deposition and burial of sediments occurred to sufficient depth for lithification to occur. Diagenetic enrichment in crystalline and amorphous phases occurred from deposition through post-lithification. During burial, a minor amount of potassium metasomatism occurred and enriched the bulk composition in potassium (Fedo et al., 1995). Post-lithification, diagenetic products with variable morphologies and compositions formed from different fluid flow events. One of the most common phases is Ca-sulfate, which occurs as veins, concretions, and matrix cements (Achilles et a., 2020; Sun et al., 2019; Thompson et al., 2020). In addition to primary non-silicate phases (apatite), diagenetic phases can mask additional geochemical signatures, as indicated by the effects of the Ca-correction applied in this study (equation 5).

Conclusions

This study provides a detailed stratigraphic and compositional analyses of the 65-m-thick interval comprising the Hartmann's Valley and Karasburg members of the Murray formation, Gale crater, Mars. Three facies documented from orbital, outcrop, and hand-lens-scale bedrock characteristics include (1) cross-stratified sandstone, (2) planar-laminated sandstone, and (3) planar-laminated mudstone facies. The two sandstone facies are interpreted to represent associated aeolian dune and interdune subenvironments. The absence of evidence for widespread aeolian dunes and other features indicative of desiccation suggests that these facies do not signify a widespread dry interval, but rather constitute relatively isolated aeolian dunes along a lacustrine margin. The planar-laminated mudstone facies comprises the lacustrine facies association and represents deposition from density currents, with seemingly random and sparse intervals of potentially thicker laminae representing changes in depositional energy. The similar outcrop appearance, laminae thickness, and µm-scale textural features between mudstone facies of the Karasburg member and other mudstone facies in the Murray formation indicate that the planar-laminated mudstone represents similar depositional processes in a lacustrine basin and extends the stratigraphic record of lacustrine environments at Gale crater.

Compositional trends provide additional constraints for the lacustrine and lacustrine margin environments when contextualized with sedimentary processes. Weathering indices and geochemical trends between facies support moderate chemical weathering. Trends between immobile oxides indicate influence from hydrodynamic sorting, which is known to occur in aeolian and fluvial transport systems. Combined compositional and sedimentological observations indicate that the relative location of the Hartmann's Valley and Karasburg stratigraphy along the source-to-burial path is more proximal to the basin center. This study ultimately extends the range of diverse facies encountered in the Murray formation and provides a refined understanding of a unique period in the history of lacustrine activity at Gale crater.

References

Achilles, C. N., Rampe, E. B., Downs, R. T., Bristow, T. F., Ming, D. W., Morris, R. V., et al. (2020). Evidence for multiple diagenetic episodes in ancient fluvial-lacustrine sedimentary rocks in Gale crater, Mars. Journal of Geophysical Research: Planets, 125(8), e2019JE006295. https://doi.org/10.1029/2019JE006295

Al-Masrahy, M. A., & Mountney, N. P. (2015). A classification scheme for fluvial–aeolian system interaction in desert-margin settings. Aeolian Research, 17, 67–88. https://doi.org/10.1016/j.aeolia.2015.01.010

Anderson, R. Y., & Dean, W. E. (1988). Lacustrine varve formation through time. Palaeogeography, Palaeoclimatology, Palaeoecology, 62(1–4), 215–235. https://doi.org/10.1016/0031-0182(88)90055-7

Babechuk, M. G., Widdowson, M., & Kamber, B. S. (2014). Quantifying chemical weathering intensity and trace element release from two contrasting basalt profiles, Deccan Traps, India. Chemical Geology, 363, 56–75. https://doi.org/10.1016/j.chemgeo.2013.10.027

Banham, S. G., Gupta, S., Rubin, D. M., Edgett, K. S., Barnes, R., Van Beek, J., et al. (2021). A rock record of complex Aeolian bedforms in a hesperian desert landscape: The Stimson formation as exposed in the Murray Buttes, Gale Crater, Mars. Journal of Geophysical Research: Planets, 126(4), e2020JE006554. https://doi.org/10.1029/2020je006554

Banham, S. G., Gupta, S., Rubin, D. M., Watkins, J. A., Sumner, D. Y., Edgett, K. S., et al. (2018). Ancient Martian aeolian processes and palaeomorphology reconstructed from the Stimson formation on the lower slope of Aeolis Mons, Gale crater, Mars. Sedimentology, 65(4), 993–1042. https://doi.org/10.1111/sed.12469

Bedford, C. C., Bridges, J. C., Schwenzer, S. P., Wiens, R. C., Rampe, E. B., Frydenvang, J., & Gasda, P. J. (2019). Alteration trends and geochemical source region characteristics preserved in the fluviolacustrine sedimentary record of Gale crater, Mars. Geochimica et Cosmochimica Acta, 246, 234–266. https://doi.org/10.1016/j.gca.2018.11.031

Bedford, C. C., Schwenzer, S. P., Bridges, J. C., Banham, S., Wiens, R. C., Gasnault, O., et al. (2020). Geochemical variation in the Stimson formation of Gale crater: Provenance, mineral sorting, and a comparison with modern Martian dunes. Icarus, 341, 113622. https://doi.org/10.1016/j.icarus.2020.113622

Bennett, K., Fox, V., Bryk, A., Dietrich, W., Fedo, C. M., Edgar, L., et al. (2022). The Curiosity Rover's exploration of Glen Torridon, Gale crater, Mars: An overview of the campaign and scientific results. Journal of Geophysical Research: Planets. https://doi.org/10.1029/2022je007185

Berger, J. A., Gellert, R., Boyd, N. I., King, P. L., McCraig, M. A., O'Connell-Cooper, C. D., et al. (2020). Elemental composition and chemical evolution of geologic materials in Gale Crater, Mars: APXS results from Bradbury landing to the Vera Rubin ridge. Journal of Geophysical Research: Planets, 125(12). https://doi.org/10.1029/2020JE006536

Bibring, J. P., Langevin, Y., Mustard, J. F., Poulet, F., Arvidson, R., Gendrin, A., et al. (2006). Global mineralogical and aqueous Mars history derived from OMEGA/Mars Express data. Science, 312(5772), 400–404. https://doi.org/10.1126/science.1122659

Bohacs, K. M., Carroll, A. R., Neal, J. E., & Mankiewicz, P. J. (2000). Lake-basin type, source potential, and hydrocarbon character: An integrated sequence-stratigraphic-geochemical framework. Lake basins through space and time: AAPG Studies in Geology, 46, 3–34.

Bohacs, K. M., Grabowski, G., Jr., & Carroll, A. R. (2007). Lithofacies architecture and variations in expression of sequence stratigraphy within representative intervals of the green river formation, greater green river basin, Wyoming and Colorado. Mountain Geologist, 44(2), 39–60.

Boulesteix, K., Poyatos-Mor., M., Flint, S. S., Taylor, K. G., Hodgson, D. M., & Hasiotis, S. T. (2019). Transport and deposition of mud in deep-water environments: Processes and stratigraphic implications. Sedimentology, 66(7), 2894–2925. https://doi.org/10.1111/sed.12614

Bowler, J. M. (1973). Clay dunes: Their occurrence, formation and environmental significance. Earth-Science Reviews, 9(4), 315–338. https://doi.org/10.1016/0012-8252(73)90001-9

Bristow, T. F., Grotzinger, J. P., Rampe, E. B., Cuadros, J., Chipera, S. J., Downs, G. W., et al. (2021). Brine-driven destruction of clay minerals in Gale crater, Mars. Science, 373(6551), 198–204. https://doi.org/10.3390/min11080847

Bristow, T. F., Rampe, E. B., Achilles, C. N., Blake, D. F., Chipera, S. J., Craig, P., et al. (2018). Clay mineral diversity and abundance in sedimentary rocks of Gale crater, Mars. Science Advances, 4(6). https://doi.org/10.1126/sciadv.aar3330

Brookfield, M. E. (1977). The origin of bounding surfaces in ancient aeolian sandstones. Sedimentology, 24(3), 303–332. https://doi.org/10.1111/j.1365-3091.1977.tb00126.x

Calef, F. J., III, Abarca, H. E., Soliman, T., Abercrombie, S. P., & Powell, M. W. (2019). Multi-mission geographic information system: An open-source solution for planetary science operations. In 4th planetary data workshop. Abstract 7071.

Calef, F. J., III, Gengl, H. E., Soliman, T., Abercrombie, S. P., & Powell, M. W. (2017). MMGIS: A multi-mission geographic information system for in situ Mars operations. In The 48th lunar and planetary science conference. Abstract #2541.

Calef, F. J., III, & Parker, T. (2016). MSL Gale merged orthophoto mosaic. PDS Annex, U.S. Geological Survey. Retrieved from http://bit.ly/MSL_Basemap

Campbell, J. L., Perrett, G. M., Gellert, R., Andrushenko, S. M., Boyd, N. I., Maxwell, J. A., et al. (2012). Calibration of the Mars Science Laboratory alpha particle X-ray spectrometer. Space Science Reviews, 170(1–4), 319–340. https://doi.org/10.1007/s11214-012-9873-5

Caravaca, G., Mangold, N., Dehouck, E., Schieber, J., Zaugg, L., Bryk, A. B., et al. (2022). From lake to river: Documenting an environmental transition across the Jura/Knockfarril hill members boundary in the Glen Torridon region of Gale crater (Mars). Journal of Geophysical Research: Planets. https://doi.org/10.1029/2021JE007093

Carroll, A. R., & Bohacs, K. M. (1999). Stratigraphic classification of ancient lakes: Balancing tectonic and climatic controls. Geology, 27(2), 99–102. https://doi.org/10.1130/0091-7613(1999)027<0099:scoalb>2.3.co;2

Chojnacki, M., Burr, D. M., & Moersch, J. E. (2014). Valles Marineris dune fields as compared with other Martian populations: Diversity of dune compositions, morphologies, and thermophysical properties. Icarus, 230, 96–142. https://doi.org/10.1016/j.icarus.2013.08.018

Christensen, P. R., Bandfield, J. L., Clark, R. N., Edgett, K. S., Hamilton, V. E., Hoefen, T., et al. (2000). Detection of crystalline hematite mineralization on Mars by the Thermal Emission Spectrometer: Evidence for near-surface water. Journal of Geophysical Research, 105(E4), 9623–9642. https://doi.org/10.1029/1999JE001093

Cisneros, J., Best, J., van Dijk, T., Almeida, R. P. D., Amsler, M., Boldt, J., et al. (2020). Dunes in the world's big rivers are characterized by low-angle lee-side slopes and a complex shape. Nature Geoscience, 13(2), 156–162. https://doi.org/10.1038/s41561-019-0511-7

Clemmensen, L. B., & Abrahamsen, K. (1983). Aeolian stratification and facies association in desert sediments, Arran basin (Permian), Scotland. Sedimentology, 30(3), 311–339. https://doi.org/10.1111/j.1365-3091.1983.tb00676.x

Colombera, L., & Mountney, N. P. (2019). The lithofacies organization of fluvial channel deposits: A meta-analysis of modern rivers. Sedimentary Geology, 383, 16–40. https://doi.org/10.1016/j.sedgeo.2019.01.011

Dos Santos, A. L. S., Borges, H. P., Junior, C. H. L. S., Junior, R. N. P., & da Silva Bezerra, D. (2019). Modelling dunes from Lençóis Maranhenses National park (Brazil): Largest dune field in South America. Scientific Reports, 9(1), 1–7. https://doi.org/10.1038/s41598-019-43735-0

Edgar, L. A., Fedo, C. M., Gupta, S., Banham, S. G., Fraeman, A. A., Grotzinger, J. P., et al. (2020). A lacustrine paleoenvironment recorded at Vera Rubin ridge, Gale crater: Overview of the sedimentology and stratigraphy observed by the Mars science laboratory Curiosity rover. Journal of Geophysical Research: Planets, 125(3). https://doi.org/10.1029/2019je006307

Edgar, L. A., Gupta, S., Rubin, D. M., Lewis, K. W., Kocurek, G. A., Anderson, R. B., et al. (2017). Shaler: In situ analysis of a fluvial sedimentary deposit on Mars. Sedimentology, 65(1), 96–122. https://doi.org/10.1111/sed.12370

Edgett, K. S. (2013a). MSL MARS HAND LENS IMAGER 2 EDR IMAGE V1.0 [Data set]. NASA Planetary Data System. https://doi.org/10.17189/1520187

Edgett, K. S. (2013b). MSL MARS HAND LENS IMAGER 2 EDR ZSTACK V1.0 [Data set]. NASA Planetary Data System. https://doi.org/10.17189/1520396

Edgett, K. S., Yingst, R. A., Ravine, M. A., Caplinger, M. A., Maki, J. N., Ghaemi, F. T., et al. (2012). Curiosity's Mars hand lens imager (MAHLI) investigation. Space Science Reviews, 170(1), 259–317. https://doi.org/10.1007/s11214-012-9910-4

Edwards, P. H., Bridges, J. C., Wiens, R., Anderson, R., Dyar, D., Fisk, M., et al. (2017). Basalt–trachybasalt samples in Gale crater, Mars. Meteoritics & Planetary Sciences, 52(11), 2931–2410. https://doi.org/10.1111/maps.12953

Ehlmann, B. L., & Buz, J. (2015). Mineralogy and fluvial history of the watersheds of Gale, Knobel, and sharp craters: A regional context for the Mars science laboratory Curiosity's exploration. Geophysical Research Letters, 42(2), 264–273. https://doi.org/10.1002/2014GL062553

Ewing, R. C., & Kocurek, G. (2010). Aeolian dune-field pattern boundary conditions. Geomorphology, 114(3), 175–187. https://doi.org/10.1016/j.geomorph.2009.06.015

Fairén, A. G., Davila, A. F., Lim, D., Bramall, N., Bonaccorsi, R., Zavaleta, J., et al. (2010). Astrobiology through the ages of Mars: The study of terrestrial analogues to understand the habitability of Mars. Astrobiology, 10(8), 821–843. https://doi.org/10.1089/ast.2009.0440

Fedo, C. M. (2021). Exploration of chemical weathering and diagenesis in weathering profiles, paleosols, and sedimentary rocks in 3-D compositional space. In The geological association of Canada and mineralogical association of Canada joint conference.

Fedo, C. M., Grotzinger, J., Gupta, S., Fraeman, A., Edgar, L., Edgett, K., et al. (2018). Sedimentology and stratigraphy of the Murray formation, Gale crater, Mars. In The 49th lunar and planetary science conference. Abstract #2083.

Fedo, C. M., McGlynn, I. O., & McSween, H. Y., Jr. (2015). Grain size and hydrodynamic sorting controls on the composition of basaltic sediments: Implications for interpreting Martian soils. Earth and Planetary Science Letters, 423, 67–77. https://doi.org/10.1016/j.epsl.2015.03.052

Fedo, C. M., Wayne Nesbitt, H., & Young, G. M. (1995). Unraveling the effects of potassium metasomatism in sedimentary rocks and paleosols, with implications for paleoweathering conditions and provenance. Geology, 23(10), 921–924. https://doi.org/10.1130/0091-7613(1995)023<0921:uteopm>2.3.co;2

Fraeman, A. A., Edgar, L. A., Rampe, E. B., Thompson, L. M., Frydenvang, J., Fedo, C. M., et al. (2020). Evidence for a diagenetic origin of Vera Rubin ridge, Gale crater, Mars: Summary and synthesis of Curiosity's exploration campaign. Journal of Geophysical Research: Planets, 125(12). https://doi.org/10.1029/2020JE006527

Frydenvang, J., Mangold, N., Wiens, R. C., Fraeman, A. A., Edgar, L. A., Fedo, C. M., et al. (2020). The chemostratigraphy of the Murray formation and role of diagenesis at Vera Rubin ridge in Gale crater, Mars, as observed by the ChemCam instrument. Journal of Geophysical Research: Planets, 125(9). https://doi.org/10.1029/2019JE006320

Garzanti, E. (1986). Source rock versus sedimentary control on the mineralogy of deltaic volcanic arenites (Upper Triassic, northern Italy). Journal of Sedimentary Research, 56(2), 267–275. https://doi.org/10.1306/212F88E1-2B24-11D7-8648000102C1865D

Gellert, R. (2013). MSL MARS ALPHA PARTICLE X-RAY SPECTROMETER 4/5 RDR V1.0 [Data set]. NASA Planetary Data System. https://doi.org/10.17189/1519440

Gellert, R. (2019). MER APXS derived oxide data bundle [Data set]. NASA Planetary Data System. https://doi.org/10.17189/1518973

Gellert, R., Campbell, J. L., King, P. L., Leshin, L. A., Lugmair, G. W., Spray, J. G., et al. (2009). The alpha-particle-X-ray-spectrometer (APXS) for the Mars science laboratory (MSL) rover mission. In The 40th lunar and planetary science conference. Abstract # 2364.

Gellert, R., & Clark, B. C., III, & MSL and MER Science Teams. (2015). In Situ compositional measurements of rocks and soils with the alpha particle x-ray spectrometer on NASA's Mars rovers. Elements, 11(1), 39–44. https://doi.org/10.2113/gselements.11.1.39

Gellert, R., Rieder, R., Brückner, J., Clark, B. C., Dreibus, G., Klingelhöfer, G., et al. (2006). Alpha particle X-ray spectrometer (APXS): Results from Gusev crater and calibration report. Journal of Geophysical Research, 111(E2). https://doi.org/10.1029/2005JE002555

Greeley, R. (1979). Silt-clay aggregates on Mars. Journal of Geophysical Research, 84(B11), 6248–6254. https://doi.org/10.1029/JB084iB11p06248

Grotzinger, J. P., Arvidson, R. E., Bell, J. F., III, Calvin, W., Clark, B. C., Fike, D. A., et al. (2005). Stratigraphy and sedimentology of a dry to wet eolian depositional system, Burns formation, Meridiani Planum, Mars. Earth and Planetary Science Letters, 240(1), 11–72. https://doi.org/10.1016/j.epsl.2005.09.039

Grotzinger, J. P., Gupta, S., Malin, M. C., Rubin, D. M., Schieber, J., Siebach, K., et al. (2015). Deposition, exhumation, and paleoclimate of an ancient lake deposit, Gale crater, Mars. Science, 350(6257). https://doi.org/10.1126/science.aac.7575

Grotzinger, J. P., & Milliken, R. (2012). The sedimentary rock record of Mars: Distribution, origins, and global stratigraphy. Society for Sedimentary Geology Special Publication: Sedimentary Geology of Mars, 102, 1–48. https://doi.org/10.2110/pec.12.102.0001

Grotzinger, J. P., Sumner, D. Y., Kah, L. C., Stack, K., Gupta, S., Edgar, L., et al. (2014). A habitable fluvio-lacustrine environment at Yellowknife Bay, Gale crater, Mars. Science, 343(6169), 1242777. https://doi.org/10.1126/science.1242777

Gwizd, S., Fedo, C., Grotzinger, J., Edgett, K., Rivera-Hernandez, F., & Stein, N. (2018). Depositional history of the Hartmann's valley member, Murray formation, Gale crater, Mars. In The 49th lunar and planetary science conference. Abstract #2083.

Hadlari, T., Rainbird, R. H., & Donaldson, J. A. (2006). Alluvial, eolian and lacustrine sedimentology of a paleoproterozoic half-graben, baker Lake Basin, Nunavut, Canada. Sedimentary Geology, 190(1–4), 47–70. https://doi.org/10.1016/j.sedgeo.2006.05.005

Hilbert, N. N., Guedes, C. C., & Giannini, P. C. (2016). Morphologic and sedimentologic patterns of active aeolian dune-fields on the east coast of Maranhão, northeast Brazil. Earth Surface Processes and Landforms, 41(1), 87–97. https://doi.org/10.1002/esp.3786

Hunter, R. E. (1977). Basic types of stratification in small eolian dunes. Sedimentology, 24(3), 361–387. https://doi.org/10.1111/j.1365-3091.1977.tb00128.x

Hurowitz, J., Grotzinger, J., Fischer, W., McLennan, S. M., Milliken, R., Stein, N., et al. (2017). Redox stratification of an ancient lake in Gale crater, Mars. Science, 356(6341). https://doi.org/10.1126/science.aah6849

Ielpi, A., & Rainbird, R. H. (2015). Architecture and morphodynamics of a 1. 6 Ga fluvial sandstone: Ellice formation of Elu Basin, Arctic Canada. Sedimentology, 62(7), 1950–1977. https://doi.org/10.1111/sed.12211

Johnsson, M. J. (1993). The system controlling the composition of clastic sediments. In M. J. Johnsson & A. Basu (Eds.), Processes controlling the composition of clastic sediments (Vol. 284, pp. 1–19). Geological Society of America Special Paper.

Johnsson, M. J., & Meade, R. H. (1990). Chemical weathering of fluvial sediments during alluvial storage; the Macuapanim Island point bar, Solimoes River, Brazil. Journal of Sedimentary Research, 60(6), 827–842. https://doi.org/10.1306/212F9296-2B24-11D7-8648000102C1865D

Johnsson, M. J., & Stallard, R. F. (1989). Physiographic controls on the composition of sediments derived from volcanic and sedimentary terrains on Barro Colorado Island, Panama. Journal of Sedimentary Research, 59(5), 768–781. https://doi.org/10.1306/212F9296- 2B24-11D7-8648000102C1865D

Kocurek, G., Carr, M., Ewing, R., Havholm, K. G., Nagar, Y. C., & Singhvi, A. K. (2007). White sands dune field, New Mexico: Age, dune dynamics and recent accumulations. Sedimentary Geology, 197(3–4), 313–331. https://doi.org/10.1016/j.sedgeo.2006.10.006

Kocurek, G., & Havholm, K. (1993). Eolian sequence stratigraphy – A conceptual framework. In P. Weimer & H. Posamentier (Eds.), Siliciclastic sequence stratigraphy (Vol. 58, pp. 393–409). American Association of Petroleum Geologists Memoir.

Kronyak, R. E., Kah, L. C., Edgett, K. S., VanBommel, S. J., Thompson, L. M., Wiens, R. C., et al. (2019). Mineral-filled fractures as indicators of multigenerational fluid flow in the Pahrump Hills member of the Murray formation, Gale crater, Mars. Earth and Space Science, 6(2), 238–265. https://doi.org/10.1029/2018EA000482

Langford, R. P., & Chan, M. A. (1989). Fluvial-aeolian interactions: Part II, ancient systems. Sedimentology, 36(6), 1037–1051. https://doi.org/10.1111/j.1365-3091.1989.tb01541.x

Lapôtre, M. G., & Rampe, E. B. (2018). Curiosity's investigation of the Bagnold Dunes, Gale crater: Overview of the two-phase scientific campaign and introduction to the special collection. Geophysical Research Letters, 45(19), 10–200. https://doi.org/10.1029/2018GL079032

Lazar, O. R., Bohacs, K., Schieber, J., Macquaker, J. H. S., & Demko, T. (2015). Mudstone primer: Lithofacies variations, diagnostic criteria, and sedimentological/stratigraphical implications at lamina to bedset scale. SEPM Concepts in Sedimentology and Paleontology, 12.

Leclair, S. F., & Bridge, J. S. (2001). Quantitative interpretation of sedimentary structures formed by river dunes. Journal of Sedimentary Research, 71(5), 713–716. https://doi.org/10.1306/2DC40962-0E47-11D7-8643000102C1865D

Le Deit, L., Hauber, E., Fueten, F., Pondrelli, M., Rossi, A. P., & Jaumann, R. (2013). Sequence of infilling events in Gale Crater, Mars: Results from morphology, stratigraphy, and mineralogy. Journal of Geophysical Research: Planets, 118(12), 2439–2473. https://doi.org/10.1002/2012JE004322

Long, D. G. (2006). Architecture of pre-vegetation sandy-braided perennial and ephemeral river deposits in the Paleoproterozoic Athabasca Group, northern Saskatchewan, Canada as indicators of Precambrian fluvial style. Sedimentary Geology, 190(1–4), 71–95. https://doi.org/10.1016/j.sedgeo.2006.05.006

Luna, M. C. D. M., Parteli, E. J., & Herrmann, H. J. (2012). Model for a dune field with an exposed water table. Geomorphology, 159, 169–177. https://doi.org/10.1016/j.geomorph.2012.03.021

Maki, J., Thiessen, D., Pourangi, A., Kobzeff, P., Litwin, T., Scherr, L., et al. (2012). The Mars science laboratory engineering cameras. Space Science Reviews, 170(1-4), 77–93. https://doi.org/10.1007/s11214-012-9882-4

Malin, M. C. (2007). MRO CONTEXT CAMERA EXPERIMENT DATA RECORD LEVEL 0 V1.0 [Data set]. NASA Planetary Data System. https://doi.org/10.17189/1520266

Malin, M. C. (2013). MSL MARS MAST CAMERA 2 EDR IMAGE V1.0 [Data set]. NASA Planetary Data System. https://doi.org/10.17189/1520190

Malin, M. C., & Edgett, K. S. (2000). Sedimentary rocks of early Mars. Science, 290(5498), 1927–1937. https://doi.org/10.1126/science.290.5498.1927

Malin, M. C., Ravine, M. A., Caplinger, M. A., Ghaemi, F. T., Schaffner, J. A., Maki, J. N., et al. (2017). The Mars science laboratory (MSL) mast cameras and descent imager: Investigation and instrument descriptions. Earth and Space Science, 4(8), 506–539. https://doi.org/10.1002/2016EA000252

Mangold, N., Baratoux, D., Arnalds, O., Bardintzeff, J. M., Platevoet, B., Gregoire, M., & Pinet, P. (2011). Segregation of olivine grains in volcanic sands in Iceland and implications for Mars. Earth and Planetary Science Letters, 310(3–4), 233–243. https://doi.org/10.1016/j.epsl.2011.07.025

Mangold, N., Dehouck, E., Fedo, C., Forni, O., Achilles, C., Bristow, T., et al. (2019). Chemical alteration of fine-grained sedimentary rocks at Gale crater. Icarus, 321, 619–631. https://doi.org/10.1016/j.icarus.2018.11.004

Maurice, S., Wiens, R. C., Saccoccio, M., Barraclough, B., Gasnault, O., Forni, O., et al. (2012). The ChemCam instrument suite on the Mars science laboratory (MSL) rover: Science objectives and mast unit description. Space Science Reviews, 170(1-4), 95–166. https://doi.org/10.1007/s11214-012-9912-2

McEwen, A. S. (2005). MRO MARS HIGH RESOLUTION IMAGE SCIENCE EXPERIMENT EDR V1.0 [Data set]. NASA Planetary Data System. https://doi.org/10.17189/1520179

McEwen, A. S., Eliason, E. M., Bergstrom, J. W., Bridges, N. T., Hansen, C. J., Delamere, W. A., et al. (2007). Mars Reconnaissance Orbiter's high resolution imaging science experiment (HiRISE). Journal of Geophysical Research, 112(E5), E05S02. https://doi.org/10.1029/2005JE002605

McGlynn, I. O., Fedo, C. M., & McSween, H. Y., Jr. (2012). Soil mineralogy at the Mars Exploration Rover landing sites: An assessment of the competing roles of physical sorting and chemical weathering. Journal of Geophysical Research, 117(E1). https://doi.org/10.1029/2011JE003861

McKee, E. D., Crosby, E. J., & Berryhill, H. L. (1967). Flood deposits, bijou creek, Colorado, June 1965. Journal of Sedimentary Research, 37(3), 829–851. https://doi.org/10.1306/74D717B2-2B21-11D7-8648000102C1865D

McLennan, S. M., Anderson, R. B., Bell, J. F., Bridges, J. C., Calef, F., Campbell, J. L., et al. (2014). Elemental geochemistry of sedimentary rocks at Yellowknife bay, Gale crater, Mars. Science, 343(6169). https://doi.org/10.1126/science.1244734

McLennan, S. M., Bell, J. F., III, Calvin, W. M., Christensen, P. R., Clark, B. D., De Souza, P. A., et al. (2005). Provenance and diagenesis of the evaporite-bearing burns formation, Meridiani planum, Mars. Earth and Planetary Science Letters, 240(1), 95–121. https://doi.org/10.1016/j.epsl.2005.09.041

McSween, H. Y., Ruff, S. W., Morris, R. V., Gellert, R., Klingelhoefer, G., Christensen, P. R., et al. (2008). Mineralogy of volcanic rocks in Gusev crater, Mars: Reconciling mössbauer, alpha particle X-ray spectrometer, and miniature thermal emission spectrometer spectra. Journal of Geophysical Research, 113(E6), E06S04. https://doi.org/10.1029/2007JE002970

Milliken, R. E., Grotzinger, J. P., & Thomson, B. J. (2010). Paleoclimate of Mars as captured by the stratigraphic record in Gale Crater. Geophysical Research Letters, 37(4). https://doi.org/10.1029/2009GL041870

Ming, D. W., Gellert, R., Morris, R. V., Arvidson, R. E., Brueckner, J., Clark, B. C., et al. (2008). Geochemical properties of rocks and soils in Gusev crater, Mars: Results of the alpha particle X-ray spectrometer from cumberland ridge to home plate. Journal of Geophysical Research, 113(E12), E12S39. https://doi.org/10.1029/2008JE003195

Morris, R. V., Vaniman, D. T., Blake, D. F., Gellert, R., Chipera, S. J., Rampe, E. B., et al. (2016). Silicic volcanism on Mars evidenced by tridymite in high-SiO2 sedimentary rock at Gale crater. Proceedings of the National Academy of Sciences, 113(26), 7071–7076. https://doi.org/10.1073/pnas.1607098113

Mountney, N. P. (2012). A stratigraphic model to account for complexity in aeolian dune and interdune successions. Sedimentology, 59(3), 964–989. https://doi.org/10.1111/j.1365-3091.2011.01287.x

Mountney, N. P., & Jagger, A. (2004). Stratigraphic evolution of an aeolian erg margin system: The Permian cedar mesa sandstone, SE Utah, USA. Sedimentology, 51(4), 713–743. https://doi.org/10.1111/j.1365-3091.2004.00646.x

Mountney, N. P., & Russell, A. J. (2009). Aeolian dune-field development in a water table-controlled system: Skeiđarársandur, Southern Iceland. Sedimentology, 56(7), 2107–2131. https://doi.org/10.1111/j.1365-3091.2009.01072.x

Muhlbauer, J. G., Fedo, C. M., & Moersch, J. E. (2020). Architecture of a distal pre-vegetation braidplain: Cambrian middle member of the Wood Canyon Formation, southern Marble Mountains, California, USA. Sedimentology, 67(2), 1084–1113. https://doi.org/10.1111/sed.12677

Mulder, T., & Syvitski, J. P. (1995). Turbidity currents generated at river mouths during exceptional discharges to the world oceans. The Journal of Geology, 103(3), 285–299. https://doi.org/10.1086/629747

Nesbitt, H. W., Fedo, C. M., & Young, G. M. (1997). Quartz and feldspar stability, steady and non-steady-state weathering, and petrogenesis of siliciclastic sands and muds. The Journal of Geology, 105(2), 173–192. https://doi.org/10.1086/515908

Nesbitt, H. W., & Wilson, R. E. (1992). Recent chemical weathering of basalts. American Journal of Science, 292(10), 740–777. https://doi.org/10.2475/ajs.292.10.740

Nesbitt, H. W., & Young, G. M. (1982). Early Proterozoic climates and plate motions inferred from major element chemistry of lutites. Nature, 299(5885), 715–717. https://doi.org/10.1038/299715a0

Nesbitt, H. W., & Young, G. M. (1984). Prediction of some weathering trends of plutonic and volcanic rocks based on thermodynamic and kinetic considerations. Geochimica et Cosmochimica Acta, 48(7), 1523–1534. https://doi.org/10.1016/0016-7037(84)90408-3

Nesbitt, H. W., & Young, G. M. (1996). Petrogenesis of sediments in the absence of chemical weathering: Effects of abrasion and sorting on bulk composition and mineralogy. Sedimentology, 43(2), 341–358. https://doi.org/10.1046/j.1365-3091.1996.d01-12.x

Nesbitt, H. W., Young, G. M., McLennan, S. M., & Keays, R. R. (1996). Effects of chemical weathering and sorting on the petrogenesis of siliciclastic sediments, with implications for provenance studies. The Journal of Geology, 104(5), 525–542. https://doi.org/10.1086/629850

Palucis, M. C., Dietrich, W. E., Hayes, A. G., Williams, R. M., Gupta, S., Mangold, N., et al. (2014). The origin and evolution of the Peace Vallis fan system that drains to the Curiosity landing area, Gale Crater, Mars. Journal of Geophysical Research: Planets, 119(4), 705–728. https://doi.org/10.1002/2013JE004583

Parteli, E. J. R., Schwaemmle, V., Herrmann, H. J., Monteiro, L. H. U., & Maia, L. P. (2006). Profile measurement and simulation of a transverse dune field in the Lençóis Maranhenses. Geomorphology, 81(1–2), 29–42. https://doi.org/10.1016/j.geomorph.2006.02.015

Rampe, E. B., Blake, D. F., Bristow, T. F., Ming, D. W., Vaniman, D. T., Morris, R. V., et al. (2020). Mineralogy and geochemistry of sedimentary rocks and eolian sediments in Gale crater, Mars: A review after six Earth years of exploration with Curiosity. Geochemistry, 80(2), 125605. https://doi.org/10.1016/j.chemer.2020.125605

Rapin, W., Ehlmann, B. L., Dromart, G., Schieber, J., Thomas, N. H., Fischer, W. W., et al. (2019). An interval of high salinity in ancient Gale crater lake on Mars. Nature Geoscience, 12(11), 889–895. https://doi.org/10.1038/s41561-019-0458-8

Rasband, W. S. (1997-2018). ImageJ, [software]. U. S. National Institutes of Health. Retrieved From https://imagej.nih.gov/ij/, Date: February 28, 2022 .

Renaut, R. W., & Gierlowski-Kordesch, E. H. (2010). Lakes. In R. Dalrymple & N. James (Eds.) (Vol. 4, pp. 541–575). Facies models.

Riebe, C. S., Sklar, L. S., Lukens, C. E., & Shuster, D. L. (2015). Climate and topography control the size and flux of sediment produced on steep mountain slopes. Proceedings of the National Academy of Sciences, 112(51), 15574–15579. https://doi.org/10.1073/pnas.1503567112

Rivera-Hernández, F., Sumner, D. Y., Mangold, N., Banham, S. G., Edgett, K. S., Fedo, C. M., et al. (2020). Grain size variations in the Murray formation: Stratigraphic evidence for changing depositional environments in Gale crater, Mars. Journal of Geophysical Research: Planets, 125(2), e2019JE006230. https://doi.org/10.1029/2019je006230

Rivera-Hernández, F., Sumner, D. Y., Mangold, N., Stack, K. M., Forni, O., Newsom, H., et al. (2019). Using ChemCam LIBS data to constrain grain size in rocks on Mars: Proof of concept and application to rocks at Yellowknife Bay and Pahrump Hills, Gale crater. Icarus, 321, 82–98. https://doi.org/10.1016/j.icarus.2018.10.023

Rubin, D. M., & Hunter, R. E. (1982). Bedform climbing in theory and nature. Sedimentology, 29(1), 121–138. https://doi.org/10.1111/j.1365-3091.1982.tb01714.x

Schmidt, M. E., Campbell, J. L., Gellert, R., Perrett, G. M., Treiman, A. H., Blaney, D. L., et al. (2014). Geochemical diversity in first rocks examined by the Curiosity Rover in Gale Crater: Evidence for and significance of an alkali and volatile-rich igneous source. Journal of Geophysical Research: Planets, 119(1), 64–81. https://doi.org/10.1002/2013JE004481

Schmidt, M. E., Perrett, G. M., Bray, S. L., Bradley, N. J., Lee, R. E., Berger, J. A., et al. (2018). Dusty rocks in Gale Crater: Assessing areal coverage and separating dust and rock contributions in APXS analyses. Journal of Geophysical Research: Planets, 123(7), 1649–1673. https://doi.org/10.1029/2018JE005553

Siebach, K. L., Baker, M. B., Grotzinger, J. P., McLennan, S. M., Gellert, R., Thompson, L. M., & Hurowitz, J. A. (2017). Sorting out compositional trends in sedimentary rocks of the Bradbury group (Aeolis Palus), Gale crater, Mars. Journal of Geophysical Research: Planets, 122(2), 295–328. https://doi.org/10.1002/2016JE005195

Stack, K. M., Grotzinger, J. P., Lamb, M. P., Gupta, S., Rubin, D. M., Kah, L. C., et al. (2019). Evidence for plunging river plume deposits in the Pahrump Hills member of the Murray formation, Gale crater, Mars. Sedimentology, 66(5), 1768–1802. https://doi.org/10.1111/sed.12558

Stein, N., Grotzinger, J. P., Schieber, J., Mangold, N., Hallet, B., Newsom, H., et al. (2018). Desiccation cracks provide evidence of lake drying on Mars, Sutton Island member, Murray formation, Gale crater. Geology, 46(6), 515–518. https://doi.org/10.1130/G40005

Stein, N. T., Quinn, D. P., Grotzinger, J. P., Fedo, C., Ehlmann, B. L., Stack, K. M., et al. (2020). Regional structural orientation of the Mount Sharp group revealed by in situ dip measurements and stratigraphic correlations on the Vera Rubin ridge. Journal of Geophysical Research: Planets, 125(5). https://doi.org/10.1029/2019JE006298

Stewart, E. K., & Mauk, J. L. (2017). Sedimentology, sequence-stratigraphy, and geochemical variations in the Mesoproterozoic Nonesuch Formation, northern Wisconsin, USA. Precambrian Research, 294, 111–132. https://doi.org/10.1016/j.precamres.2017.03.023

Sun, V. Z., Stack, K. M., Kah, L. C., Thompson, L., Fischer, W., Williams, A., et al. (2019). Late-stage concretions in the Murray formation, Gale crater, Mars. Icarus, 321, 866–890. https://doi.org/10.1016/j.icarus.2018.12.030

Taylor, S. M., & McLennan, S. M. (2009). Planetary crusts: Their composition, origin, and evolution. Cambridge University Press.

Thompson, L. M., Berger, J. A., Spray, J. G., Fraeman, A. A., McCraig, M. A., O'Connell-Cooper, C. D., et al. (2020). APXS-derived compositional characteristics of Vera Rubin Ridge and Murray formation, Gale crater, Mars: Geochemical implications for the origin of the ridge. Journal of Geophysical Research: Planets, 125(10). https://doi.org/10.1029/2019JE006319

Thompson, L. M., Schmidt, M. E., Spray, J. G., Berger, J. A., Fairén, A. G., Campbell, J. L., et al. (2016). Potassium-rich sandstones within the Gale impact crater, Mars:

The APXS perspective. Journal of Geophysical Research: Planets, 121(10), 1981–2003. https://doi.org/10.1002/2016je005055

Thomson, B. J., Bridges, N. T., Milliken, R., Baldridge, A., Hook, S. J., Crowley, J. K., et al. (2011). Constraints on the origin and evolution of the layered mound in Gale crater, Mars using Mars Reconnaissance Orbiter data. Icarus, 214(2), 413–432. https://doi.org/10.1016/j.icarus.2011.05.002

Thorpe, M. T., & Hurowitz, J. A. (2020). Unraveling sedimentary processes in fluvial sediments from two basalt dominated watersheds in northern Idaho, USA. Chemical Geology, 550, 119673. https://doi.org/10.1016/j.chemgeo.2020.119673

Thorpe, M. T., Hurowitz, J. A., & Dehouck, E. (2019). Sediment geochemistry and mineralogy from a glacial terrain river system in southwest Iceland. Geochimica et Cosmochimica Acta, 263, 140–166. https://doi.org/10.1016/j.gca.2019.08.003

Thorpe, M. T., Hurowitz, J. A., & Siebach, K. L. (2020). Source-to-Sink terrestrial analogs for the paleoenvironment of Gale Crater, Mars. Journal of Geophysical Research: Planets, 126(2). https://doi.org/10.1029/2020JE006530

VanBommel, S. J., Gellert, R., Boyd, N. I., & Hanania, J. U. (2019). Empirical simulations for further characterization of the Mars science laboratory alpha particle X-ray spectrometer: An introduction to the ACES program. Nuclear Instruments and Methods in Physics Research Section B: Beam Interactions with Materials and Atoms, 441, 79–87. https://doi.org/10.1016/j.nimb.2018.12.040

Whitney, D. L., & Evans, B. W. (2010). Abbreviations for names of rock-forming minerals. American Mineralogist, 95(1), 185–187. https://doi.org/10.2138/am.2010.3371

Wiens, R. C., Edgett, K. S., Stack, K. M., Dietrich, W. E., Bryk, A. B., Mangold, N., et al. (2020). Origin and composition of three heterolithic boulder-and cobble-bearing deposits overlying the Murray and Stimson formations, Gale Crater, Mars. Icarus, 350, 113897. https://doi.org/10.1016/j.icarus.2020.113897

Wiens, R. C., Maurice, S., Barraclough, B., Saccoccio, M., Barkley, W. C., Bell, J. F., et al. (2012). The ChemCam instrument suite on the Mars Science Laboratory (MSL) rover: Body unit and combined system tests. Space Science Reviews, 170(1), 167–227. https://doi.org/10.1007/s11214-012-9902-4

Williams, R. M. E., Grotzinger, J. P., Dietrich, W. E., Gupta, S., Sumner, D. Y., Wiens, R. C., et al. (2013). Martian fluvial conglomerates at Gale crater. Science, 340(6136), 1068–1072. https://doi.org/10.1126/science.1237317

Yen, A. S., Gellert, R., Thompson, L. M., Treiman, A. H., Morris, R. V., Vaniman, D. T., et al. (2018). Mobility of potassium-rich fluids on Mars: Implications for diagenesis. In The 49th lunar and planetary science conference. Abstract #2690.

Young, G. M., & Nesbitt, H. W. (1998). Processes controlling the distribution of Ti and Al in weathering profiles, siliciclastic sediments and sedimentary rocks. Journal of Sedimentary Research, 68(3), 448–455. https://doi.org/10.2110/jsr.68.448

Zavala, C., Arcuri, M., Di Meglio, M., Gamero Diaz, H., & Contreras, C. (2011). A genetic facies tract for the analysis of sustained hyperpycnal flow deposits. In R. M. Slatt & C. Zavala (Eds.), Sediment transfer from shelf to deep water—revisiting the delivery system (Vol.61, pp. 31–51). AAPG Studies in Geology.

Zolitschka, B., Francus, P., Ojala, A. E., & Schimmelmann, A. (2015). Varves in lake sediments–a review. Quaternary Science Reviews, 117, 1–41. https://doi.org/10.1016/j.quascirev.2015.03.019

Appendix
Chapter 1 supplementary information

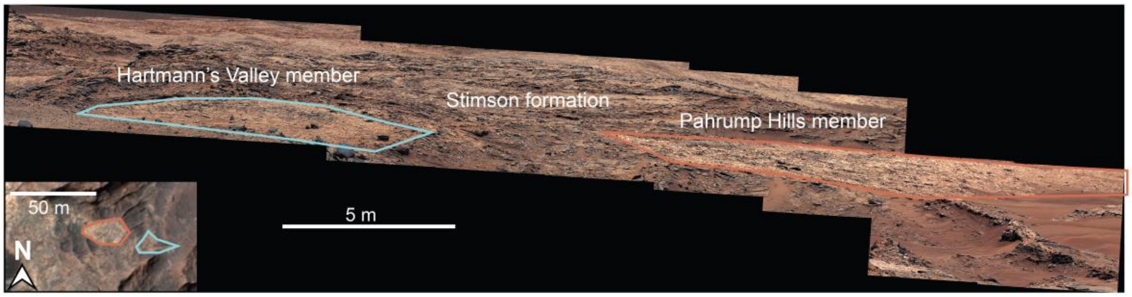

Figure 1.13 Mastcam M100 mosaic (Image ID: MR004875) acquired on sol 1100 outlining the differences in albedo between the Hartmann's Valley and Pahrump Hills bedrock. The stratigraphic contact is inferred to be covered by the Stimson formation. Image credit: NASA/JPL-Caltech/MSSS.

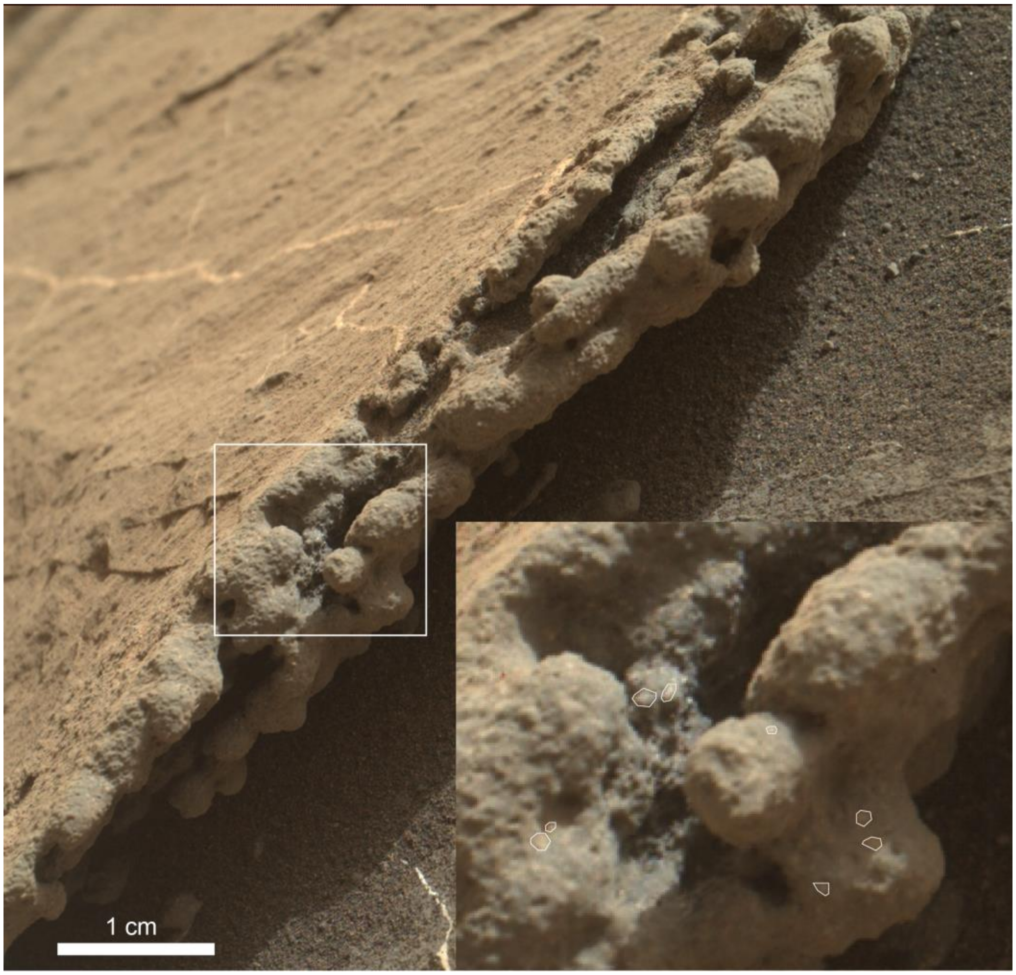

Figure 1.14 MAHLI target Sacajawea consisting of pervasive sand grains. Example grains are outlined in inset figure (MAHLI mosaic ID: 1106MH0003690000401267R00). Image credit: NASA/JPL-Caltech/MSSS.

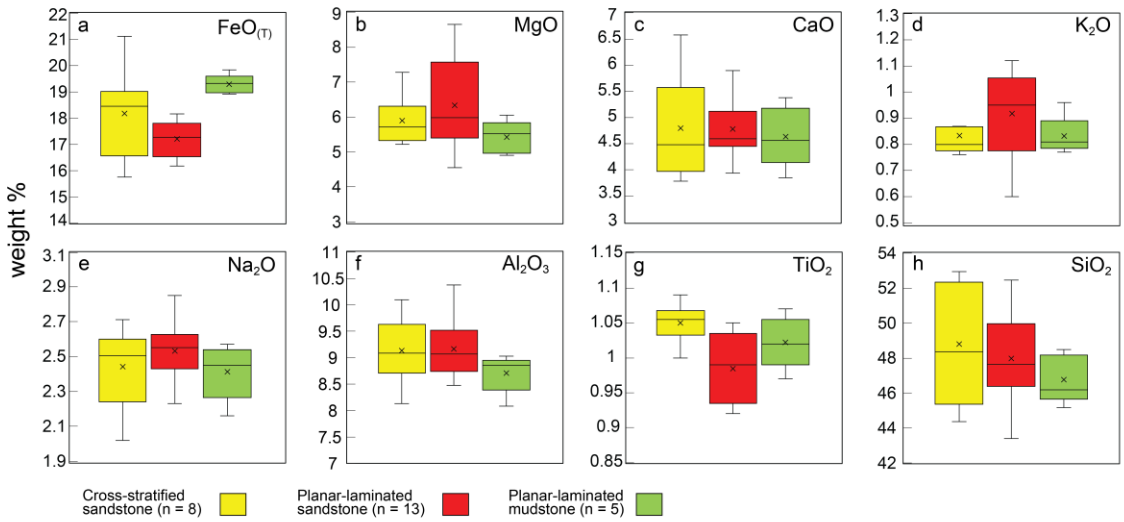

Figure 1.15 Box-and-whisker plots for cross-stratified sandstone (yellow), planar-laminated sandstone (red), and planar-laminated mudstone (green) facies. The "x" symbols within the boxes represents the average wt% for each facies. The horizontal lines within boxes.

Table 1.1 Hartmann's Valley and Karasburg sedimentary facies

Sedimentary facies					
Facies	**Description**	**Stratigraphic member**	**Interpretation**	**Key outcrops**	**Key outcrops (image ID)**
Cross-stratified sandstone	Truncated surfaces bounding inferred sets of dm-m-scale concave-curvilinear laminae; apparent alternating dip directions; alternating resistant and recessive laminae	Hartmann's Valley and Karasburg	Sparsely-distributed aeolian dunes formed from wind-ripple migration in a lacustrine margin setting	(1) Saddle (2) W. Naukluft contact (3) E. Naukluft contact (4) Baynes Mountain (5) Keetmanshoop (6) Murray Buttes contact (7) Capelongo (8) Longonjo	(1) mcam04883 (2) mcam06561 (3) mcam05957 (4) mcam06768 (5) mcam06838 (6) mcam07067 (7) mcam07135 and mcam07157 (8) mcam07362
Planar-laminated sandstone	Continuous succession of horizontally-lying laminae exhibiting a rough surface texture with some intervals of resistant laminae	Hartmann's Valley	Interaction of dune toesets and interdune laminae in a low-energy ponded interdune setting	(1) Sol 1157 outcrop (2) Sol 1189 outcrop (3) Sol 1196 workspace (4) Hardap	(1) mcam05228 (2) mcam05389 (3) mcam05453 (4) mcam06771
Planar-laminated mudstone	Continuous succession of horizontally-lying smooth bedrock forming resistant and recessive millimeter- scale laminae with minor intervals of apparent thicker laminae	Karasburg	Laminae formed in a stable and long-lived lacustrine basin by suspension fallout; thicker laminae reflect potential changes in sediment supply; possible event beds formed from distal lofting of plumes and suspension fallout	(1) Kuito (2) Savungo (3) Caxito (4) Biula	(1) mcam07198 (2) mcam07097 (3) mcam07170 (4) mhli00321

Table 1.2 Laminae measurements for three planar-laminated mudstone targets and one planar-laminated sandstone target

Laminae measurements							
Sol	**Elevation**	**Target**	**Image type and ID**	**# measurements**	**Average thickness (mm)**	**Standard deviation (mm)**	**Facies**
1436	-4398.36	Buila	MAHLI: 1436MH0003210010503468C00	35	2.0	0.5	Planar-laminated mudstone
1455	-4379.46	Clast Survey	Mastcam	32	1.3	0.21	Planar-laminated mudstone
1455	-4379.80	Kuito	Mastcam: mcam07198	25	9.1	2.44	Planar-laminated mudstone
1386	-4421.23	Hardap	Mastcam: mcam06807	12	1.8	0.38	Planar-laminated sandstone

CHAPTER 2 : EVOLUTION OF A LAKE MARGIN RECORDED IN THE SUTTON ISLAND MEMBER OF THE MURRAY FORMATION, GALE CRATER, MARS

Abstract

This study documents facies of the 95 m thick Sutton Island member of the Murray formation to interpret paleoenvironments and establish key stratigraphic transitions. Two facies associations were identified: Facies Association 1 (FA1) and Facies Association 2 (FA2). Individual facies in FA1 include planar-laminated mudstone with minor intervals of planar sandstone, ripple cross-laminated sandstone, cross-stratified sandstone, and alternating laminated sandstone and mudstone. Meter-thick packages of planar-laminated mudstone in FA1 are interpreted to represent deposition in low-energy ponded environments along the lake margin. Straight- and curve-crested ripple cross-laminated facies are interpreted to represent current-influenced deposition along a delta plain. Cross-stratified sandstone facies consist of dm-thick sets that represent deposition in distal distributary channels. Intercalated mudstone and sandstone laminae represent waning flow conditions and possible distributary channel abandonment. Facies in FA1 collectively represent deposition in a distal delta plain. Facies Association 2 is comprised of planar-laminated mudstone with minor sandstone and is interpreted to represent deposition in a lacustrine-basin setting by suspension settling and/or density-flow processes below wave base. Facies Association 1 transitions upward into FA2, defining a rapid transgression substantial enough to facilitate deposition of distal lake facies above delta plain facies. The abrupt transition from FA2 back to FA1 deltaic deposits is suggestive of a forced regression. Facies in FA1 and FA2 are ultimately consistent with the prevalence of aqueous environments recorded in other Murray formation members.

Introduction

Ongoing investigation of the Martian stratigraphic record through rover exploration has corroborated long-held hypotheses that aqueous environments once persisted within the ancient landscape (Grotzinger et al., 2013; McLennan et al., 2019). Fluvial (Caravaca et al., 2022; Edgar et al., 2017; Fedo et al., 2022; Grotzinger et al., 2014; Williams et al., 2013), lacustrine (Edgar et al., 2020; Fedo et al., 2022; Grotzinger et al., 2014; Gwizd et al., 2022; Stack et al., 2019), wet aeolian (Gwizd et al., 2022), and deltaic (Grotzinger et al., 2015) environments have been identified in the stratigraphic successions at Gale crater, as well as at Jezero crater (Mangold et al., 2021) and Meridiani Planum (Edgar et al., 2014; Grotzinger et al., 2005, 2006). Lithofacies characteristics and stratal stacking patterns also exhibit strong similarities with terrestrial stratigraphic records. Consequently, the sedimentary rocks are interpreted in the context of analogous environments involving similar sedimentary processes (Edgett et al., 2020; Gwizd et al., 2022; Schieber et al., 2022; Williams et al., 2013). Rover-based sedimentological and stratigraphic studies are crucial in ongoing efforts to evaluate the evolution of ancient depositional environments on Mars, and subsequent links between environments and habitable conditions (Grotzinger et al., 2014; Squyres & Knoll, 2005).

Since landing in 2012, the Mars Science Laboratory (MSL) Curiosity rover mission at Gale crater (155-km diameter; 5º S, 138º E; Figure 2.1a) has provided an opportunity to assess the evolution of ancient aqueous environments over a comparably thicker stratigraphic interval relative to other rover-explored regions. As of February

2023, Curiosity has ascended through more than 600 m of elevation, a measure used as a proxy for stratigraphic thickness (Fedo et al., 2022), documenting the intracrater plains (Aeolis Palus) and the preserved stratigraphy of the crater's 5.5 km thick central mound (Figure 2.1a; Aeolis Mons, informally Mt. Sharp; Grotzinger et al., 2012). Strata of the Bradbury Group (Aeolis Palus), Murray formation (lower ~320 m of the Mt. Sharp group), and Carolyn Shoemaker formation (overlying stratigraphy of the Mt. Sharp group) record diverse environments associated with long-lived aqueous activity (Edgar et al., 2017; Edgar et al., 2020, Fedo et al., 2022; Gwizd et al., 2022; Stack et al., 2019).

Detailed sedimentologic and stratigraphic analyses have been conducted on six of seven stratigraphic members that comprise the Murray formation. These studies have interpreted facies assemblages characteristic of lacustrine (Edgar et al., 2020; Fedo et al., 2022; Stack et al., 2019) and lacustrine-margin (Gwizd et al., 2022) environments. A detailed assessment of lithofacies and stratigraphy for the 95 m thick Sutton Island member has not been completed, precluding a cohesive model for the evolution of depositional environments throughout the Murray formation. Prior work has described the range of Sutton Island rocks as heterolithic, representing a variety lacustrine and lacustrine-margin environments (Fedo et al, 2018). Some lithologies within the Sutton Island member are enriched in $MgSO_4$, which has been interpreted to signify the onset of aridity (Rapin et al., 2019). Such interpretations collectively suggest that strata may record transitions in characteristics of depositional systems. Understanding the evolution of paleoenvironments and depositional processes in the Sutton Island member will not only support future investigations of aqueous, potentially habitable environments at the facies- and member-scales, but also will ultimately help to complete the larger-scale picture of sustained aqueous activity in Murray formation strata.

Consequently, the objectives of this study are to (a) define and characterize sedimentary lithofacies, (b) identify facies associations and recognize stratal stacking patterns, (c) interpret depositional environments within each facies association, (d) contextualize the pattern of associations within the stratigraphy to determine the evolution of paleoenvironments, and (e) discuss the significance of findings with regard to the nature and evolution of aqueous systems at Gale crater.

Geologic and stratigraphic context

Gale crater is a 155-km diameter, complex crater located at the dichotomy boundary between the northern lowlands and the southern highlands of Mars (Figure 2.1a). The intracrater plains (Aeolus Palus) and central mound (Aeolus Mons, informally Mount Sharp) are comprised of exhumed strata of the interfingering Bradbury group and Mount Sharp group (Grotzinger et al., 2015), which are unconformably overlain by Siccar Point group strata (Banham et al., 2021). As of this writing, more than 600 m of stratigraphy have been documented along the rover traverse since landing in 2012 and are illustrated as a stratigraphic column (Figure 2.1b).

The Mount Sharp group consists of the Murray, Carolyn Shoemaker, and Mirador formations (Figure 2.1b). The ~320 m thick Murray formation is subdivided into seven stratigraphic members based on lithology. Facies of the Pahrump Hills member (PHm), Hartmann's Valley member (HVm), Karasburg member (Km), Blunts Point member

(BPm), Pettegrove Point member (PPm), and Jura member (Jm) are interpreted to represent long-lived lake (Edgar et al., 2020; Fedo et al., 2022; Stack et al., 2019) and lake-margin (Gwizd et al., 2022) environments. Strata of the Sutton Island member (SIm; 95 m) comprise approximately 30% of Murray formation stratigraphy, making the SIm one of the thickest stratigraphic members (Figure 2.1b). Previous work has identified a heterolithic assemblage of facies with variable grain sizes and sedimentary structures (Fedo et al., 2018; Stein et al., 2018). Facies of the overlying Carolyn Shoemaker formation are interpreted to represent a shift from lacustrine facies to marginal-fluvial facies (Caravaca et al., 2022; Fedo et al., 2022).

Methods

Instruments

Qualitative and quantitative analyses of stratigraphy and sedimentology were primarily done using a suite of instruments on the Curiosity rover payload. Navigation Camera (Navcam) stereo-mesh products (Maki et al., 2012) permit thickness measurements of outcrops and larger-scale bedding. Sedimentary structures and other notable outcrop-scale observations were interpreted using Mast Camera (Mastcam) images (Malin et al., 2017). Laminae (cm to µm-scale), smaller-scale bedrock textures, and grain sizes are documented and measured using Mars Hand Lens Imager (MAHLI) images (Edgett et al., 2012) with pixel scales down to tens of micrometers per pixel. Orbiter images and digital elevation models derived from HiRISE and Mars Orbiter Laser Altimeter (MOLA) data (Calef & Parker, 2016; McEwen et al., 2007) were used with the Multi-Mission Geographic Information System (MMGIS) interface (Calef et al., 2017;

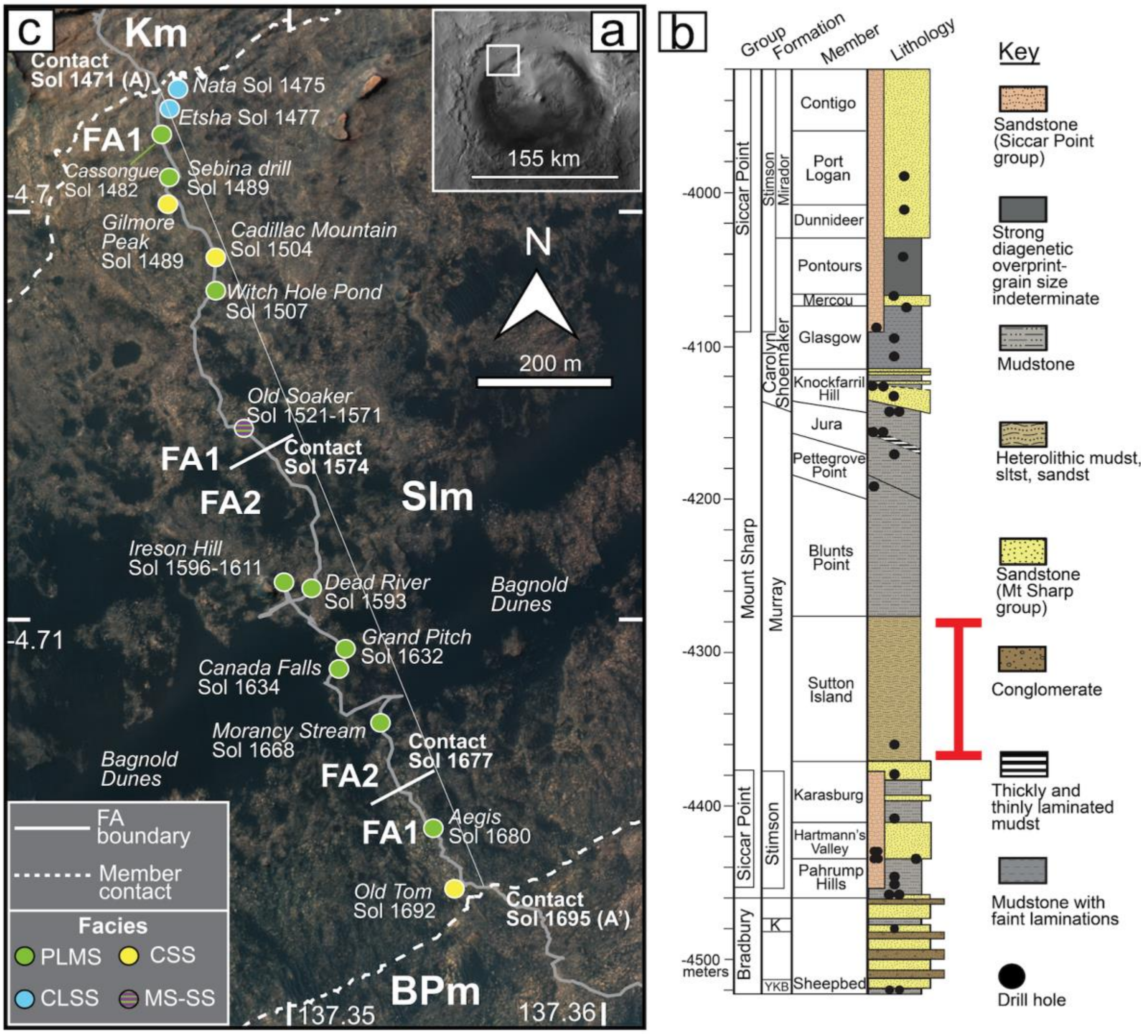

Figure 2.1 (a) Mars Reconnaissance Orbiter (MRO) Context Camera (CTX) mosaic of Gale crater showing Curiosity's exploration area (white box). (b) Simplified stratigraphic column showing the thickness and relationships of strata within the Bradbury group, the Mount Sharp group, and the unconformable Stimson formation and the facies comprising individual formations and members. The red bracket denotes the stratigraphy of the Sutton Island member. Modified from the Sedimentology and Stratigraphy Working Group. (c) Traverse path across the Sutton Island member of the Murray formation. Contacts, key outcrops included in Figures 2.4-2.7 & 2.9, and other notable localities are marked by sol and facies color (where applicable). The thin white line corresponds to the simplified topographic profile shown in Figure 3 (A-A'). The base map is a merged HiRISE orthophoto mosaic from Calef and Parker (2016).

2019) to corroborate the location and elevation of member boundaries, outcrops, and key facies transitions.

Data synthesis

Data were acquired along a rover traverse across 1.96 km of bedrock from Sol 1471 to Sol 1695 (Figure 2.1c). Two ~90-100 m lateral traverse segments (Sol 1559-1611 and Sol 1642-1659) allowed for some assessment of lateral facies variability, but the majority of the rover traverse across the SIm progressed toward higher elevation. The SIm stratigraphy is presented as a vertical stratigraphic column (Figure 2.2); any potential lateral facies variability is addressed in the discussions of facies associations below (see section "Facies associations").

Lamina thickness

Individual lamina thicknesses were measured from MAHLI or Mastcam images where laminae were imaged orthogonally. Thicknesses were computed from the pixel distance between visually determined laminae boundaries and converted to millimeters based on the image resolution. Measurements were obtained from a total of 8 images (Table 2.1). Grayscale pixel intensity was also assessed in one of the images across multiple laminae, where changes in grayscale intensity are a proxy for changes in erosion associated with grain size. Qualitative assessments of laminae thickness were done in lower-resolution images or images taken at greater standoff distances.

Grain size

Grain size of detrital material was measured from MAHLI images of bedrock with observable grain boundaries. Measurements were obtained using ImageJ software (Rasband, https://imagej.nih.gov) by overlaying a randomized grid over a MAHLI image to eliminate any bias and measuring the pixel length of the long axis of grains at each grid node. Measurements were then converted to metric units from the pixel scale of each image, and converted to Phi (Φ) using Equation 1, where *d* = grain size in millimeters:

$$\phi = -log_2(d) \qquad (1)$$

Grain measurements were acquired from a total of five images (Table 2.2; Supplemental Figure 2.11). In two images that contain a more limited quantity of visible grains, grain sizes were measured from a subset of representative grains and are also included in Table 2.2. Given the range of grain sizes and the likely polishing effects of aeolian abrasion, resolution of images was insufficient to permit assessments of roundness and sphericity in any of the five targets (Eibl, 2016).

In MAHLI images where rain boundaries could not be identified, grain size was qualitatively assessed from additional parameters such as mm-scale surface textures and apparent resistance of bedrock to erosion. Interpretations of grain size were supplemented by GINI Index Mean Score (GIMS) values (Rivera-Hernández et al., 2019) calculated from the Chemistry and Camera (ChemCam) Laser Induced Breakdown Spectroscopy (LIBS)

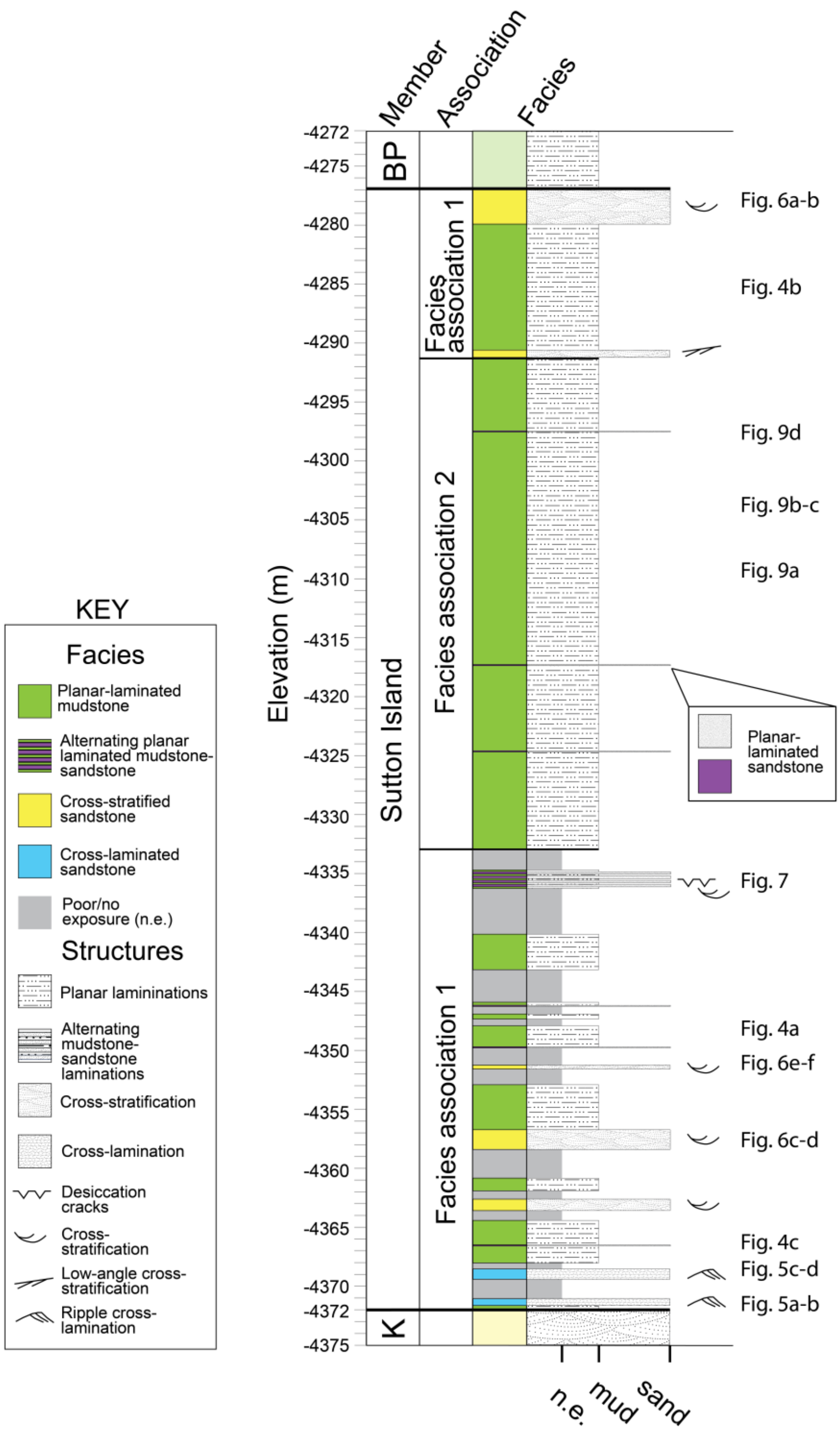

Figure 2.2 Detailed stratigraphic column of the Sutton Island member showing the distribution and abundance of facies in FA1 and FA2. K: Karasburg member; BP = Blunts Point member; n.e.: poor/no exposure;

Table 2.1 Measurements of average lamina thickness.

Facies Association	Facies	Target	Sol	Elevation	Measurements (n)	Average laminae thickness (mm) and range	Standard deviation
FA1	Planar-laminated mudstone with minor sandstone	Cassongue	1482	-4366.81	66	0.49 (0.07-1.01)	0.29
FA1	Ripple cross-laminated sandstone	Etsha	1477	-4368.92	45	3.2 (2-5)	0.75
FA1	Cross-stratified sandstone	Ox Hill	1692	-4278.55	47	3.0 (1.58-4.35)	0.60
FA1	Cross-stratified sandstone	Pejepscot Falls	1692	-4278.93	220	1.68 (0.56-3.37)	0.51
FA1	Cross-stratified sandstone	Mitchell Hill	1695	-4278.74	101	10.56 (3.23-21.15)	5.85
FA1	Alternating laminated sandstone and mudstone	Seawall	1523	-4335.95	74	1.4 (0.42-2.82)	0.71
FA1	Alternating laminated sandstone and mudstone	The Anvil	1552	-4335.45	117	0.53 (0.24-0.80)	0.12
FA2	Planar-laminated mudstone with minor sandstone	Dead River	1593	-4310.75	80	0.66 (0.33-1.08)	0.14

measurements (Wiens et al., 2012). Studies by Rivera-Hernández et al. (2019, 2020) utilize the laser spot size of the ChemCam instrument, which has a diameter of medium- to coarse-sand, to determine point-to-point geochemical variability of a bedrock target and interpret these changes in terms of average grain size. Bedrock comprised of grains sufficiently smaller than the laser size will produce relatively geochemically homogenous point-to-point measurements, whereas bedrock comprised of grains similar to, or larger than, the laser spot size will exhibit more point-to-point heterogeneity (Rivera-Hernández et al., 2019).

Geologic contacts

Ongoing efforts aim to augment existing geologic maps of Gale crater (Stack et al., 2017) with a stratigraphy-based geologic map that delineates formation and member boundaries (Fedo et al., 2022). Contacts of the SIm were mapped based on characteristics observed in orbital images (degree of bedrock fracture, tonal differences) as well as sedimentologic and stratigraphic characteristics documented at the rover-scale (lithologic and facies changes).

The contact between the and SIm and underlying Km is detailed in Gwizd et al. (2022) and is located at an elevation of -4372 m (Figure 2.1c). Relative to the Km landscape, the SIm exhibits a greater degree of erosion and sand cover when viewed in HiRISE and rover images (Figure 2.1c; Gwizd et al., 2022); however, erosional changes appear to be gradual and rather than defined by a distinctive boundary. The Km-SIm contact was placed at the boundary between the uppermost interval of cross-bedded

Table 2.2 Measurements of average grain size.

Grain size										
Facies Association	**Facies**	**Target**	**Sol**	**Elevation**	**Point Count**	**Spot Measure**	**Measurements (n)**	**Average grain size (mm)**	**Average grain size (phi)**	**Average grain size**
FA1	Planar-laminated mudstone with minor sandstone	Cassongue	1482	-4366.8		x	27	0.26	1.9	medium sand
FA1	Cross-stratified sandstone	Newport Ledge	1686	-4280.2	x		180	0.19	2.4	fine sand
FA1	Cross-stratified sandstone	Mason Point	1695	-4278.9	x		459	0.15	3.0	very fine-fine sand
FA1	Alternating laminated sandstone and mudstone	Manset	1523	-4336.0	x		407	0.27	1.9	medium sand
FA1	Alternating laminated sandstone and mudstone	Sutton Island	1523	-4336.0	x		758	0.29	1.8	medium sand
FA1	Alternating laminated sandstone and mudstone	Seawall	1523	-4336.0	x		791	0.27	1.9	medium sand
FA2	Planar-laminated mudstone with minor sandstone	Isle Au Haut	1572	-4334.8		x	11	0.14	2.9	fine sand

sandstone facies in the Km and the first exposure of planar-laminated lacustrine mudstone facies characteristic of the SIm (dashed white line in Figure 2.1c; Gwizd et al., 2022). Geomorphic differences proximal to the contact are also observable in HiRISE, as the contact occurs at a transition between distinctive ridged topography of the uppermost Km and broadly correlates with the gradational changes in erosion (Figure 2.1c).

Several lithologic and geomorphic characteristics documented in previous studies have constrained the contact between the SIm and BPm to approximately -4280 m. Previous work by Fedo et al. (2018) identified a noticeable increase in planar and curvi-planar sulfate veins in the region where the BPm mudstone facies were first observed along the rover traverse. A topographic break observable in HiRISE was also correlated to this transition (Fedo et al., 2019), though an interpretation of the contact based on topography is complicated by the rover traverse path over a distinctive NW-SE trending ridge, which obscures the topographic boundary (Figure 2.1c). The study by Edgar et al. (2020) characterized the Blunts Point mudstone facies as recessive and evenly planar laminated, and interpreted this facies to represent deposition from suspension fallout in a lacustrine setting.

This study builds off of the previous work (Edgar et al., 2020; Fedo et al., 2018) and refines the SIm-BPm contact to be located at the facies boundary between the last occurrence of cross-stratified sandstone facies in the uppermost interval of FA1 (Figures 2.2 & 2.3; see sections “Cross-stratified sandstone facies: description” and “interpretation”) and the first exposures of the recessive mudstone facies that define the

BPm. This boundary occurs at approximately -4277 m (dashed white line in Figure 2.1c; Figure 2.3), shifting the elevation of the initially interpreted contact by ~3 m.

Facies associations

Facies identified in the SIm are grouped into two facies associations, summarized in a stratigraphic column (Figure 2.2) and simplified topographic profile and cross-section of the traverse (Figure 2.3). Total thickness of the stratigraphic column encompasses observations across a lateral distance of ~1.3 km perpendicular to strike (Figure 2.3). Facies association 1 (FA1) and Facies association 2 (FA2) are differentiated by the stratigraphic distribution and sedimentologic characteristics of facies, characterized from outcrop- to grain-scale (Table 2.3). Images of key outcrops for each facies are included in Figures 2.4-2.7 (FA1) and Figure 2.8 (FA2), and are annotated on the map (Figure 2.1c) and stratigraphic column (Figure 2.2). Facies descriptions and interpretations of depositional energy and flow regimes are presented below in stratigraphic order (see section “Facies Association 1”), followed by a synthesis of environments represented in FA1 (see section “Depositional interpretation of FA1”).

Facies association 1

Facies association 1 (FA1) comprises the lowermost and uppermost strata of the SIm (Figures 2.2 & 2.3). The lower interval is 39 m thick (-4372 to -4333 m) and encompasses strata from the contact with the underlying Karasburg member through the exposure of alternating laminated sandstone and mudstone facies. The upper interval is

Table 2.3 Sutton Island member sedimentary facies.

Sedimentary facies					
Facies Association	**Facies**	**Description**	**Interpretation**	**Key outcrops**	**Key outcrops (image ID)**
FA1	Planar-laminated mudstone with minor sandstone	0.24-10.75-m thick intervals of horizontally-lying millimeter- scale laminae with minor intercalated intervals of coarser-grained laminae	Episodic deposition in ponded environments along the delta plain via density-flow processes, with relatively short-lived increases in energy or sediment supply facilitating deposition of minor sandstone interbeds	(1) Witch Hole Pond (2) Sol 1680 Clast Survey (3) Cassongue	(1) mcam07649 (2) mcam08728 (3) mhli00152
FA1	Ripple cross-laminated sandstone	Straight-crested foreset laminae with an average set thickness of 1.8 cm and mm-scale curve-crested ripple laminae	Subaqueous traction and saltation transport of sediment and deposition via current action along the delta plain;	(1) Nata (2) Etsha	(1) mcam07399 (2) mcam07411
FA1	Cross-stratified sandstone	Trough-shaped dm-thick sets that build into cosets and consist of concave-curvilinear laminae; some outcrops consist of more planar foresets with apparent low-angle dip magnitudes	Deposition of three-dimensional sand waves in distal distributary channels along the delta plain	(1) Old Tom (2) Gilmore Peak (3) Cadillac Mountain (Sol 1503 workspace)	(1) mcam08815 (2) mcam07608 (3) mcam07625
FA1	Alternating planar-laminated mudstone-sandstone	10-15-cm thick bed characterized by horizontally-lying sandstone laminae with thin intercalated mudstone laminae and with evidence for possible cross-stratification, overlain by a 1-cm thick interval of mudstone with candidate desiccation cracks (polygonal fractures)	Deposition in shallow distributary channel environments along the delta plain and possible reworking of sediment under waning flow conditions; subsequent subaerial exposure	(1) Sol 1521-1571: Old Soaker region	(1) mcam07982 (2) mhli00646 (3) mcam07981 (4) mhli00302 (5) mcam07748
FA2	Planar-laminated mudstone with minor sandstone	Continuous 42-m thick succession of horizontally-lying millimeter- scale laminae with minor intercalated intervals of coarser-grained laminae	Laminae formed in a long-lived lacustrine basin, representing possible event beds formed from distal lofting of plumes and suspension fallout; minor intercalated sandstone laminae represent punctuated increases in energy	(1) Dead River (2) Grand Pitch (3) Canada Falls (4) Morancy Stream	(1) mcam08119 (2) mcam08432 (3) mhli00306 (4) mhli00171

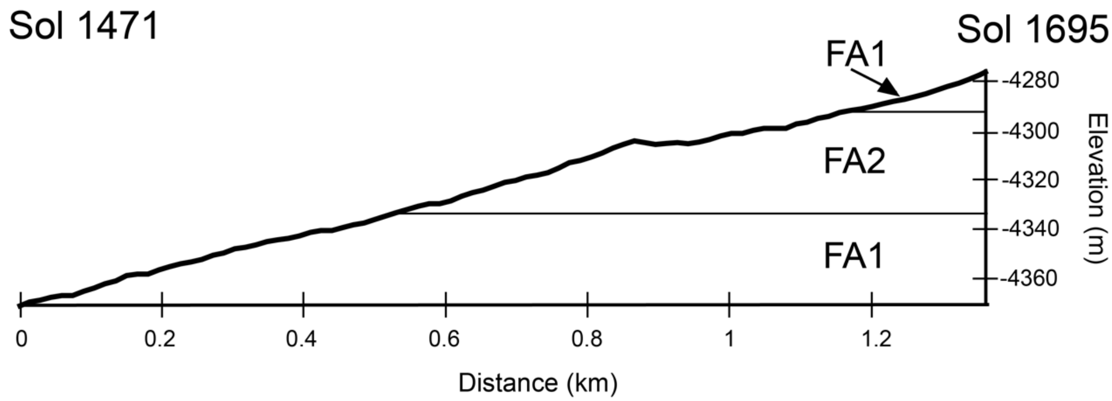

Figure 2.3 Topographic profile of the Sutton Island member traverse perpendicular to strike (Noted on Figure 1; actual traverse including lateral segments parallel to strike: 1.96 km, Sols 1471-1695). The topographic profile depicts a cross-sectional view showing the distribution of FA1 and FA2, assuming a negligible dip magnitude of strata.

approximately 14 m thick (-4291 to -4277 m), with boundaries defined by exposures of cross-stratified sandstone facies at -4291 m and -4280 m. Facies association 1 comprises 56% of the total SIm thickness. Key outcrop exposures of FA1, shown in Figures 2.4-2.7, are noted in the map in Figure 2.1 and the stratigraphic column in Figure 2.3.

Both intervals of FA1 are characterized by a variable distribution of facies (Figure 2.2). Facies comprising the lower interval of FA1 include planar-laminated mudstone with minor sandstone, ripple cross-laminated sandstone, cross-stratified sandstone, and alternating laminated sandstone and mudstone (Table 2.3). The upper interval of FA1 consists of planar-laminated mudstone and two intervals of cross-stratified sandstone. Contacts between different facies intervals are not visible due to extensive fracturing and sand cover of bedrock across the landscape.

The lower interval of FAl displays a higher degree of bedrock fracturing, erosion, and sand cover, preventing facies identification through 18.5 m (20%) of total stratigraphy. Where bedding was identified but poor outcrop exposure precludes further interpretation, intervals are marked in the stratigraphic column in gray (Figure 2.2).

<u>Planar-laminated mudstone with minor sandstone facies: description</u>

Exposures of planar-laminated mudstone occur in both intervals of FA1 (Figure 2.2). The thickness of stratigraphic intervals ranges from 0.24 m to 10.75 m, comprising 36% of total measured stratigraphy. Exposures vary from loose dm-scale eroded blocks to m-scale outcrops **(**Figure 2.4). Fractures, veins, and concretions disrupt lateral continuity of laminae, and preclude lateral tracing of sedimentologic attributes within some images (Figure 2.4a).

Outcrops primarily consist of continuous successions of horizontal planar laminae which are more recessive relative to coarser-grained facies in FA1 (Figure 2.4; Table 2.3). In some outcrops, planar veins and concretions appear to enhance erosional resistance of laminae (Figure 2.4a). Individual lamina boundaries are defined by differences in erosional resistance that range from more subtle (Figure 2.4a) to more pronounced (Figure 2.4b). Transects of grayscale values across laminae in the target Witch Hole Pond (Figure 2.4a) show regularly spaced color variation corresponding to the scale of individual laminae, but do not reveal any correlation with possible textures associated with gradational patterns that are characteristic of specific depositional processes (e.g., tempestite, turbidite; Lazar et al., 2015).

Individual grains are not resolvable in the majority of MAHLI images. Individual laminae generally exhibit a smooth surface texture (Figure 2.4b), suggesting that grains are polished from aeolian abrasion (e.g., Gwizd et al., 2018) or are finer than the resolution of MAHLI images (very coarse silt; Edgett et al., 2012).

Sandstone occurs at three elevations as interbeds with planar-laminated mudstone (Figures 2.3 & 2.4c). Sandstone exposures have visible grains and rougher surface textures relative to adjacent mudstones (Figure 2.4c). Sandstone beds are up to several cm thick and consist of sub-mm- to mm-scale laminae that are generally planar to slightly undulose. Laminae measured from the target Cassongue (Figure 2.4c; -4366.8 m) have an average thickness of 0.49 mm (Table 2.1), similar to the mudstone laminae in this facies. Punctuated intervals of a relatively coarser lithology are also supported by GIMS values within Facies 1 that indicate the presence of sand (Rivera-Hernández et al., 2020).

Planar-laminated mudstone with minor sandstone facies: interpretation

Planar-laminated mudstone in FA1 is interpreted to represent deposition in a subaqueous setting. Mudstone laminae are indicative of a depositional system whose overall energy was low enough to allow for suspension fallout of silt- and clay-size fractions (Lazar et al., 2015). Successions of uniform, millimeter-thick mudstone laminae suggest episodic deposition from density-flow processes (Boulesteix et al., 2019; Renaut & Gierlowski-Kordesch, 2010). Minor sandstone interbeds represent traction transport and rapid deposition via relatively short-lived increases in energy or grain size within the depositional system (Pickering et al., 1986; Pontén & Plink-Björklund, 2007). Overall, outcrop expressions, laminae thicknesses, and grain size of this facies resemble characteristics of facies in FA2 (see section "Facies association 2"), but the maximum thickness (10.7 m) of mudstone intervals in FA1 indicates that deposition occurred in a short-lived environment compared with the facies of FA2. Upper-flow-regime conditions generate horizontal sandstone laminae associated with flooding (Colombera & Mountney, 2019), but the stratigraphic association of sandstone and mudstone laminae and the lack of any observable traction structures (e.g., ripples) associated with sandstone interbeds does not support such an interpretation. Additionally, upper-flow-regime conditions are typically cm-scale in thickness (McKee et al., 1967), and are inconsistent with the comparably thicker intervals of this facies.

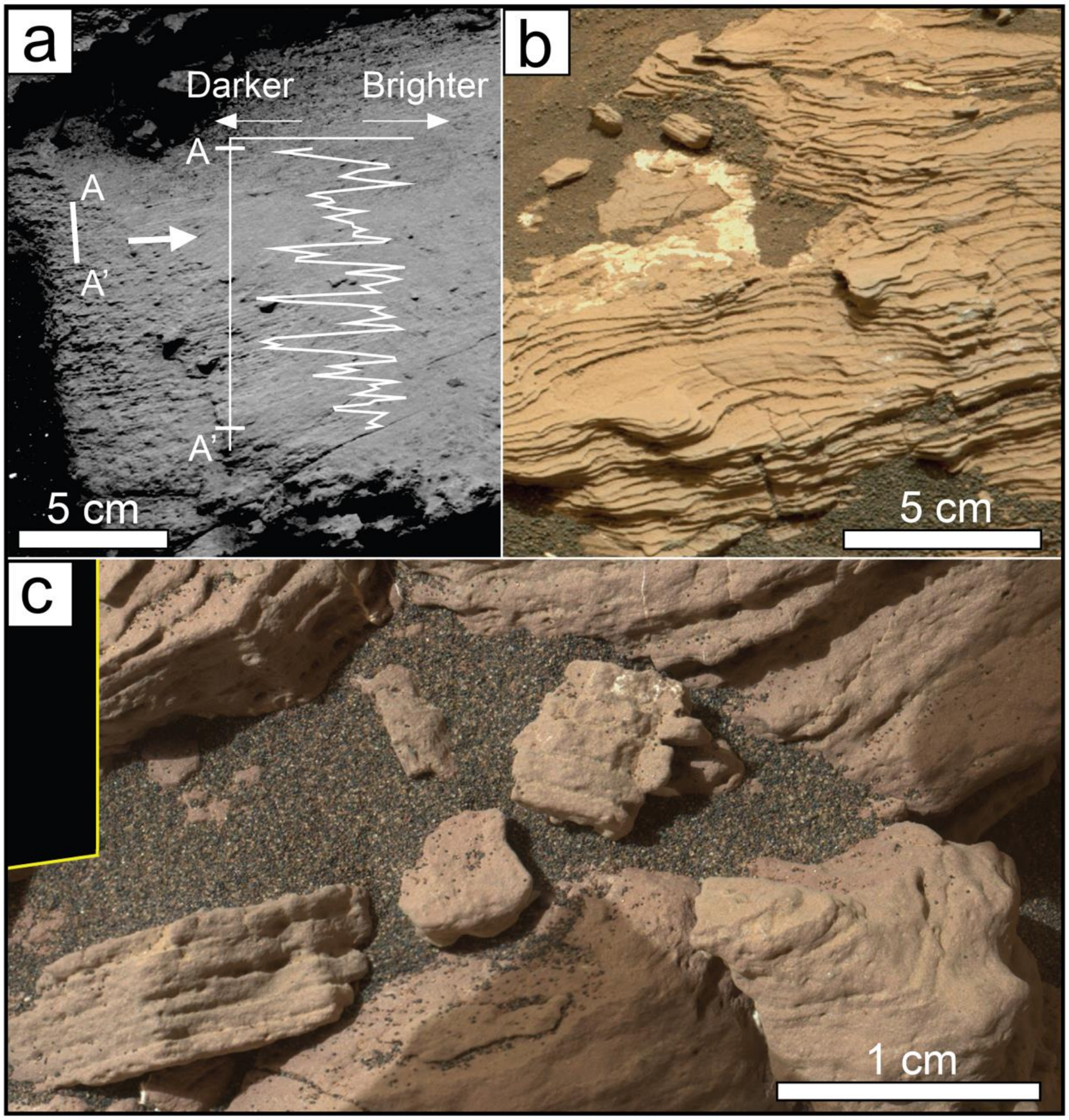

Figure 2.4 Representative outcrops of the planar-laminated mudstone with minor sandstone facies in FA1. (a) Greyscale image of target Witch Hole Pond including a transect of greyscale values highlighting individual laminae thicknesses (M100 Mastcam image, mcam07649, Sol 1507). (b) Outcrop displaying sharp boundaries between individual laminae (M100 Mastcam image, mcam08728, Sol 1680). (c) Exposure of planar-laminated sandstone at -4366.81 m (MAHLI ID: mhli00152, Sol 1482). Image credit: NASA/JPL-Caltech/MSSS.

The association with other facies in FA1 suggests that deposition occurred in relatively low-energy environments along the lake margin. Delta plain lakes and overbank environments are plausible interpretations of depositional environments for mudstone laminae with sandstone interbeds (MacNaughton et al., 1997; Pontén & Plink-Björklund, 2007). The association with subaqueous and subaerial processes in other FA1 facies indicates that some component of subaerial exposure and sediment reworking may have also influenced this facies (MacNaughton et al., 1997; Muhlbauer & Fedo, 2020), but the lack of evidence for flow structures or subaerial exposure suggests that ponded environments were relatively sheltered.

Ripple cross-laminated sandstone facies: description

Ripple cross-laminated sandstone was observed at two exposures in the lower interval of FA1 (Figure 2.2). Collectively, this facies represents 1.9 % of total stratigraphy. Due to the discontinuity of eroded and fractured outcrops, lateral continuity of this facies could not be determined.

Evidence for straight-crested ripple cross lamination was documented in the outcrop Nata (Figure 2.5a & b). This outcrop consists of sets of foreset laminae that generally dip southward relative to inferred bedding. The average thickness of individual sets is approximately 1.8 cm, with set boundaries along horizontal to slightly undulose surfaces (Figure 2.5a & b). Individual lamina thicknesses cannot be accurately measured from the available image, though laminae are thinner than the 1.8 cm average set

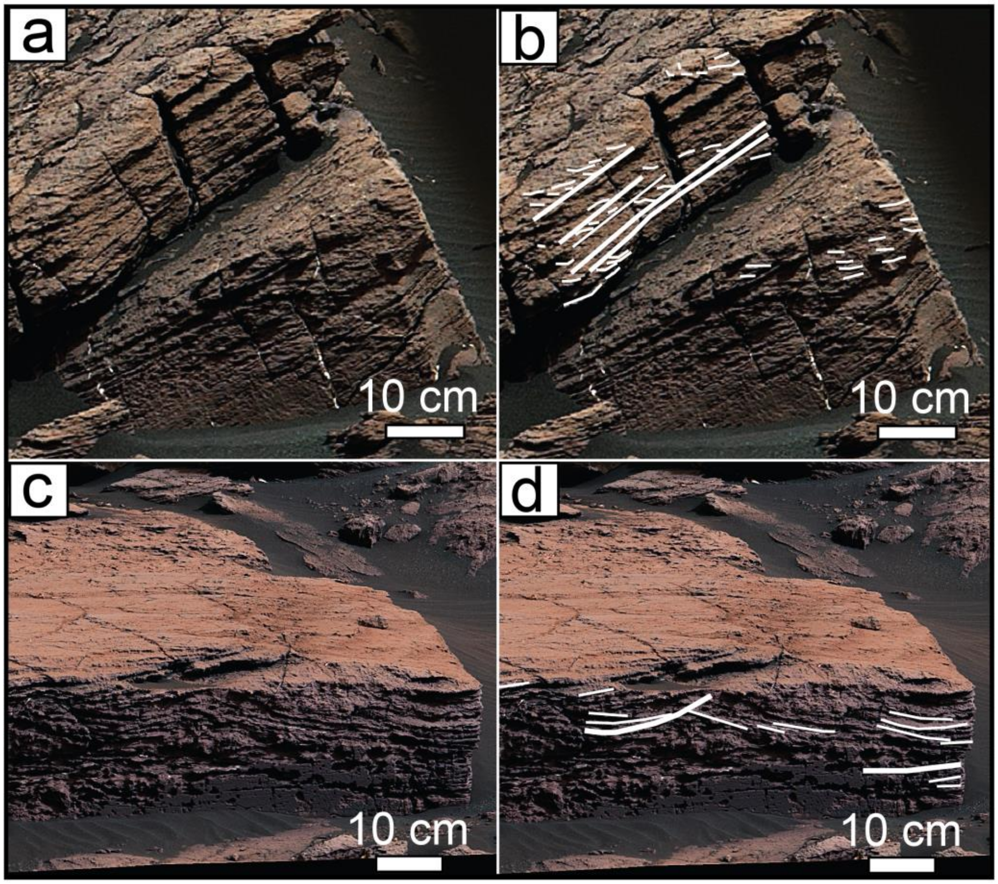

Figure 2.5 Representative outcrops of the ripple cross-laminated sandstone facies in FA1. (a) Outcrop Nata showing planar ripple cross-lamination (M100 Mastcam mosaic, mcam07399, Sol 1475). Image (b) includes outlines of set boundaries (thick white lines) and foreset laminae (thin white lines) on Nata. (c) Outcrop Etsha showing trough ripple cross-lamination (M100 Mastcam mosaic, mcam07411, Sol 1477). Image (d) includes outlines of set boundaries (thick white lines) and foreset laminae (thin white lines) on Etsha. Image credit: NASA/JPL-Caltech/MSSS.

thickness. Interpretations of GIMS values from this locality are indicative of a sand-size fraction (Rivera-Hernández et al., 2020).

Evidence for curve-crested ripple cross-lamination was documented in the outcrop Etsha (Figure 2.5c & d). Although poor exposure precludes measurements of set thicknesses in this outcrop, sets are identifiable from alternations in apparent dip between laminae. Sets are classified as curve-crested due to the presence of concave-curvilinear laminae identifiable throughout the outcrop. Measurements of individual laminae in Etsha average 3.2 mm in thickness (Table 2.1; Figure 2.5c & d). Individual grains cannot be resolved, but the closer relative standoff distance at which the Etsha outcrop was imaged allows for resolution of rough, dimpled surface textures on individual laminae (Figure 2.5c & d). Together with GIMS data (Rivera-Hernández et al., 2020), these observations suggest a sand grain-size fraction.

<u>Ripple cross-laminated sandstone facies: interpretation</u>

Planar and trough ripple cross-lamination identified in the SIm are consistent with formation of two- and three-dimensional ripples, respectively (Allen, 1962). The association of this facies with other subaqueous facies in FA1 (see section "Depositional interpretation of FA1") suggests ripples formed from subaqueous traction and saltation sediment transport and deposition in lower flow-regime conditions (Southard & Boguchwal, 1973). The apparent uniform dip direction identified in successive sets of the two-dimensional ripples in Nata (Figure 2.5a & b) are indicative of asymmetric ripples formed under the action of unidirectional currents (Harms, 1969; Reineck & Singh, 1980). Ripple morphologies are typically characteristic of variable flow-, topographic-, and sediment-related factors (Baas, 1994; Rubin, 2012). Two-dimensional ripples interpreted from the outcrop Nata may represent formation in comparably lower flow velocities compared to three-dimensional ripples interpreted from the outcrop Etsha (Figure 2.5c & d; Reineck & Singh, 1980), highlighting fluctuating energy within the depositional system.

Cross-stratified sandstone facies: description

Outcrops of cross-stratified sandstone were identified in both intervals of FA1, and comprise five stratigraphic intervals ranging in thickness from 10 cm to 3 m (Figure 2.2). Cumulatively, cross-stratified facies comprise 9% of SIm stratigraphy. This facies primarily occurs as interbeds within planar-laminated mudstone (Figure 2.2). Cross-stratification is laterally continuous across the scale of individual outcrops (Figure 2.6). Cross-stratification comprising the stratigraphically highest interval at the contact with the Blunt's Point member (-4280 m to -4277 m; Figure 2.1c) can be traced laterally over a distance of ~25 meters.

Exposures of cross-stratification are primarily characterized by trough-shaped sets that build into cosets (Figure 2.6; Table 2.3). Truncation surfaces subdivide individual sets, but the oblique nature of images precludes an assessment of the relative dip magnitude and direction of surfaces (Figure 2.6a & d). Evaluation of set and coset scale at outcrops is limited due to incomplete outcrop exposure, and some measurements described in this section therefore represent minimum bounds of thickness and width.

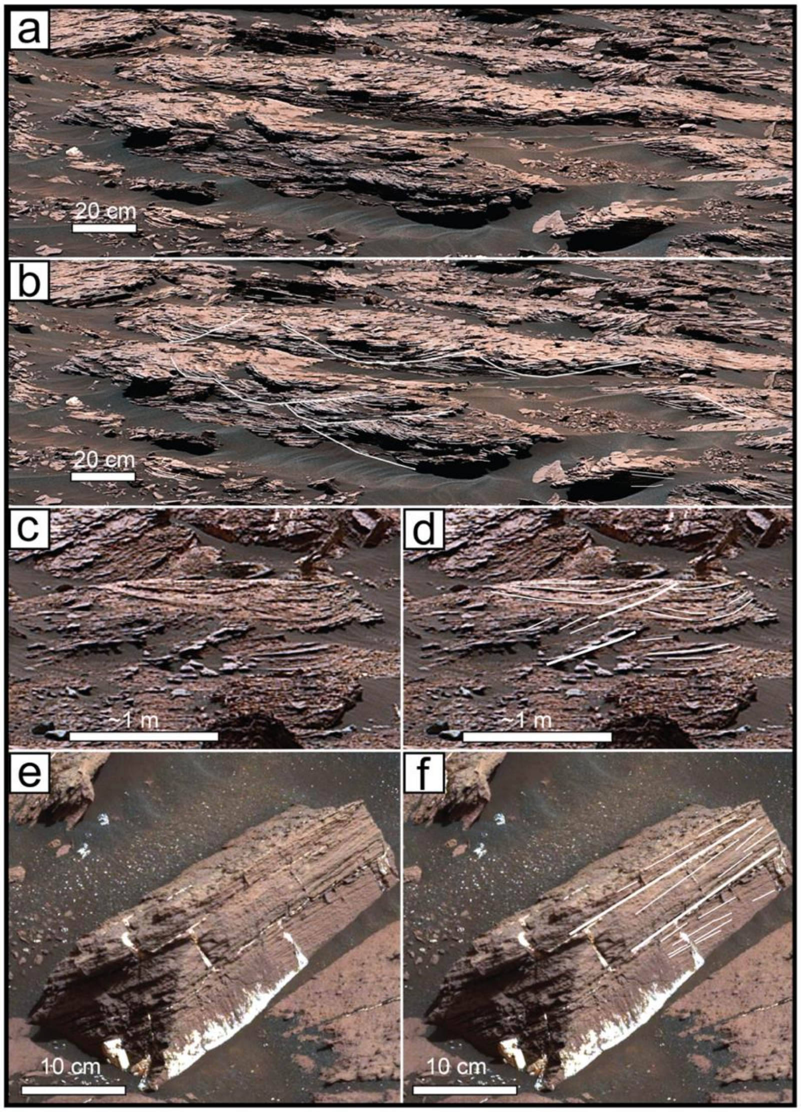

Figure 2.6 Representative outcrops of the cross-stratified sandstone facies in FA1. (a) Outcrop Old Tom showing multiple preserved troughs with thickness of 5-14 cm that build into cosets (M100 Mastcam mosaic, mcam08815, Sol 1692). Image (b) includes outlines of set boundaries (thick white lines) and individual foreset laminae (thin white lines) on Old Tom. (c) Outcrop Gilmore Peak showing preserved troughs with a minimum thickness of 30 cm (M100 Mastcam mosaic, mcam07608, Sol 1501). Image (d) includes outlines of set boundaries (thick white lines) and individual foreset laminae (thin white lines) on Gilmore Peak. (e) Image of target Cadillac Mountain showing foreset laminae with more planar expressions and apparent low-angle dip magnitudes (M34 Mastcam mosaic, mcam07625, Sol 1503). Image (f) includes outlines of set boundaries (thick white lines) and individual foreset laminae (thin white lines) on Cadillac Mountain. Image credit: NASA/JPL-Caltech/MSSS.

The outcrop Old Tom (Figure 2.6a & b) consists of multiple preserved troughs with thicknesses ranging from 5-14 cm, and an average coset thickness of approximately 24 cm. Individual troughs visible within the Old Tom outcrop exhibit a minimum width of approximately 0.5 m. Documented sets within the Gilmore Peak outcrop (Figure 2.6c & d) have a minimum thickness of approximately 30 cm, and troughs have a minimum width of 1 m. Although several measurements across both outcrops represent minimum bounds, the similar thicknesses and widths suggest that decimeter-scale set heights and meter-scale trough widths may be characteristic of other stratigraphic intervals of this facies. Some outcrops of cross-stratification consist of foresets with more planar expressions and apparent low-angle dip magnitudes (Figure 2.6e & f).

Individual lamina display apparent uniform thicknesses across the majority of outcrops. Foreset laminae are thinly laminated to laminated (McKee & Weir, 1953). Average laminae thicknesses of three targets (Pejepscot Falls, Sol 1692; Ox Hill, Sol 1692; Mitchell Hill, Sol 1695) are 1.68 mm, 3 mm, and 10.6 mm (Table 2.1).

Grain size was measured on two targets (Newport Ledge, Sol 1686; Mason Point, Sol 1695) from the uppermost interval of cross-stratified facies (Table 2.2; Supplemental Figure 2.11). Both targets have average measured grain sizes of fine sand. Grain sizes derived from GIMS values vary, but indicate that sand is a predominant grain-size fraction comprising cross-stratification (Rivera-Hernández et al., 2020).

Cross-stratified sandstone facies: interpretation

Trough cross-stratified sandstone identified in FA1 represents deposition of decimeter-scale three-dimensional sand waves (Hunter, 1985). Trough cross-stratification does not unambiguously constrain a depositional environment, but the association of cross-stratified intervals with mudstone facies of FA1 (see section "Planar-laminated mudstone with minor sandstone: description" within FA1) and the absence of evidence for subaerial exposure within underlying or overlying intervals of mudstone facies (desiccation cracks were only observed at the Old Soaker locality noted in Figure 1) favors a subaqueous interpretation for deposition of cross-stratification. In subaqueous settings, decimeter-scale three-dimensional bedforms represent traction and saltation transport of sediment and deposition in transitional flow regimes (Ashley, 1990). Low-angle cross-stratification may represent deposition in transitional flow regimes, or infill of scours (Todd, 1996). The low energy of the distal plain along with the increased susceptibility of basaltic lithologies to weathering (Gislason & Oelkers, 2003) relative to more felsic lithologies typical of terrestrial settings could explain the relatively finer grain-size fraction.

Cross-stratified sandstone in the SIm is interpreted to represent sand deposition as bedforms within distributary channels in a delta plain setting. Terrestrial studies of distributary systems show that channels are commonly wide and shallow (Olariu & Bhattacharya, 2006), and distal most channels on the delta plain are relatively isolated and intercalated with thick successions of laminated mudstone (Nichols & Fisher, 2007; Owen et al., 2015). The relatively thin stratigraphic intervals of cross-stratified facies observed in the SIm (10 cm – 3 m; Figure 2.2) and the association with intervals of planar-laminated mudstone (see sections "Planar-laminated mudstone with minor sandstone: description" and "interpretation" within FA1) are consistent with stratigraphic records of distributary systems. Set thicknesses and the fine sand grain-size measurements in SIm cross-stratified facies are consistent terrestrial records that depict a reduced set thickness and grain size toward the shoreline (Went, 2019), further indicating that cross-stratified deposits represent deposition the distal regions of the distributary system.

Alternating laminated sandstone and mudstone facies: description

Alternating sandstone and mudstone laminae were documented at an outcrop near the Old Soaker locality in the lower interval of FA1 (Figure 2.1c). Lack of complete exposure due to erosion and sand cover precludes an assessment of all lithologic transitions across the stratigraphic interval, but observations of this facies were documented across the total 1.6 m thickness of the outcrop (Figure 2.2). The distribution and abundance of sandstone relative to mudstone as well as variable sedimentary structures identified across the outcrop, detailed below, differentiate this facies from the planar-laminated mudstone facies in FA1 (see section "Planar-laminated mudstone with minor sandstone: description" within FA1).

This facies is characterized by a variable assemblage of intercalated sandstone and mudstone laminae (Figure 2.7). Figure 2.7a shows a portion of a 10-15 cm bed of

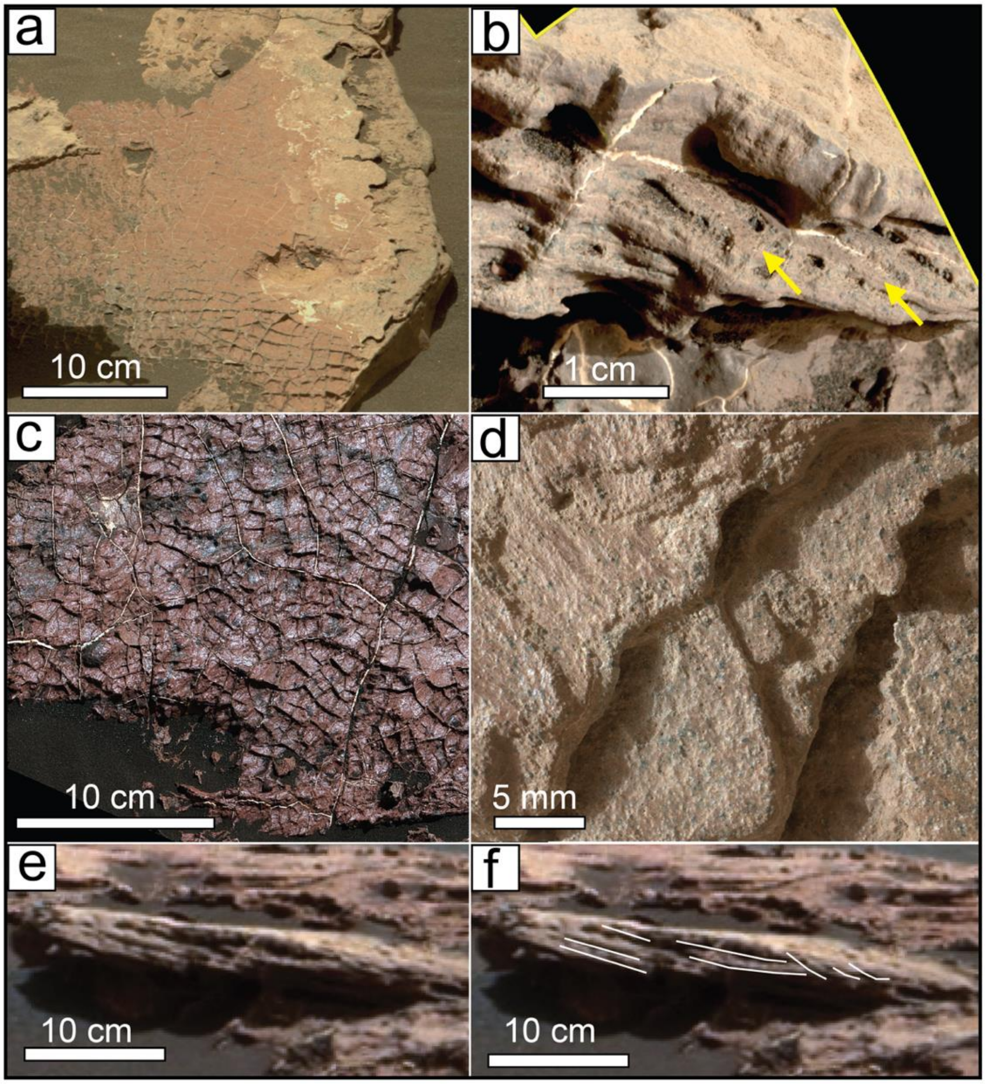

Figure 2.7 Representative outcrops of the alternating laminated sandstone and mudstone facies in FA1. (a) Outcrop Schooner Head showing the primary 10-15 cm bed of intercalated sandstone and mudstone and the overlying 1 cm thick mudstone bed comprised of candidate desiccation cracks (M100 Mastcam mosaic, mcam07982, Sol 1555). (b) Intercalated sandstone and mudstone laminae in the outcrop Seawall (MAHLI ID: mhli00646, Sol 1523). (c) Candidate desiccation cracks on outcrop Old Soaker (M100 Mastcam mosaic, mcam07981, Sol 1555). (d) Outcrop Sutton Island showing medium sand grains (MAHLI ID: mhli00302, Sol 1521). (e) Curvilinear laminae showing apparent differences in dip magnitude and a possible stratal cutoff (M100 Mastcam mosaic, mcam07748, Sol 1555). Image (f) includes outlines of curvilinear laminae on the outcrop in (e). Image credit: NASA/JPL-Caltech/MSSS.

laminated sandstone overlain by a 1 cm interval of mudstone, highlighting the close association of sandstone and mudstone lithologies in this facies. Intervals of sandstone are comprised of planar- to undular-laminae, with laminae in the target Seawall (Sol 1523) exhibiting an average thickness of 1.4 mm (Figure 2.7b; Table 2.1). Several intercalated smoother and red-toned layers (yellow arrows in Figure 2.7b) represent mudstone laminae. Measurements of one mudstone target (The Anvil, Sol 1552) show laminae to have an average thickness of 0.53 mm (Table 2.1). There is no evidence of gradation between medium-sand and mud intervals, signifying that such transitions are abrupt. A 1 cm thick mudstone bed overlies the sandstone bed in Figure 2.7b (red-toned layer in Figure 2.7a). Individual mudstone laminae are not visible, but the 1 cm thick interval of mudstone at the target Old Soaker (-4335.74) is segmented into four- and five-sided polygons bounded by $CaSO_4$ veins (Figure 2.7c), which have been interpreted as desiccation cracks (Stein et al., 2018) or the result of burial and compaction (Cosgrove et al., 2022). It is notable that although mm-scale fluctuations between sandstone and mudstone interbeds were identified within the sandstone bed, the uppermost part of the stratigraphic interval of this facies is comprised of mudstone.

Grain size is constrained by measurements, surface textures, and GIMS values from Rivera-Hernández et al., 2020. Measurements of three images from the 10-15 cm sandstone bed suggest an average grain size of medium sand for the sandstone lithology (Figure 2.7d & Supplemental Figure 2.11; Table 2.2). Within the red-toned beds, a relatively smooth surface texture and GIMS values support a mudstone interpretation (Figure 2.7c).

In addition to planar laminae and polygonal fractures, evidence for possible cross-stratification was identified. Evidence includes curvilinear laminae that display apparent relative differences in dip magnitude as well as several possible stratal cutoffs (Figure 2.7e & f). Incomplete exposure precludes exact measurements of set thickness, but laminae and cutoffs are broadly located along a similar stratigraphic interval as the planar-laminated sandstone facies, suggesting that structures could occur over a similar decimeter-scale.

Alternating laminated sandstone and mudstone facies: interpretation

Alternating sandstone and mudstone laminae are interpreted to represent deposition in a subaqueous setting characterized by variable energy. We interpret mudstone laminae to indicate deposition by suspension fallout (Lazar et al., 2015), whereas sandstone laminae represent formation by traction deposition, a pairing that indicates fluctuations in energy (Pontén & Plink-Björklund, 2007). Cross-stratification may be indicative of deposition in a transitional flow regime (Ashley, 1990). Additionally, the occurrence of cross-stratification over the decimeter-thick sandstone interval suggests that the scale of sets may be consistent with other cross-stratified sandstone facies in FA1 (see section "Cross-stratified sandstone facies: description"), suggesting that subaqueous depositional processes may be similar. Abrupt alternations between sand and mud signify shifting depositional energy from a flow velocity sufficient for deposition of medium sandstone in a succession of planar-laminae and cross-stratification to a velocity low enough to allow suspension fallout of mudstone. The predominance of mudstone within the upper part of the 1.6 m interval suggests that overall energy waned throughout deposition of this facies.

This facies is interpreted to represent deposition along the lake margin from subaqueous processes, accompanied by subaerial exposure of strata. Within distributary systems, shifting channels can facilitate channel abandonment and coincide with deposition of mudstone over sandstone facies as flow conditions become stagnant (Nichols & Fisher, 2007; Syvitski, 2012). Intercalated medium sandstone and mudstone could also represent reworking of strata within the distributary channel during fluctuations in flow (Shaw & Mohrig, 2014). Candidate desiccation cracks (Figure 2.7c) described in Stein et al. (2018) are characterized by a network of polygonal ridges that form T-junctions and are therefore interpreted to result from a single desiccation event. Desiccation indicates that strata experienced at least temporary subaerial exposure, meaning that strata were deposited in very shallow water. We note that desiccation cracks were not identified at any other exposure along the SIm traverse, despite the predominance of exposed bedding planes within this member. Overall, this facies records deposition from subaqueous processes along the lake margin involving both subaerial and subaqueous processes.

Depositional interpretation of FA1

Facies in FA1 represent deposition in dynamic environments that represent subaqueous and subaerial processes along a lake margin. Further characterization of the lake margin requires reconciliation of subenvironments that are characterized by large sand waves made via bedload transport and suspension fallout with the abundance of planar-laminated mudstone. Stratigraphic records of delta plain environments consist of similar facies to the facies interpreted within FA1 (Bhattacharya, 2010) and best capture the variability and distribution of environments in this study.

Sedimentologic and stratigraphic characteristics aid in classification of the delta associated with the delta plain in FA1. Deltas are classified in three main varieties, all characterized by a combination of subaerial and subaqueous subenvironments: fan, braid, and common (McPherson et al., 1987). Facies in FA1 do not support a fan delta interpretation; such deltas are characterized by gravel-rich debris flow deposits and commonly lack cross-stratified facies (Blair & McPherson, 2008; McPherson et al., 1987). Facies in common deltas and braid deltas typically contain distributary channels (Bhattacharya, 2010; Olariu & Bhattacharya, 2006), consistent with the interpretations of cross-stratified sandstone facies in FA1 (see section "Cross-stratified sandstone facies: interpretation"). Common deltas are more consistent with fine grain sizes of FA1 (Orton & Reading, 1993), but are often linked to single thread rivers that build into distinct upward-coarsening cycles (Bhattacharya, 2010). The variable facies assemblage and lack of evidence for substantial channelization of distributary facies is more consistent with stratigraphic records of braid delta environments, which are characterized by sheet-like channel elements and involve variable amounts of channel avulsion (Hadlari et al., 2006; MacNaughton et al., 1997; Magalhaes et al., 2015; Muhlbauer & Fedo, 2020). The absence of clear channelization would support a braidplain as the associated delta with FA1 strata, but the abundant mudstone in FA1 contrasts with typical braid-plain to braid-delta systems. The abundance of mudstone relative to sandstone within FA1 indicates that the overall energy of the delta plain system was low, suggesting that deposition occurred in a distal region adjacent to the lake shoreline (Went, 2019). The presence of mudstone may be explained by inherent compositional differences in the source rocks between studies of more felsic terrestrial lithologies relative to the more mafic lithologies documented at Gale crater. Basalt is more unstable and susceptible to weathering compared with more felsic compositions comprising terrestrial continental crust (Gislason & Oelkers, 2003; Ibarra et al., 2016).

Terrestrial environments provide analogues for elements of depositional conditions in FA1, and can further constrain the depositional processes and relative position of environments along the delta plain landscape. Figure 2.8 depicts an unvegetated braid delta landscape on Baffin Island, Canada as a potential modern analogue for elements of the distal delta plain system in this study, though it is noted that this analogue is only presented to represent certain aspects of the SIm depositional system, discussed below. The more distal regions of the delta plain are characterized by wider channels and an increased ratio of subaqueous to subaerial deposition. The distal delta plain landscape is characterized by closely associated, shallow distributary channels

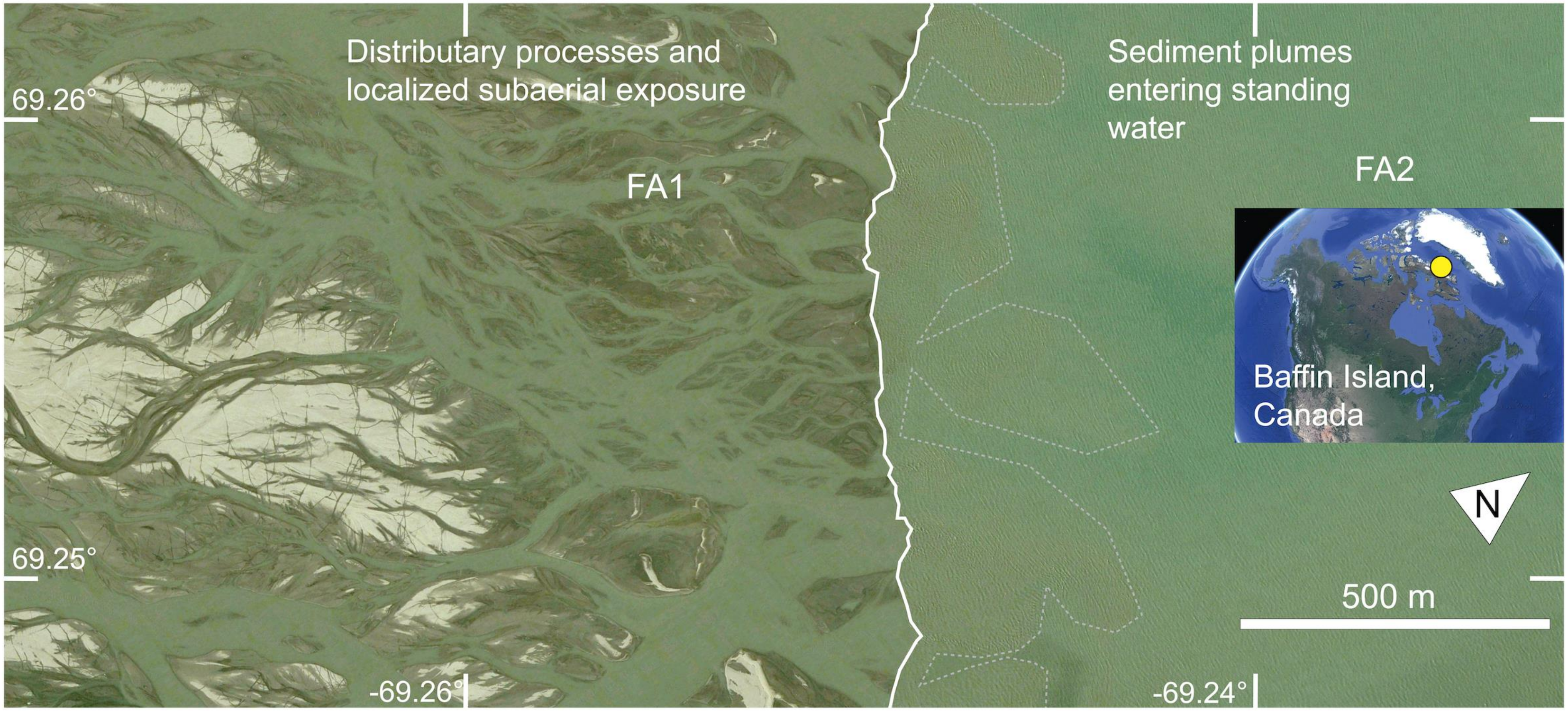

Figure 2.8 Distal braid plain environment adjacent to a subaqueous basin on the coast of Baffin Island. Certain characteristics of facies and depositional processes along the braid plain (distributary channels, subaerial exposure, proximity to base level) and within the basin (suspension fallout from lofted plumes) are interpreted as analogous to aspects of the processes and environments interpreted from SIm facies. Image from Google™ Earth.

that may be influenced by the water level in the adjacent basin. Channel avulsion facilitates channel abandonment, which can cause subaerial exposure and reworking of sediments similar to the exposed regions in Figure 2.8 (Muhlbauer & Fedo, 2020; Syvitski , 2012). Meter-scale cracks are visible on the subaerially exposed regions, illustrating localized exposure and possible desiccation similar to the Old Soaker region (Figure 2.7c), though it is noted that the cracks in this specific analogue example are larger in scale and may represent seasonal freezing and thawing as opposed to desiccation (e.g., Syvitski et al., 1987). Channel abandonment and development of regions of stagnant, ponded water along the delta plain provide a plausible explanation for the deposition of relatively thicker intervals of planar-laminated mudstone within FA1 (MacNaughton et al., 1997). Overall, the sedimentary processes responsible for deposition of FA1 strata are consistent with aspects of the distal plain setting depicted in Figure 2.8, characterized by autogenic processes facilitating shifting subenvironments along lake and marine margins (Muhlbauer & Fedo, 2020).

Facies association 2

Facies association 2 (FA2) comprises the middle part of the SIm, which is approximately 42 m thick and extends from approximately -4333 to -4291 m (Figures 2.2 & 2.3). Exposures in FA2 exhibit an increased degree of erosion and fracturing relative to exposures in both intervals of FA1 (Figure 2.1c). The FA2 succession is characterized by one facies detailed below. Key outcrop exposures of FA2 shown in Figure 2.9 are noted in the map in Figure 2.1 and the stratigraphic column in Figure 2.3.

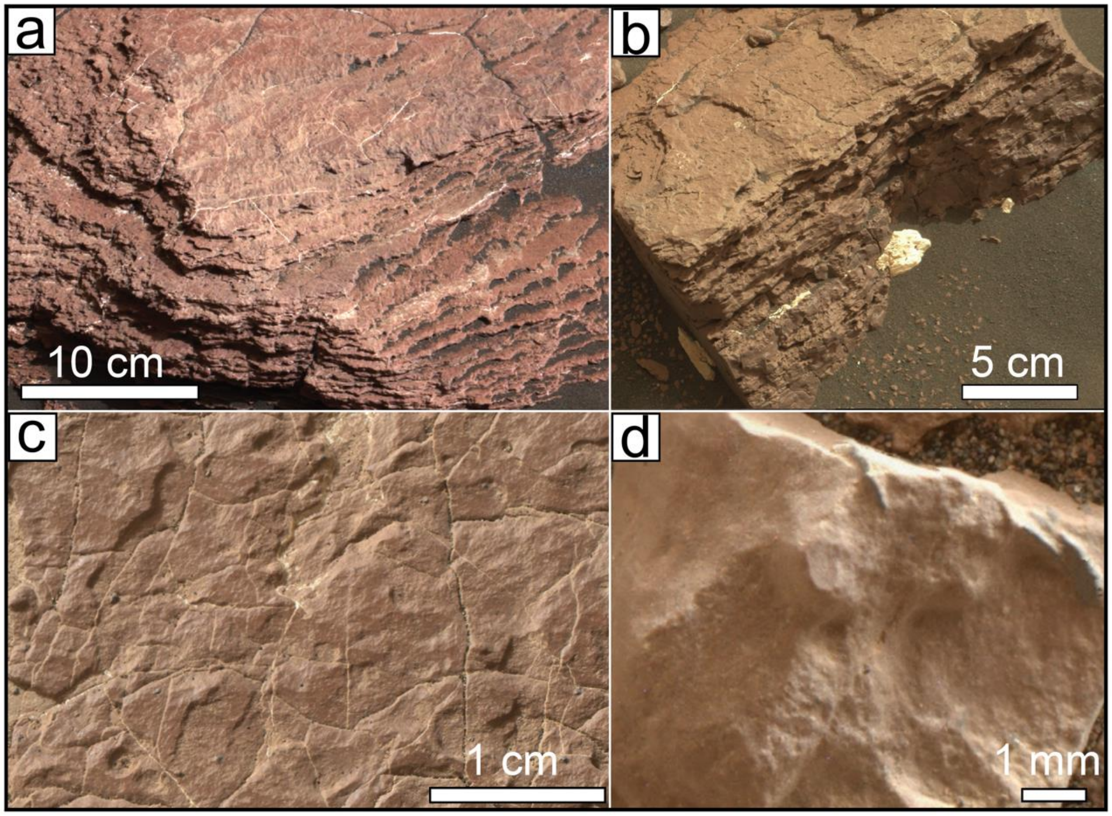

Figure 2.9 Representative outcrops of the planar-laminated mudstone with minor sandstone facies in FA2. (a) Outcrop Dead River depicting a continuous interval of planar laminae with relatively sharper boundaries (M100 Mastcam mosaic, mcam08119, Sol 1593). (b) Outcrop Grand Pitch showing more subtle laminae boundaries and exhibiting a more polished surface texture (M100 Mastcam image, mcam08432, Sol 1632). (c) Smooth surface texture indicative of the mudstone lithology in FA2 (MAHLI ID: mhli00306, Sol 1634). (d) Example of minor sandstone exposures observed in target Morancy Stream showing visible sand grains (MAHLI ID: mhli00171, Sol 1668). Image credit: NASA/JPL-Caltech/MSSS.

Planar-laminated mudstone with minor sandstone facies: description

Exposures of planar-laminated mudstone with minor interbeds of sandstone comprise the entirety of FA2 (Figures 2.3 & 2.9), representing 42% of total measured SIm stratigraphy. Planar laminations are laterally continuous across the E-W rover traverse of ~98 m, at the elevation range of -4310 to -4314 m (Sol 1598-1611; Figure 2.1c). Continuity along this lateral part of the traverse along similar elevations suggests that mudstone facies generally extend beyond the region of the rover traverse at other stratigraphic elevations.

Outcrops of this facies are defined by continuous intervals of millimeter-thick horizontal planar laminae (Figure 2.9). One measured target (Dead River, Sol 1593) consists of sub-mm- to mm-scale laminae with an average measured thickness of 0.66 mm (Table 2.1). Where large image standoff distances or oblique outcrop angles preclude thickness measurements, visual assessments suggest that laminae are generally mm-scale (Fig. 2.9). Individual laminae boundaries are defined by differences in resistance to erosion. Boundaries vary from sharp (Figure 2.9a) to subtle (Figure 2.9b). Crinkly or nodular surface textures in cross-section or plan-view (e.g., Figure 2.9a) likely represent some amount of diagenetic overprinting. The lack of visible grain boundaries and the smooth textures across the majority of this facies support a mud grain-size interpretation (Figure 2.9c). A mudstone lithology is also supported by GIMS data for this facies, which suggest grains within the clay and silt (mud) size fraction (Rivera-Hernández et al., 2020).

Sandstone was identified at three stratigraphic intervals within FA2 (Figures 2.3 & 2.9d). Limited image coverage over these intervals precludes identification of boundaries and measurements of exact stratigraphic thickness, though minimum constraints from imaged portions suggest that exposures are at least cm-scale in thickness. Evidence for sandstone interbeds includes visible grains within the very-fine to fine size-range (Figure 2.9d).

Planar-laminated mudstone with minor sandstone facies: interpretation

The thickness of this facies and interpreted fine grain size indicates subaqueous deposition via suspension fallout in a low-energy environment. Continuous intervals of fine-grained, millimeter-thick laminae are characteristic of deposition influenced by subtle, episodic changes in sediment supply or flow strength (Anderson & Dean, 1988; Zolitschka et al., 2015). Minor intervals of increased grain size are interpreted to represent changes in the current velocity that carried sediment, but such fluctuations were likely relatively minor.

Depositional interpretation of FA2

The succession of mudstone laminae comprising FA2 is interpreted to represent deposition in a lake basin setting. Deposition of fine-grained mm-thick laminae into a lake basin commonly occurs via sediment density flows (i.e., hyper-, homo, and hypopycnal processes; Boulesteix et al., 2019; Zavala et al., 2021; Zavala & Pan, 2018). As an incoming flow enters a standing body of water of lesser density, sediment in the river discharge will plunge and travel basinward along the basin floor (hyperpycnal). Incoming flows whose density is equal to that of the standing body of water will cause sediment to rapidly collapse, generating Gilbert-Type deltas (homopycnal). Incoming flows whose density is lower than that of the standing body of water will result in rapid deceleration and loss of confinement of discharge, with coarse-grained material deposited proximal to the river mouth and fine-grained material entrained in plumes (hypopycnal).

The mudstone facies of FA2 exhibits similar characteristics as planar-laminated mudstone facies interpreted in other Murray formation members to represent deposition in lake settings facilitated by density flows (Edgar et al., 2020; Gwizd et al., 2022; Stack et al., 2019), lending support to such an interpretation for FA2. Punctuated intervals of sandstone signify short-lived increases in flow energy, but the lack of any associated flow structures indicates that intervals broadly correlate with deposition in similarly distal regions of the basin. The generally fine-grained component of FA2 facies suggests that deposition occurred at a distal location within the lake basin relative to the sediment entry point into the lake (Boulesteix et al., 2019).

Of the different density flows, the most likely flow classification for deposition of FA2 is hyperpycnal. Continuity of mudstone strata across the lateral portion of the rover traverse (98 m) is consistent with both hyper- or hypopycnal flow deposits, which can extend laterally across substantial distances (Zavala et al., 2006); however, the lower density of a hypopycnal flow relative to the density of water in the basin facilitates formation of steep prodelta deposits proximal to the shoreline (Rajchl et al. 2008; Zavala et al., 2021) that are not recorded in SIm stratigraphy. Hyperpycnal flows can generate lofted plumes that carry fine-grained sediment to more distal regions (reaching distances of up to 100's of km within larger brackish lakes or marine basins) within a basin upon settling of coarser-grained components of the suspended load from a jet. The absence of deposits indicative of steep gradients and the predominance of mud laminae within FA2 suggests that lacustrine facies in FA2 represent the influence of hyperpycnal flow processes involving suspension setting of lofted material. Figure 2.8 depicts the formation of plumes within a subaqueous basin facilitated by subaqueous input of sediment from the delta plain environment. The inundation of the distal delta plain from flooding within the basin highlights the connection between deltaic and lacustrine sedimentary environments, characterized by continuous sediment input into the basin. Similar conditions are interpreted to facilitate deposition of the thick succession of mudstone laminae in FA2.

Several observations indicate that the lake was characterized by standing water that persisted throughout deposition of FA2. Thickness and homogeneity of mudstone facies across the entire FA2 interval indicates that the relative balance between sedimentation and lake level, primary controls over accommodation space (Bohacs et al., 2000), had to be sufficient enough to allow for accumulation of mudstone throughout the 42 m interval. Additional evidence is shown through the relatively minor changes in grain size and the lack of evidence for any localized or widespread subaerial exposure, suggesting that the lake basin was characterized by the continued presence of standing water. The absence of structures indicative of wave influence suggests that laminae formed below wave base (Peters & Loss, 2012). Given the facies characteristic of FA2 and the association with the marginal delta plain environments of FA1 (see section "Depositional interpretation of FA1"), the lake environment represented by FA2 stratigraphy is most consistent with hydrologically open lakes (overfilled).

Collectively, FA2 characteristics do not support a playa lake setting (e.g. Hardie et al., 1978), which has been proposed to explain stratigraphic intervals of high calcium- and magnesium-sulfate (Rapin et al., 2019). Magnesium-sulfate enrichments do not appear to be primary depositional features, but rather cross-cut stratigraphy, consistent with a diagenetic origin (Gwizd et al., Chapter 3). A playa lake setting (e.g. Hardie et al., 1978) has been proposed to explain stratigraphic intervals of high calcium- and magnesium-sulfate (Rapin et al, 2019). Where sulfate enrichments do not correspond to obvious diagenetic features (e.g., veins, concretions), Achilles et al. (2020) and Bristow et al. (2021) have interpreted that enrichments are generally more consistent with a diagenetic origin rather than evaporite deposits. Continuous intervals of mudstone facies in FA2 are most consistent with interpretations of mudstone in underlying and overlying Murray formation members (Edgar et al., 2020; Fedo et al., 2022; Gwizd et al., 2022; Stack et al., 2019), and extend the continuity of the ancient lake systems at Gale crater.

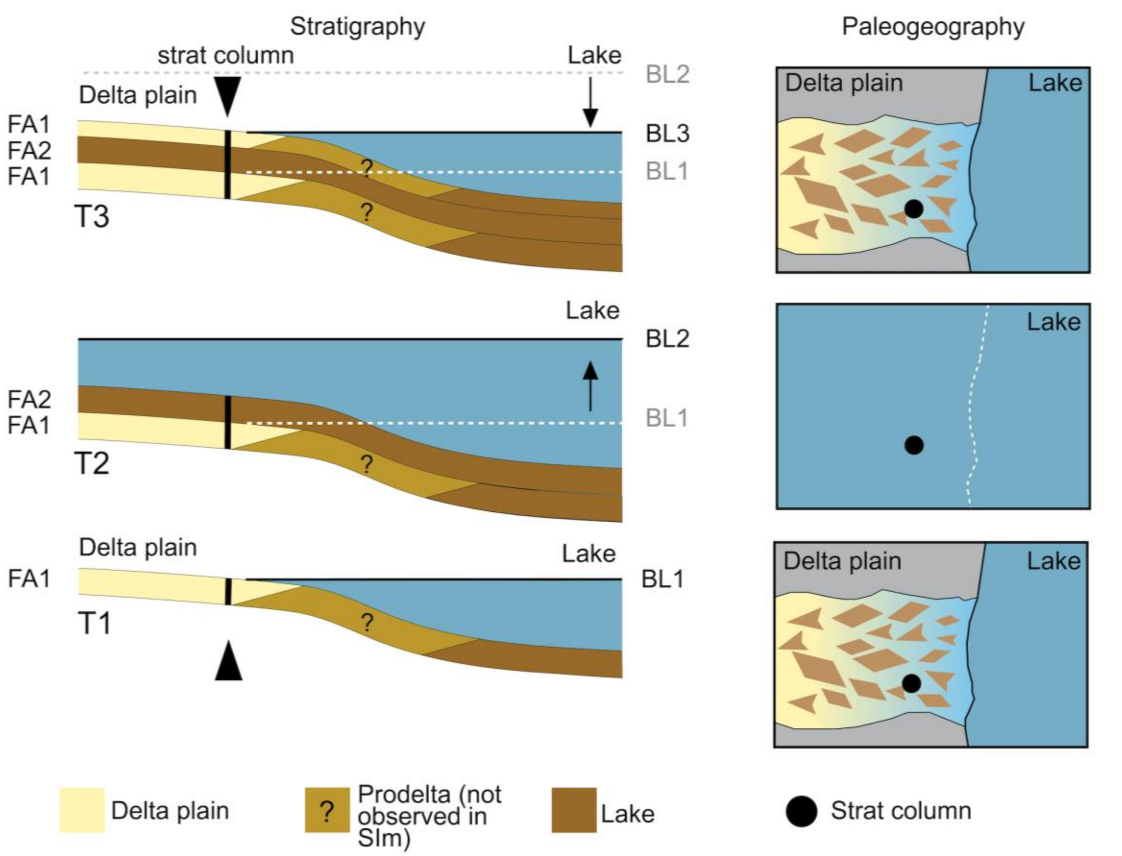

Figure 2.10 Model showing the stratigraphic and paleogeographic evolution of facies the delta plain and lacustrine environments recorded in FA1 and FA2. Time 1 (T1) shows deposition of distal delta plain facies near base level. Time 2 (T2) shows deposition of FA2 and represents a transition in the column between delta plain and lake basin facies due to a rapid transgression. Finally, deposition of the uppermost interval of FA1 at Time 3 (T3) is interpreted as an abrupt regression and an associated basinward shift of the lake margin facies of FA2.

Stratigraphic synthesis and implications for the evolution of the ancient lake shoreline

The transitions between FA1 and FA2 recorded in the SIm stratigraphy provide a unique opportunity in the Murray formation to assess characteristics of the shifting lake-margin and lake environments. Contacts between individual facies and the facies associations are mostly not observable, but estimates on the relative extent of shifting environments and on possible causes behind stratigraphic transitions can be constrained through the distribution of facies associations throughout the SIm.

Figure 2.10 shows the stratigraphic and paleogeographic progression of the environments throughout deposition of the lowermost interval of FA1, FA2, and the uppermost interval of FA1. At time 1 (T1 in Figure 2.10), distal delta plain facies are deposited adjacent to the lake margin at base level, where energy is minimal and conducive to deposition of mud. The predominance of mudstone and overall fine-grained nature of FA1 suggests that the delta plain environments captured in the stratigraphic column at T1 occur essentially at base level, adjacent to the shoreline (Figure 2.8). Deposition of FA2 at time 2 (T2) represents an abrupt transition between delta plain and lake basin facies as a result of transgression. Finally, deposition of the uppermost interval of FA1 at time 3 (T3) is interpreted as a regression and an associated basinward shift of the lake margin facies of FA2.

The transition between the lowermost interval of FA1 to FA2 (Figures 2.3 & 2.10) indicates a substantial shift in environments from delta plain to lake settings. The lack of any transitional deltaic deposits (e.g. clinoforms) linking the underlying delta plain environment of FA1 with the lake environment of FA2 suggests that a transgression would have been rapid and significant enough to flood the delta plain facies and bypass deposition of any potential deltaic clinoforms (T2 in Figure 2.10). Subsequently, the transition between FA2 and the upper interval of FA1 is interpreted as a forced regression characterized by base-level fall (Cataneau et al., 2005) that facilitated deposition of the uppermost interval of FA1 over FA2.

Transgressions and regressions indicative of lake level change can be climate- or tectonic-induced (Bohacs et al., 2000; Ilgar & Nemec, 2005). Gale crater, as an impact basin, has no mechanism to produce long term tectonic subsidence, especially later in its history following the decay of impact-related thermal anomalies and deposition of several kilometers of sediment (Grotzinger et al., 2015). However, several studies have utilized geochemistry and sedimentology to interpret aspects of the ancient climate represented by the Murray formation (e.g., Gwizd et al., 2022; Mangold et al., 2019). Geochemical trends and calculated weathering indices derived from ChemCam data show a progressive increase in chemical weathering through the SIm stratigraphy (Mangold et al., 2019). An exact characterization of climate conditions cannot be ascertained solely from weathering indices, as additional factors (e.g., topography, source rock) also affect the geochemical record of weathering (Johnsson, 1993). Nevertheless, the notable increase in weathering likely suggests some component of shifting aqueous activity throughout the ancient landscape, which may correspond to the transgression observed between FA1 and FA2 and possibly facilitate the regression between FA2 and the uppermost interval of FA1. Future work (Chapter 3) will aim to assess links between the compositional record of sedimentary processes (source, weathering, transport, diagenesis) and facies identified in this study in order to further understand driving controls behind the intervals of transgression and regression recorded in the SIm.

Summary

This study presents detailed facies associations and a stratigraphic compilation for the 95-m-thick Sutton Island member from which the depositional history and evolution of the ancient lake margin is interpreted. Two facies associations were identified within the stratigraphy and include (a) Facies Association 1 and (b) Facies Association 2. Facies Association 1 comprises the lowermost (39 m) and uppermost (14 m) intervals of stratigraphy, and consists of a diverse assemblage of facies that represent subaerial and subaqueous delta plain subenvironments. Facies in Association 1 primarily represent deposition in a delta plain environment characterized by distributary systems, ponded water, and localized subaerial exposure facilitating sediment desiccation and reworking. The variable facies and overall fine grain size are consistent with deposition in a distal delta plain setting. Facies Association 2 includes the middle (42 m) interval of Sutton Island stratigraphy and is comprised of planar-laminated mudstone. Mudstone facies in Facies Association 2 are interpreted to represent deposition in a lacustrine environment characterized by sufficient standing water to allow for deposition of the entire interval.

Stratigraphic transitions between delta plain to lake and back to delta plain facies associations are indicative of episodes of lake expansion (transgression) and contraction (regression). The transition between delta plain environment of Facies Association 1 and the lake environment of Facies Association 2 represents a transgression that drowned delta plain environments and shifted the lake margin. The transition between Facies Association 2 and the uppermost interval of Facies Association 1 likely signifies a forced regression. Large-scale lake level shifts may result from a combination of factors, including aspects of climate. Collectively, the facies associations and stratigraphic record of the Sutton Island member represent the prevalence of aqueous environments within the ancient landscape. Such environments are consistent with the continued presence of water characteristic of environments recorded in the ancient Murray formation.

References

Achilles, C. N., Rampe, E. B., Downs, R. T., Bristow, T. F., Ming, D. W., Morris, R. V., et al. (2020). Evidence for multiple diagenetic episodes in ancient fluvial-lacustrine sedimentary rocks in Gale crater, Mars. *Journal of Geophysical Research: Planets*, *125*(8), e2019JE006295. https://doi.org/10.1029/2019JE006295

Allen, J. R. L. (1962). Asymmetrical ripple marks and the origin of cross-stratification. *Nature*, *194*(4824), 167-169. https://doi.org/10.1038/194167a0

Ashley, G. M. (1990). Classification of large-scale subaqueous bedforms; a new look at an old problem. *Journal of Sedimentary Research*, *60*(1), 160-172. https://doi.org/10.2110/jsr.60.160

Baas, J. H. (1994). A flume study on the development and equilibrium morphology of current ripples in very fine sand. *Sedimentology*, *41*(2), 185-209. https://doi.org/10.1111/j.1365-3091.1994.tb01400.x

Banham, S. G., Gupta, S., Rubin, D. M., Edgett, K. S., Barnes, R., Van Beek, J., et al. (2021). A rock record of complex Aeolian bedforms in a hesperian desert landscape: The Stimson formation as exposed in the Murray Buttes, Gale Crater, Mars. *Journal of Geophysical Research: Planets*, *126*(4). https://doi.org/10.1029/2020je006554

Bhattacharya, J. P. (2010). Deltas. *In: Facies Models*. Eds. Dalrymple, R. & James, N.), *4*, 233-264.

Blair, T. C., & McPherson, J. G. (2008). Quaternary sedimentology of the Rose Creek fan delta, Walker Lake, Nevada, USA, and implications to fan-delta facies models. *Sedimentology*, *55*(3), 579-615. https://doi.org/10.1111/j.1365-3091.2007.00913.x

Bohacs, K. M., Carroll, A. R., Neal, J. E., & Mankiewicz, P. J. (2000). Lake-basin type, source potential, and hydrocarbon character: an integrated sequence-stratigraphic-geochemical framework. *Lake basins through space and time: AAPG Studies in Geology*, 46, 3-34.

Boulesteix, K., Poyatos-Moré, M., Flint, S. S., Taylor, K. G., Hodgson, D. M., & Hasiotis, S. T. (2019). Transport and deposition of mud in deep-water environments: Processes and stratigraphic implications. *Sedimentology*, *66*(7), 2894-2925. https://doi.org/10.1111/sed.12614

Bristow, T. F., Grotzinger, J. P., Rampe, E. B., Cuadros, J., Chipera, S. J., Downs, G. W., et al. (2021). Brine-driven destruction of clay minerals in Gale crater, Mars. *Science*, *373*(6551), 198-204. https://doi.org/10.3390/min11080847

Calef, III, F. J., Abarca, H. E., Soliman, T., Abercrombie, S. P., & Powell, M. W. (2019). Multi-mission geographic information system: An open-source solution for planetary science operations. In the 4th Planetary Data Workshop, Abstract #7071.

Calef III, F. J., Gengl, H. E., Soliman, T., Abercrombie, S. P., & Powell, M. W. (2017). MMGIS: A multi-mission geographic information system for in situ Mars operations. In the 48th Lunar and Planetary Science Conference, Abstract #2541.

Calef, III, F. J., Abarca, H. E., Soliman, T., Abercrombie, S. P., & Powell, M. W. (2019). Multi-mission geographic information system: An open-source solution for planetary science operations. In the 4th Planetary Data Workshop, Abstract #7071.

Calef III, F. J., Gengl, H. E., Soliman, T., Abercrombie, S. P., & Powell, M. W. (2017). MMGIS: A multi-mission geographic information system for in situ Mars operations. In the 48th Lunar and Planetary Science Conference, Abstract #2541.

Calef III, F. J., & Parker, T. (2016). MSL Gale Merged Orthophoto Mosaic, Publisher: PDS Annex, U.S. Geological Survey. http://bit.ly/MSL_Basemap

Caravaca, G., Mangold, N., Dehouck, E., Schieber, J., Zaugg, L., Bryk, A. B., et al. (in press) From Lake to River: Documenting an Environmental Transition across the Jura/Knockfarril Hill Members Boundary in the Glen Torridon Region of Gale crater (Mars). *Journal of Geophysical Research: Planets*, https://doi.org/10.1029/2021JE007093

Catuneanu, O., Martins-Neto, M. A., & Eriksson, P. G. (2005). Precambrian sequence stratigraphy. *Sedimentary Geology*, *176*(1-2), 67-95. https://doi.org/10.1016/j.sedgeo.2004.12.009

Colombera, L., & Mountney, N. P. (2019). The lithofacies organization of fluvial channel deposits: a meta-analysis of modern rivers. *Sedimentary Geology*, *383*, 16-40. https://doi.org/10.1016/j.sedgeo.2019.01.011

Cosgrove, J. W., Banham, S. G., Gupta, S., & Barnes, R. (2022). The origin of the fracture networks in the mudstones of Gale crater Mars; their implications regarding the state of stress and fluid pressure during their formation and the depth to which they were buried. *Journal of Geophysical Research: Planets*. https://doi.org/10.1029/2022JE007313

Edgar, L. A., Fedo, C. M., Gupta, S., Banham, S. G., Fraeman, A. A., Grotzinger, J. P., et al. (2020). A lacustrine paleoenvironment recorded at Vera Rubin ridge, Gale crater: Overview of the sedimentology and stratigraphy observed by the Mars science laboratory Curiosity rover. *Journal of Geophysical Research: Planets, 125*(3). https://doi.org/10.1029/2019je006307

Edgar, L. A., Grotzinger, J. P., Bell III, J. F., & Hurowitz, J. A. (2014). Hypotheses for the origin of fine-grained sedimentary rocks at Santa Maria crater, Meridiani Planum. Icarus, 234, 36-44. https://doi.org/10.1016/j.icarus.2014.02.019

Edgar, L. A., Gupta, S., Rubin, D. M., Lewis, K. W., Kocurek, G. A., Anderson, R. B., et al. (2017). Shaler: in situ analysis of a fluvial sedimentary deposit on Mars. *Sedimentology*, *65*(1), 96-122. https://doi.org/10.1111/sed.12370

Edgett, K. S. (2013a). MSL MARS HAND LENS IMAGER 2 EDR IMAGE V1.0 [Data set]. NASA Planetary Data System. https://doi.org/10.17189/1520187

Edgett, K. S. (2013b). MSL MARS HAND LENS IMAGER 2 EDR ZSTACK V1.0 [Data set]. NASA Planetary Data System. https://doi.org/10.17189/1520396

Edgett, K. S., Banham, S. G., Bennett, K. A., Edgar, L. A., Edwards, C. S., Fairén, A. G., et al., (2020). Extraformational sediment recycling on Mars. *Geosphere*, *16*(6), 1508-1537. https://doi.org/10.1130/GES02244.1

Edgett, K. S., Yingst, R. A., Ravine, M. A., Caplinger, M. A., Maki, J. N., Ghaemi, F. T., et al. (2012). Curiosity's Mars hand lens imager (MAHLI) investigation. *Space science reviews*, *170*(1), 259-317. https://doi.org/10.1007/s11214-012-9910-4

Eibl, M. A. (2016). A Textural Image Analysis Study of Mars-Analog Sediment: Comparisons of 2D and 3D Textural Analysis Methods, Image Resolution, and the Effects of Shadows (Master's thesis). Retrieved from TRACE. (http://trace.tennessee.edu). Knoxville, TN: University of Tennessee

El-Maarry, M. R., Watters, W. A., Yoldi, Z., Pommerol, A., Fischer, D., Eggenberger, U., & Thomas, N. (2015). Field investigation of dried lakes in western United States as an analogue to desiccation fractures on Mars. *Journal of Geophysical Research: Planets*, *120*(12), 2241-2257. https://doi.org/10.1002/2015JE004895

Escavy, J. I., & Herrero, M. J. (2019). Enterolithic folds in evaporites as microbially induced sedimentary structures: New model of formation and interpretation in the geological record. *Sedimentology*, *66*(6), 2214-2233. https://doi.org/10.1111/sed.12588

Fedo, C. M., Bryk, A. B., Edgar, L. A., Bennett, K. A., Fox, V. K., Dietrich, W. E., et al. (2022). Geology and stratigraphic correlation of the Murray and Carolyn Shoemaker formations across the Glen Torridon region, Gale crater, Mars. *Journal of Geophysical Research: Planets*. https://doi.org/10.1029/2022JE007408

Fedo, C.M., Grotzinger, J. P., Gupta, S., Banham, S., Bennett, K., Edgar, L. A., et al. (2019). Evidence for persistent, water-rich lacustrine deposition preserved in the Murray formation, Gale crater: A depositional system suitable for sustained habitability. *Presented at the Ninth International Conference on Mars.* Retrieved from. https://www.hou.usra.edu/meetings/ninthmars2019/pdf/6308.pdf

Fedo, C. M., Grotzinger, J., Gupta, S., Fraeman, A., Edgar, L., Edgett, K., et al. (2018). Sedimentology and stratigraphy of the Murray formation, Gale crater, Mars. In the 49th Lunar and Planetary Science Conference, Abstract #2083.

Fedo, C. M., Grotzinger, J. P., Schieber, J., Gupta, S., House, C. H., Edgett, K. S., et al. (2018). Things are not always as they seem: Detangling intersecting planar and curvi-planar veins and fractures from primary bedding in the Vera Rubin ridge member, Murray formation, Mars. *Geological Society of America Abstracts with Programs*, *50(3).* https://doi.org/10.1130/abs/2018SE-312748

Fedo, C. M., McGlynn, I. O., & McSween Jr, H. Y. (2015). Grain size and hydrodynamic sorting controls on the composition of basaltic sediments: Implications for interpreting Martian soils. *Earth and Planetary Science Letters*, *423*, 67-77. https://doi.org/10.1016/j.epsl.2015.03.052

Gislason, S. R., & Oelkers, E. H. (2003). Mechanism, rates, and consequences of basaltic glass dissolution: II. An experimental study of the dissolution rates of basaltic glass as a function of pH and temperature. *Geochimica et Cosmochimica Acta*, *67*(20), 3817-3832. https://doi.org/10.1016/S0016-7037(03)00176-5

Grotzinger, J. P., Arvidson, R. E., Bell III, J. F., Calvin, W., Clark, B. C., Fike, D. A., et al. (2005). Stratigraphy and sedimentology of a dry to wet eolian depositional system, Burns formation, Meridiani Planum, Mars. *Earth and Planetary Science Letters*, *240*(1), 11-72. https://doi.org/10.1016/j.epsl.2005.09.039

Grotzinger, J., Bell III, J., Herkenhoff, K., Johnson, J., Knoll, A., McCartney, E., et al. (2006). Sedimentary textures formed by aqueous processes, Erebus crater, Meridiani Planum, Mars. *Geology*, *34*(12), 1085-1088. https://doi.org/10.1130/G22985A.1

Grotzinger, J. P., Crisp, J., Vasavada, A. R., Anderson, R. C., Baker, C. J., Barry, R., et al., (2012). Mars Science Laboratory mission and science investigation. *Space science reviews*, *170*(1), 5-56. https://doi.org/10.1007/s11214-012-9892-2

Grotzinger, J. P., Gupta, S., Malin, M. C., Rubin, D. M., Schieber, J., Siebach, K., et al. (2015). Deposition, exhumation, and paleoclimate of an ancient lake deposit, Gale crater, Mars. *Science, 350(*6257). https://doi.org/10.1126/science.aac.7575

Grotzinger, J. P., Hayes, A. G., Lamb, M. P., & McLennan, S. M. (2013). Sedimentary processes on Earth, Mars, titan, and Venus. In: *Comparative climatology of terrestrial planets*, *1*, 439-472. DOI: 10.2458/azu_uapress_9780816530595-ch18.

Grotzinger, J. P., Sumner, D. Y., Kah, L. C., Stack, K., Gupta, S., Edgar, L., et al. (2014). A habitable fluvio-lacustrine environment at Yellowknife Bay, Gale crater, Mars. *Science*, *343*(6169), 1242777. https://doi.org/10.1126/science.1242777

Gwizd, S., Fedo, C., Grotzinger, J., Banham, S., Rivera-Hernández, F., Stack, K. M., et al. (2022). Sedimentological and Geochemical Perspectives on a Marginal Lake Environment Recorded in the Hartmann's Valley and Karasburg Members of the Murray Formation, Gale Crater, Mars. *Journal of Geophysical Research: Planets*, *127*(8). https://doi.org/10.1029/2022JE007280

Gwizd, S., Fedo, C., Grotzinger, J., Edgett, K., Rivera-Hernández, F., Stein, N. (2018). Depositional history of the Hartmann's Valley member, Murray formation, Gale crater, Mars. In the 49th Lunar and Planetary Science Conference, Abstract #2150.

Hadlari, T., Rainbird, R. H., & Donaldson, J. A. (2006). Alluvial, eolian and lacustrine sedimentology of a Paleoproterozoic half-graben, Baker Lake Basin, Nunavut, Canada. *Sedimentary Geology*, *190*(1-4), 47-70. https://doi.org/10.1016/j.sedgeo.2006.05.005

Handford, C. R. (1982). Sedimentology and evaporite genesis in a Holocene continental-sabkha playa basin—Bristol Dry Lake, California. *Sedimentology*, *29*(2), 239-253. https://doi.org/10.1111/j.1365-3091.1982.tb01721.x

Hardie, L. A., Smoot, J. P., & Eugster, H. P. (1978). Saline lakes and their deposits: a sedimentological approach. *Modern and ancient lake sediments*, 7-41. https://doi.org/10.1002/9781444303698.ch2

Harms, J. C. (1969). Hydraulic significance of some sand ripples. *Geological Society of America Bulletin*, *80*(3), 363-396. https://doi.org/10.1130/0016-7606(1969)80[363:HSOSSR]2.0.CO;2

Hunter, R. E. (1985). Subaqueous sand-flow cross strata. *Journal of Sedimentary Research*, *55*(6), 886-894. https://doi.org/10.1306/212F8832-2B24-11D7-8648000102C1865D

Ibarra, D. E., Caves, J. K., Moon, S., Thomas, D. L., Hartmann, J., Chamberlain, C. P., & Maher, K. (2016). Differential weathering of basaltic and granitic catchments from concentration–discharge relationships. *Geochimica et Cosmochimica Acta*, *190*, 265-293. https://doi.org/10.1016/j.gca.2016.07.006

Ilgar, A., & Nemec, W. (2005). Early Miocene lacustrine deposits and sequence stratigraphy of the Ermenek Basin, Central Taurides, Turkey. *Sedimentary Geology*, *173*(1-4), 233-275. https://doi.org/10.1016/j.sedgeo.2003.07.007

Johnsson, M.J. (1993). The system controlling the composition of clastic sediments. *In: Processes Controlling the Composition of Clastic Sediments*, *Geological Society of America Special Paper* (Eds. Johnsson, M.J. & Basu, A.), *284*, 1-19.

Lazar, O. R., Bohacs, K., Schieber, J., Macquaker, J. H. S., & Demko, T. (2015). Mudstone Primer: Lithofacies Variations, Diagnostic Criteria, and Sedimentological/stratigraphical Implications at Lamina to Bedset Scale. *SEPM Concepts in Sedimentology and Paleontology*, *12*.

Lemons, D. R., & Chan, M. A. (1999). Facies architecture and sequence stratigraphy of fine-grained lacustrine deltas along the eastern margin of late Pleistocene Lake Bonneville, northern Utah and southern Idaho. *AAPG bulletin*, *83*(4), 635-665. https://doi.org/10.1306/00AA9C14-1730-11D7-8645000102C1865D

MacNaughton, R. B., Dalrymple, R. W., & Narbonne, G. M. (1997). Early Cambrian braid-delta deposits, MacKenzie Mountains, north-western Canada. *Sedimentology*, *44*(4), 587-609. https://doi.org/10.1046/j.1365-3091.1997.d01-41.x

Magalhães, A. J. C., Scherer, C. M. S., Gabaglia, G. R., & Catuneanu, O. (2015). Mesoproterozoic delta systems of the Açuruá Formation, Chapada Diamantina, Brazil. *Precambrian Research*, *257*, 1-21. https://doi.org/10.1016/j.precamres.2014.11.016

Maki, J., Thiessen, D., Pourangi, A., Kobzeff, P., Litwin, T., Scherr, L., et al. (2012). The Mars Science Laboratory engineering cameras. *Space Science Reviews*, *170*(1-4), 77–93. https://doi.org/10.1007/s11214-012-9882-4

Malin, M. C. (2007). MRO CONTEXT CAMERA EXPERIMENT DATA RECORD LEVEL 0 V1.0 [Data set]. NASA Planetary Data System. https://doi.org/10.17189/1520266

Malin, M. C. (2013). MSL MARS MAST CAMERA 2 EDR IMAGE V1.0 [Data set]. NASA Planetary Data System. https://doi.org/10.17189/1520190

Malin, M. C., Ravine, M. A., Caplinger, M. A., Ghaemi, F. T., Schaffner, J. A., Maki, J. N., et al. (2017). The Mars Science Laboratory (MSL) Mast cameras and Descent imager: Investigation and instrument descriptions. *Earth and Space Science, 4*, 506–539. https://doi.org/10.1002/2016EA000252

Mangold, N., Dehouck, E., Fedo, C., Forni, O., Achilles, C., Bristow, T., et al. (2019). Chemical alteration of fine-grained sedimentary rocks at Gale crater. *Icarus, 321*, 619–631. https://doi.org/10.1016/j.icarus.2018.11.004

Mangold, N., Gupta, S., Gasnault, O., Dromart, G., Tarnas, J. D., Sholes, S. F., et al. (2021). Perseverance rover reveals an ancient delta-lake system and flood deposits at Jezero crater, Mars. *Science*, *374*(6568), 711-717. https://doi.org/10.1126/science.abl4051

McEwen, A. S. (2005). MRO MARS HIGH RESOLUTION IMAGE SCIENCE EXPERIMENT EDR V1.0 [Data set]. NASA Planetary Data System. https://doi.org/10.17189/1520179

McEwen, A. S., Eliason, E. M., Bergstrom, J. W., Bridges, N. T., Hansen, C. J., Delamere, W. A., et al. (2007). Mars Reconnaissance Orbiter's high resolution imaging science experiment (HiRISE). *Journal of Geophysical Research, 112*, E05S02. https://doi.org/10.1029/2005JE002605

McKee, E.D., Crosby, E.J., & Berryhill, H.L. (1967). Flood deposits, Bijou Creek, Colorado, June 1965. *Journal of Sedimentary Research*, *37*(3), 829–851. https://doi.org/10.1306/74D717B2-2B21-11D7-8648000102C1865D

McKee, E. D., & Weir, G. W. (1953). Terminology for stratification and cross-stratification in sedimentary rocks. *Geological Society of America Bulletin*, *64*(4), 381-390. https://doi.org/10.1130/0016-7606(1953)64[381:TFSACI]2.0.CO;2

McLennan, S. M., Grotzinger, J. P., Hurowitz, J. A., & Tosca, N. J. (2019). The sedimentary cycle on early Mars. *Annual Review of Earth and Planetary Sciences*, *47*, 91-118. doi:10.1146/annurev-earth-053018-060332

McPherson, J. G., Shanmugam, G., & Moiola, R. J. (1987). Fan-deltas and braid deltas: varieties of coarse-grained deltas. *Geological Society of America Bulletin*, *99*(3), 331-340. ttps://doi.org/10.1130/0016-7606(1987)99<331:FABDVO>2.0.CO;2

Muhlbauer, J. G., & Fedo, C. M. (2020). Architecture of a river-dominated, wave-and tide-influenced, pre-vegetation braid delta: Cambrian middle member of the Wood Canyon Formation, southern Marble Mountains, California, USA. *Journal of Sedimentary Research*, *90*(9), 1011-1036. https://doi.org/10.2110/jsr.2020.023

Nichols, G. J., & Fisher, J. A. (2007). Processes, facies and architecture of fluvial distributary system deposits. *Sedimentary geology*, *195*(1-2), 75-90. https://doi.org/10.1016/j.sedgeo.2006.07.004

Olariu, C., & Bhattacharya, J. P. (2006). Terminal distributary channels and delta front architecture of river-dominated delta systems. *Journal of sedimentary research*, *76*(2), 212-233. https://doi.org/10.2110/jsr.2006.026

Olariu, C., Zhou, C., Steel, R., Zhang, Z., Yuan, X., Zhang, J., et al. (2021). Controls on the stratal architecture of lacustrine delta successions in low-accommodation conditions. *Sedimentology*, *68*(5), 1941-1963. https://doi.org/10.1111/sed.12838

Orton, G. J., & Reading, H. G. (1993). Variability of deltaic processes in terms of sediment supply, with particular emphasis on grain size. *Sedimentology*, *40*(3), 475-512. https://doi.org/10.1111/j.1365-3091.1993.tb01347.x

Owen, A., Nichols, G. J., Hartley, A. J., Weissmann, G. S., & Scuderi, L. A. (2015). Quantification of a distributive fluvial system: the Salt Wash DFS of the Morrison Formation, SW USA. Journal of Sedimentary Research, 85(5), 544-561. https://doi.org/10.2110/jsr.2015.35

Peters, S. E., & Loss, D. P. (2012). Storm and fair-weather wave base: A relevant distinction?. *Geology*, *40*(6), 511-514. https://doi.org/10.1130/G32791.1

Pickering, K., Stow, D., Watson, M., & Hiscott, R. (1986). Deep-water facies, processes and models: a review and classification scheme for modern and ancient sediments. *Earth-Science Reviews*, *23*(2), 75-174. https://doi.org/10.1016/0012-8252(86)90001-2

Pontén, A., & Plink-Björklund, P. (2007). Depositional environments in an extensive tide-influenced delta plain, Middle Devonian Gauja Formation, Devonian Baltic Basin. *Sedimentology*, *54*(5), 969-1006. https://doi.org/10.1111/j.1365-3091.2007.00869.x

Rajchl, M., Uličný, D., & Mach, K. (2008). Interplay between tectonics and compaction in a rift-margin, lacustrine delta system: Miocene of the Eger Graben, Czech Republic. *Sedimentology*, *55*(5), 1419-1447. https://doi.org/10.1111/j.1365-3091.2008.00951.x

Rapin, W., Ehlmann, B. L., Dromart, G., Schieber, J., Thomas, N. H., Fischer, W. W., et al. (2019). An interval of high salinity in ancient Gale crater lake on Mars. *Nature Geoscience*, *12*(11), 889-895. https://doi.org/10.1038/s41561-019-0458-8

Rasband, W.S. (1997-2018). ImageJ, [software], U. S. National Institutes of Health, Bethesda, Maryland, USA, https://imagej.nih.gov/ij/

Reineck, H. E., & Singh, I. B. (1980). Current and wave ripples. In *Depositional Sedimentary Environments* (pp. 22-55). Springer, Berlin, Heidelberg.

Renaut, R. W., Gierlowski-Kordesch, E. H. (2010). Lakes. *In: Facies models* (Eds. Dalrymple, R. & James, N.) , *4*, 541-575

Rivera-Hernández, F., Sumner, D. Y., Mangold, N., Stack, K. M., Forni, O., Newsom, H., et al. (2019). Using ChemCam LIBS data to constrain grain size in rocks on Mars: Proof of concept and application to rocks at Yellowknife Bay and Pahrump Hills, Gale crater. Icarus, 321, 82–98. https://doi.org/10.1016/j.icarus.2018.10.023

Rivera-Hernández, F., Sumner, D. Y., Mangold, N., Banham, S. G., Edgett, K. S., Fedo, C. M., et al. (2020). Grain size variations in the Murray formation: Stratigraphic evidence for changing depositional environments in Gale crater, Mars. *Journal of Geophysical Research: Planets*, *125*(2), e2019JE006230. https://doi.org/10.1029/2019je006230

Rubin, D. M. (2012). A unifying model for planform straightness of ripples and dunes in air and water. *Earth-science reviews*, *113*(3-4), 176-185. https://doi.org/10.1016/j.earscirev.2012.03.010

Schieber, J., Bohacs, K. M., Coleman, M., Bish, D., Reed, M. H., Thompson, L., et al, (2022). Mars is a mirror–Understanding the Pahrump Hills mudstones from a perspective of Earth analogues. *Sedimentology*, *69*(6), 2371-2435. https://doi.org/10.1111/sed.13024

Shaw, J. B., & Mohrig, D. (2014). The importance of erosion in distributary channel network growth, Wax Lake Delta, Louisiana, USA. *Geology*, *42*(1), 31-34. https://doi.org/10.1130/G34751.1

Southard, J. B., & Boguchwal, L. A. (1973). Flume experiments on the transition from ripples to lower flat bed with increasing sand size. Journal of Sedimentary Research, 43(4), 1114-1121. https://doi.org/10.1306/74D72914-2B21-11D7-8648000102C1865D

Squyres, S. W., & Knoll, A. H. (2005). Sedimentary rocks at Meridiani Planum: Origin, diagenesis, and implications for life on Mars. *Earth and Planetary Science Letters*, *240*(1), 1-10. https://doi.org/10.1016/j.epsl.2005.09.038

Stack, K. M., Cofield, S. M., & Fraeman, A. A. (2017). Geologic map of the MSL Curiosity rover extended mission traverse of Aeolis Mons, Gale crater, Mars. In the 48th Lunar and Planetary Science Conference, Abstract #1889.

Stack, K. M., Grotzinger, J. P., Lamb, M. P., Gupta, S., Rubin, D. M., Kah, L. C., et al. (2019). Evidence for plunging river plume deposits in the Pahrump Hills member of the Murray formation, Gale crater, Mars. Sedimentology, 66(5), 1768–1802. https://doi.org/10.1111/sed.12558

Stein, N., Grotzinger, J. P., Schieber, J., Mangold, N., Hallet, B., Newsom, H., et al. (2018). Desiccation cracks provide evidence of lake drying on Mars, Sutton Island member, Murray formation, Gale crater. *Geology*, 46(6), 515–518. https://doi.org/10.1130/G40005

Syvitski, J. P., Burrell, D. C., & Skei, J. M. (1987). The Fluvial-Deltaic Environment. In *Fjords* (pp. 73-110). Springer, New York, NY.

Syvitski, J. P., Overeem, I., Brakenridge, G. R., & Hannon, M. (2012). Floods, floodplains, delta plains—a satellite imaging approach. *Sedimentary Geology*, *267*, 1-14. https://doi.org/10.1016/j.sedgeo.2012.05.014

Todd, S. (1996). Process deduction from fluvial sedimentary structures. In: *Advances in fluvial dynamics and stratigraphy*. Wiley, 1996.

Went, D. J. (2020). Fluvial shoal water deltas: pre-vegetation sedimentation through the fluvial–marine transition, Lower Cambrian, English Channel region. *Sedimentology*, *67*(1), 330-363. https://doi.org/10.1111/sed.12645

Wiens, R. C., Maurice, S., Barraclough, B., Saccoccio, M., Barkley, W. C., Bell, J. F., et al. (2012). The ChemCam instrument suite on the Mars Science Laboratory (MSL) rover: Body unit and combined system tests. *Space science reviews*, *170*(1), 167-227. https://doi.org/10.1007/s11214-012-9902-4

Williams, R. M. E., Grotzinger, J. P., Dietrich, W. E., Gupta, S., Sumner, D. Y., Wiens, R. C., et al. (2013). Martian fluvial conglomerates at Gale crater. *Science*, *340*(6136), 1068–1072. https://doi.org/10.1126/science.1237317

Zavala, C., & Pan, S. X. (2018). Hyperpycnal flows and hyperpycnites: Origin and distinctive characteristics. *Lithologic Reservoirs*, *30*(1), 1-27. https://doi.org/10.3969/j.issn.1673-8926.2018.01.001

Zavala, C., Arcuri, M., Di Meglio, M., Zorzano, A., Otharán, G., Irastorza, A., & Torresi, A. (2021). Deltas: a new classification expanding Bates's concepts. *Journal of Palaeogeography*, *10*(1), 1-15. https://doi.org/10.1186/s42501-021-00098-w

Zavala, C., Ponce, J. J., Arcuri, M., Drittanti, D., Freije, H., & Asensio, M. (2006). Ancient lacustrine hyperpycnites: a depositional model from a case study in the Rayoso Formation (Cretaceous) of west-central Argentina. *Journal of Sedimentary Research*, *76*(1), 41-59. https://doi.org/10.2110/jsr.2006.12

Appendix
Chapter 2 supplementary information

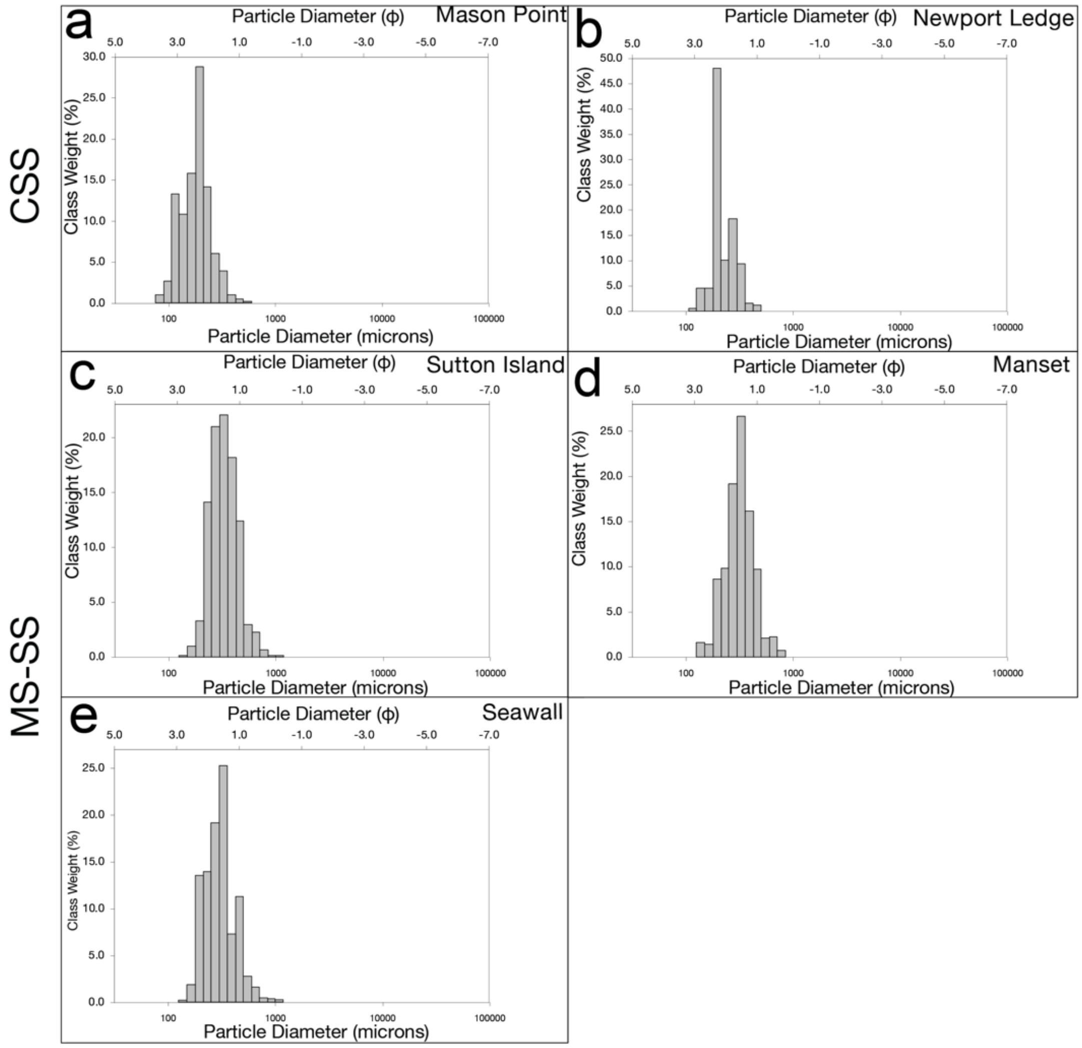

Figure 2.11 Grain size histograms showing measurements from two cross-stratified sandstone facies MAHLI images: (A) Mason_Point (Sol 1695, MAHLI ID: mhli00122) and (B) Newport_Ledge (Sol 1686, MAHLI ID: mhli00307), and three sandstone MAHLI images in the alternating laminated sandstone and mudstone facies: (C) Sutton_Island (Sol 1523, MAHLI ID: mhli00302) (D) Manset (Sol 1523, MAHLI ID: mhli00297) and D) Seawall (Sol 1523, MAHLI ID: mhli00646).

CHAPTER 3 : COMPOSITIONAL SIGNATURES OF SEDIMENT HISTORY RECORDED IN THE SUTTON ISLAND MEMBER OF THE MURRAY FORMATION, GALE CRATER, MARS

Abstract

This study utilizes whole-rock geochemistry acquired with the Curiosity rover Alpha Particle X-Ray Spectrometer to evaluate geochemical trends at the facies level and reconstruct sediment history of the 95-m thick Sutton Island member of the Murray formation, Gale crater, Mars, which has previously been interpreted to consist of delta plain (Facies Association 1) and lacustrine (Facies Association 2; see Chapter 2) facies associations. Sedimentary facies and textures provide a framework from which to evaluate source-rock composition, chemical weathering, hydrodynamic sorting, and diagenesis. Quantitative corrections for non-silicate mineral phases (e.g., Ca-sulfate) are evaluated in order to better approximate geochemical signatures in commonly used molar ternary diagrams and corresponding weathering indices, including the Chemical Index of Alteration (CIA) and Mafic Index of Alteration (MIA), of primary silicate minerals. Comparisons with geochemistry of igneous compositions measured at Gale and Gusev craters support an averaged value as a plausible source composition for the Sutton Island member facies. Weathering indices and comparisons of geochemical trends to terrestrial weathering profiles indicate moderate to substantial weathering within Sutton Island member stratigraphy and signify a slight shift toward more steady-state conditions relative to trends within underlying stratigraphic members of the Murray formation. Comparing general trends in ternary diagrams and plots of immobile oxides (wt% TiO_2 and Al_2O_3) provides evidence for hydrodynamic sorting. Source rock phenocryst size, a small overall grain-size range, and mixing of grain sizes at depositional sites along the delta plain provide possible explanations for geochemical overlap between facies and

grain sizes. Variable diagenetic phases enriched whole-rock compositions from burial to lithification, highlighting the longevity of post-depositional fluid flow. Compositional characteristics of facies are consistent with dynamic sediment processes within the distal delta plain and lake settings interpreted in the Sutton Island member and support the role of aqueous processes at all stages along the sediment source-to-sink pathway.

Introduction

The composition of sedimentary rocks records all chemical and physical processes occurring along the sediment source-to-sink pathway (Fedo & Babechuk, 2022; Johnsson et al., 1993; McLennan et al., 2019). Subsequently, whole-rock compositional data provide a composite record of source composition (Bedford et al., 2019; Fedo et al., 1997a), chemical weathering (Babechuk et al., 2014; Nesbitt & Wilson, 1992), transport processes (Nesbitt & Young, 1996; Siebach et al., 2017), and diagenesis (Fedo et al., 1995, 1997b) of clastic sediment that informs aspects of basin evolution. Whole-rock geochemical signatures are inherently linked to the physical processes that transport and deposit sediment into structures and associated facies (Gwizd et al., 2022). Sediment transport processes facilitate hydrodynamic sorting of sediment by grain size, shape, and density (McGlynn et al., 2012; Nesbitt & Young, 1996), which changes the resulting whole-rock composition from that of the original source rock. Therefore, a combined assessment with facies and depositional environments (e.g., Gwizd et al., 2022) is essential to interpret compositional trends within a sedimentary succession.

The sedimentary record at Gale crater (5°S, 138°E), a 155 km diameter complex crater and the site of the Mars Science Laboratory (MSL) Curiosity rover mission (Figure 3.1a), records complex compositional trends that fluctuate on basin- (e.g., Milliken et al., 2010) to facies-scales (e.g., Caravaca et al., 2022; Gwizd et al., 2022; Siebach et al., 2017). Since the start of the mission, rover-scale assessments of geochemical and mineralogical trends within the stratigraphy comprising the 5.5-km-high central mound (Aeolus Mons, informally known as Mount Sharp) reveal sedimentary processes along the sediment source-to-sink pathway that varied in composition and extent (Mangold et al., 2019; Rampe et al., 2020a; Siebach et al., 2017; Sun et al., 2019). Throughout stratigraphy of the ~320-m-thick lacustrine and lacustrine-margin Murray formation (Caravaca et al., 2022; Edgar et al., 2020; Fedo et al., 2022; Grotzinger et al., 2015; Gwizd et al., 2022; Stack et al., 2019), geochemical trends are interpreted to represent fluctuations in source-rock composition (Bedford et al., 2019), chemical weathering extent (Frydenvang et al., 2020; Mangold et al., 2019), hydrodynamic sorting (Gwizd et al., 2022), and diagenetic enrichment (Kronyak et al., 2019; L'Haridon et al., 2020; Sun et al., 2019). These findings are corroborated by studies of Chemistry and Mineralogy (CheMin) mineralogical data that show diverse crystalline as well as amorphous phases throughout the Murray formation (Achilles et al., 2020; Bristow et al., 2018, 2021; Rampe et al., 2020a).

Various studies incorporate depositional processes and sedimentary textures into interpretations of compositional trends of the Murray formation at the facies level within

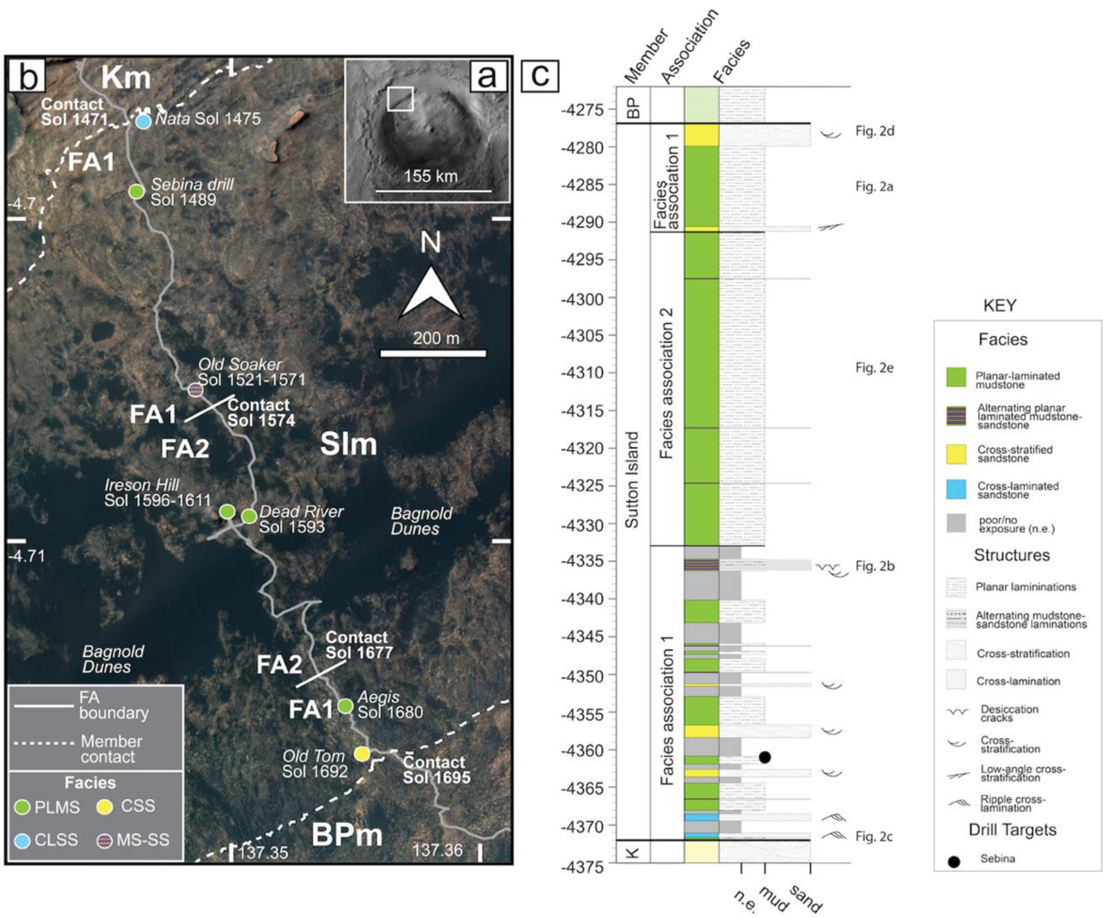

Figure 3.1 (a) Mars Reconnaissance Orbiter (MRO) Context Camera (CTX) mosaic of Gale crater showing the region explored by Curiosity (white box). (b) Traverse path across the Sutton Island member of the Murray formation. Contacts, key outcrops included in Figure 2, and other notable localities are annotated by sol and corresponding facies color where relevant. (c) Stratigraphic column showing the distribution of facies associations within the Sutton Island member, including the thickness and distribution of individual facies. The base map is a merged HiRISE orthophoto mosaic from Calef and Parker (2016). Modified from Gwizd et al. (Chapter 2).

individual stratigraphic members, (e.g., Caravaca et al., 2022; Gwizd et al., 2022), but combined assessments remain to be accomplished for numerous stratigraphic members. The 95-m-thick Sutton Island member consists of facies interpreted to represent deposition in delta plain and lacustrine environments (see Chapter 2). Geochemical (Mangold et al, 2019; Rapin et al., 2019; Sun et al., 2019; Thompson et al., 2020) and mineralogical (Achilles et al., 2020; Bristow et al., 2018; Haber et al., 2022) signatures for this member have been interpreted to indicate changes in the extent and conditions of alteration of mineral phases via chemical weathering and diagenetic fluid flow. Contextualization of composition with interpretations of facies and sedimentary textures is required to fully understand compositional trends recorded in the Sutton Island member as they relate to the evolution of depositional environments throughout the succession.

This study utilizes the detailed sedimentologic and stratigraphic work presented in Chapter 2 to develop an integrated compositional assessment of sedimentary processes along the source-to-sink pathway within the Sutton Island member. Specific goals of the study are to assess geochemistry of the Sutton Island member at the facies level to: (1) decipher the signatures of source rock composition, weathering, sediment transport, and diagenesis, and (2) develop an integrated compositional and depositional model to assess the evolution of depositional environments recorded in the Sutton Island member.

Geologic, stratigraphic, and compositional context

Geologic and stratigraphic context

Gale crater is located at the topographic boundary between the northern lowlands and southern highlands of Mars. Exhumed strata of the intracrater plains (Aeolus Palus) correspond to the fluvial-deltaic Bradbury group, and strata of the 5.5-km high central mound (Aeolus Mons, informally Mount Sharp; assigned to the Mount Sharp and Siccar Point groups). Mount Sharp group strata are subdivided into the Murray, Carolyn Shoemaker, and Mirador formations (Fedo et al., 2022; Grotzinger et al., 2015; Gupta et al., 2022). Stratigraphy of the 320-m thick Murray formation, which contains the Sutton Island member (SIm), consists of facies that are interpreted to represent deposition in lacustrine and lacustrine-margin environments characterized by the continued presence of standing water (Caravaca et al., 2022; Edgar et al., 2020; Fedo et al., 2022; Gwizd et al., 2022; Stack et al., 2019). The unconformable Siccar Point group overlies Mount Sharp group strata (Banham et al., 2021; Watkins et al, 2022).

Detailed sedimentologic and stratigraphic analyses on the facies, sedimentary processes, and evolution of paleoenvironments recorded in the 95-m thick SIm was done by Gwizd et al. (Chapter 2). Facies were differentiated by observations along the 2 km rover traverse (Figure 3.1b) of stratigraphic thickness, sedimentary structures, grain sizes, and other distinguishing features. Stratigraphy documented along the 2 km rover traverse through the SIm (Figure 3.1b) is subdivided into two facies associations: Facies Association 1 (FA1) and Facies Association 2 (FA2; Figure 3.1c).

Facies in FA1 indicate deposition in a distal delta plain environment (Chapter 2). In order of first appearance in stratigraphy, facies documented in FA1 include planar-laminated mudstone with minor sandstone (FA1 PLMS; Figure 3.2a), ripple cross-laminated sandstone (FA1 CLSS; Figure 3.2b), cross-stratified sandstone (FA1 CSS; Figure 3.2c), and alternating laminated sandstone and mudstone (FA1 MS-SS; Figure 3.2d). Planar-laminated mudstone with minor sandstone is interpreted to signify subaqueous deposition via suspension fallout and traction transport (sandstone interbeds), likely from density-flow processes, in regions of ponded water or overbank environments (MacNaughton et al., 1997). Ripple-cross laminated sandstone is interpreted as the product of subaqueous deposition via traction and saltation transport in lower flow-regime conditions (Southard & Boguchwal, 1973). Cross-stratified sandstone is interpreted to record subaqueous deposition via saltation and traction transport of sand as bedforms within distal distributary channels (Olariu & Bhattacharya, 2006). Alternating sandstone and mudstone laminae are interpreted to represent traction transport and deposition of sandstone and suspension fallout of mudstone associated with the delta plain distributary system (Nichols & Fisher, 2007), followed by localized subaerial exposure and formation of desiccation cracks (Stein et al., 2018).

Facies in FA2 indicate deposition in a lake basin (Chapter 2). Facies in FA2 include planar-laminated mudstone with minor sandstone (FA2 PLMS; Figure 3.2e). This facies is interpreted to represent deposition mostly via suspension fallout and less commonly via traction transport (sandstone interbeds) from density flows entering a lake basin characterized by sufficient accommodation space throughout deposition of FA2 (Gwizd et al., Chapter 2).

Gwizd et al. (Chapter 2) utilizes depositional processes and subenvironments from facies in FA1 and FA2 and assesses the juxtaposition of both associations (Figure 3.1c) to interpret the evolution of the lake margin. The transition between FA1 and FA2 is interpreted to signify a rapid and substantial lake transgression. The transition between FA2 and the upper interval of FA1 is interpreted as a forced regression.

Compositional context

Geochemical and mineralogical measurements throughout the majority of the Murray formation, including the SIm, are indicative of a basaltic composition (Gwizd et al., 2022; Mangold et al., 2017; Rampe et al., 2020a; Thompson et al., 2020). Within the SIm, Bedford et al. (2019) proposed a silica-rich subalkaline basaltic composition as the dominant compositional source. Geochemical enrichment and depletion of major elements in SIm bedrock is then interpreted to represent modification from the source during weathering and diagenesis (Mangold et al., 2019; Thompson et al., 2020). Enrichment in Mg-bearing sulfate has been interpreted to suggest localized transitions to more evaporitic conditions (Rapin et al., 2019); however, these sulfate-rich bodies are more consistent with a diagenetic interpretation (see below; also Gwizd et al., Chapter 2). Other mineralogical (Achilles et al., 2020; Bristow et al., 2021) and morphological (Sun et al., 2019) studies of SIm stratigraphy interpreted sulfate-rich (particularly Ca) features

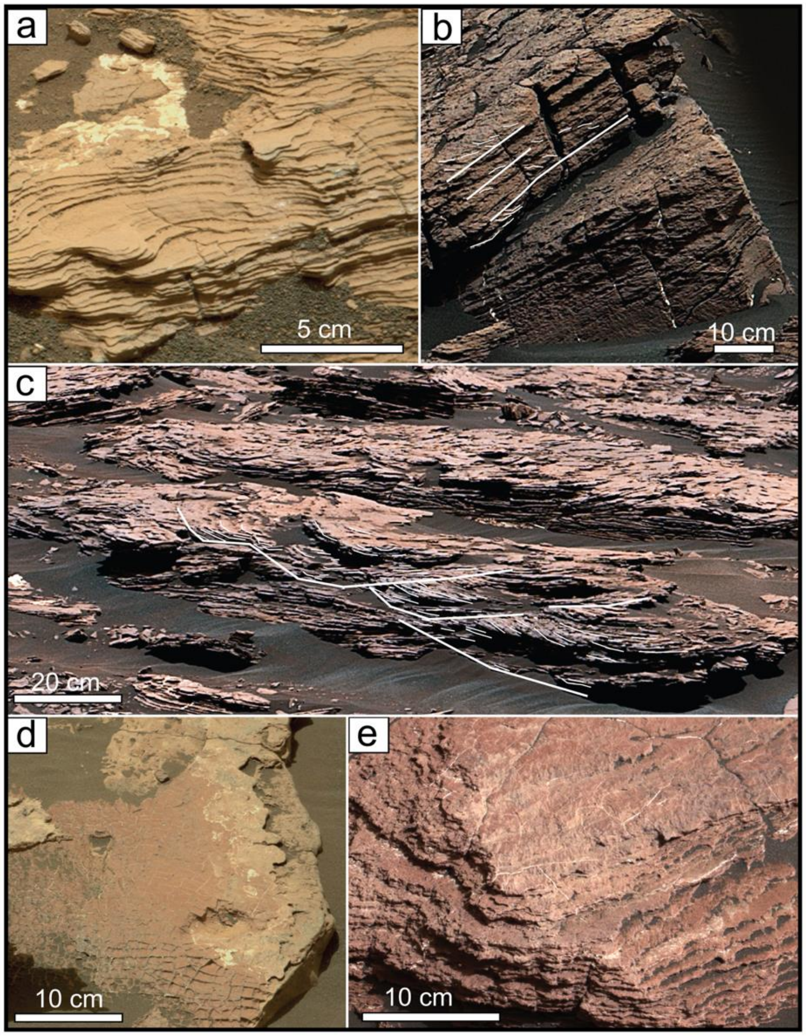

Figure 3.2 Representative images of all facies identified within the Sutton Island member (Gwizd et al., Chapter 2). Facies Association 1: (a) Planar-laminated mudstone with minor sandstone (M100 Mastcam image, mcam08728, Sol 1680). (b) Ripple cross-laminated sandstone (M100 Mastcam mosaic Nata, mcam07399, Sol 1475). (c) Cross-stratified sandstone facies, including outlines of set boundaries (thick white lines) and individual foreset laminae (thin white lines; M100 Mastcam mosaic Old Tom, mcam08815, Sol 1692). Modified from Gwizd et al. (Chapter 2). (d) Alternating laminated sandstone and mudstone facies, showing mudstone (red-toned rock) overlying a ~10-15-cm thick interval of sandstone and mudstone-laminae (lighter-toned rock; M100 Mastcam mosaic Schooner Head, mcam07982, Sol 1555). Facies Association 2: (e) Planar-laminated mudstone with minor sandstone (M100 Mastcam mosaic Dead River, mcam08119, Sol 1593). Image credit: NASA/JPL-Caltech/MSSS.

as diagenetic formation of veins, concretions, and disseminated cements. Mineralogical data was measured with the Chemistry and Mineralogy (CheMin) X-ray Diffraction (XRD) instrument of the only drill sample in the SIm, Sebina (-4361 m; Figure 3.1c). This drill sample was acquired from the FA1 planar-laminated mudstone with minor sandstone facies, and reveals a range of phases interpreted as crystalline and amorphous, detailed in Achilles et al. (2020) and Bristow et al. (2018).

Methods

Whole-rock geochemical data were acquired with the Alpha Particle X-Ray Spectrometer (APXS). The APXS instrument utilizes particle induced X-Ray emission and X-Ray fluorescence techniques (Campbell et al., 2012; Gellert et al., 2009, 2015) to acquire average compositional data over a 1.5–2-cm diameter field of view (FOV). Major-element abundances are reported in oxide weight percent (wt.%); trace elements are reported in parts per million (ppm). Interpretations in this study account for the statistical error of precision, which corresponds to repeatability of measurements (Gellert et al., 2015). Additional details regarding methodology and data calibration can be found in Campbell et al. (2012) and Gellert et al. (2015).

A total of seventy seven APXS measurements from the Sutton Island member were utilized in this study (additional file attachment Table 3.1). Measurements of primary bedrock (n = 56) include targets with a FOV that contains little to no obvious diagenetic features (e.g., veins, concretions; grey patches; Sun et al., 2019). Measurements with a FOV that includes a component of veins or concretions were included and are considered accordingly in discussions of geochemical signatures.

Twenty-one measurements that represent a primary contribution from diagenetic features are included in the discussion of diagenesis but are otherwise excluded from interpretations. Measurements acquired on bedrock that had not been brushed with the Dust Removal Tool (DRT) are included in this study. Dust affects the compositions of light elements, but Schmidt et al. (2018) shows that measurements that have not been brushed with the DRT can still record an accurate bedrock composition. Based on context from previous geochemical and mineralogical studies (e.g., Achilles et al., 2020; Rampe et al., 2020a; Thompson et al., 2020), all SO_3 is assumed to be bound in secondary Ca-, Mg-, or Fe-sulfate, but dominantly Ca-sulfate. Previous studies (Achilles et al., 2020; Bristow et al., 2018; Mangold et al., 2019) are also considered when interpreting the oxidation state of Fe, which is reported by the APXS instrument as $FeO_{(T)}$.

Geochemical tools

Evaluation of the source-to-sink sediment pathway within the SIm stratigraphy requires the utilization of terrestrial principles and techniques. Experimental, modeling, and field studies have established the major elemental signatures associated with chemical weathering, transport, and diagenesis in basaltic terrestrial sedimentary systems (e.g., Babechuk et al., 2014; Babechuk & Fedo, 2022; Fedo et al., 2015; Nesbitt & Young, 1984; Nesbitt & Wilson, 1992; Thorpe & Hurowitz, 2020) and have corroborated the applicability of compositional signatures to sedimentary systems on Mars (e.g., Mangold et al., 2019; McLennan et al., 2005; Siebach et al., 2017). Understanding geochemical changes in a basaltic sedimentary system is especially critical for studies of

Martian sedimentary systems, where a starting source composition typically can only be approximated and is typically basaltic.

This study includes four ternary diagrams to evaluate source composition and subsequent sedimentary processes responsible for sediment alteration from the initial source composition (Figure 3.3). Ternary diagrams utilized include molar proportions of Al_2O_3 – CaO* + Na_2O – K_2O (A-CN-K; Figure 3.3a), Al_2O_3 – CaO* + Na_2O + K_2O – $FeO_{(T)}$ + MgO (A-CNK-FM; Figure 3.3b), Al_2O_3 + $FeO_{(T)}$ – CaO* + Na_2O + K_2O – MgO (AF-CNK-M; Figure 3.3c), and Al_2O_3 – CaO* + Na_2O + K_2O + MgO – $FeO_{(T)}$ (A-CNKM-F; Figure 3.3d). The molar proportions of major elements correspond to primary (CaO, Na_2O, K_2O, $FeO_{(T)}$, MgO) and secondary (Al_2O_3, $FeO_{(T)}$) mineral phases present in the whole-rock sample. Within each ternary diagram, alteration from a starting source composition via weathering, hydrodynamic sorting, and diagenesis is typically characterized by distinct pathways (labeled arrows in Figure 3.3; Babechuk et al., 2014; Babechuk & Fedo, 2022; Fedo & Babechuk, 2022).

Chemical weathering of basaltic source rocks results in geochemical trends that correlate with hydrolysis of susceptible mineral phases and enrichment in secondary alteration phases (Eggleton, 1987; Nesbitt & Wilson, 1992). Within the ternary diagrams in Figure 3.3, weathering of primary minerals (e.g. feldspars, pyroxenes, olivines) via hydrolysis drives data points toward the A apices as aluminous phases concentrate. The extent of chemical weathering is commonly quantified via the Chemical Index of Alteration (CIA; Equation 1; A in A-CN-K space; Nesbitt & Young, 1982; Fedo et al., 1995) and Mafic Index of Alteration

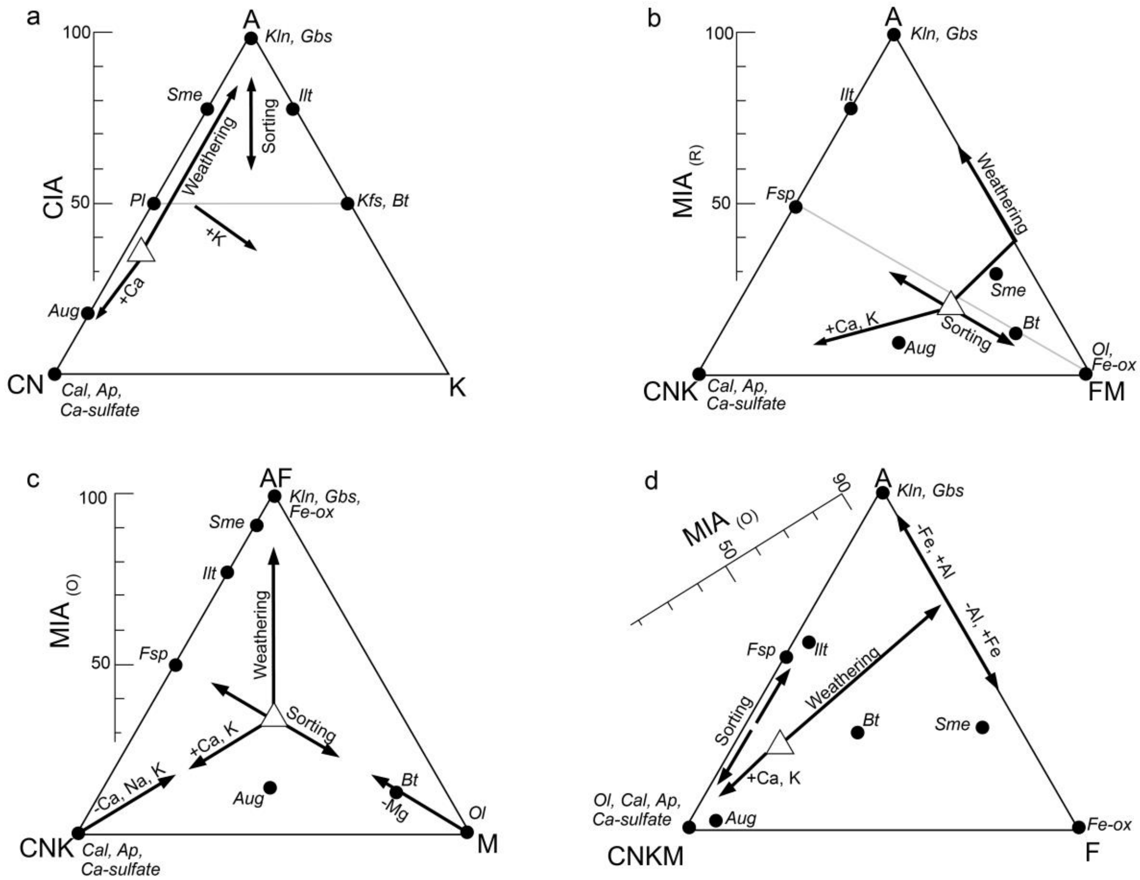

Figure 3.3 (a) A-CN-K, (b) A-CNK-FM, (c) AF-CNK-M, and (d) A-CNKM-F ternary diagrams depicting geochemical pathways produced from chemical weathering, sorting, and diagenesis (labeled lines) emanating from a starting basaltic source composition (small triangles). Reference minerals include: Fsp = feldspar; Pl = plagioclase feldspar; Kfs = K-feldspar; Bt = biotite; Ilt = illite; Sme = smectite; Kln = Kaolinite; Gbs = gibbsite; Aug = augite; Ol = olivine; Fe-ox = Fe-oxides. Most mineral abbreviations from Whitney and Evans (2010).

(MIA$_{(O)}$ and MIA$_{(R)}$; Equations 2 & 3; AF in AF-CNK-M space and A in A-CNK-FM space; Babechuk et al., 2014):

$$CIA = [Al_2O_3/(Al_2O_3+CaO^*+Na_2O+K_2O)]*100 \quad (1)$$

$$MIA_{(O)} = [(Al_2O_3 + FeO_{(T)})/(Al_2O_3+CaO^*+Na_2O+K_2O+MgO+FeO_{(T)})]*100 \quad (2)$$

$$MIA_{(R)} = [(Al_2O_3)/(Al_2O_3+CaO^*+Na_2O+K_2O+MgO+FeO_{(T)})]*100 \quad (3)$$

The MIA$_{(O)}$ is utilized for oxidizing conditions in which Fe^{3+} is immobile and, therefore, included in the numerator with Al^{3+}, and the MIA$_{(R)}$ is utilized for reducing conditions in which Fe^{2+} is mobilized (Babechuk et al., 2014). The key difference between the CIA and MIA calculations is the inclusion of the mafic Fe and Mg components in MIA to provide a more accurate assessment of basaltic weathering of olivine, pyroxene, and Fe-oxide phases and the presence of secondary alteration phases of those minerals (Figure 3.3b-d).

To constrain the oxidation state of Fe in the SIm, and to determine which MIA Equation should be utilized, previous mineralogical and geochemical assessments are considered. Estimates of the Fe^{2+}/Fe^{3+} ratio from the Karasburg member drill sample Marimba, whose mineralogy is similar to Sebina (Achilles et al., 2020), suggest that ferric oxides are predominant (Mangold et al., 2019). Additionally, the presence of hematite and dioctahedral smectite in Sebina and other drill samples in underlying Murray formation members suggests that pre- and post-burial conditions were oxidizing (Achilles et al., 2020; Bristow et al., 2018). This study therefore considers iron measurements to represent Fe^{3+} and utilizes the $MIA_{(O)}$ equation; nonetheless, we emphasize the uncertainty inherent with this assumption, especially that regarding the abundant amorphous Fe-rich phases documented in the Murray formation (Achilles et al., 2020; Rampe et al., 2020a).

Weathering indices and geochemical trends can be visualized on A-CN-K (CIA; Figure 3.3a), A-CNK-FM ($MIA_{(R)}$; Figure 3.3b), AF-CNK-M ($MIA_{(O)}$; Figure 3.3c), and A-CNK-FM ($MIA_{(O)}$; Figure 3.3d) ternary diagrams. In the A-CN-K diagram, unweathered basaltic source compositions generally plot at a CIA value of 35–40 (open triangle in Figure 3.3a; Babechuk et al., 2014). Typical unaltered basaltic source compositions are also plotted in A-CNK-FM, AF-CNK-M, and A-CNKM-F diagrams (open triangle in Figure 3.3b-d). Weathered compositions will typically plot more proximal to the A apices as samples become enriched in alteration phases (e.g., kaolinite). Ternary diagrams incorporating Fe and Mg further enhance analysis of weathering trends in basaltic systems by showing the relative loss of mafic (e.g., pyroxene, olivine) versus felsic (e.g., feldspars) phases (Figure 3.3b-c) as well as assessment of relative enrichment in Fe (Figure 3.3d; Babechuk et al., 2014). Recent studies (Babechuk & Fedo, 2022; Fedo & Babechuk, 2022) address the need to investigate weathering trends via multiple ternary, or even tetrahedral, diagrams. Such studies emphasize the use of multiple diagrams and tetrahedral diagrams to integrate all compositional signatures (e.g., Fe redox behavior, diagenesis, Si loss; Babechuk & Fedo, 2022) and more accurately show the compositional range and shifts of mafic and felsic phases during weathering and diagenesis

In addition to weathering, the ternary diagrams in Figure 3.3 can reveal the effects of sorting (e.g., Fedo et al., 2015) on chemical compositions. Physical sorting of basaltic sediment in transport will segregate mineral phases from within mafic and felsic mineral groups by density (McGlynn et al., 2012; Nesbitt & Young, 1996), and even. In a basaltic sedimentary system that has undergone initial weathering to produce phyllosilicate phases, sorting will result in deposition of coarse-grained primary phases with fine-grained phyllosilicate phases (e.g., labeled arrows in Figure 3.3a). Arrows in Figure 3.3b-d emanating from source rock compositions depict linear trends of sorting in a sedimentary system that has undergone minimal to no weathering, in which olivine and pyroxene correspond to finer grain sizes and feldspar corresponds to coarser grain sizes.

Diagenesis in the SIm commonly enriches sedimentary rocks in non-silicate diagenetic phases. In Equations 1–3, CaO* typically corresponds to a value of molar Ca in silicates calculated by subtracting stoichiometric proportions of CO_2 (calcite) and P_2O_5 (apatite; Fedo et al., 1995). The lack of carbonate detected in drill samples of the Murray formation, including Sebina, precludes need for a calcite correction. Although apatite was not detected in Sebina, the majority of P_2O_5 (0.67 wt%) is attributed to the amorphous fraction (Achilles et al., 2020) and may be associated with apatite. At Gale crater, Ca-sulfate occurs throughout the stratigraphy in the form of veins, concretions, and cements (Kronyak et al., 2019; Sun et al., 2019; Vaniman et al., 2018). Enrichment in Ca-sulfate drives data points toward Ca-included apices in Figure 3.3. Addition of Ca lowers the apparent CIA and MIA. Calculations implemented in this study for CaO* corrected for Ca-sulfate are detailed in the section “Correction for non-silicate Ca-bearing phases”.

Another diagenetic trend documented in previous studies of Gale crater stratigraphy is potassium enrichment via metasomatism (Mangold et al., 2019). Potassium metasomatism enriches whole-rock geochemistry in potassium via illitization or the replacement of plagioclase by K-feldspar (Fedo et al., 1995), thus lowering apparent weathering indices by shifting data points toward the K apices along the arrows in Figure 3.3. A graphical approach of Fedo et al. (1995) can be applied to datasets to correct for the effects of K-metasomatism in A-CN-K ternary space. Enrichment in diagenetic Fe-oxides has been interpreted from mineralogical data from Sebina (Achilles et al., 2020), and would enrich whole-rock geochemistry in Fe.

Correction for non-silicate Ca-bearing phases

Assessment of primary silicate sedimentary processes is complicated by the occurrence of non-silicate primary and diagenetic phases documented in the mineralogy of drill samples (Rampe et al., 2020a). The most abundant non-silicate phase documented at Gale crater is Ca-sulfate (Kronyak et al., 2019; Sun et al., 2019). When wt% CaO is plotted against wt% SO_3, all SIm data points generally plot along a 1:1 line that projects ratios of known Ca-sulfate phases (anhydrite, gypsum, bassanite; Figure 3.4) documented in Gale crater drill samples (including Sebina; Achilles et al., 2020) to the origin, which suggests that SO_3 constitutes a significant portion of Ca-bearing phases in the SIm.

In addition to correcting CaO for apatite (P_2O_5), a correction for non-silicate Ca-sulfate is explored in this study to better decipher primary silicate signatures of weathering and sediment transport. Previous geochemical studies of Gale crater source-

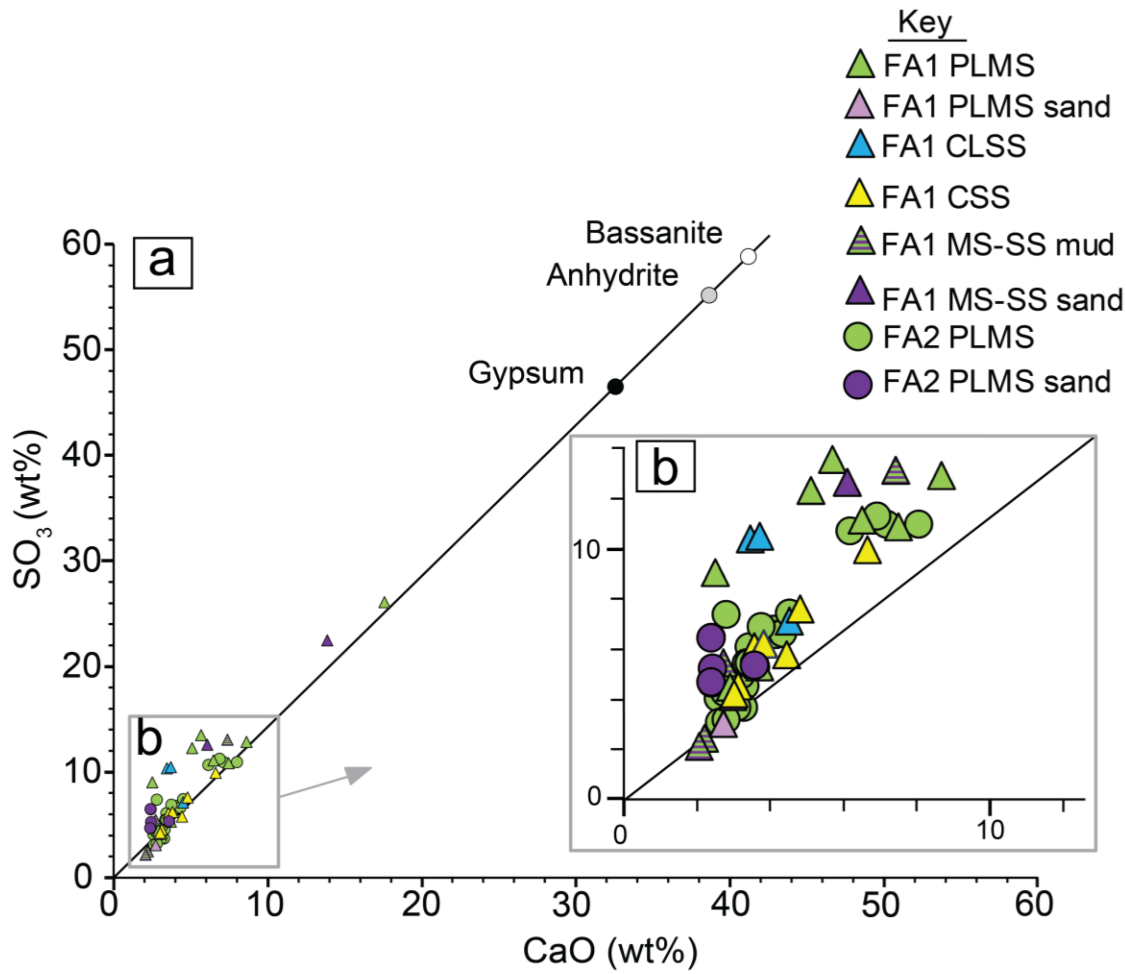

Figure 3.4 (a) Plot comparing wt% CaO and SO_3 of SIm facies to the trendline that depicts mixing with Ca-sulfate mineral phases. Also shown are data points representing wt% CaO and SO_3 of Ca-sulfate phases identified at Gale crater, including gypsum (black circle), anhydrite (grey circle), and bassanite (white circle). (b) Expanded inset view of SIm facies from (a).

to-sink history have approached corrections for CaO associated with SO_3 using various qualitative and quantitative methods. Several studies excluded measurements acquired on obvious diagenetic features such as and including Ca-sulfate veins and concretions (Mangold et al., 2019; Thompson et al., 2020). Other studies did not apply a Ca correction and instead interpreted calculated weathering indices and geochemical trends as minimum values (Hurowitz et al., 2017; McLennan et al., 2014; Siebach et al., 2017; Thorpe et al., 2021). Schieber et al. (2017) utilized APXS data from Gale crater stratigraphy and geochemical values of known Martian basaltic compositions (McSween et al., 2006) in conjunction with CheMin mineralogical results to estimate a ratio of silicate to non-silicate Ca-bearing phases and subtract a fraction of SO_3 from CaO accordingly.

Although calculations of CaO contributed only by silicate phases (CaO*) typically involve subtraction in stoichiometric proportions, Gwizd et al. (2022) highlights the inaccuracy of applying a proportional molar correction (subtracting the total molar SO_3 from the total molar proportion of CaO) by concluding that a 1:1 correction inaccurately drives most values of CaO* in the Hartmann's Valley and Karasburg members of the Murray formation to negative values. Primary Ca-bearing phases (e.g., plagioclase, pyroxene) are sufficiently common throughout Murray formation drill samples; therefore, a negative value of CaO* is incorrect (Achilles et al., 2020; Rampe et al., 2020a). The presence of other sulfate-bearing phases (e.g., Mg- and Fe-sulfate) in the Murray formation indicates that Ca-sulfates are not the only contributor to the total proportion of SO_3, which further corroborates the interpretation made by Gwizd et al., (2022).

This study explores two possible CaO* calculations accounting non-silicate primary and diagenetic Ca-bearing phases with CheMin mineralogical data from Achilles et al. (2020). Based on similarity of measured mineral proportions between drill samples Marimba (Km), Quela (Km), and Sebina (SIm), we constructed an average proportion of silicate Ca phases to use in the calculation of CaO* (additional file attachment Table 3.1). Phases interpreted as Ca-bearing silicates in relevant drill samples include plagioclase, pyroxene, and smectite (Achilles et al., 2020; Bristow et al., 2018). To estimate molar proportions of CaO associated with each phase, wt% oxide values of known mineral compositions were selected and are included in additional file attachment Table 3.1 (Deer et al., 1992 and citations within). To best approximate the andesine average of An_{40}, wt% oxide values of an andesine antiperthite were employed (Deer et al., 1992; Howie, 1955). Overlapping peaks in CheMin XRD data and the low angular resolution of the instrument preclude a definitive interpretation of pyroxene composition (Rampe et al., 2020a); nevertheless, variable amounts of augite, pigeonite, and orthopyroxene have been modeled from drill samples at lower stratigraphic intervals (Morrison et al., 2018). Therefore, this study utilizes geochemical data from a ferroaugite sample (Deer et al., 1992; Kuno, 1955), explicitly noting the uncertainty associated with lacking an exact interpretation of pyroxene composition. The phyllosilicate fraction of Marimba, Quela, and Sebina has been interpreted to consist of Al-rich dioctahedral and Fe-rich trioctahedral smectite (Bristow et al., 2018). Because there is inherent complexity in interpreting exact phyllosilicate compositions, this study utilizes a value of nontronite to approximate a plausible Ca-bearing clay phase (Brigatti, 1983; Deer et al., 1992) while recognizing that the choice in composition is an oversimplification and does not capture the trioctahedral component interpreted by Bristow et al. (2018).

From the chosen plagioclase, pyroxene, and phyllosilicate mineral compositions and the relative wt% proportions of minerals calculated in the averaged drill sample (additional file attachment Table 3.1), a molar proportion value of 0.027 was calculated as the silicate component of CaO (CaO*) in the averaged drill sample. Lacking the capacity to fully correct the CaO value for silicate phases only, we explore two options for making this correction (Equations 4 & 5):

$$CaO^* = 0.027 \tag{4}$$

$$CaO^* = (0.2)^*CaO_{(T)} \tag{5}$$

In Equation 4, the calculated value of 0.027 represents the amount of silicate-hosted molar CaO extrapolated to all targets in the SIm. Equation 5 represents a derivation of a mathematical relationship for CaO* as it relates to total molar CaO ($CaO_{(T)}$) based on the portion of silicate-hosted CaO (0.027) compared to CaO hosted in non-silicate phases in Sebina, the one drill sample from the SIm. From this comparison, the fraction of plagioclase, pyroxene, and phyllosilicate molar CaO (CaO*) is calculated as 20% of the measured total molar CaO ($CaO_{(T)}$) in a given target, and this 20% fraction is applied to each APXS target within the SIm. While Equation 4 utilizes an averaged mineralogical composition from three similar drill samples and assumes a uniform quantity of silicate minerals across all APXS targets in the SIm, Equation 5 applies a ratio derived from the mineralogical composition of the SIm at Sebina to each target to account for possible variability in the amount of primary silicates between targets. Both corrections exhibit uncertainty: Equation 4 assumes the same amount of silicate Ca-bearing minerals throughout all targets, and Equation 5 assumes the same ratio of silicate Ca-bearing minerals to non-silicate Ca-bearing minerals throughout all targets. Despite this uncertainty, evaluation of CIA and geochemical trends from both calculations of CaO* will better approximate pre-diagenetic values.

Figure 3.5 compares resulting values of CIA (Equation 1) and $MIA_{(O)}$ (Equation 2) for both Ca-correction schemes (additional file attachment Table 3.2). The x-axis represents CIA and MIA values calculated using Equation 4, and the y-axis represents CIA and MIA values calculated using Equation 5. Calculations of CaO* from both Ca corrections result in differences in the range and extent of calculated CIA values (Figure 3.5a). Values plot above 1:1 (Figure 3.5a), indicating that utilization of Equation 5 generates greater CIA values. The range of calculated CIA values for Ca-correction 1 (Equation 4) is 9 units (49–58); whereas the range of calculated CIA values for Ca-correction 2 (Equation 5) is 28 units (38–66). Differences shown in Figure 3.5a highlight the sensitivity of interpretations of CIA and weathering to both Ca-correction schemes. In contrast to CIA, $MIA_{(O)}$ values are generally similar between both Ca-correction schemes (Figure 3.5b). Values of CIA plot proximal to 1:1, indicating a correlation of CIA values between both Ca-corrections. The range of $MIA_{(O)}$ values for Ca-correction 1 is 21 units

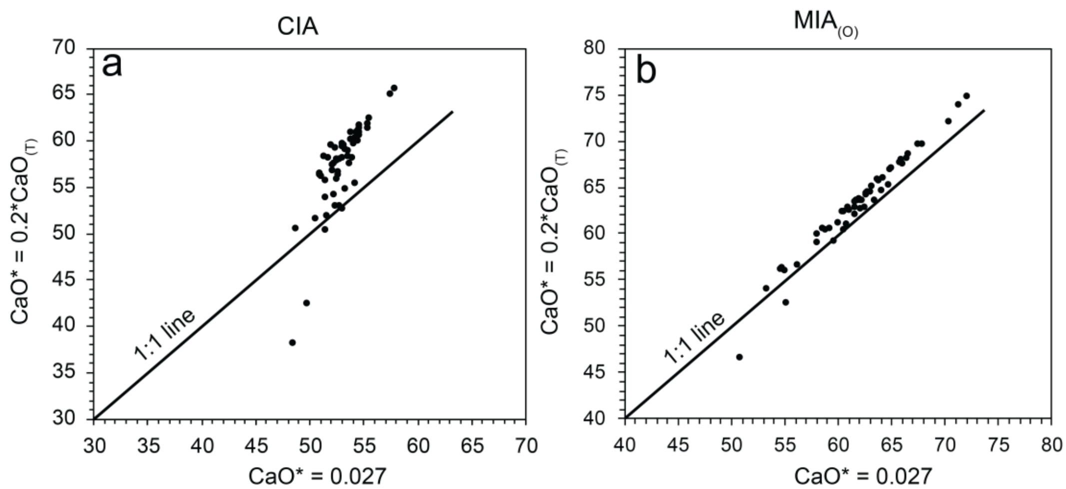

Figure 3.5 Plots of CIA (a) and $MIA_{(O)}$ (b) values comparing CaO* calculated with Equation 4 and Equation 5.

(51–72), and the range of $MIA_{(O)}$ values for Ca-correction 2 is 28 units (47–75). The sensitivity of the CIA calculation to each Ca-correction scheme is likely due to the absence of the -FM component. A full comparison of the distribution of facies in ternary diagrams using both Ca-correction schemes is included in supplemental Figure 3.14 and shows the significant difference in the distribution of facies in the A-CN-K ternary diagram and the largely similar distribution of facies in A-CNK-FM, AF-CNK- M, and A-CNKM-F ternary space between both corrections.

Relationship between depositional processes and composition

Fifty-six APXS whole-rock, major-element, geochemistry measurements (additional file attachment Table 3.1) from SIm facies are employed in the evaluation of signatures of source rock composition, chemical weathering, transport, and diagenesis. Plots of individual wt% oxides (Figure 3.6) do not show significant geochemical differences between facies.

The following sections utilize conventional plots in addition to ternary diagrams to assess source-to-sink sediment history of SIm facies. Given the differences in calculated CIA values and in the resulting distribution of facies in A-CN-K ternary space, the main text of this paper includes data Ca-corrected by both Ca-correction schemes in all A-CN-K diagrams (Figures 3.7 & 3.8). Given the similarities in calculated $MIA_{(O)}$

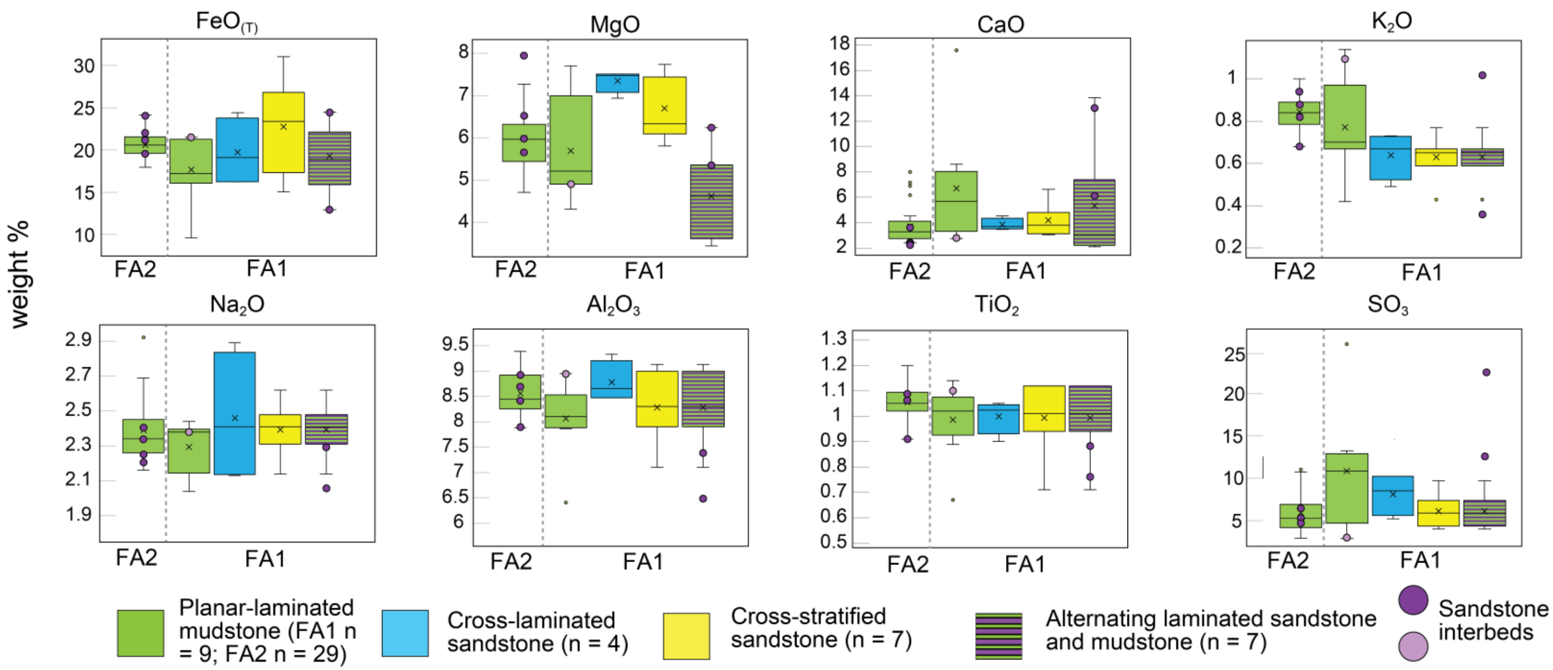

Figure 3.6 Box-and-whisker plots for facies in Facies Association 1 & 2 (FA1, FA2) including: planar-laminated mudstone with minor sandstone (FA1, FA2, green), ripple cross-laminated sandstone (FA1, blue), cross-stratified sandstone (FA1, yellow), and laminated sandstone and mudstone (FA1, striped). The "x" symbols within the boxes represents the average wt% for each facies. The horizontal lines within boxes represent median values, and outer bounds represent maximum and minimum values excluding outliers (small circles). The larger purple circles represent sandstone interbeds within each facies.

values and in the distribution of facies across the remaining ternary diagrams, A-CNK-FM (Figure 3.9), AF-CNK-M (Figure 3.10), and A-CNKM-F (Figure 3.11) plots are simplified to display data Ca-corrected only with Equation 4, though we note that the distribution of data in these diagrams is generally representative of both corrections (supplemental Figure 3.14). Uncorrected data are also included in Figures 3.7-3.11, though we emphasize that uncorrected geochemical trends and weathering indices cannot represent the composition at the time of deposition, and that data are only included as a reference to compare resulting shifts in geochemical trends and weathering indices with Ca-corrected data.

Source composition

Understanding the source composition of sediment within a stratigraphic succession is critical in using whole rock geochemistry to evaluate the extent of physical and chemical sedimentary processes in the system. An exact provenance assessment for SIm facies cannot be deduced from the available data, but a source composition can be estimated from known Martian compositions (Figure 3.7a) and linear arrays produced by data (Figure 3.7b). Given the substantial difference between Ca-corrected data in the distribution of facies in A-CN-K space depending on the Ca-correction scheme, data Ca-corrected with both Equation 4 and Equation 5 are included in this assessment.

Figure 3.7a includes APXS geochemistry of Martian igneous compositions from Gale and Gusev craters (additional file attachment Table 3.1). Orange circles represent float

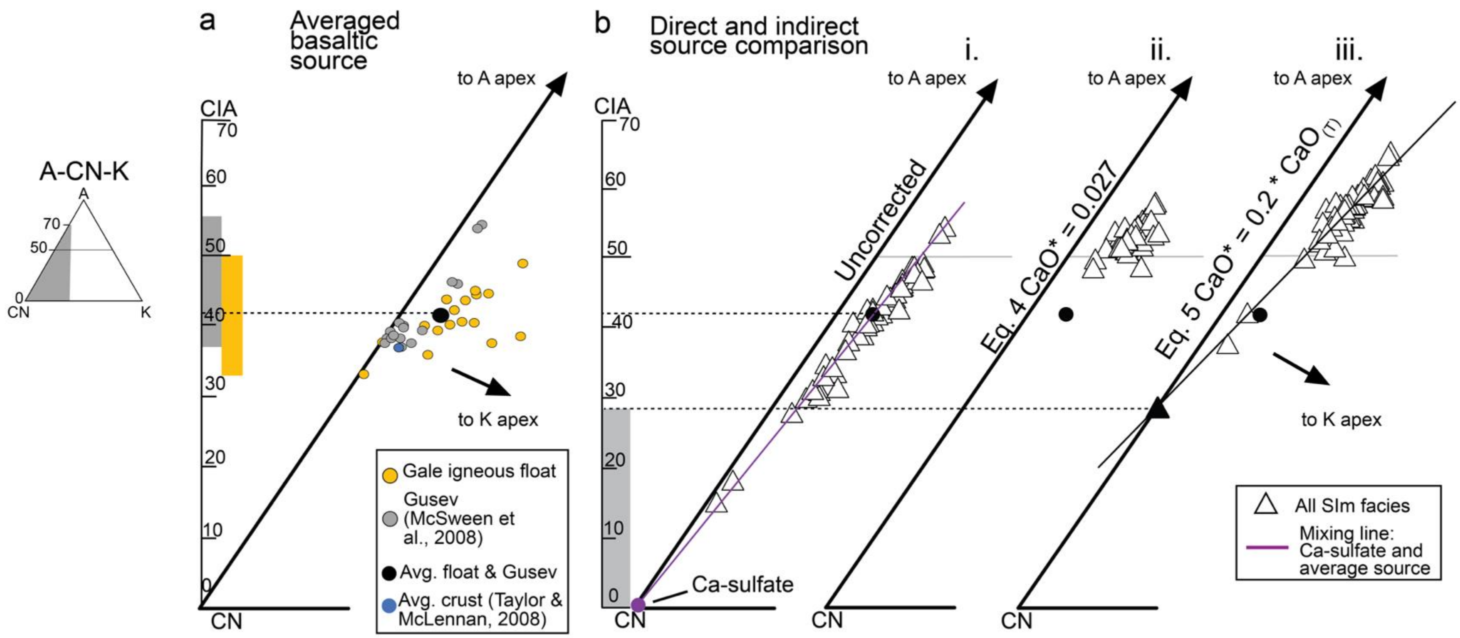

Figure 3.7 Assessment of possible source rock compositional ranges in A-CN-K ternary diagrams. The shaded region in the small triangle corresponds to the portion shown in (a) & (b). (a) Plot of Gale igneous float rocks, Gusev basalt classes, average Mars crust, and a calculated average of the float rocks and average Gusev basalt classes (the dashed line indicates a CIA of 42 for the averaged source composition). Modified from Gwizd et al. (2022; Figure 1.10). (b) Plots of uncorrected facies (i) and facies corrected for non-silicate Ca phases using Equation 4 (ii) and Equation 5 (iii). Included on diagrams (i) and (iii) are linear trendlines compared to the averaged basalt source composition (black circle). Diagram (i) also includes a mixing line (purple line) between Ca-sulfate and the averaged source basalt composition (purple line) highlighting the influence of Ca-sulfate on the whole-rock composition of SIm facies. The grey box shows lower bounds for source rock CIA constrained by the linear trendlines in (i) and (iii).

rocks from Gale crater (n = 19), which are interpreted to represent igneous alkaline and basaltic compositions (Berger et al., 2020; Schmidt et al., 2014; Thompson et al., 2016; Wiens et al., 2020). Gray circles represent Gusev basalt classes (Gellert et al., 2006; McSween et al., 2008; Ming et al., 2008). The blue circle represents the average value for Martian crust (Taylor & McLennan, 2009), included for reference. These data points were Ca-corrected for CaO in apatite (Fedo et al., 1995) using Equation 6:

$$CaO^* = CaO_{(T)} - (3.33 * P_2O_5) \tag{6}$$

Although some data points plot above the typical CIA range of unweathered basalt (35–40; Babechuk et al., 2014), float rocks and basalt classes plot proximal to this range overall (Figure 3.7a)**.** As determined in Gwizd et al. (2022), the averaged source composition employed in this study plots at a CIA of 42. This value generally agrees with the typical CIA of unweathered basalts (35–40; Babechuk et al., 2014), and is therefore representative of a plausible source rock composition.

Similar to Gwizd et al. (2022), this study also explored an estimate of a lower bound for source rock CIA by assessing linear trends of SIm facies (Figure 3.7b). In A-CN-K ternary diagrams, sediment weathered and eroded from source bedrock will plot along a predicted linear pathway (Nesbitt et al., 1997; Nesbitt & Wilson, 1992) and trend away from a starting source rock composition toward the A apex (labeled arrow in Figure 3.3a). Compared to weathered samples, the unaltered source rock composition plots at a lower value of CIA (small triangle in Figure 3.3a). Where SIm data points define linear trends in A-CN-K space, a lower bound for source rock CIA may therefore be estimated at the point where trendlines intersect the A-CN join.

Figure 3.7b shows the distribution of all facies in A-CN-K space as uncorrected data points (Figure 3.7bi), data points Ca-corrected with Equations 4 (Figure 3.7bii) and 5 (Figure 3.7biii). Uncorrected data define a linear trendline (Figure 3.7bi), but the relative position of facies compared to the averaged source composition and the overlap of data with a mixing line for Ca-sulfate and the averaged source composition (purple line) emphasize the influence of Ca-sulfate and the need to assess source composition using the Ca-corrected datasets. Facies in both corrected datasets plot almost entirely above the average source composition (Figure 3.7bii–iii). Data Ca-corrected using Equation 4 plot along a relatively clustered range and do not define a linear trend (Figure 3.7bii); data Ca-corrected using Equation 5 plot as linear arrays (Figure 3.7biii). The linear trend in Figure 3.7biii intersects the A-CN join at a CIA of 28. This value is also lower than the range of typical values of CIA for unweathered basalts, but nevertheless provides a lower bound for a source rock CIA.

Comparisons of CIA ranges of corrected datasets (Figure 3.7bii–iii) and trendline in Figure 3.7biii to the averaged source composition (black circles) provide support for the averaged composition of Gwizd et al. (2022) as a plausible source rock composition for the SIm facies. All data points within the Equation 4 Ca-corrected dataset plot along a CIA range greater than the averaged source rock (Figure 3.7bii). Data Ca-corrected with Equation 5 (Figure 3.7biii) see only two data points plot at or below the CIA of the averaged source rock. Additionally, the linear trend of the Equation 5 Ca-corrected dataset (Figure 3.7biii) plots proximal to the averaged source composition. Overall, the relative CIA ranges captured by both Ca-corrected datasets compared to the averaged source composition and the proximity of the linear trend in Figure 3.7biii provide evidence that the average of Gusev basalt classes and Gale crater float rocks defines a plausible source rock composition for the sediments in this study, consistent with previous interpretations of a subalkaline source composition for the SIm facies (Bedford et al., 2019).

Weathering

Previous mineralogical and geochemical studies have established that chemical weathering is recorded in the strata of the Murray formation (Bristow et al., 2018; Frydenvang et al., 2020; Gwizd et al., 2022; Mangold et al., 2019) The following sections compare weathering indices and geochemical trends between facies in A-CN-K (Figure 3.8), A-CNK-FM (Figure 3.9), AF-CNK-M (Figure 3.10), and A-CNKM-F (Figure 3.11) ternary diagrams to deduce possible links between sedimentary processes and weathering extent and to interpret geochemical depletions and enrichments that signify mineralogical changes within the SIm system. All ternary diagrams in Figures 3.9-3.11 include uncorrected data in addition to Ca-corrected data (simplified to only plot data Ca-corrected using Equation 4) to highlight the extent to which Ca-corrections shift apparent weathering extent. For the A-CN-K ternary diagram, data Ca-corrected with both correction schemes (Equations 4 & 5) are included because there is a significant

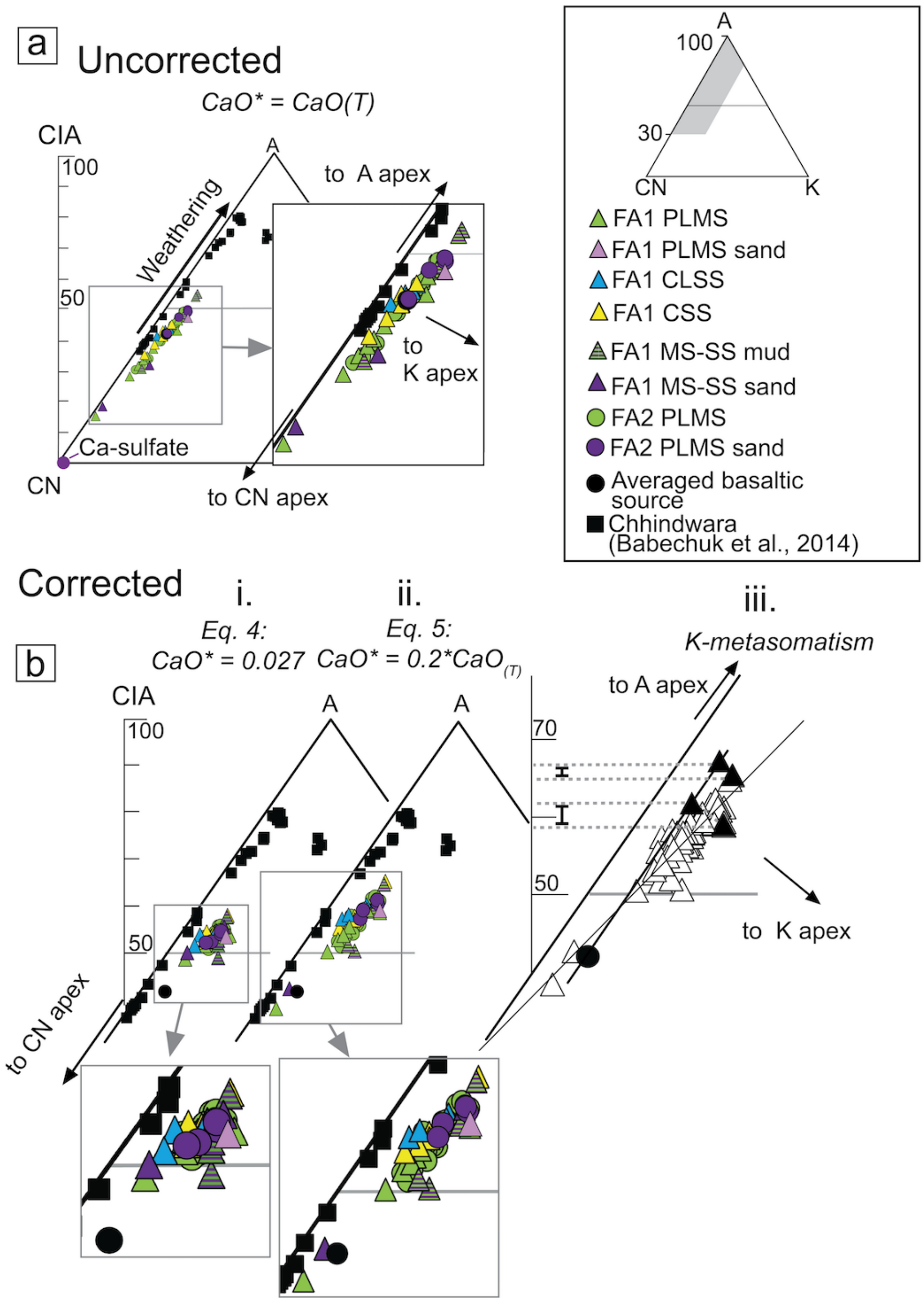

Figure 3.8 Weathering trends shown in A-CN-K molar ternary diagrams. (a) Uncorrected data. (b) Ca-corrected data using the calculation from Equation 4 (i) and Equation 5 (ii). A second A-CN-K diagram corresponding to calculated CaO* from Equation 5 shows examples of the visual correction for K-enrichment (See Fedo et al., 1995 for methodology). Included for comparison is the terrestrial Chhindwara weathering profile (black squares; Babechuk et al., 2014) and the averaged source composition (black circle; Gwizd et al., 2022).

difference in the distribution of data and CIA values between both datasets. Also included for comparison in ternary diagrams is the post-Pleistocene Chhindwara weathering profile (black boxes), a moderately weathered profile developed on Deccan Trap basalt (Babechuk et al., 2014).

A-CN-K

Figure 3.8a shows the distribution of uncorrected facies. Uncorrected data plot along a mixing line between the pre-diagenesis composition and $CaSO_4$, which plots on the CN apex (Figure 3.8a). The uncorrected data array shows that post-depositional Ca-sulfate plays a big role in present day composition.

Relative to uncorrected data, both Ca-correction schemes provide strong evidence for moderate chemical weathering. When Ca-corrected with Equation 4, CIA values shift from an uncorrected a range of 15–55 (40 units) to a range of 49–58 (9 units) (Figure 3.8bi; additional file attachment Table 3.2), signifying a slight increase in the overall weathering extent. Facies plot close to moderately weathered data points within the Chhindwara profile (black squares; Babechuk et al., 2014). Compared to uncorrected data, the distribution of data Ca-corrected with Equation 4 is substantially more clustered. Additionally, the distribution of data does not show any differences between facies and grain sizes. Geochemical trends for the Equation 4 correction are consistent with steady state weathering conditions where relatively equal rates of chemical and mechanical weathering facilitate derivation of sediment from similar zones within a weathering profile, producing more clustered distributions of datapoints in A-CN-K space (Nesbitt et al., 1997).

Data Ca-corrected with Equation 5 produce a slightly more linear trend (Figure 3.8bii) compared to data in Figure 3.8bi, with facies plotting along a CIA range of 38–65 (27 units; additional file attachment Table 3.2). No differences between facies and grain sizes are observable from this correction in A-CN-K space. Data plot close to more substantially weathered data points in the Chhindwara profile compared to data generated with the Equation 4 correction (Figure 3.8bi), which implies a relatively greater overall extent of weathering. The greater range of CIA units over which data plot in Figure 3.8bii signifies more non-steady state weathering conditions compared to Figure 3.8bi, involving increased rates of erosion relative to weathering and derivation of sediment from slightly different mineralogical zones within the weathering profile, which generates data that plot along linear trends similar to the Chhindwara weathering profile (Nesbitt et al., 1997).

In all three diagrams, data plot away from the predicted weathering trend along the A-CN join, which likely indicates some K-addition through diagenesis (Mangold et al., 2019). This diagenetic enrichment needs to be considered when interpreting chemical weathering signatures. Though geochemical trends depicted by both Ca-correction schemes are considered throughout this study, the graphical correction for diagenetic K-addition developed by Fedo et al. (1995) was only carried out on the dataset Ca-corrected with Equation 5 in order to determine the maximum possible extent of weathering for SIm facies (Figure 3.8biii). Correcting for K-addition only raises individual CIA values by several units, indicating negligible influence by K-addition. Overall, corrections for non-silicate phases provide a more accurate depiction of weathering extent relative to uncorrected data.

Both Ca-correction schemes generate CIA values indicative of moderate chemical weathering recorded in SIm facies, but corresponding geochemical trends depict two differing weathering scenarios. Geochemical similarities observed between all facies in Figure 3.8bi are consistent with steady state weathering during which the relative rates of chemical weathering and mechanical erosion of sediment from the source rock are equal (Nesbitt et al., 1997). Although data points Ca-corrected with Equation 5 also overlap in A-CN-K space, the greater range of calculated CIA units (28 units) compared to data Ca-corrected using Equation 4 (9 units) suggests more non-steady state conditions (Figure 3.8bii). Such conditions may have been characterized by intervals in which the relative rate of chemical weathering lagged behind the rate of erosion, enabling erosion of sediment from multiple zones within the weathered source (Nesbitt et al., 1997). Differing geochemical trends observed in Figure 3.8bi and ii highlight the sensitivity of the SIm dataset to interpretations of corrections made to CaO values and emphasize the importance of such corrections for geochemical datasets on Mars. Further constraints on the conditions of chemical weathering recorded in SIm facies are discussed below using additional ternary diagrams that incorporate molar proportions of Fe and Mg.

A-CNK-FM

Incorporation of Fe and Mg ("FM") in the A-CNK-FM ternary diagram permits visualization of mafic components of basaltic sediments (e.g., olivine, pyroxene, Fe-oxides; Babechuk et al., 2014). Figure 3.9 includes SIm facies compositions uncorrected for non-silicate Ca-phases (Figure 3.9a) and corrected for non-silicate Ca-phases using Equation 4 (Figure 3.9b), respectively. The distribution of Equation 4 Ca-corrected data shown in Figure 3.9 is generally consistent with the distribution of data Ca-corrected using Equation 5. Data Ca-corrected with Equation 5, which display a similar trend to data Ca-corrected with Equation 4 in A-CNK-FM space, are included in supplemental Figure 3.14.

Within the A-CNK-FM diagram, the majority of uncorrected facies plot below the feldspar-olivine join (Figure 3.9a). In contrast to the Chhindwara weathering profile (black squares; Babechuk et al., 2014), which follows the expected trend for weathering profiles, uncorrected facies are relatively clustered and show the same minimal weathering extent in A-CNK-FM space. Several data points plot along a linear trend extending toward the CNK apex, signifying the influence of Ca-sulfate in the uncorrected dataset and the need to utilize corrected data to assess the pre-diagenesis weathering signature.

Ca-corrected facies follow a trend along the feldspar-olivine join, with some data points plotting slightly above this line (Figure 3.9b). No differences were observed

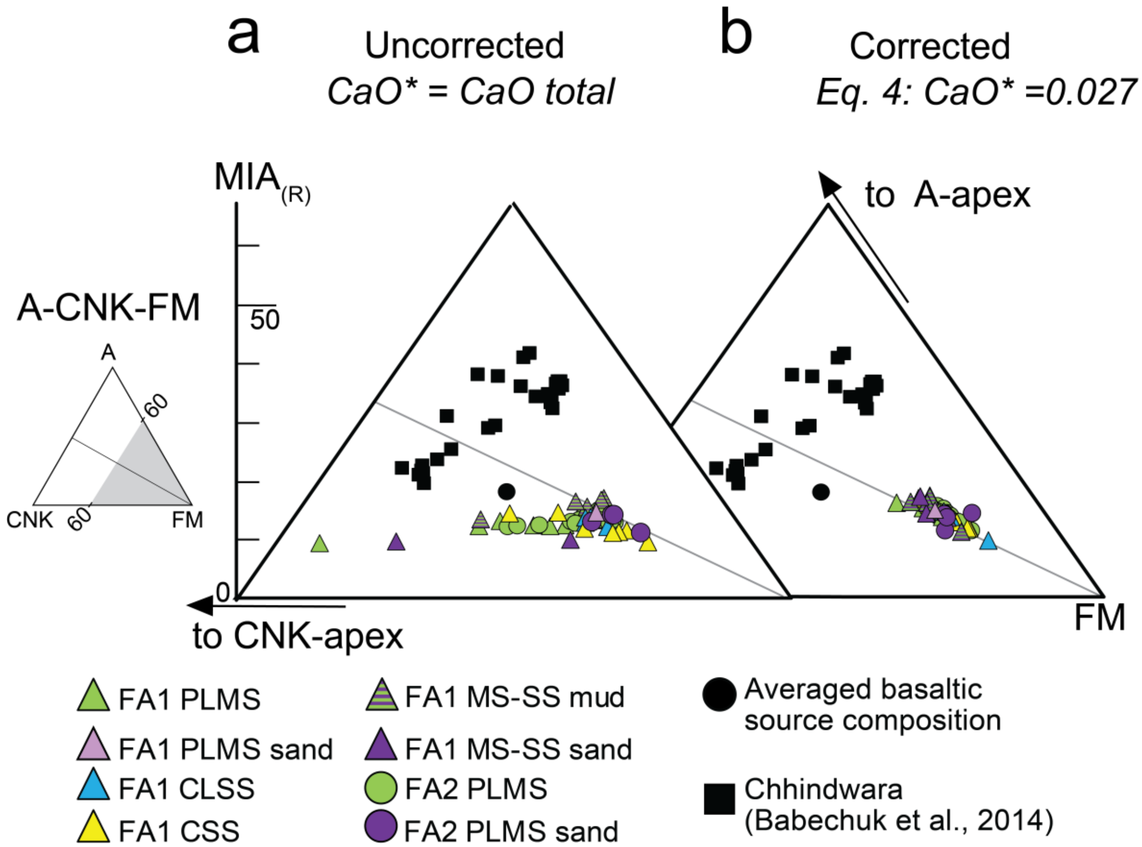

Figure 3.9 Weathering trends shown in A-CNK-FM molar ternary diagrams. The grey shaded region within the small triangle corresponds to the expanded regions in (a) and (b). (a) depicts uncorrected data and (b) depicts data Ca-corrected using Equation 4. Included for comparison is the terrestrial Chhindwara weathering profile (black squares; Babechuk et al., 2014) and the averaged source composition (black circle; Gwizd et al., 2022).

between facies or grain sizes in the Ca-corrected dataset. Similar to uncorrected data, corrected data do not follow a predicted weathering pathway depicted with the Chhindwara weathering profile nor show evidence of extensive weathering. The discrepancy between SIm facies and the Chhindwara weathering profile contrasts with the weathering indices and geochemical trends observed in Figure 3.8bi and ii. The proximity of facies to the FM-apex suggests possible Fe-enrichment, which may represent the effects of sorting (discussed below; Fedo et al., 2015; McGlynn et al., 2012) or diagenesis (discussed below; Achilles et al., 2020).

AF-CNK-M

Evaluation of trends in the AF-CNK-M diagram, which allows for differentiation of feldspar (CNK) and oxidative mafic mineral weathering (M; Babechuk et al., 2014; Babechuk & Fedo, 2022), may help to explain the contradictory trends between the A-CN-K ternary diagrams (Figure 3.8b) and the A-CNK-FM ternary diagram (Figure 3.9b). Uncorrected facies plot along a $MIA_{(O)}$ range of 29–71 (42 units; additional file attachment Table 3.2) with most data points plotting at values of $MIA_{(O)}$ at or above the averaged source composition (Figure 3.10a). Several data points exhibit a slight trend toward the CNK apex, but this trend is interpreted to be indicative of Ca-sulfate enrichment rather than feldspar weathering.

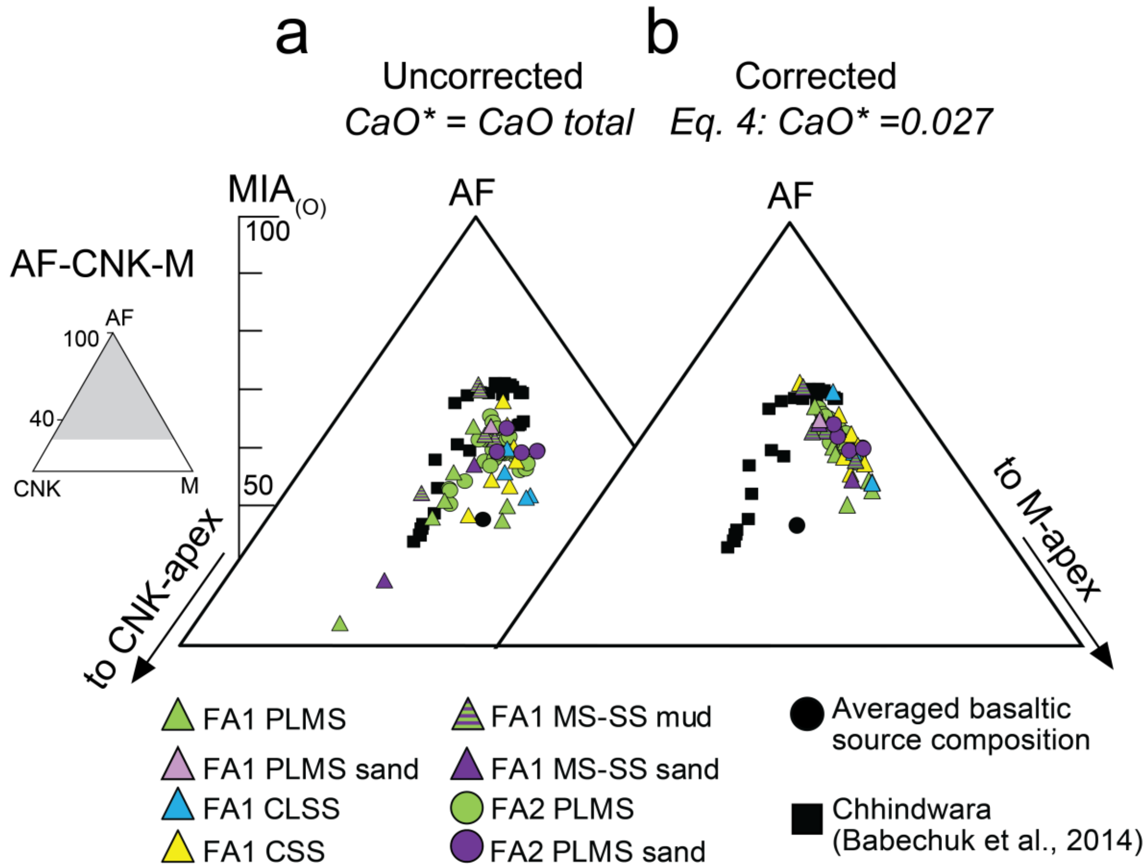

Figure 3.10 Weathering trends shown in AF-CNK-M molar ternary diagrams. The grey shaded region within the small triangle corresponds to the expanded regions in (a) and (b). (a) depicts uncorrected data and (b) depicts data Ca-corrected using Equation 4. Included for comparison is the terrestrial Chhindwara weathering profile (black squares; Babechuk et al., 2014) and the averaged source composition (black circle; Gwizd et al., 2022).

Correcting facies for non-silicate Ca-bearing phases with Equation 4 shifts values of $MIA_{(O)}$ to a range of 51–72 (21 units; Figure 3.10b; additional file attachment Table 3.2). Ca-corrected data exhibit a linear trend sub-parallel to the AF-M join. This sub-parallel trend is slightly offset from the M apex, suggesting that facies in Figure 3.10b are not recording a mafic weathering vector (Figure 3.3c). All data plot at $MIA_{(O)}$ values above the averaged source composition, at a similar range as more extensively weathered samples in the Chhindwara weathering profile (black squares). Ca-corrected data show no differences between facies in the AF-CNK-M diagram.

A-CNKM-F

Given the proximity of facies to the FM apex in Figure 3.9b and the linear trend observed by the Ca-corrected data in Figure 3.10b, the A-CNKM-F diagram further constrains the relative role of Fe and Mg on the geochemical signature of SIm facies. Figure 3.11a shows the distribution of uncorrected facies. Data from the Chhindwara weathering profile plot along a trend emanating toward the A apex, signifying the loss of labile cations Ca, Na, Mg, and K during weathering (Babechuk et al., 2014). In contrast to the Chhindwara profile, uncorrected facies from the SIm plot along a trend projecting toward the F apex (Figure 3.11a), signifying Fe-enrichment within the whole-rock geochemical signatures. Correcting for non-silicate Ca-bearing phases shifts data slightly more proximal to the F apex (Figure 3.11b). The distribution of data in both the uncorrected and Ca-corrected diagrams shows overlap between facies and overall grain sizes. Overall, Fe-enrichment is indicated by the distribution of SIm facies in the

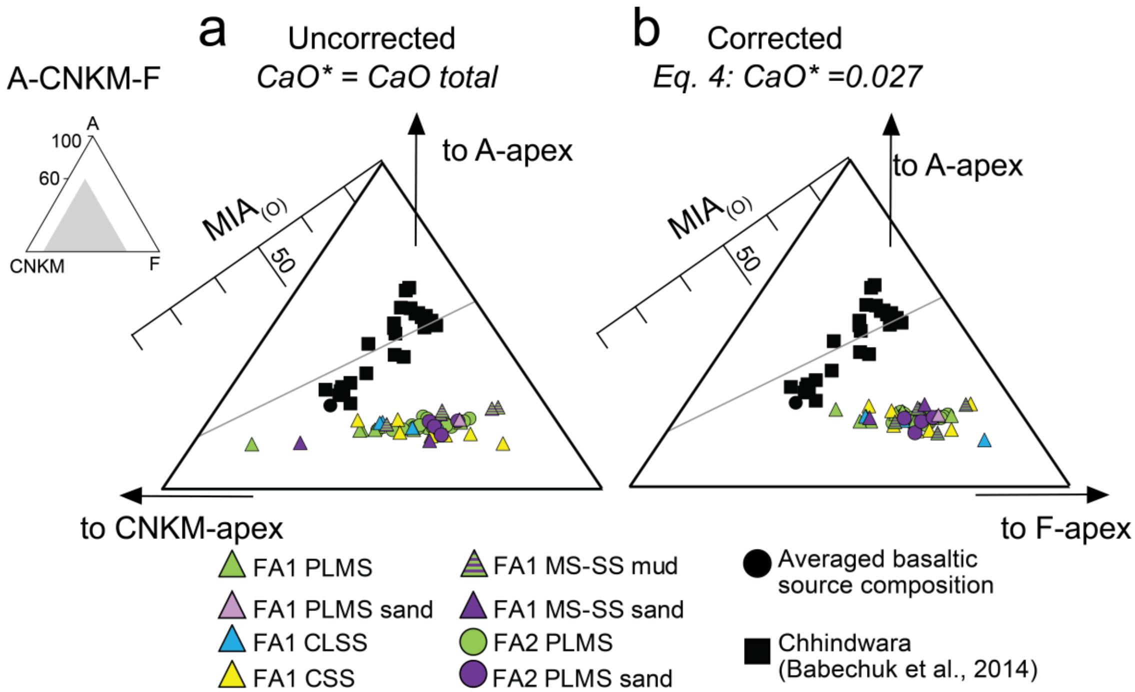

Figure 3.11 Weathering trends shown in A-CNKM-F molar ternary diagrams. The grey shaded region within the small triangle corresponds to the expanded regions in (a) and (b). (a) depicts uncorrected data and (b) depicts data Ca-corrected using Equation 4. Included for comparison is the terrestrial Chhindwara weathering profile (black squares; Babechuk et al., 2014) and the averaged source composition (black circle; Gwizd et al., 2022).

A-CNKM-F ternary diagram, and likely accounts for the trend of facies in the A-CNK-FM ternary diagram (Figure 3.9b).

Weathering synthesis

Weathering indices and geochemical trends of Ca-corrected data in A-CN-K, A-CNK-FM, AF-CNK-M and A-CNKM-F ternary diagrams provide evidence for variable chemical weathering recorded in SIm facies (Figures 3.8-3.11; additional file attachment Table 3.2). Within the A-CN-K ternary diagram, plots of both Ca-correction schemes show moderate-to-extensive weathering (Figure 3.8b) under possible steady- (Equation 4; Figure 3.8bi) or more non-steady-state (Equation 5; Figure 3.8bii) conditions. Given the contrast between the greater range over which data plot in Figures 3.9b, 3.10b, and 3.11b relative to the significantly clustered distribution of data Ca-corrected with Equation 4 in Figure 3.8bi, the greater range over which data Ca-corrected using Equation 5 plot in Figure 3.8bii may represent a more accurate depiction of weathering conditions.

Non-steady-state conditions could signify an outpacing of weathering of the source composition by the relative rate of erosion, enabling sediments sourced from differing parts of a weathering profile (Nesbitt et al., 1997), or indicate the occurrence of additional chemical weathering of sediment during transport in temporary storage sites (Bouchez et al., 2012; Thorpe et al., 2019). Compositional and geomorphologic assessments of the rocks along the northern crater rim propose this locality as a likely source for the Gale crater sediments (Buz et al., 2017; Mangold et al., 2016; Grotzinger et al., 2015), though more regional watersheds have also been proposed (Ehlmann & Buz, 2014). A northern crater rim source would signify a total source-to-sink pathway of <30 meters in length, suggesting that the time sediment may have spent within temporary storage was relatively short-lived. Therefore, the trends observed in Figure 3.8bii are more likely indicative of increased rates of erosion at the source region.

Geochemical trends in A-CN-K space and corresponding CIA values for SIm facies (additional file attachment Table 3.2) indicate moderately extensive geochemical weathering, whereas geochemical trends in ternary diagrams that include the mafic FM-component deviate from predicted weathering trends (Figure 3.9). Similar to the findings of Gwizd et al. (2022) in an assessment of weathering in the underlying Hartmann's Valley and Karasburg member facies, a key difference between the A-CN-K ternary diagram and A-CNK-FM ternary diagram is the proximity of facies to the A apex. This discrepancy in apparent weathering extent between ternary diagrams has been documented in samples in two previous terrestrial studies (Fedo & Babechuk, 2022; Nesbitt & Young, 1996), where a trend between mud and sand was observed in A-CN-K space but both grain size fractions plotted at a similar distance from the A apex in A-CNK-FM space. The study by Nesbitt and Young (1996) attributes this discrepancy to the effect of sorting of feldspars. The study by Fedo and Babechuk (2022) emphasizes the importance of the Fe- and Mg-bearing phases in assessing compositional differentiation and the need to interpret weathering from multiple ternary diagrams that incorporate the mafic component. Both weathering and hydrodynamic sorting may account for the discrepancy in apparent weathering extent between the A-CN-K and A-CNK-FM diagrams. Some component of the Fe-enrichment depicted in the A-CNK-FM (Figure

3.9b) and the A-CNKM-F (Figure 3.11b) ternary diagrams may also represent alteration of olivine, pyroxene, or basaltic glass to Fe-oxides during lithification and burial, as has been previously interpreted from CheMin mineralogical data (Achilles et al., 2020).

Facies associations and depositional environments interpreted from SIm stratigraphy (Gwizd et al., Chapter 2) suggest that aqueous activity was prevalent across the landscape at the time of deposition. Processes recorded in the delta plain environment interpreted in FA1 and the lacustrine environment interpreted in FA2 involved aqueous conditions that were conducive chemical weathering and subsequent alteration of the geochemistry of SIm sediment. Chemical weathering is also supported from the presence of phyllosilicate phases measured in the Sebina drill sample (Achilles et al., 2020; Bristow et al., 2018). Overall, the findings in this study indicate at least a moderate amount of chemical weathering and emphasize the critical need for interpretation of geochemical data with CaO values corrected to represent only that hosted by silicate minerals. The above discussion also supports recent studies that emphasize multiple ternary diagrams for cohesive interpretations of all weathering-related processes and highlight the inherent pitfalls in interpreting mafic weathering trends solely from the A-CN-K ternary diagram (Babechuk & Fedo, 2022; Fedo & Babechuk, 2022).

Sorting

Although delta plain and lacustrine environments constitute the relatively finer-grained sediment fraction toward the end of the source-to-sink sediment pathway, sediment transport and depositional processes interpreted in the deltaic (FA1) and lacustrine (FA2) environments of the SIm are capable of segregating grains based on size, shape, and density (Frihy et al., 2022; Mangold et al., 2011; Siebach et al., 2017; Thorpe et al., 2019). As a result, some degree of compositional modification of whole-rock geochemistry should occur via hydrodynamic sorting in SIm facies. Interpretation of geochemical sorting signatures in SIm stratigraphy requires assessment of relationships between facies, grain size, and composition.

Geochemical trends of SIm facies in the ternary diagrams in Figures 3.8-3.11 contradict expected sorting trends where mineral phases are segregated in transport based on density, producing a correlation between composition and grain size. Ternary diagrams of Ca-corrected data show the significant geochemical overlap between facies and associated grain sizes. This observation contrasts with typical sorting trends where data show a distribution of finer grain-sizes more proximal to the minerals that plot on the FM apex (olivine, pyroxene, Fe-Ti oxides) and coarser grain-sizes more proximal to feldspars (Fedo et al., 2015; McGlynn et al., 2012). Despite the interpretations of sediment transport processes in SIm facies (Gwizd et al., Chapter 2), geochemical trends in ternary diagrams are not indicative of significant compositional segregation of grain size fractions, indicating that diagrams record additional processes that overprint this signature.

Another common indicator of sorting is the relative wt% of Al_2O_3 and TiO_2. In basaltic lithologies, TiO_2 typically occurs in oxides, glass, and biotite (Nesbitt &

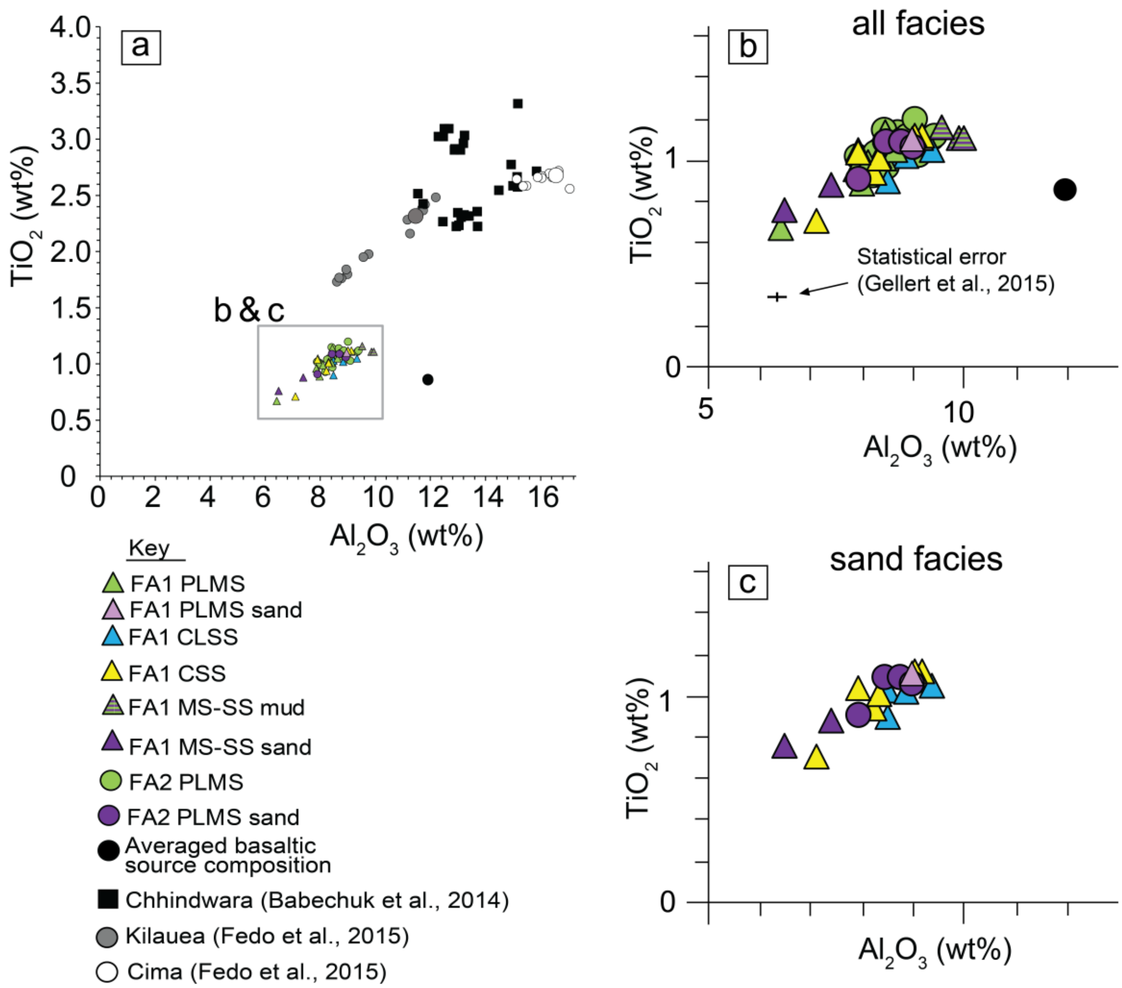

Figure 3.12 (a) Comparison of wt% Al_2O_3 and TiO_2 of SIm facies. Included for comparison is the averaged source composition (black circle; Gwizd et al., 2022), the terrestrial Chhindwara weathering profile (black squares; Babechuk et al., 2014), the Baynton Basalt profile (Nesbitt & Wilson, 1992), and the experimentally crushed and sieved Kilauea and Cima Basalt samples (Fedo et al., 2015). (b) Expanded inset showing SIm facies. (c) Expanded inset showing facies comprised of sand-sized sediment. Error bars correspond to values in Table 1 of Gellert et al. (2015), and are representative of typical APXS statistical error of precision.

Markovics, 1997; Nesbitt & Wilson, 1992). Both Al_2O_3 and TiO_2 are relatively immobile within the sedimentary system during weathering and diagenesis (Young & Nesbitt, 1998). Figure 3.12 includes SIm facies as well as data from several basaltic sedimentary systems. The Chhindwara weathering profile (black squares; Babechuk et al., 2014) is included to compare Al_2O_3-TiO_2 trends in a system affected by weathering. Also included for comparison are unweathered samples of Kilauea (grey circles) and Cima (white circles) basalt that have been experimentally sieved to simulate the effects of sorting (Fedo et al., 2015). Within SIm facies (Figure 3.12b), mudstone facies generally appear more clustered relative to sandstone facies, which exhibit a slight linear trend similar to the sorted Kilauea dataset (Figure 3.12c). Compared to terrestrial weathering profiles, SIm facies plot at a relatively lower range of wt% Al_2O_3 (wt% 6.4 – 10) and TiO_2 (wt% 0.7 – 1.2). Facies are offset to lower wt% Al_2O_3 relative to the averaged source composition (black circle). This observation contrasts with the Kilauea and Cima data points, which plot along a diagonal trend that includes source composition (large grey and white circles). Planar-laminated mudstone with minor sandstone comprising FA2 exhibits a slightly clustered distribution relative to FA1 facies, plotting in the relatively higher Al_2O_3-TiO_2 region within the SIm dataset (green circles), but in general, facies and grain sizes plot along a similar overall range of wt% Al_2O_3 and TiO_2.

The linear trend of sandstone facies and the relative position of facies to the averaged source rock composition (Figure 3.12) indicates that sorting influenced the geochemical distribution of SIm facies. Both observations are consistent with sedimentary systems that record both weathering and sorting. Young & Nesbitt (1998) interpret diagonal trends in recent sediments from the Mallacoota drainage system to indicate the combined effects of weathering and sorting, where Ti exhibits a similar behavior (in Fe and Ti oxides or oxyhydroxides or adsorbed on clays) as Al and is relatively concentrated in finer-grained weathered sediment fraction relative to the sand-sized fraction (feldspars and quartz). The offset between the best fit line of the linear array and the source composition (Figure 3.4b in Young & Nesbitt, 1998) is interpreted to signify the loss from the sand-sized fraction of aluminous minerals (feldspars) due to weathering and of clays due to removal in transport.

One key difference between the trends of Mallacoota sediments and SIm facies is the lack of Al-Ti enrichment in the finer grain-size fraction in SIm sediments as compared to the coarser grain-size fraction (Figure 3.12). The lack of distinct geochemical differences between grain-size fractions may signify a small overall grain size range between the distal delta plain and lacustrine environments. Furthermore, dynamic processes interpreted along the delta plain environments of FA1 (subaerial exposure, channel avulsion, fluctuations in flow energy; Gwizd et al., Chapter 2) are capable of facilitating deposition of different grain-size fractions in close proximity and could also result in some degree of mixing of different grain sizes. At the facies level, Gwizd et al., Chapter 2) interprets fluctuations in grain size interpreted across relatively thin (mm-cm) stratigraphic intervals in the planar-laminated mudstone facies in FA1 and FA2 and the alternating laminated sandstone and mudstone facies in FA1 (Figure 3.2a, d–e).

Another possible factor is the phenocryst size of the basaltic source composition. Fedo et al. (2015) found that mechanical crushing and sieving of the porphyritic Kilauea basalt resulted in substantial compositional change between grain-size fractions, whereas the aphyric Cima basalt shows comparably limited compositional change from sorting. Crystal size for the source composition of SIm facies may have been aphyric and therefore limited compositional variability from sediment sorting.

Given the depositional processes associated with the facies in the SIm (traction transport, sediment gravity flows), sorting of mineral phases is expected. Depositional processes interpreted in SIm facies indicate that hydrodynamic sorting occurred and limited compositional variability from sorting may have resulted from a combination of factors including source phenocryst size, a restricted grain-size range across the delta plain and lacustrine environments, and homogenization of different grain-size fractions within individual facies.

Diagenesis

Diagenetic enrichment of Murray formation stratigraphy has been interpreted from geochemistry (Gwizd et al., 2022; Thompson et al., 2020), mineralogy (Achilles et al., 2020; Bristow et al., 2018, 2021), and macro-scale diagenetic features (e.g., veins, concretions; Bennett et al., 2021; Kronyak et al., 2019; Sun et al., 2019). Relative timelines for diagenetic episodes, derived from compositional interpretations of temperature conditions (Rampe et al., 2020a, 2020b) as well as stratigraphic relationships (Bristow et al., 2021; De Toffoli et al., 2020), are indicative of early- to late-stage episodes involving compositionally variable fluid flow. Within the SIm, morphologically irregular features (Sun et al, 2019) and compositional interpretations (Haber et al., 2022; Rapin et al., 2019) suggest a complex history of early- and late-stage diagenetic enrichment. Contextualization of geochemical trends with mineralogical measurements from Sebina (Achilles et al., 2020; Bristow et al., 2020) and assessments of macroscale diagenetic features in the SIm can further demonstrate the extent to which diagenetic phases enrich the whole-rock geochemical signatures of SIm facies.

Calcium sulfate is the most common diagenetic phase throughout the Murray formation, including SIm stratigraphy. Within SIm stratigraphy, Ca-sulfate occurs as veins, concretions, and disseminated cement (Rapin et al., 2019; Sun et al., 2019; Thompson et al., 2020). The APXS dataset utilized in this study excludes measurements acquired on macro-scale diagenetic features, but several uncorrected data points nevertheless show a clear trend toward the C apices (Figures 3.8-3.11). Such trends support the correlation of wt% CaO and SO_3 observed in Figure 3.4 and highlight the influence of disseminated Ca-sulfate cement on the whole-rock geochemical signature of SIm facies. Abundant Ca-sulfate veins and concretions (Sun et al., 2019) support a diagenetic interpretation for Ca-sulfate cements rather than a primary depositional interpretation involving saline conditions (e.g., Rapin et al., 2019).

Iron oxide constitutes another common diagenetic phase (Achilles et al., 2020; Horgan et al., 2020; Rampe et al., 2020b). Within SIm facies, ternary diagrams in Figures 3.9 and 3.11 show a clear enrichment in wt% $FeO_{(T)}$. Diagenetic Fe-oxides likely account, in part, for the observed wt% $FeO_{(T)}$ enrichment. Achilles et al. (2020)

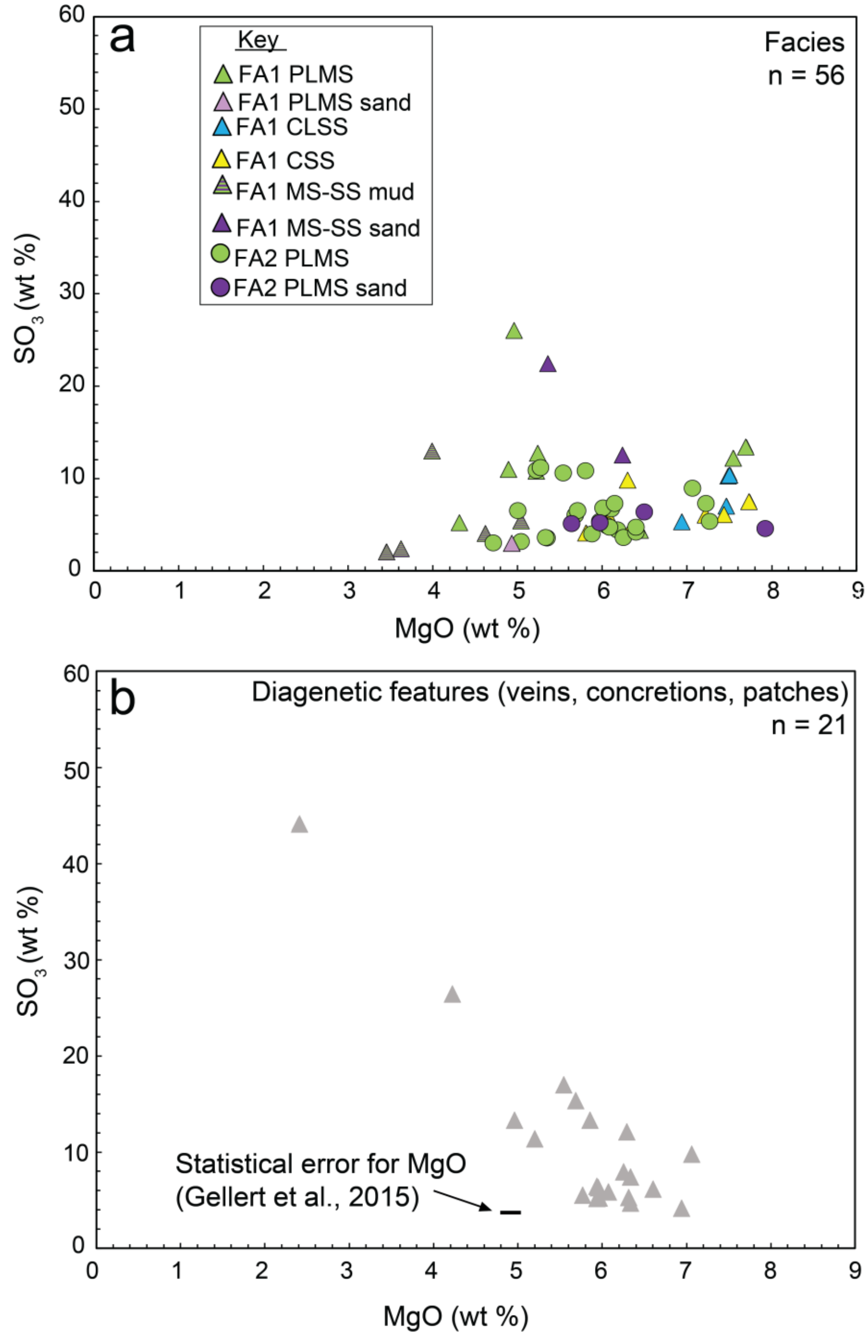

Figure 3.13 Comparison of wt% MgO and SO_3 in (a) SIm facies (n = 56) and (b) APXS measurements of diagenetic features or bedrock characterized by abundant diagenetic features (e.g., veins, concretions; n = 21). The error bar for MgO corresponds to the value in Table 1 of Gellert et al. (2015), and is representative of typical APXS statistical error of precision (error bar for SO_3 is below the resolution of the image).

interpreted hematite in Sebina to represent diagenetic fluid flow in oxidizing conditions and at relatively low temperatures. Geochemical trends identified in SIm facies may result from a similar diagenetic origin.

In contrast with previous mineralogical and geochemical studies (Achilles et al., 2020; Rapin et al., 2019), APXS geochemical trends of SIm facies do not indicate the predominance of Mg-sulfate. Comparisons of wt% MgO and SO_3 in APXS data points acquired on primary bedrock (n = 56; Figure 3.13a) and data points acquired on bedrock with diagenetic features (e.g., veins, concretions, grey patches; n = 21; Figure 3.13b) do not show a correlation between oxides. Rapin et al. (2019) interpreted dark-toned bedrock with Mg-sulfate enrichments identified around an elevation of -4287 m to represent evapo-concentrated brines and signify the onset of widespread aridity. Around this interval, proximal to the contact between the SIm and BPm, concretions, gray layers, and nodular patchy features that are enriched in Fe, Mn, Mg, P, and Zn have been interpreted to represent multiple diagenetic fluid episodes (Sun et al., 2019; Thompson et al., 2020). Bristow et al. (2021) interpreted Mg-sulfate to have formed via diagenetic infiltration of brines originating from the sulfate-bearing unit. Given the patchy, cross-cutting relationship between dark-toned material and primary laminae observed at the stratigraphic interval noted by Rapin et al. (2019; supplemental Figure 3.15), a diagenetic interpretation for Mg-sulfate is preferred over a primary interpretation. Nevertheless, the lack of geochemical trends indicative of Mg-sulfate (Figure 3.13) suggests that the influence of Mg-sulfate on the overall SIm geochemical signature was relatively minimal.

Geochemical trends of facies in A-CN-K ternary space are indicative of minor K-enrichment. Potassium metasomatism is a process by which aluminous clays are converted to illite and enriched in K^+ (Fedo et al., 1995). Data points are offset from the A-CN join in both ternary diagrams featuring Ca-corrected data (Figure 3.8b) implying that some K-enrichment occurred. Mangold et al. (2019) calculated the wt% K_2O associated with sanidine in the Marimba drill sample (Km) to account for 0.4 out of 1.0 wt% K_2O, utilizing an average value of 14 wt% K_2O in sanidine based on data in Morrison et al. (2018). Application of this calculation to the proportion of sanidine in the Sebina drill sample (Achilles et al., 2020) generates a value of 0.18 wt% K_2O. Some of the remaining ~0.52 wt% K_2O in Sebina may represent K-enrichment via metasomatism, but phases such as amorphous K-bearing phases or jarosite may also be responsible for the remaining wt% K_2O (Bristow et al., 2018).

Additional context from the Sebina drill sample, acquired from the planar-laminated mudstone with minor sandstone facies of FA1 (Gwizd et al., Chapter 2), indicates the presence of abundant diagenetic phases (Achilles et al., 2020). In addition to crystalline phases, Achilles et al. (2020) interpret amorphous phases in Sebina, comprising 51% of the total mineralogy, as evidence of diagenetic fluid flow in oxidizing conditions and at relatively low temperatures. Overall, Ca-sulfate is the most prevalent diagenetic phase recorded in SIm geochemistry, but additional compositional interpretations suggest that variable fluid compositions representing early- to late-stage diagenetic processes are recorded in the SIm (Achilles et al., 2020; Sun et al., 2019).

Diagenetic phases within the geochemistry of SIm facies capture the longevity and variability of post-depositional fluid flow.

Discussion: Integrated depositional and compositional pathway

Geochemical trends identified in this study are indicative of a basaltic sedimentary system that primarily represents moderate to substantial amounts of chemical weathering and enrichment from numerous diagenetic fluids of various compositions. Most trends do not unambiguously show links between grain size and composition (Figure 3.10) although hydrodynamic sorting in sediment transport is shown and expected based on interpretations of depositional processes and environments recorded in SIm facies (Gwizd et al., Chapter 2). The following discussion applies the well-established links between whole-rock compositional records and depositional sedimentary processes (Johnsson et al., 1993) to build a source-to-sink history of the SIm facies.

Sediment comprising SIm stratigraphy was most likely sourced from the crater rim (Buz et al., 2017), which is interpreted as a plausible source of sediment for the SIm facies based on previous interpretations of composition (Mangold et al., 2016) and geomorphology as well as calculations of sediment supply from rates of crater rim and wall erosion (Grotzinger et al., 2015). Some sediment may also derive from more regional watersheds (Ehlmann et al., 2014). Comparison of facies to known igneous compositions measured at Gale (Berger et al., 2020; Schmidt et al., 2014; Thompson et al., 2016; Wiens et al., 2020) and basalt classes measured at Gusev crater (additional file attachment Table 3.1; Gellert et al., 2006; McSween et al., 2008; Ming et al., 2008) indicates that the SIm source rock composition was basaltic, which correlates with previous interpretations of Murray formation source rock lithologies (Bedford et al., 2019; Edwards et al., 2017). Relatively homogenous whole-rock geochemistry between facies and associated grain-size fractions indicates that all SIm sediment likely derived from a similar source composition. Low compositional variability may also indicate an aphyric basalt as the predominant source composition, such that sorting would naturally play a smaller role in segregating mineral phases (Fedo et al., 2015).

Weathering of the crater rim or within regional watersheds produced a sediment mixture of primary mineral (e.g., pyroxene, feldspar) and secondary phyllosilicate phases. Coupled with geochemical trends, CIA values of Ca-corrected data points suggest that weathering was moderate with some potential for substantial modification (Figure 3.8b; additional file attachment Table 3.2). Interpretating corresponding climate conditions at the time of sediment formation is difficult due to the possibility for additional weathering of sediment in transport, though the relatively small transport distance suggests that temporary storage would have been relatively minimal for sediments sourced from the crater rim. Regardless, production of phyllosilicates via hydrolysis, transport of sediment into the basin (Grotzinger et al., 2015; Williams et al, 2013), and subsequent deposition in aqueous lacustrine and lacustrine margin environments (Gwizd et al., Chapter 2) required an environment capable of sustaining water and facilitating a modest amount of chemical weathering.

Weathering conditions recorded in SIm stratigraphy represent a slight shift from conditions in the underlying, older Hartmann's Valley and Karasburg member stratigraphy. Correcting data points for non-silicate Ca-bearing phases generates a more clustered distribution of SIm facies (Figure 3.8b) relative to uncorrected data (Figure 3.8a). Calculated CIA ranges for the majority of Ca-corrected data (9 units with Equation 4; 15 units with Equation 5, excluding two outliers) are more restricted than the CIA range of HVm and Km facies (19 CIA units; Gwizd et al., 2022). The lower CIA ranges in SIm facies may signify a slight shift from underlying members toward more steady-state weathering conditions defined by equal rates of weathering and erosion, resulting in erosion of sediment from a similar compositional zone of a weathering profile (Nesbitt et al., 1997). Such a shift could represent a relative decrease in the rate of erosion of material from the northern crater rim compared to erosion recorded in underlying stratigraphic members.

Erosion from the initial source basalt and entrainment in transport results in physical modification of sediment. Along the source-to-sink pathway, initial transport of sediment proximal to the crater rim (Grotzinger et al., 2015) would have occurred via high-energy processes (e.g., flooding, mass-wasting) and produced coarser-grained deposits (Palucis et al., 2014; Williams et al., 2013). Subsequent to these processes, entrainment of sediment in fluvial transport facilitated conditions for hydrodynamic sorting. Trends in immobile oxides are consistent with geochemical signatures of sorting (Figure 3.12), with geochemical similarities between facies and associated grain sizes indicative of restricted compositional variability due to a more aphyric source composition (Fedo et al., 2015). At the site of deposition, dynamic processes of delta plain subenvironments may have facilitated mixing of different grain sizes (e.g., channel avulsion or cutoff; Muhlbauer et al., 2020) and further homogenized resulting whole-rock compositions.

Diagenetic enrichment and alteration of sediments occurred during burial and lithification. Following lithification, Ca-sulfate was deposited via multiple episodes of diagenetic fluid flow in veins, concretions, and matrix cements (Achilles et al., 2020; Sun et al., 2019). Enrichment in Fe-oxide may have occurred via multiple episodes of early- to late-stage diagenesis, interpreted in Achilles et al. (2020). The shift of SIm data as a result of the Ca-corrections applied in this study (Equations 4 & 5) highlights the substantial influence of Ca-sulfate on the whole-rock geochemical signature. Magnesium sulfate has been interpreted from ChemCam data in a localized layer by Rapin et al. (2019), but this study does not interpret this phase to be a predominant phase throughout SIm stratigraphy. Given the discontinuity of dark-toned material with respect to primary stratigraphy, Mg-sulfate likely represents a diagenetic phase (Bristow et al., 2021). Burial of sediments facilitated potassium metasomatism and enrichment of whole-rock geochemistry in K^+ (Fedo et al., 1995). Mineralogical measurements from the Sebina drill sample show various diagenetic phases (Achilles et al., 2020), which corroborate geochemical interpretations for prolonged and compositionally diverse aqueous activity from deposition to post-lithification.

Conclusions

This study deciphers the geochemical signatures of source rock composition, chemical weathering, sediment transport, and diagenesis in the context of individual facies and depositional processes recorded in the Sutton Island member of the Murray formation.

- Comparisons of APXS whole-rock geochemistry with igneous float rocks documented at Gale crater and basalt classes documented at Gusev crater indicate that an averaged value derived from these compositions is a plausible source composition.
- Weathering indices and geochemical trends of facies corrected for non-silicate Ca-bearing phases support moderate to substantial chemical weathering characterized by a slight shift toward comparably steady-state conditions relative to the underlying Hartmann's Valley and Karasburg member geochemistry.
- Contrasting trends between ternary diagrams suggest that facies also record the effects of grain segregation from hydrodynamic sorting in transport. Comparisons of immobile oxides between facies, terrestrial weathering profiles, and mechanically crushed and sieved basalt suggest that general trends in Sutton Island member facies record the effects of hydrodynamic sorting. The significant geochemical overlap between facies contrasts with expected sorting signatures and may be due to several factors. The source basalt may have an aphyric phenocryst size, which produces more limited compositional change via sorting.

Homogeneity between facies may signify a small overall grain-size range captured by the Sutton Island member facies or mixing of different grain sizes within facies from dynamic processes on the delta plain.

- Diagenetic processes involving variable fluid compositions occurred from deposition to post-lithification. Calcium sulfate represents the most significant diagenetic phase as supported by the shift in calculated CIA values and the distribution of data in A-CN-K ternary diagrams between uncorrected data and data corrected for non-silicate Ca-bearing phases using two different correction schemes. Subsequently, the findings of this study highlight the need for similar studies of Gale crater geochemistry to apply corrections for non-silicate Ca-bearing phases and introduce the potential need for correction schemes useful in addressing other geochemical fractions contained in non-silicate phases, especially regarding interpretations of weathering extent and conditions.

Overall, assessments of the compositional record of the Sutton Island member corroborate the sedimentologic and stratigraphic interpretations of dynamic aqueous environments from Gwizd et al. (Chapter 2) and highlight the role of water at all stages of the sediment source-to-sink pathway at Gale crater.

References

Achilles, C. N., Rampe, E. B., Downs, R. T., Bristow, T. F., Ming, D. W., Morris, R. V., et al. (2020). Evidence for multiple diagenetic episodes in ancient fluvial-lacustrine sedimentary rocks in Gale crater, Mars. *Journal of Geophysical Research: Planets*, *125*(8), e2019JE006295. https://doi.org/10.1029/2019JE006295

Babechuk, M. G., & Fedo, C. M. (2022). Analysis of chemical weathering trends across three compositional dimensions: applications to modern and ancient mafic-rock weathering profiles. *Canadian Journal of Earth Sciences*, (ja). https://doi.org/10.1139/cjes-2022-0053

Babechuk, M. G., Widdowson, M., & Kamber, B. S. (2014). Quantifying chemical weathering intensity and trace element release from two contrasting basalt profiles, Deccan Traps, India. *Chemical Geology*, *363*, 56-75. https://doi.org/10.1016/j.chemgeo.2013.10.027

Banham, S. G., Gupta, S., Rubin, D. M., Edgett, K. S., Barnes, R., Van Beek, J., et al. (2021). A Rock Record of Complex Aeolian Bedforms in a Hesperian Desert Landscape: The Stimson Formation as Exposed in the Murray Buttes, Gale Crater, Mars. *Journal of Geophysical Research: Planets*, *126*(4). https://doi.org/10.1029/2020JE006554

Bedford, C. C., Bridges, J. C., Schwenzer, S. P., Wiens, R. C., Rampe, E. B., Frydenvang, J., & Gasda, P. J. (2019). Alteration trends and geochemical source region characteristics preserved in the fluviolacustrine sedimentary record of Gale crater, Mars. *Geochimica et Cosmochimica Acta*, *246*, 234-266. https://doi.org/10.1016/j.gca.2018.11.031

Bennett, K. A., Rivera-Hernández, F., Tinker, C., Horgan, B., Fey, D. M., Edwards, C., et al. (2021). Diagenesis Revealed by Fine-Scale Features at Vera Rubin Ridge, Gale Crater, Mars. *Journal of Geophysical Research: Planets*, *126*(5). https://doi.org/10.1029/2019JE006311

Berger, J. A., Gellert, R., Boyd, N. I., King, P. L., McCraig, M. A., O'Connell-Cooper, C. D., et al. (2020). Elemental composition and chemical evolution of geologic materials in Gale Crater, Mars: APXS results from Bradbury landing to the Vera Rubin ridge. *Journal of Geophysical Research: Planets*, 125(12). https://doi.org/10.1029/2020JE006536

Bouchez, J., Gaillardet, J., Lupker, M., Louvat, P., France-Lanord, C., Maurice, L., et al. (2012). Floodplains of large rivers: Weathering reactors or simple silos? *Chemical Geology*, *332*, 166-184. https://doi.org/10.1016/j.chemgeo.2012.09.032

Brigatti, M.F. (1983). Relationships between composition and structure in Fe-rich smectites. *Clay Minerals*, *18*, 177-186. https://doi.org/10.1180/claymin.1983.018.2.06

Bristow, T. F., Grotzinger, J. P., Rampe, E. B., Cuadros, J., Chipera, S. J., Downs, G. W., et al. (2021). Brine-driven destruction of clay minerals in Gale crater, Mars. *Science*, *373*(6551), 198-204. https://doi.org/10.3390/min11080847

Bristow, T. F., Rampe, E. B., Achilles, C. N., Blake, D. F., Chipera, S. J., Craig, P., et al. (2018). Clay mineral diversity and abundance in sedimentary rocks of Gale crater, Mars. *Science Advances*, *4*(6). https://doi.org/10.1126/sciadv.aar3330

Buz, J., Ehlmann, B. L., Pan, L., & Grotzinger, J. P. (2017). Mineralogy and stratigraphy of the Gale crater rim, wall, and floor units. *Journal of Geophysical Research: Planets*, *122*(5), 1090-1118. https://doi.org/10.1002/2016JE005163

Calef, III, F. J., Abarca, H. E., Soliman, T., Abercrombie, S. P., & Powell, M. W. (2019). Multi-mission geographic information system: An open-source solution for planetary science operations. In the 4th Planetary Data Workshop, Abstract #7071.

Calef III, F. J., & Parker, T. (2016). MSL Gale Merged Orthophoto Mosaic, Publisher: PDS Annex, U.S. Geological Survey. http://bit.ly/MSL_Basemap

Campbell, J. L., Perrett, G. M., Gellert, R., Andrushenko, S. M., Boyd, N. I., Maxwell, J. A., et al. (2012). Calibration of the Mars Science Laboratory alpha particle X-ray spectrometer. *Space Science Reviews*, *170*(1–4), 319–340. https://doi.org/10.1007/s11214-012-9873-5

Caravaca, G., Mangold, N., Dehouck, E., Schieber, J., Zaugg, L., Bryk, A. B., et al. (2022) From Lake to River: Documenting an Environmental Transition across the Jura/Knockfarril Hill Members Boundary in the Glen Torridon Region of Gale crater (Mars). *Journal of Geophysical Research: Planets*. https://doi.org/10.1029/2021JE007093

De Toffoli, B., Mangold, N., Massironi, M., Zanella, A., Pozzobon, R., Le Mouélic, S., et al. (2020). Structural analysis of sulfate vein networks in Gale crater (Mars). *Journal of Structural Geology*, *137*. https://doi.org/10.1016/j.jsg.2020.104083

Deer, W., Howie, R. A., Zussman, J. (1992). *An introduction to the rock-forming minerals* (p. 696). London, UK: Longman.

Edgar, L. A., Fedo, C. M., Gupta, S., Banham, S. G., Fraeman, A. A., Grotzinger, J. P., et al. (2020). A lacustrine paleoenvironment recorded at Vera Rubin Ridge, Gale crater: Overview of the sedimentology and stratigraphy observed by the Mars Science Laboratory Curiosity Rover. *Journal of Geophysical Research: Planets*, *125*(3). https://doi.org/10.1029/2019je006307

Edwards, P. H., Bridges, J. C., Wiens, R., Anderson, R., Dyar, D., Fisk, M., et al. (2017). Basalt–trachybasalt samples in Gale crater, Mars. *Meteoritics & Planetary Sciences*, 52(11), 2931–2410. https://doi.org/10.1111/maps.12953

Eggleton, R. A., Foudoulis, C., & Varkevisser, D. (1987). Weathering of basalt: changes in rock chemistry and mineralogy. *Clays and Clay Minerals*, *35*(3), 161-169. https://doi.org/10.1346/CCMN.1987.0350301

Ehlmann, B. L., & Buz, J. (2015). Mineralogy and fluvial history of the watersheds of Gale, Knobel, and sharp craters: A regional context for the Mars science laboratory Curiosity's exploration. *Geophysical Research Letters*, 42(2), 264–273. https://doi.org/10.1002/2014GL062553

Fedo, C. M., & Babechuk, M. G. (2022). Petrogenesis of siliciclastic sediments and sedimentary rocks explored in three-dimensional Al_2O_3–CaO*+ Na_2O–K_2O–FeO+ MgO (A-CN-K-FM) compositional space. *Canadian Journal of Earth Sciences*, (ja). https://doi.org/10.1139/cjes-2022-0051

Fedo, C. M., Bryk, A. B., Edgar, L. A., Bennett, K. A., Fox, V. K., Dietrich, W. E., ... & Sutter, B. (2022). Geology and stratigraphic correlation of the Murray and Carolyn Shoemaker formations across the Glen Torridon region, Gale crater, Mars. *Journal of Geophysical Research: Planets*, *127*(9)/ https://doi.org/10.1029/2022JE007408

Fedo, C. M., Eriksson, K. A., & Krogstad, E. J. (1996). Geochemistry of shales from the Archean (~ 3.0 Ga) Buhwa Greenstone Belt, Zimbabwe: implications for provenance and source-area weathering. *Geochimica et Cosmochimica Acta*, *60*(10), 1751-1763. https://doi.org/10.1016/0016-7037(96)00058-0

Fedo, C. M., McGlynn, I. O., & McSween Jr, H. Y. (2015). Grain size and hydrodynamic sorting controls on the composition of basaltic sediments: Implications for interpreting Martian soils. *Earth and Planetary Science Letters*, *423*, 67-77. https://doi.org/10.1016/j.epsl.2015.03.052

Fedo, C. M., Nesbitt, H.W., & Young, G. M. (1995). Unraveling the effects of potassium metasomatism in sedimentary rocks and paleosols, with implications for paleoweathering conditions and provenance. *Geology*, *23*(10), 921-924. https://doi.org/10.1130/0091-7613(1995)023<0921:UTEOPM>2.3.CO;2

Fedo, C. M., Young, G. M., Nesbitt, H. W., & Hanchar, J. M. (1997). Potassic and sodic metasomatism in the southern province of the Canadian Shield: evidence from the Paleoproterozoic Serpent Formation, Huronian Supergroup, Canada. *Precambrian Research, 84*(1-2), 17-36. https://doi.org/10.1016/S0301-9268(96)00058-7

Frihy, O. E., Deabes, E. A., Abudia, A. A., & Adawi, A. (2022). Heavy mineral composition and texture of the recently formed fluvial delta sediment of Lake Nasser/Nubia, Egypt and Sudan. *International Journal of Sediment Research*, *37*(1), 70-82. https://doi.org/10.1016/j.ijsrc.2021.07.002

Frydenvang, J., Mangold, N., Wiens, R. C., Fraeman, A. A., Edgar, L. A., Fedo, C. M., et al. (2020). The chemostratigraphy of the Murray formation and role of diagenesis at Vera Rubin ridge in Gale crater, Mars, as observed by the ChemCam instrument. *Journal of Geophysical Research: Planets*, *125*(9). https://doi.org/10.1029/2019JE006320

Gellert, R. (2013). MSL MARS ALPHA PARTICLE X-RAY SPECTROMETER 4/5 RDR V1.0 [Data set]. NASA Planetary Data System. https://doi.org/10.17189/1519440

Gellert, R. (2019). MER APXS derived oxide data bundle [Data set]. NASA Planetary Data System. https://doi.org/10.17189/1518973

Gellert, R., Campbell, J.L., King, P.L., Leshin, L.A., Lugmair, G.W., Spray, J.G., et al. (2009). The Alpha-Particle-X-Ray-Spectrometer (APXS) for the Mars Science Laboratory (MSL) rover mission. In the 40th Lunar and Planetary Science Conference, Abstract # 2364.

Gellert, R., Clark III, B. C., & MSL and MER Science Teams. (2015). In Situ compositional measurements of rocks and soils with the alpha particle x-ray spectrometer on NASA's Mars rovers. *Elements*, *11*(1), 39-44. https://doi.org/10.2113/gselements.11.1.39

Gellert, R., Rieder, R., Brückner, J., Clark, B. C., Dreibus, G., Klingelhöfer, G., et al. (2006). Alpha particle X-ray spectrometer (APXS): Results from Gusev crater and calibration report. *Journal of Geophysical Research*, 111(E2). https://doi.org/10.1029/2005JE002555

Grotzinger, J. P., Gupta, S., Malin, M. C., Rubin, D. M., Schieber, J., Siebach, K., et al. (2015). Deposition, exhumation, and paleoclimate of an ancient lake deposit, Gale crater, Mars. *Science, 350*(6257), aac7575. https://doi.org/10.1126/science.aac.7575

Gupta, S., Edgar, L., Yingst, R. A., Bryk, A., Caravaca, G., Dietrich, W., ... & Vasavada, A. (2022, September). Episodic aqueous conditions punctuated dominantly aeolian deposition within the layered sulphate-bearing unit, Gale crater (Mars). In *Europlanet Science Congress 2022* (Vol. 16, pp. EPSC2022-963).

Gwizd, S., Fedo, C., Grotzinger, J., Banham, S., Rivera-Hernandez, F., Stack, K. M., et al. (2022). Sedimentological and Geochemical Perspectives on a Marginal Lake Environment Recorded in the Hartmann's Valley and Karasburg Members of the Murray Formation, Gale Crater, Mars. *Journal of Geophysical Research: Planets*, *127*(8). https://doi.org/10.1029/2022JE007280

Haber, J. T., Horgan, B., Fraeman, A. A., Johnson, J. R., Bell III, J. F., Rice, M. S., et al. (2022). Mineralogy of a possible ancient lakeshore in the Sutton Island member of Mt. Sharp, Gale crater, Mars, from Mastcam multispectral images. *Journal of Geophysical Research: Planets*, *127*(10). https://doi.org/10.1029/2022JE007357

Horgan, B. H., Johnson, J. R., Fraeman, A. A., Rice, M. S., Seeger, C., Bell III, J. F., et al. (2020). Diagenesis of Vera Rubin Ridge, Gale crater, Mars, from mastcam multispectral images. *Journal of Geophysical Research: Planets*, *125*(11). https://doi.org/10.1029/2019JE006322

Howie, R. A. (1955). The geochemistry of the charnockite series of Madras, India. *Earth and Environmental Science Transactions of the Royal Society of Edinburgh*, *62*(3), 725-768. https://doi.org/10.1017/S0080456800009431

Hurowitz, J., Grotzinger, J., Fischer, W., McLennan, S. M., Milliken, R., Stein, N., et al. (2017). Redox stratification of an ancient lake in Gale crater, Mars. *Science*, *356*(6341). https://doi.org/10.1126/science.aah6849

Johnsson, M.J. (1993). The system controlling the composition of clastic sediments. *In: Processes Controlling the Composition of Clastic Sediments*, *Geological Society of America Special Paper* (Eds. Johnsson, M.J. & Basu, A.), *284*, 1-19.

Kronyak, R. E., Kah, L. C., Edgett, K. S., VanBommel, S. J., Thompson, L. M., Wiens, R. C., et al. (2019). Mineral-filled fractures as indicators of multigenerational fluid flow in the Pahrump Hills member of the Murray formation, Gale crater, Mars. *Earth and Space Science*, *6*(2), 238-265. https://doi.org/10.1029/2018EA000482

Kuno, H. (1955). Ion substitution in the diopside-ferropigeonite series of clinopyroxenes. *American Mineralogist: Journal of Earth and Planetary Materials*, *40*(1-2), 70-93.

L'Haridon, J., Mangold, N., Fraeman, A. A., Johnson, J. R., Cousin, A., Rapin, W., et al. (2020). Iron Mobility During Diagenesis at Vera Rubin Ridge, Gale Crater, Mars. *Journal of Geophysical Research: Planets*, *125*(11), e2019JE006299.

MacNaughton, R. B., Dalrymple, R. W., & Narbonne, G. M. (1997). Early Cambrian braid-delta deposits, MacKenzie Mountains, north-western Canada. *Sedimentology*, *44*(4), 587-609. https://doi.org/10.1046/j.1365-3091.1997.d01-41.x

Malin, M. C. (2007). MRO CONTEXT CAMERA EXPERIMENT DATA RECORD LEVEL 0 V1.0 [Data set]. NASA Planetary Data System. https://doi.org/10.17189/1520266

Malin, M. C. (2013). MSL MARS MAST CAMERA 2 EDR IMAGE V1.0 [Data set]. NASA Planetary Data System. https://doi.org/10.17189/1520190

Mangold, N., Baratoux, D., Arnalds, O., Bardintzeff, J. M., Platevoet, B., Grégoire, M., & Pinet, P. (2011). Segregation of olivine grains in volcanic sands in Iceland and implications for Mars. *Earth and Planetary Science Letters*, *310*(3-4), 233-243. https://doi.org/10.1016/j.epsl.2011.07.025

Mangold, N., Dehouck, E., Fedo, C., Forni, O., Achilles, C., Bristow, T., et al. (2019). Chemical alteration of fine-grained sedimentary rocks at Gale crater. *Icarus*, *321*, 619-631. https://doi.org/10.1016/j.icarus.2018.11.004

Mangold, N., Schmidt, M. E., Fisk, M. R., Forni, O., McLennan, S. M., Ming, D. W., et al. (2017). Classification scheme for sedimentary and igneous rocks in Gale crater, Mars. *Icarus*, *284*, 1-17. https://doi.org/10.1016/j.icarus.2016.11.005

Mangold, N., Thompson, L. M., Forni, O., Williams, A. J., Fabre, C., Le Deit, L., et al. (2016). Composition of conglomerates analyzed by the Curiosity rover: Implications for Gale Crater crust and sediment sources. *Journal of Geophysical Research: Planets*, *121*(3), 353-387. https://doi.org/10.1002/2015JE004977

McEwen, A. S. (2005). MRO MARS HIGH RESOLUTION IMAGE SCIENCE EXPERIMENT EDR V1.0 [Data set]. NASA Planetary Data System. https://doi.org/10.17189/1520179

McGlynn, I. O., Fedo, C. M., & McSween Jr, H. Y. (2012). Soil mineralogy at the Mars Exploration Rover landing sites: An assessment of the competing roles of physical sorting and chemical weathering. *Journal of Geophysical Research: Planets*, *117*(E1). https://doi.org/10.1029/2011JE003861

McLennan, S. M., Anderson, R. B., Bell, J. F., Bridges, J. C., Calef, F., Campbell, J. L., et al. (2014). Elemental geochemistry of sedimentary rocks at Yellowknife Bay, Gale crater, Mars. *Science*, *343*(6169). https://doi.org/10.1126/science.1244734

McLennan, S. M., Bell III, J. F., Calvin, W. M., Christensen, P. R., Clark, B. D., De Souza, P. A., et al. (2005). Provenance and diagenesis of the evaporite-bearing Burns formation, Meridiani Planum, Mars. Earth and Planetary Science Letters, 240(1), 95-121. https://doi.org/10.1016/j.epsl.2005.09.041

McLennan, S. M., Grotzinger, J. P., Hurowitz, J. A., & Tosca, N. J. (2019). The sedimentary cycle on early Mars. *Annual Review of Earth and Planetary Sciences*, *47*, 91-118. doi:10.1146/annurev-earth-053018-060332

McSween, H. Y., Ruff, S. W., Morris, R. V., Gellert, R., Klingelhoefer, G., Christensen, P. R., et al. (2008). Mineralogy of volcanic rocks in Gusev crater, Mars: Reconciling mössbauer, alpha particle X-ray spectrometer, and miniature thermal emission spectrometer spectra. *Journal of Geophysical Research*, 113(E6), E06S04. https://doi.org/10.1029/2007JE002970

McSween, H. Y., Wyatt, M. B., Gellert, R., Bell III, J. F., Morris, R. V., Herkenhoff, K. E. et al. (2006). Characterization and petrologic interpretation of olivine-rich basalts at Gusev Crater, Mars. *Journal of Geophysical Research: Planets*, *111*(E2). https://doi.org/10.1029/2005JE002477

Milliken, R. E., Grotzinger, J. P., & Thomson, B. J. (2010). Paleoclimate of Mars as captured by the stratigraphic record in Gale Crater. *Geophysical Research Letters*, *37*(4). https://doi.org/10.1029/2009GL041870

Ming, D. W., Gellert, R., Morris, R. V., Arvidson, R. E., Brueckner, J., Clark, B. C., et al. (2008). Geochemical properties of rocks and soils in Gusev crater, Mars: Results of the alpha particle X-ray spectrometer from cumberland ridge to home plate. *Journal of Geophysical Research*, 113(E12), E12S39. https://doi.org/10.1029/2008JE003195

Morrison, S. M., Downs, R. T., Blake, D. F., Vaniman, D. T., Ming, D. W., Hazen, R. M., et al. (2018). Crystal chemistry of martian minerals from Bradbury Landing through Naukluft Plateau, Gale crater, Mars. *American Mineralogist: Journal of Earth and Planetary Materials*, *103*(6), 857-871. https://doi.org/10.2138/am-2018-6124

Muhlbauer, J. G., Fedo, C. M., & Moersch, J. E. (2020). Architecture of a distal pre-vegetation braidplain: Cambrian middle member of the Wood Canyon Formation, southern Marble Mountains, California, USA. *Sedimentology*, 67(2), 1084–1113. https://doi.org/10.1111/sed.12677

Nesbitt, H. W., Fedo, C. M., & Young, G. M. (1997). Quartz and feldspar stability, steady and non-steady-state weathering, and petrogenesis of siliciclastic sands and muds. *The Journal of Geology*, 105(2), 173–192. https://doi.org/10.1086/515908

Nesbitt, H. W., & Markovics, G. (1997). Weathering of granodioritic crust, long-term storage of elements in weathering profiles, and petrogenesis of siliciclastic sediments. *Geochimica et Cosmochimica Acta*, *61*(8), 1653-1670. https://doi.org/10.1016/S0016-7037(97)00031-8

Nesbitt, H. W., & Wilson, R.E. (1992), Recent chemical weathering of basalts. *American Journal of Science*, *292*(10), 740–777. https://doi.org/10.2475/ajs.292.10.740

Nesbitt, H. W., & Young, G. M. (1984). Prediction of some weathering trends of plutonic and volcanic rocks based on thermodynamic and kinetic considerations. *Geochimica et cosmochimica acta*, *48*(7), 1523-1534. https://doi.org/10.1016/0016-7037(84)90408-3

Nesbitt, H., & Young, G. M. (1982). Early Proterozoic climates and plate motions inferred from major element chemistry of lutites. *nature*, *299*(5885), 715-717. https://doi.org/10.1038/299715a0

Nesbitt, H. W., & Young, G. M. (1996). Petrogenesis of sediments in the absence of chemical weathering: effects of abrasion and sorting on bulk composition and mineralogy. *Sedimentology*, *43*(2), 341-358. https://doi.org/10.1046/j.1365-3091.1996.d01-12.x

Nichols, G. J., & Fisher, J. A. (2007). Processes, facies and architecture of fluvial distributary system deposits. *Sedimentary geology*, *195*(1-2), 75-90. https://doi.org/10.1016/j.sedgeo.2006.07.004

Olariu, C., & Bhattacharya, J. P. (2006). Terminal distributary channels and delta front architecture of river-dominated delta systems. *Journal of sedimentary research*, *76*(2), 212-233. https://doi.org/10.2110/jsr.2006.026

Palucis, M. C., Dietrich, W. E., Hayes, A. G., Williams, R. M., Gupta, S., Mangold, N., et al. (2014). The origin and evolution of the Peace Vallis fan system that drains to the Curiosity landing area, Gale Crater, Mars. *Journal of Geophysical Research: Planets*, 119(4), 705–728. https://doi.org/10.1002/2013JE004583

Rampe, E. B., Blake, D. F., Bristow, T. F., Ming, D. W., Vaniman, D. T., Morris, R. V., et al. (2020a). Mineralogy and geochemistry of sedimentary rocks and eolian sediments in Gale crater, Mars: A review after six Earth years of exploration with Curiosity. *Geochemistry*, *80*(2), 125605. https://doi.org/10.1016/j.chemer.2020.125605

Rampe, E. B., Bristow, T. F., Morris, R. V., Morrison, S. M., Achilles, C. N., Ming, D. W., et al. (2020b). Mineralogy of Vera Rubin ridge from the Mars science laboratory CheMin instrument. *Journal of Geophysical Research: Planets*, *125*(9). https://doi.org/10.1029/2020JE006527

Rapin, W., Ehlmann, B. L., Dromart, G., Schieber, J., Thomas, N. H., Fischer, W. W., et al. (2019). An interval of high salinity in ancient Gale crater lake on Mars. *Nature Geoscience, 12*(11), 889-895. https://doi.org/10.1038/s41561-019-0458-8

Schieber, J., Bish, D., Coleman, M., Reed, M., Hausrath, E. M., Cosgrove, J., et al. (2017). Encounters with an unearthly mudstone: Understanding the first mudstone found on Mars. *Sedimentology*, *64*(2), 311-358. https://doi.org/10.1111/sed.12318

Schmidt, M. E., Campbell, J. L., Gellert, R., Perrett, G. M., Treiman, A. H., Blaney, D. L., et al. (2014). Geochemical diversity in first rocks examined by the Curiosity Rover in Gale Crater: Evidence for and significance of an alkali and volatile-rich igneous source. *Journal of Geophysical Research: Planets*, 119(1), 64–81. https://doi.org/10.1002/2013JE004481

Schmidt, M. E., Perrett, G. M., Bray, S. L., Bradley, N. J., Lee, R. E., Berger, J. A., et al. (2018). Dusty rocks in Gale Crater: Assessing areal coverage and separating dust and rock contributions in APXS analyses. *Journal of Geophysical Research: Planets*, *123,* 1649–1673. https://doi.org/10.1029/2018JE005553

Siebach, K. L., Baker, M. B., Grotzinger, J. P., McLennan, S. M., Gellert, R., Thompson, L. M., & Hurowitz, J. A. (2017). Sorting out compositional trends in sedimentary rocks of the Bradbury group (Aeolis Palus), Gale crater, Mars. *Journal of Geophysical Research: Planets*, *122,* 295–328. https://doi.org/10.1002/2016JE005195

Southard, J. B., & Boguchwal, L. A. (1973). Flume experiments on the transition from ripples to lower flat bed with increasing sand size. *Journal of Sedimentary Research*, *43*(4), 1114-1121. https://doi.org/10.1306/74D72914-2B21-11D7-8648000102C1865D

Stack, K. M., Grotzinger, J. P., Lamb, M. P., Gupta, S., Rubin, D. M., Kah, L. C., et al. (2019). Evidence for plunging river plume deposits in the Pahrump Hills member of the Murray formation, Gale crater, Mars. *Sedimentology, 66*(5), 1768-1802. https://doi.org/10.1111/sed.12558

Stein, N., Grotzinger, J. P., Schieber, J., Mangold, N., Hallet, B., Newsom, H., ... & Dehouck, E. (2018). Desiccation cracks provide evidence of lake drying on Mars, Sutton Island member, Murray formation, Gale Crater. *Geology*, *46*(6), 515-518. https://doi.org/10.1130/G40005.1

Sun, V. Z., Stack, K. M., Kah, L. C., Thompson, L., Fischer, W., Williams, A. J., et al. (2019). Late-stage diagenetic concretions in the Murray formation, Gale crater, Mars. *Icarus*, *321*, 866-890. https://doi.org/10.1016/j.icarus.2018.12.030

Taylor, S. M., & McLennan, S. M. (2009). *Planetary crusts: Their composition, origin, and evolution*. Cambridge University Press.

Thompson, L.M., Berger, J.A., Spray, J.G., Fraeman, A.A., McCraig, M.A., O'Connell-Cooper, C.D., et al. (2020). APXS-derived compositional characteristics of Vera Rubin Ridge and Murray formation, Gale crater, Mars: Geochemical implications for the origin of the ridge. *Journal of Geophysical Research: Planets*, *125*(10). https://doi.org/10.1029/2019JE006319

Thompson, L. M., Schmidt, M. E., Spray, J. G., Berger, J. A., Fairén, A. G., Campbell, J. L., et al. (2016). Potassium-rich sandstones within the Gale impact crater, Mars: The APXS perspective. *Journal of Geophysical Research: Planets*, 121(10), 1981–2003. https://doi.org/10.1002/2016je005055

Thorpe, M. T., & Hurowitz, J. A. (2020). Unraveling sedimentary processes in fluvial sediments from two basalt dominated watersheds in northern Idaho, USA. *Chemical Geology*, *550*, 119673. https://doi.org/10.1016/j.chemgeo.2020.119673

Thorpe, M. T., Hurowitz, J. A., & Dehouck, E. (2019). Sediment geochemistry and mineralogy from a glacial terrain river system in southwest Iceland. *Geochimica et Cosmochimica Acta*, *263*, 140-166. https://doi.org/10.1016/j.gca.2019.08.003

Thorpe, M. T., Hurowitz, J. A., & Siebach, K. L. (2021). Source-to-Sink Terrestrial Analogs for the Paleoenvironment of Gale Crater, Mars. *Journal of Geophysical Research: Planets*, *126*(2). https://doi.org/10.1029/2020JE006530

Vaniman, D. T., Martínez, G. M., Rampe, E. B., Bristow, T. F., Blake, D. F., Yen, A. S., et al. (2018). Gypsum, bassanite, and anhydrite at Gale crater, Mars. *American Mineralogist: Journal of Earth and Planetary Materials*, *103*(7), 1011-1020. https://doi.org/10.2138/am-2018-6346

Watkins, J. A., Grotzinger, J. P., Stein, N. T., Banham, S. G., Gupta, S., Rubin, D. M., et al. (2022). Burial and exhumation of sedimentary rocks revealed by the base Stimson erosional unconformity, Gale crater, Mars. *Journal of Geophysical Research: Planets*. https://doi.org/10.1029/2022JE007293

Whitney, D. L., & Evans, B. W. (2010). Abbreviations for names of rock-forming minerals. *American Mineralogist*, *95*(1), 185–187. https://doi.org/10.2138/am.2010.3371

Williams, R. M. E., Grotzinger, J. P., Dietrich, W. E., Gupta, S., Sumner, D. Y., Wiens, R. C., et al. (2013). Martian fluvial conglomerates at Gale crater. *Science*, 340(6136), 1068–1072. https://doi.org/10.1126/science.1237317

Wiens, R. C., Edgett, K. S., Stack, K. M., Dietrich, W. E., Bryk, A. B., Mangold, N., et al. (2020). Origin and composition of three heterolithic boulder-and cobble-bearing deposits overlying the Murray and Stimson formations, Gale Crater, Mars. *Icarus*, 350, 113897. https://doi.org/10.1016/j.icarus.2020.113897

Young, G. M., & Nesbitt, H. W. (1998). Processes controlling the distribution of Ti and Al in weathering profiles, siliciclastic sediments and sedimentary rocks. *Journal of Sedimentary research*, *68*(3), 448-455. https://doi.org/10.2110/jsr.68.448

Appendix
Chapter 3 supplementary information

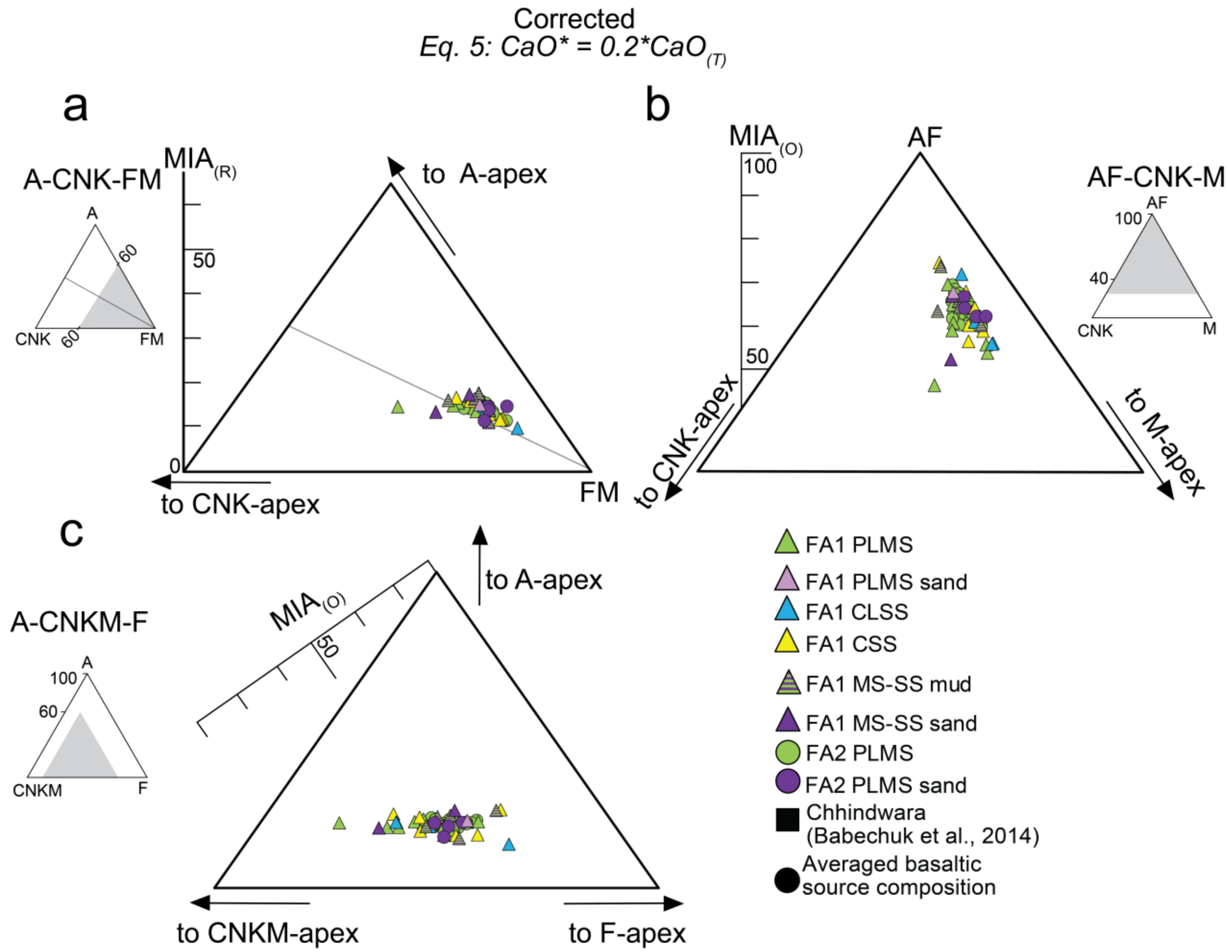

Figure 3.14 Weathering trends shown in (a) A-CNK-FM (b) AF-CNK-M and (c) A-CNKM-F molar ternary diagrams using data corrected with Equation 5. Shaded regions within small triangles correspond to the expanded regions in a-c.

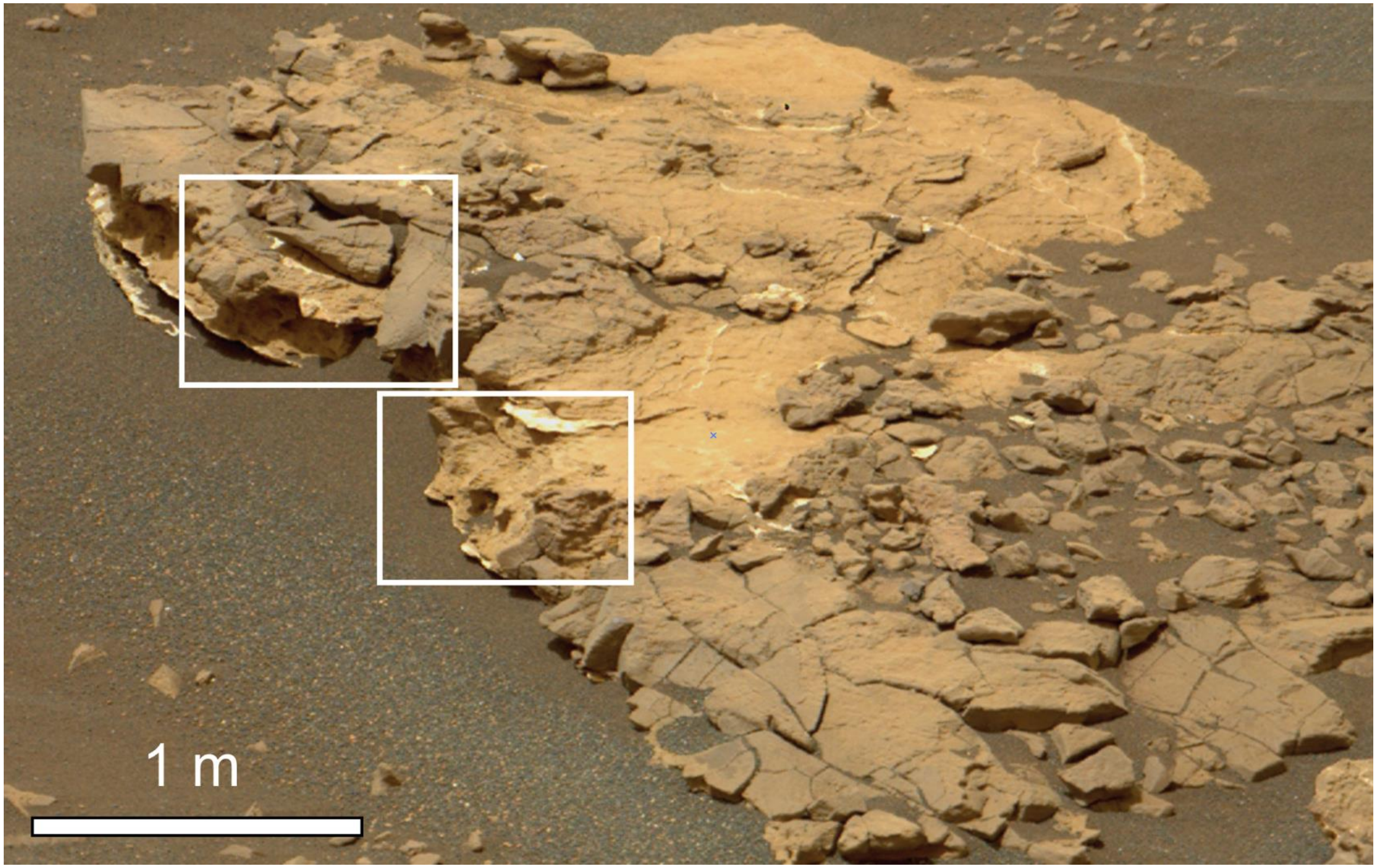

Figure 3.15 Outcrop of planar-laminated mudstone with minor sandstone facies in FA1 showing regions of discontinuity (highlighted in white boxes) of dark-toned Mg-sulfate-enriched zones (interpreted from ChemCam data in Rapin et al., 2019) with respect to primary stratigraphy (M100 Mastcam image, mcam08708, Sol 1678).

CONCLUSIONS

Facies in the Murray formation record lacustrine paleoenvironments characterized by standing water (Edgar et al., 2020; Fedo et al., 2022; Stack et al., 2019) and lacustrine-margin paleoenvironments characterized by fluctuations in energy and variable aqueous activity (Gwizd et al., 2022). This dissertation provides insight into the depositional environments and sedimentary processes recorded in the Hartmann's Valley, Karasburg, and Sutton Island members of the Murray formation at Gale crater, Mars. Prior to this research, these members were noted for their distinctive facies assemblages (Fedo et al., 2018; Stein et al., 2018), but had only been studied on a cursory level. Observations and measurements from Navcam, Mastcam, MAHLI, and ChemCam RMI images acquired with the Curiosity rover were used to interpret the facies and stratal stacking patterns and to contextualize APXS compositional signatures of source rock composition, weathering, transport, and diagenesis within the 160-m stratigraphic record. This research ultimately extends the range of facies and sedimentary processes recorded in the Murray formation and provides a refined understanding of paleoenvironments on ancient Mars.

Facies documented in the Hartmann's Valley and Karasburg members include cross-stratified sandstone, planar-laminated sandstone, and planar-laminated mudstone. Both sandstone facies are interpreted to represent aeolian dune and interdune paleoenvironments deposited along a lacustrine margin. Relative thicknesses and stratal stacking patterns between cross-stratified and planar-laminated sandstone facies are consistent with isolated dune and interdune environments in wet aeolian settings (e.g. Skeiđarársandur. Mountney & Russell, 2009). Planar-laminated mudstone is interpreted to represent deposition via density currents in a lacustrine basin and is consistent with interpretations of similar facies in other stratigraphic members (Edgar et al., 2020; Stack et al., 2019). Facies are interpreted to derive from a basaltic source at the northern crater rim (Buz et al., 2014; Grotzinger et al., 2015) or from regional watersheds (Ehlmann & Buz, 2017). The source rock composition exhibits a similar geochemical signature to Gale crater igneous float rocks (Berger et al., 2020; Schmidt et al., 2014; Thompson et al., 2016; Wiens et al., 2020) and Gusev crater basalt classes (Gellert et al., 2006; McSween et al., 2008; Ming et al., 2008). Weathering indices and geochemical trends indicate moderate levels of chemical weathering. Immobile oxides show the influence of hydrodynamic sorting of sediment in transport, consistent with the environments interpreted along the lacustrine margin. Diagenetic phases are prevalent throughout all facies, with calcium sulfate constituting the most common composition. This study highlights the importance of correcting for common non-silicate phases such as calcium sulfate in order to more accurately decipher geochemical signatures of primary silicate sedimentary processes along the source-to-sink path (Johnsson et al., 1993). Geochemical similarity between facies indicates that the total grain-size range captured in the Hartmann's Valley and Karasburg paleoenvironments was relatively restricted, and that depositional environments were likely located more proximal to the basin center.

The Sutton Island member consists of two facies associations: Facies Association 1 (FA1) and Facies Association 2 (FA2). Facies Association 1 comprises the lower (39 m) and upper (14 m) intervals of stratigraphy, and FA2 comprises the middle (42 m) interval of stratigraphy. Facies in FA1 include planar-laminated mudstone with minor sandstone, ripple cross-laminated sandstone, cross-stratified sandstone, and alternating laminated sandstone and mudstone. The distribution of facies in FA1 is consistent with a distal delta plain environment characterized by distributary systems, ponded water, and localized subaerial exposure facilitating desiccation and reworking. Facies in FA2 include planar-laminated mudstone with minor sandstone. The thick succession of continuous planar laminae is consistent with deposition in a lake basin. The lower stratigraphic transition between FA1 and FA2 signifies a rapid interval of lake expansion (transgression) that was substantial enough to drown delta plain environments and rapid enough to facilitate deposition of lacustrine facies below wave base over delta plain facies. The upper stratigraphic transition between FA2 and FA1 signifies an interval of lake regression characterized by base-level fall. Lake-level shifts may result from aspects of basin physiography or climate (Bohacs et al., 2000). Overall, the facies identified in the Sutton Island member are consistent with aqueous environments identified throughout the Murray formation.

Alpha Particle X-Ray Spectrometer whole-rock geochemical data are evaluated within the framework of Sutton Island facies associations interpreted in Chapter 2. Facies are consistent with a similar basaltic source composition as the Hartmann's Valley and Karasburg stratigraphy (Gwizd et al., 2022), and may have derived from the northern crater rim (Buz et al., 2017) or more regional watersheds (Ehlmann & Buz, 2014). Chemical weathering generated a sediment mixture of primary and phyllosilicate mineral phases (Achilles et al., 2020; Bristow et al., 2018). Weathering indices and geochemical trends signify a slight shift to more steady-state conditions (Nesbitt et al., 1997) relative to the underlying Hartmann's Valley and Karasburg members (Gwizd et al., 2022). Given the depositional processes responsible for FA1 and FA2, sorting is expected to occur. Overall trends in immobile oxides in Sutton Island stratigraphy are indicative of hydrodynamic sorting of sediment in transport (Young & Nesbitt, 1998), but the lack of differences between facies contrasts with expected compositional links with sediment size, shape, and density (Nesbitt & Young, 1996). This finding may be due to source phenocryst size (Fedo et al., 2015) or a small overall grain-size range captured by the Sutton Island member facies. Mixing of grain sizes within facies subject to reworking may also explain the geochemical homogeneity. Contextualization of geochemical signatures with textural observations (Rapin et al., 2019; Sun et al., 2019) and mineralogical measurements (Achilles et al., 2020; Bristow et al., 2018) indicates variable fluid episodes representative of early- to late-stage diagenesis. Calcium sulfate is the most prevalent interpreted phase. Compared to the findings in Chapter 1, the findings of this study highlight the need to apply a more refined correction for non-silicate calcium sulfate in order to more accurately decipher the geochemical source-to-sink history of primary silicate sediments within the basin.

References

Achilles, C. N., Rampe, E. B., Downs, R. T., Bristow, T. F., Ming, D. W., Morris, R. V., et al. (2020). Evidence for multiple diagenetic episodes in ancient fluvial-lacustrine sedimentary rocks in Gale crater, Mars. *Journal of Geophysical Research: Planets*, *125*(8), e2019JE006295. https://doi.org/10.1029/2019JE006295

Berger, J. A., Gellert, R., Boyd, N. I., King, P. L., McCraig, M. A., O'Connell-Cooper, C. D., et al. (2020). Elemental composition and chemical evolution of geologic materials in Gale Crater, Mars: APXS results from Bradbury landing to the Vera Rubin ridge. *Journal of Geophysical Research: Planets*, 125(12). https://doi.org/10.1029/2020JE006536

Bohacs, K. M., Carroll, A. R., Neal, J. E., & Mankiewicz, P. J. (2000). Lake-basin type, source potential, and hydrocarbon character: an integrated sequence-stratigraphic-geochemical framework. *Lake basins through space and time: AAPG Studies in Geology*, 46, 3-34.

Bristow, T. F., Rampe, E. B., Achilles, C. N., Blake, D. F., Chipera, S. J., Craig, P., et al. (2018). Clay mineral diversity and abundance in sedimentary rocks of Gale crater, Mars. *Science Advances, 4*(6). https://doi.org/10.1126/sciadv.aar3330

Buz, J., Ehlmann, B. L., Pan, L., & Grotzinger, J. P. (2017). Mineralogy and stratigraphy of the Gale crater rim, wall, and floor units. *Journal of Geophysical Research: Planets*, *122*(5), 1090-1118. https://doi.org/10.1002/2016JE005163

Edgar, L. A., Fedo, C. M., Gupta, S., Banham, S. G., Fraeman, A. A., Grotzinger, J. P., et al. (2020). A lacustrine paleoenvironment recorded at Vera Rubin Ridge, Gale crater: Overview of the sedimentology and stratigraphy observed by the Mars Science Laboratory Curiosity Rover. *Journal of Geophysical Research: Planets*, *125*(3). https://doi.org/10.1029/2019je006307

Ehlmann, B. L., & Buz, J. (2015). Mineralogy and fluvial history of the watersheds of Gale, Knobel, and sharp craters: A regional context for the Mars science laboratory Curiosity's exploration. *Geophysical Research Letters*, 42(2), 264–273. https://doi.org/10.1002/2014GL062553

Fedo, C. M., Bryk, A. B., Edgar, L. A., Bennett, K. A., Fox, V. K., Dietrich, W. E., et al. (2022). Geology and stratigraphic correlation of the Murray and Carolyn Shoemaker formations across the Glen Torridon region, Gale crater, Mars. *Journal of Geophysical Research: Planets*. https://doi.org/10.1029/2022JE007408

Fedo, C. M., Grotzinger, J., Gupta, S., Fraeman, A., Edgar, L., Edgett, K., et al. (2018). Sedimentology and stratigraphy of the Murray formation, Gale crater, Mars. In the 49th Lunar and Planetary Science Conference, Abstract #2083.

Fedo, C. M., McGlynn, I. O., & McSween Jr, H. Y. (2015). Grain size and hydrodynamic sorting controls on the composition of basaltic sediments: Implications for interpreting Martian soils. *Earth and Planetary Science Letters*, *423*, 67-77. https://doi.org/10.1016/j.epsl.2015.03.052

Gellert, R., Rieder, R., Brückner, J., Clark, B. C., Dreibus, G., Klingelhöfer, G., et al. (2006). Alpha particle X-ray spectrometer (APXS): Results from Gusev crater and calibration report. *Journal of Geophysical Research*, 111(E2). https://doi.org/10.1029/2005JE002555

Grotzinger, J. P., Gupta, S., Malin, M. C., Rubin, D. M., Schieber, J., Siebach, K., et al. (2015). Deposition, exhumation, and paleoclimate of an ancient lake deposit, Gale crater, Mars. *Science*, *350*(6257), aac7575. https://doi.org/10.1126/science.aac.7575

Gwizd, S., Fedo, C., Grotzinger, J., Banham, S., Rivera-Hernández, F., Stack, K. M., et al. (2022). Sedimentological and Geochemical Perspectives on a Marginal Lake Environment Recorded in the Hartmann's Valley and Karasburg Members of the Murray Formation, Gale Crater, Mars. *Journal of Geophysical Research: Planets*, *127*(8). https://doi.org/10.1029/2022JE007280

Johnsson, M.J. (1993). The system controlling the composition of clastic sediments. *In: Processes Controlling the Composition of Clastic Sediments*, *Geological Society of America Special Paper* (Eds. Johnsson, M.J. & Basu, A.), *284*, 1-19.

McSween, H. Y., Ruff, S. W., Morris, R. V., Gellert, R., Klingelhoefer, G., Christensen, P. R., et al. (2008). Mineralogy of volcanic rocks in Gusev crater, Mars: Reconciling mössbauer, alpha particle X-ray spectrometer, and miniature thermal emission spectrometer spectra. *Journal of Geophysical Research*, 113(E6), E06S04. https://doi.org/10.1029/2007JE002970

Ming, D. W., Gellert, R., Morris, R. V., Arvidson, R. E., Brueckner, J., Clark, B. C., et al. (2008). Geochemical properties of rocks and soils in Gusev crater, Mars: Results of the alpha particle X-ray spectrometer from cumberland ridge to home plate. *Journal of Geophysical Research*, 113(E12), E12S39. https://doi.org/10.1029/2008JE003195

Mountney, N. P., & Russell, A. J. (2009). Aeolian dune-field development in a water table-controlled system: Skeiđarársandur, Southern Iceland. *Sedimentology*, 56(7), 2107–2131. https://doi.org/10.1111/j.1365-3091.2009.01072.x

Nesbitt, H. W., Fedo, C. M., & Young, G. M. (1997). Quartz and feldspar stability, steady and non-steady-state weathering, and petrogenesis of siliciclastic sands and muds. *The Journal of Geology*, 105(2), 173–192. https://doi.org/10.1086/515908

Nesbitt, H. W., & Young, G. M. (1996). Petrogenesis of sediments in the absence of chemical weathering: effects of abrasion and sorting on bulk composition and mineralogy. *Sedimentology*, *43*(2), 341-358. https://doi.org/10.1046/j.1365-3091.1996.d01-12.x

Rapin, W., Ehlmann, B. L., Dromart, G., Schieber, J., Thomas, N. H., Fischer, W. W., et al. (2019). An interval of high salinity in ancient Gale crater lake on Mars. *Nature Geoscience*, *12*(11), 889-895. https://doi.org/10.1038/s41561-019-0458-8

Schmidt, M. E., Campbell, J. L., Gellert, R., Perrett, G. M., Treiman, A. H., Blaney, D. L., et al. (2014). Geochemical diversity in first rocks examined by the Curiosity Rover in Gale Crater: Evidence for and significance of an alkali and volatile-rich igneous source. *Journal of Geophysical Research: Planets*, 119(1), 64–81. https://doi.org/10.1002/2013JE004481

Stack, K. M., Grotzinger, J. P., Lamb, M. P., Gupta, S., Rubin, D. M., Kah, L. C., et al. (2019). Evidence for plunging river plume deposits in the Pahrump Hills member of the Murray formation, Gale crater, Mars. *Sedimentology*, 66(5), 1768–1802. https://doi.org/10.1111/sed.12558

Stein, N., Grotzinger, J. P., Schieber, J., Mangold, N., Hallet, B., Newsom, H., ... & Dehouck, E. (2018). Desiccation cracks provide evidence of lake drying on Mars, Sutton Island member, Murray formation, Gale Crater. *Geology*, *46*(6), 515-518. https://doi.org/10.1130/G40005.1

Sun, V. Z., Stack, K. M., Kah, L. C., Thompson, L., Fischer, W., Williams, A. J., et al. (2019). Late-stage diagenetic concretions in the Murray formation, Gale crater, Mars. *Icarus*, *321*, 866-890. https://doi.org/10.1016/j.icarus.2018.12.030

Thompson, L. M., Schmidt, M. E., Spray, J. G., Berger, J. A., Fairén, A. G., Campbell, J. L., et al. (2016). Potassium-rich sandstones within the Gale impact crater, Mars: The APXS perspective. *Journal of Geophysical Research: Planets*, 121(10), 1981–2003. https://doi.org/10.1002/2016je005055

Wiens, R. C., Edgett, K. S., Stack, K. M., Dietrich, W. E., Bryk, A. B., Mangold, N., et al. (2020). Origin and composition of three heterolithic boulder-and cobble-bearing deposits overlying the Murray and Stimson formations, Gale Crater, Mars. *Icarus*, 350, 113897. https://doi.org/10.1016/j.icarus.2020.113897

Young, G. M., & Nesbitt, H. W. (1998). Processes controlling the distribution of Ti and Al in weathering profiles, siliciclastic sediments and sedimentary rocks. *Journal of Sedimentary research*, *68*(3), 448-455. https://doi.org/10.2110/jsr.68.448

VITA

Samantha Gwizd was born and raised on Cape Cod, Massachusetts. She attended Barnstable High School and graduated in 2009. She attended Boston University and graduated with a B.A. in Earth Sciences in 2013. Samantha did her senior work for distinction project as a member of Dr. Rick Murray's lab group under the supervision of Dr. Rachel Scudder, investigating compositional signatures of dispersed volcanic ash within a deep sea drilling core from the northwest Pacific. Subsequent to graduation, Samantha attended a five-week summer field camp in Sardinia, Italy through Boise State. Following her travels, she moved to Santa Barbara, California to pursue a M.S. in Geological Sciences working with Dr. David Lea. Her thesis involved analysis of stable isotopes of foraminifera in an ocean drilling core from the eastern equatorial Pacific ocean. After graduating in September 2015, Samantha worked at Princeton University as a lab manager for Drs. Adam Maloof and Blair Schoene. Samantha began the Ph.D. program at the University of Tennessee in the fall of 2016, working under the supervision of Dr. Chris Fedo. She joined the Mars Science Laboratory Curiosity rover team in the spring of 2017, and began fulfilling regular operations shifts as the "keeper of the plan". While pursuing her Ph.D., Samantha has been a teaching assistant for numerous undergraduate and graduate classes, given guest and invited lectures, volunteered for numerous outreach events, been a treasurer/secretary of the Geoclub, coordinated Soft Rock Brown Bag seminar, collaborated on a Mars analog study (RAVEN), presented at conferences and MSL team meetings, and co-chaired a session at the Geological Society of America annual meeting. Following graduation from UT, Samantha will begin a postdoctoral fellowship at the Jet Propulsion Laboratory in Pasadena, CA, under the supervision of Dr. Kathryn Stack Morgan.